Annual Research Journal

Electrical Engineering
Research Experience for Undergraduates

Vol. III

August 2005

National Science Foundation
Grant No. EEC-0244030

Principal Investigators:
Ruyan Guo and Kenneth Jenkins

PENNSTATE

Department of Electrical Engineering
University Park, Pennsylvania

EEREU Annual Research Journal

Ruyan Guo (editor)
W. Kenneth Jenkins (co-editor)

Published in 2005 by
The Department of Electrical Engineering
The Pennsylvania State University
University Park, Pennsylvania, 16802

NSF EE REU Site Program Contact

316 Electrical Engineering East
The Pennsylvania State University
University Park, PA 16802
Telephone (814) 865-0184
Fax (814) 865-7065
E-Mail: eereu@engr.psu.edu
Web Site: http://www.ee.psu.edu/reu/

ISBN 0-913260-05-3

PREFACE

The third year of the National Science Foundation (NSF) Research Experience for Undergraduates (REU) Site Program was hosted by the Department of Electrical Engineering during the summer of 2005. This year we had distinctive pleasure of working with eighteen outstanding young men and women in the EEREU program at Penn State's University Park Campus. The participating students, primarily college sophomores or juniors with outstanding academic backgrounds, were selected from nation-wide applicants interested in exploring research in electrical engineering and related areas.

During the nine-week summer program, the REU students were engaged in research projects, each working under the guidance of a faculty mentor(s). Eighteen research projects were carried out, individual findings were presented at the annual *EEREU Symposium*, and technical papers were written by the EEREU students as the primary authors. We are happy to present this year's *Annual Research Journal – Electrical Engineering Research Experience for Undergraduates, Vol. III* that contains the technical reports from the 2005 EEREU program. Nearly all these reports document original research and are of value for scientific dissemination and publication. The journal showcases the achievement of our EEREU students and demonstrates the effective mentorship provided by the faculty and graduate student mentoring teams.

Besides research activities, the EEREU program organized a *Weekly Scientific Seminar Series* that involved leading researchers/scientists at Penn State who introduced the broad research frontier to the REU students. Students also went on *field trips* to visit prominent local, national and international industrial research sites, and they were engaged in debate and analysis of real ethical problems in engineering through *Weekly Workshop on Professional Development and Ethics*. For more information about Penn State's Research Experience for Undergraduates Program in Electrical Engineering, please visit our website at: http://www.ee.psu.edu/reu/.

We are confident that this journal can serve as a stepping-stone for our EEREU students at the beginning stage of their long research career. We are also hopeful that this journal may stimulate more college students to consider research career and pursue graduate studies in electrical engineering.

Ruyan Guo and W. Kenneth Jenkins
Co-Directors of the NSF EE REU Site Program
Dept. EE, The Pennsylvania State University

July 2005
University Park, Pennsylvania

TABLE OF CONTENTS

Research Articles (* indicates REU student author)

2005 NSF EEREU FACULTY AND STAFF MEMBERS

Faculty Mentors

Prof. Amar Bhalla
Prof. Sven Bilén
Prof. Charles Croskey
Prof. Craig Grimes
Prof. Ruyan Guo, Co-Director
Prof. Heath Hofmann
Prof. Ken Jenkins, Co-Director
Prof. I. C. Khoo
Prof. Mike Lanagan
Prof. John Mitchell, Seminar Chair
Prof. Victor Pasko
Prof. Joan Redwing
Prof. Jeff Schiano
Prof. Srinivas Tadigadapa
Prof. Kenji Uchino

Prof. Andy Lau, Ethics Workshop Chair
Prof. David Salvia, Activities Chair
Ms. Amy Freeman, Director, Multicultural Program

Mrs. Linda Becker, Administration
Miss Amanda Skrabut, Assistant Director
Mr. Andrew Fontanella, Publ. Chair

2005 NSF EEREU SCHOLARS, RESEARCH AREAS, AND FACULTY MENTORS

REU SCHOLARS	RESEARCH AREAS	FACULTY MENTORS
Mr. Stephen Tomko Computer Engineering Penn State University	Interactions of Electric and Magnetic Components in MetaMaterials	Prof. Amar Bhalla 187 MATERIALS RES LAB BLDG
Mr. Thomas Riccobono Electrical Engineering New Jersey Institute of Technology	Research and Development of the LionSat Sensor System Hardware	Prof. Sven Bilén 213N HAMMOND BLDG
Miss Urenna Onyewuchi Electrical Engineering George Mason University	Demonstration of Distributed Sensor Networks	Prof. Sven Bilén 213N HAMMOND BLDG
Mr. Brian Park Electrical Engineering Swarthmore College	Solar Generation of Hydrogen by Water Photolysis	Prof. Craig Grimes 217 MATERIALS RES LAB BLDG
Mr. Kong "Chhay" Tep Electrical Engineering Michigan State University	Solar Generation of Hydrogen by Water Photolysis	Prof. Craig Grimes 217 MATERIALS RES LAB BLDG
Mr. Jonathan Taylor Electrical Engineering Cedarville University	Microwave Photonic Interactions in Piezoelectric Materials	Prof. Ruyan Guo 108B RUA, MATERIALS RES LAB
Miss Mintiwab Sahele Electrical engineering New Jersey Institute of Technology	Piezoelectric Energy Harvesting	Prof. Heath Hofmann 209K ELEC ENGR WEST
Mr. Navjit Grewal Electrical Engineering & Applied Math University of Rhode Island	Study of Using High Speed RNS Arithmetic for the VLSI Implementation of Neural Networks	Prof. Ken Jenkins 121 ELEC ENGR EAST
Mr. Scott Jobling Electrical Engineering University of Massachusetts - Lowell	Supra-nonlinear Liquid Crystalline Materials & Nano-particulate Doped Nonlinear Liquid Crystals and Photonic Crystals	Prof. I. C. Khoo 217 ELEC ENGR EAST
Mr. Kevin Deily Electrical Engineering Ohio Northern University	High Frequency Characterization of Semiconductors	Prof. Mike Lanagan 278 MATERIALS RES LAB BLDG

2005 NSF EEREU SCHOLARS, RESEARCH AREAS, AND FACULTY MENTORS (CONT.)

Mr. Andrew Casperson Electrical Engineering U. of North Carolina at Charlotte	System Development for A Small Sounding Rocket Payload	Prof. J. Mitchell 330 ELEC ENGR EAST and Prof. Charles Croskey 304 ELEC ENGR EAST
Mr. David Burkhardt Physics Haverford College	Studies of Lightning Induced Electrical Discharges in the Upper Atmosphere	Prof. Victor Pasko 121 ELEC ENGR EAST
Mr. Liang Di Electrical Engineering Penn State	Studies of Atmospheric Gravity Waves	Prof. Victor Pasko 121 ELEC ENGR EAST
Mr. Eric Dattoli Computer Engineering, Hardware Emphasis University of Florida	Assembly and Characterization of Silicon Nanowires for Nanoelectronic Applications	Prof. Joan Redwing 108 STEIDLE BLDG
Mr. Stephen Hall Electrical Engineering Penn State University (Date bachelor: 5/2006)	Characterization of the Dynamic Behavior of Loss Mechanisms in Thin-Film High Temperature Superconducting Resonators	Prof. Jeff Schiano 227D ELEC ENGR WEST
Mr. Timo Mechler Computer Science, Math, and Physics Luther College	Effect of Nanomaterials on the Resonant Characteristics of MEMS Structures	Prof. Srinivas Tadigadapa 121 ELEC ENGR EAST
Mr. Vincent Hood Aerospace and Mechanical Engineering Rensselaer Polytech Inst.	Development and Analysis for Optimization of An ICP-RIE System	Prof. Srinivas Tadigadapa 121 ELEC ENGR EAST
Mr. Daniel Gallagher Electrical Engineering Cedarville University	Nano Factory	Prof. Kenji Uchino 134 MATERIALS RES LAB BLDG

NSF EE REU 2005 Summer Program
Weekly Scientific Seminar

Department of Electrical Engineering
Pennsylvania State University, University Park, PA 16802

Room 225 E E West, 11:00 – 11:45 AM, Tuesdays
Seminar Chair: **Prof. John Mitchell** (jdm4@psu.edu)

(Followed by **REU Weekly Workshop on Professional Development,** 12:30-1:30 PM)

Date	*Topic*	*Speaker*
June 7, 2005	Topics in Digital Speech Signal Processing	Robert Nickel
June 14, 2005	Lightning-related Transient Luminous Events in the Middle Atmosphere	Victor Pasko
June 21, 2005	Software Defined Radio Applications	Sven Bilén
June 28, 2005	Semiconductor Nanowires: Building Blocks for Nanoscale Devices	Joan Redwing
July 5, 2005	Sensors Using Micro and Nanoscale Structures	Srinivas Tadigadapa
July 12, 2005	What's Next? Graduate School, of Course!	Ken Jenkins
July 19, 2005	Energy Harvesting	Heath Hofmann
July 26, 2005	(Field Trip Lab Tours)	
July 28, 2006	2005 NSF EEREU Symposium (8:30 am – 4:00pm)	REU Students

NSF EE REU 2005 Summer Program
Weekly Workshop on Professional Development and Ethics in Science and Engineering

Department of Electrical Engineering
Pennsylvania State University, University Park, PA 16802

Room 225 EE West, 12:30 pm –1:30 pm, Tuesdays
Chair: **Prof. Andrew Lau** (andylau@psu.edu)

Date	*Workshop Topic Addressed*	*Weekly*	*Faculty Leader*
June 1	(Welcome Meeting, 11:00 am)	***Week 1***	Prof. Andy Lau (Chair)
June 7	Introduction; Types of Moral Problems; Academic Integrity	***Week 2***	
June 14	Central Professional Responsibilities of Engineers – Codes of Ethics and Their Application; The Responsible Conduct of Research	***Week 3***	
June 21	Global Environmental Issues: Climate Change, Oil Depletion, Sustainability	***Week 4***	
June 28	Happy Valley Values - The Game	***Week 5***	
July 5	Intellectual Property and Proposal Writing	***Week 6***	
July 12	Student Presentations of Ethical Issues in Their Research - Round 1	***Week 7***	
July 19	Student Presentations of Ethical Issues in Their Research - Round 2	***Week 8***	
July 26	(Reserved for local field trip 'Lab show & tell')	***Week 9***	
July 28	(2005 EEREU Symposium)		

2005 NSF EE REU Bi-Weekly Field Trips and Industrial Sponsors

Nanofabrication National Facility
Penn State University
University Park, Pennsylvania

AccuWeather, Inc.
State College, Pennsylvania

Videon Central, Inc.
State College, Pennsylvania

Sound Technology, Inc.
State College, Pennsylvania

State of The Art, Inc.
State College, Pennsylvania

Applied Research Laboratory
Penn State University
University Park, Pennsylvania

VertexRSI
State College, Pennsylvania

2005 NSF EE REU SYMPOSIUM

Final Program

8:30 AM to 4:00 PM, Thursday, July 28, 2005
Room 225 Electrical Engineering West Building
Pennsylvania State University
University Park, PA 16802

Time	Sessions and Topics	Chairs and Speakers
8:30 - 8:55 am	**Symposium Registration (Refreshments Provided)**	**Linda Becker/ Amanda Skrabut**
8:55 – 9:00 am	**Welcome**	**Jack Mitchell**
9:00 – 10:15 am	**Session I** Session Chairs:	**Croskey/Mitchell/ Bilén/Pasko**
9:00 – 9:15	RESEARCH AND DEVELOPMENT OF LIONSAT SENSOR BOARD HARDWARE	Thomas Riccobono
9:15 – 9:30	DEMONSTRATION OF DISTRIBUTED SENSOR NETWORKS	Urenna Onyewuchi
9:30 – 9:45	ELECTROMETER DESIGN FOR A SOUNDING ROCKET PAYLOAD	Andrew Casperson
9:45 – 10:00	ATMOSPHERIC ABSORPTION OF SPRITE EMISSIONS OBSERVED BY ISUAL INSTRUMENTATION	David Burkhardt
10:00 – 10:15	INTERPOLATION OF WIND DATA FOR THE ANALYSIS OF DUCTED GRAVITY WAVE VERTICAL STRUCTURE	Liang Di
	10:15 – 10:30 am Coffee Break	
10:30 – 11:45 am	**Session II** Session Chairs:	**Grimes/Schiano/ /Hofmann**
10:30 – 10:45	DETECTING TOUCH-TONE FREQUENCY IN TELEPHONE SYSTEMS USING ADAPTIVE FILTERING AND CLASSIFICATION OF SPEECH SIGNALS	Navjit Grewal
10:45 – 11:00	DESIGN OF A CONTINUOUS WAVE QUADRUPOLE RESONANCE SPECTROMETER FOR UNDERGRADUATE LABORATORY STUDIES IN PHYSICS AND CHEMISTRY	Stephen Hall
11:00 – 11:15	NITROGEN DOPING OF TITANIUM OXIDE VIA ANODIC OXIDATION	Kong Chhay Tep
11:15 – 11:30	FABRICATION OF IRON (III) OXIDE NANOSTRUCTURES BY POTENTIOSTATIC ANODIZATION	Brian Park
11:30 – 11:45	PIEZOELECTRIC ENERGY HARVESTING USING DIFFERENT APPROACHES INCLUDING CONTROL SYSTEM	Mintiwab Sahele
11:45 Noon	**(Group Photo – All invited. Please plan to be available)**	(Andrew Fontanella)
	12:00 – 1:15 pm Luncheon (Atherton Hotel)	

2005 NSF EE REU SYMPOSIUM (cont.)

Final Program

8:55 AM to 3:45 PM, Thursday, July 28, 2005
Room 225 Electrical Engineering West Building
Pennsylvania State University
University Park, PA 16802

Time	Sessions and Topics	Chairs and Speakers
1:30 – 2:30 pm	**Session III** Session Chairs:	**Khoo/Tadigadapa**
1:30 – 1:45	ELECTRICAL CHARACTERIZATION OF SILICON NANOWIRE *P-N* JUNCTIONS	Eric Dattoli
1:45 – 2:00	DEVELOPMENT OF A CONSTANT LEVEL OSCILLATOR CIRCUIT FOR DYNAMIC MONITORING OF RESONANCE FREQUENCY AND QUALITY FACTOR OF A QUARTZ CRYSTAL MICROBALANCE (QCM)	Timo Mechler
2:00 – 2:15	LOW VOLTAGE BEHAVIOR AND ELECTRO-OPTICAL SWITCHING PROPERTIES OF DUAL-FREQUENCY NEMATIC LIQUID CRYSTALS	Scott Jobling
2:15 – 2:30	HIGH SPEED ANISOTROPIC INDUCTIVELY COUPLED PLASMA (ICP) ETCHING OF GLASS	Vincent Hood
	2:30 – 2:45 pm Coffee Break	
2:45 – 3:45 pm	**Session IV** Session Chairs:	**Lanagan/Bhalla /Uchino/Guo**
2:45 – 3:00	MICROWAVE CHARACTERIZATION OF TRANSMISSION LINES WITH DIELECTRIC THIN FILMS	Kevin Deily
3:00 – 3:15	LOSS & DIELECTRIC PERMITTIVITY OF SMALL SAMPLES OF MATERIALS IN THE C BAND OF MICROWAVE FREQUENCIES	Stephen Tomko
3:15 – 3:30	INVESTIGATION OF FREQUENCY DEPENDENCE OF ELECTROOPTIC COEFFICIENTS IN EO CRYSTALS	Jonathan Taylor
3:30 – 3:45	PIEZOELECTRIC MULTILAYER ACTUATOR WITH “FLEX” ENDCAP	Daniel Gallagher
3:45 – 4:00	**CONGRATULATIONS AND CONCLUDING REMARKS**	**Skrabut/Guo**
	4:00 pm Adjournment	

Picnic at Sunset Park, 5:00 pm – sunset, ALL INVITED

Resource persons:	Amanda Skrabut and Andrew Fontanella
Special Notes:	Overhead transparency projector, PC, and LCD PC projector are provided. Speakers please upload presentation files to EEREU group web in Angel by July 27 Wed.. It is strongly recommended that speakers test-run presentation files for audio, video, or special applications prior to Thursday presentation. Each presentation is 15 min Q&A included.

ATMOSPHERIC ABSORPTION OF SPRITE EMISSIONS OBSERVED BY ISUAL INSTRUMENTATION

David H. Burkhardt*, Ningyu Liu+, Victor P. Pasko#

Department of Electrical Engineering
The Pennsylvania State University
University Park, PA 16802

* Undergraduate student of
Department of Physics
Haverford College
Haverford, PA 19041

ABSTRACT

Atmospheric transmission of electromagnetic radiation released by sprites was investigated. Ozone absorption cross-section and density profile data were used to develop a MATLAB script that models the absorption by ozone of radiation traveling from one point in the atmosphere to another as a function of the points' relative locations. MOSART software was then used to develop a model capable of accounting for all major absorbing agents in predicting the transmission of electromagnetic radiation between two points in the Earth's atmosphere. This model was used to determine the atmospheric transmission of radiation between typical sprite altitudes and 891 km, the altitude of FORMOSAT-2, a satellite that includes a set of instruments that observe sprite activity. As the current sprite theory predicts that most transmission comes from the1st and 2nd positive band systems of N_2, the Lyman-Birge-Hopfield band system of N_2, and the 1st negative band system of N^+_2, wavelengths in these bands were considered. The calculations performed indicate that while considerable absorption in the Lyman-Birge-Hopfield band system may occur, only minimal absorption in other band systems occurs. The developed model also indicates that radiation released by a related class of luminous upper atmosphere events known as blue jets may be absorbed by atmospheric ozone.

+ Graduate mentor
# Faculty mentor

1. INTRODUCTION

1.1 Sprite Production Mechanism

Sprites are luminous upper-atmosphere electrical discharges that are induced by cloud to ground lightning strikes. They occur in the mesosphere and lower ionosphere region of the atmosphere, typically between 50 and 90 km. Video of a sprite event was first obtained serendipitously on July 5, 1989 by a low-light level TV camera. Many other video images of sprites have since been captured, and have enabled discussion of sprite production and effects. Several theories explaining sprite production mechanisms have been developed. The theory that will be considered in this paper posits that they are generated by a quasi-electrostatic field that is created by cloud to ground lightning events [Pasko et al., 1997].

According to this theory, charge, both positive and negative, slowly build up in a tropospheric cloud. This accumulation of charge may lead to a lightning event, in which either the positive or negative charges from the cloud are deposited on the ground. This discharge, which transpires on the order of several milliseconds, leaves behind a large concentration of oppositely signed charge in the cloud. The cloud, which was previously an electric dipole, is now a large monopole, and will have associated with it a strong electric field. The field, referred to as a quasi-electrostatic field, will not last long. However, it will be quite strong while it lasts, and it will reach into the atmosphere above the cloud [Pasko et al., 1997].

In the atmosphere above the cloud, optical emissions may now occur through a mechanism that is comprised of several steps. The electric field causes electrons in the air to move, leading to collisions between these electrons and other air molecules. These collisions can excite and ionize the neutral particles in the air. When excited particles return to their unexcited state, they emit energy in the form of electromagnetic radiation. Emissions predicted by the model occur primarily in the 1st and 2nd positive bands of N_2, the Lyman-Birge-Hopfield band system of N_2, and the 1st negative bands of N^+_2 [Pasko et al., 1997].

Not all cloud to ground lightning events will instigate sprites. For a sprite to be initiated at any given point in space, the quasi-electrostatic field at that point must exceed a value known as the breakdown threshold. As the breakdown threshold falls off more rapidly with increasing altitude than the quasi-electrostatic field does, there is a greater chance of a sprite forming at higher altitudes. It is for this reason that sprites typically begin in the 70-80 km region [Pasko et al., 1997].

1.2 Blue Jet Generation

Blue jets and blue starters are another breed of luminous electrical discharge that occur above cloud level. Blue jets, so named for the blue light that they emit, are lightning-like events that begin at cloud tops and develop upwards, typically reaching altitudes of around 40 km. Blue starters are similar to blue jets

save for the fact that they terminate at an altitude of at most 25.5 km. Blue jets and blue starters events occur over volumes of space on the order of thousands of cubic kilometers, which is much greater than the volume of space associated with typical cloud to ground lightning events [Pasko and George, 2002].

Unlike sprites, blue jet and blue starter events are not instantiated by cloud to ground lightning. Their development, which is discussed more fully in [Pasko and George, 2002], is thought to be the result of the electric field within a cloud exceeding a certain threshold field value. When this level is approached, a leader-type discharge occurs, eventually transforming into a blue jet or a blue starter.

1.3 ISUAL Instrumentation

The scientific investigation of sprites consists of observing the electromagnetic radiation released by them. From these observations the identity of the molecules that emitted the radiation as well as their temperature and other characters can be inferred. Early sprite data were collected from land-based observation points, airplanes, and balloons. Now, the Imager of Sprites/Upper Atmospheric Lightning (ISUAL), a set of instruments on the FORMOSAT-2 satellite, is a major source of sprite data [Mende et al., 2004].

ISUAL is the product of a collaboration between the National Cheng Kung University, Taiwan, Tohoku University, Japan, and the University of California, Berkeley, and was sponsored by the National Space Program Office of Taiwan. ISUAL consists of a visible wavelength intensified CCD imager, a bore-weighted six wavelength channel spectrophotometer, and a two channel Array Photometer with 16 vertically spaced horizontally wide sensitive regions. Together, this instrumentation is capable of observing and recording electromagnetic radiation from the far ultraviolet to the near infrared regions of the visible spectrum. ISUAL is part of the payload of FORMOSAT-2, a satellite that was launched by Taiwan on March 20, 2004. FORMOSAT-2 orbits the earth at an altitude of 891 km with a periodicity of exactly 1/14 of a day, and is expected to gather data until 2009 [Mende et al., 2004].

Four of the channels of the spectrophotometer are designed to conform with the four major emission band systems that are associated with sprite events: the 1st and 2nd positive bands of N_2, the Lyman-Birge-Hopfield band system of N_2, and the 1st negative bands of N_2^+. By comparing the total intensities of radiation measured by these channels one can infer the relative significance of the band systems in sprite emissions [Mende et al., 2004].

ISUAL has several advantages over ground-based sprite observation systems. ISUAL's high altitude allows it to monitor a large portion of the Earth's surface at any given time. As sprite events are currently non-predictable, a system that is able to monitor a large area is seen as advantageous because it has a greater chance of observing a sprite when one does happen. Because the atmosphere is more dense below 50 km than it is above 50 km, there is considerably less atmospheric attenuation of radiation between ISUAL and sprite events than there is between ground based observation points and sprite events,

enabling ISUAL to detect a greater percentage of the radiation released by sprites than a ground-based system would be able to detect [Mende et al., 2004].

Thus far, ISUAL has monitored and reported data from many sprite events. However, ISUAL has not yet recorded a blue jet event [Mende et al., 2005]. As ISUAL has been orbiting the earth for over a year, this suggests that some atmospheric factor may be influencing the observation of blue jet and blue starter events by ISUAL.

1.4 Atmospheric Attenuation Considerations

As was mentioned in Section 1.3, atmospheric attenuation of radiation transmitted from sprite events to ISUAL is considerably less than the absorption that would be anticipated during the transmission of radiation from sprite events to ground-based observation points. However, attenuation still does occur and must be accounted for in any complete sprite model.

Several attenuating mechanisms exist in the atmosphere. One such mechanism is absorption. Molecules of any given species selectively absorb photons that have energy exactly equal to the energy difference between one of their occupied electron orbitals and one of their higher energy unoccupied orbitals. Molecules allow the transmission of photons whose energies do not match any orbital energy difference, meaning that some wavelengths will be heavily absorbed while other wavelengths will not be absorbed at all. The wavelengths that a given species absorbs are referred to as that species absorption lines. Absorption lines can be theoretically predicted, but because of the complexity of multi-atomic systems it is easier to measure them experimentally [Fenn et al, 1985].

When data regarding the strength of absorption lines is known, predicting atmospheric absorption along a pathway is not difficult; it can be performed by utilizing Lambert's Law:

$$dI_\lambda / I_\lambda = -n\sigma_{a\lambda} ds \qquad (1)$$

where I_λ is the intensity of radiation at wavelength λ, n is the number density of the molecule in question, $\sigma_{a\lambda}$ is the absorption cross-section of the molecule in question, and ds is an infinitesimal distance along the absorption pathway. Integrating both sides of this equations along a path of length s yields:

$$I_\lambda(s) = I_\lambda(0) e^{-\int_0^s n\sigma_{a\lambda} ds} \qquad (2)$$

where $I(0)$ is the initial intensity and $I(s)$ is the intensity transmitted across paths [e. g. Liu et al., 2005].

Molecular scattering is another mechanism that contributes to attenuation of radiation traversing the atmosphere. When a photon collides with a particle, it is possible that the oscillating electric field associated with the photon may

influence the electron distribution of atoms within the particle, causing them to oscillate and interact with the incident photon, effectively altering its trajectory. Molecular scattering refers only to scattering caused by interactions between photons and molecules with dimension on the same order as the wavelength of the photons [Fenn, 1985].

Larger particles suspended in air known as aerosols are also responsible for scattering photons that collide with them. Aerosol absorption is similar to molecular scattering except that it occurs with particles that are orders of magnitude larger than the wavelength of the radiation. These particles interfere with photons, causing them to change trajectory [Fenn, 1985].

These effects make the observed spectrum considerably different from the spectrum that is released by the sprite. Before radiation predicted by a sprite model can be compared to data gathered by ISUAL, this interference must be accounted for.

2. EXPERIMENTAL METHODS

Initially, a model for ozone absorption was generated. Data describing the cross-sectional absorption of ozone and its atmospheric density profile were obtained, and MATLAB technical computing software was used to incorporate these data into a script capable of determining absorption by ozone between two points in the atmosphere. These calculations were performed using equation (2). This script was used to predict the atmospheric absorption by ozone of radiation released by sprite events.

In order to simulate actual situations that might occur during ISUAL observations, absorption between the satellite altitude, 891 km, and altitudes at which sprites are expected to occur, 40, 50, 60, and 70 km, was calculated. The distance between sprite and satellite was set to be 2500 km. The geometry described is depicted in Figure 1.

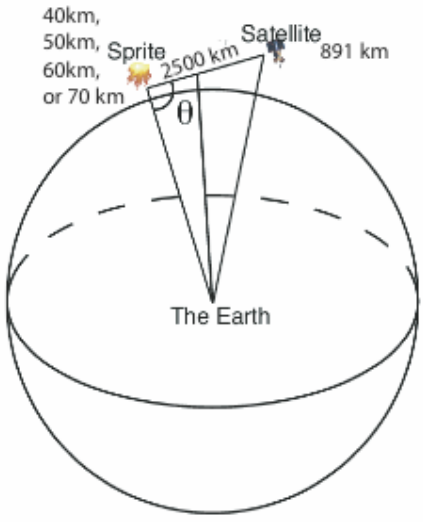

Figure 1:
ISUAL observation geometry [Liu et al., 2005].

A more complete absorption model was then developed using the Moderate Spectral Atmospheric Radiance and Transmittance Program (MOSART). MOSART is an atmospheric modeling program that combines atmospheric data from many sources in order to compute the transmission of radiation along pathways through the atmosphere. The user gives MOSART a list of geometrical situations describing lines through the atmosphere and a range of wavelengths and returns the fraction of radiation intensity at each wavelength that will be transmitted along the pathway described [Cornette et al., 1994]. Prior to the execution of this project, MOSART software had not been compiled for the Macintosh OS X operating system; considerable effort was therefore invested in determining and documenting the method for doing so.

MOSART software was used to generate Figure 1(b) presented in [Morrill et al., 1998] to insure that the software was correctly compiled. The geometry presented in Figure 1 was then entered into MOSART to determine absorption that will occur while radiation released by sprites travels to ISUAL.

These results were used to predict the absorption of radiation in the four bands that are considered in the current sprite model.

3. RESULTS AND DISCUSSION

Figure 2 shows the ozone cross-sectional data that was compiled from data presented in [Molina and Molina, 1986] and [Burrows et al., 1999]. Figure 3 displays the ozone vertical density profile, obtained through correspondence with Dr. Didier Rault and used in [Rault, 2005]. These data only represent ozone concentrations up to 50 km; it was initially assumed that because ozone density in the atmosphere falls off considerably above this altitude it does not play a significant role in absorption of radiation. Figure 4 presents the absorption of radiation by ozone predicted by the MATLAB script produced using these data.

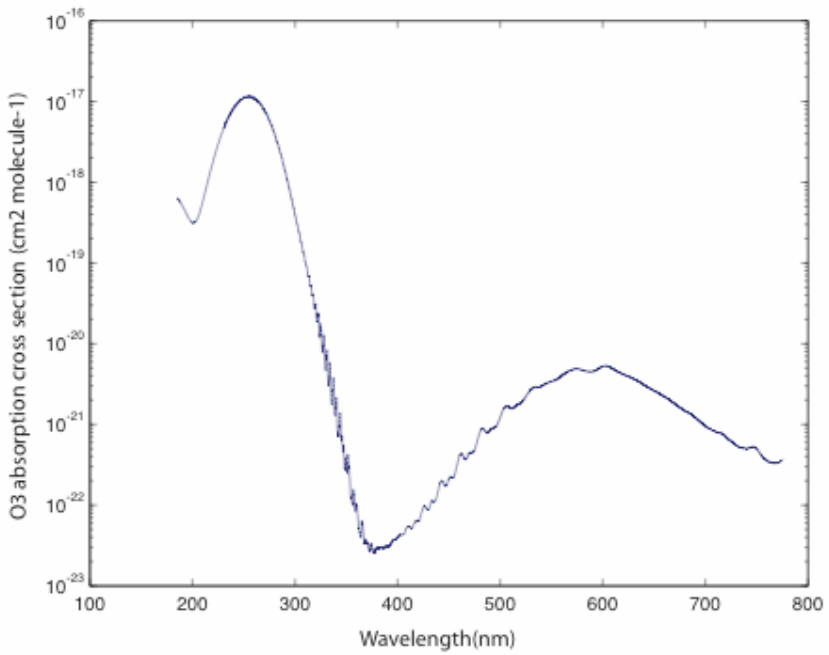

Figure 2: Ozone absorption cross-section obtained from [Molina and Molina, 1986] and [Burrows et al., 1999].

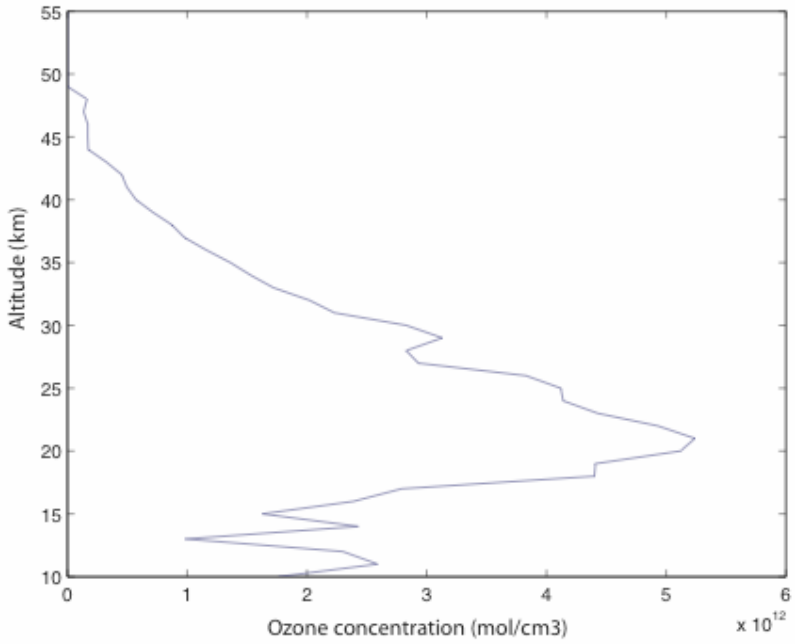

Figure 3: Ozone density profile obtained from [Rault, 2005].

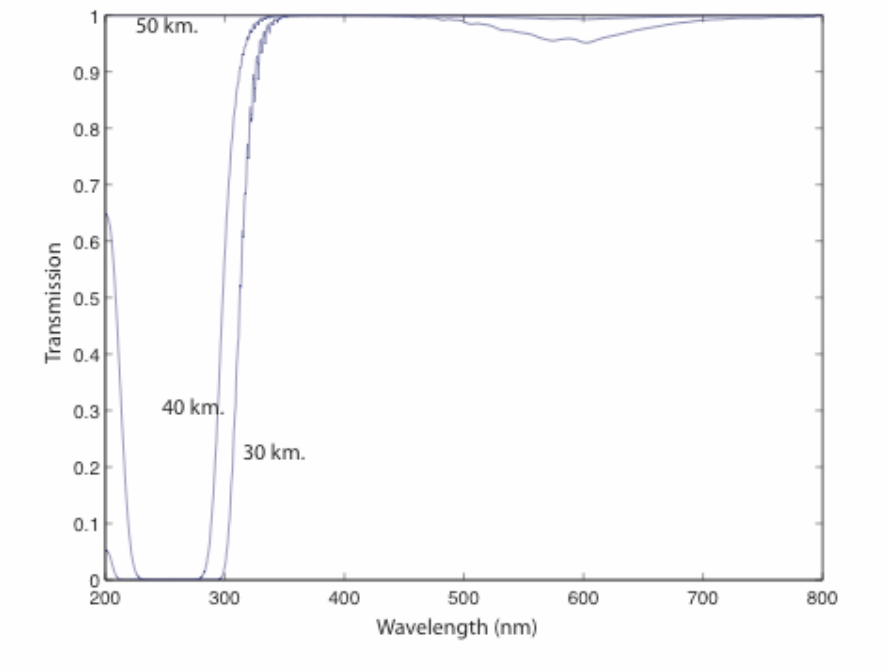

Figure 4: Ozone absorption between sprites at various altitudes and a satellite at 891 km along a 2500 km path predicted using ozone cross-section presented in Figure 2 and ozone density profile presented in Figure 3.

Several results were obtained with the software package MOSART. Figure 5 presents the absorption between sprite events at 65 km and observers at 0, 5, 10 and 20 km as presented by Morrill et al. [1998]. Figure 6 represents an attempt at the re-creation of this figure using MOSART. This figure is similar in shape to that of [Morrill et al., 1998], but the two differ in most places by approximately 10%. Several attempts were made to obtain closer values by altering the time of day, location of observer, and other calculation parameters. Altering the latitude of the observation point provided a noticeable change, but no location tested produced values similar to the results presented in [Morrill et al., 1998]. Figure 7 demonstrates the difference in the absorption between 20 km and 65 km along a 500 km path way presented in [Morrill et al., 1998] and the values obtained using MOSART. The cause of this discrepancy has not yet been discerned.

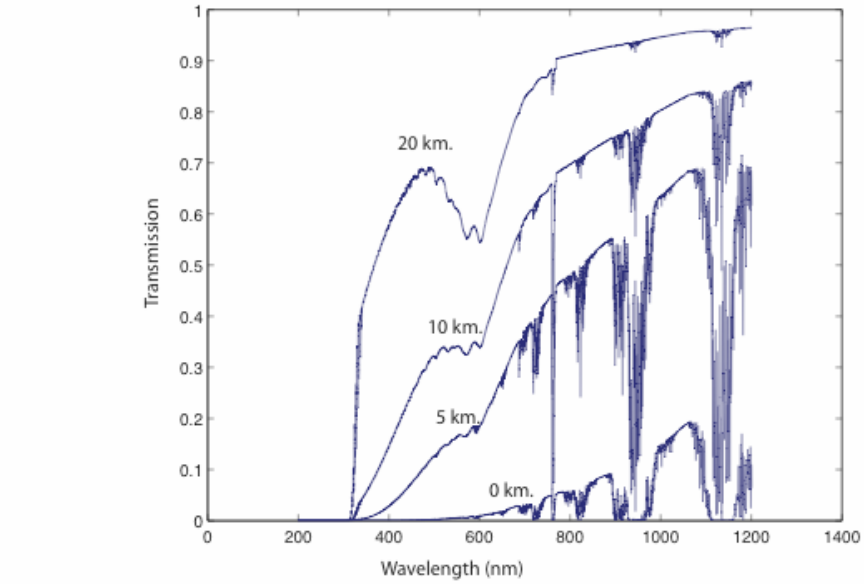

Figure 5: Atmospheric transmission between various altitudes and 65 km along a 500 km path as presented in [Morrill et al., 1998]

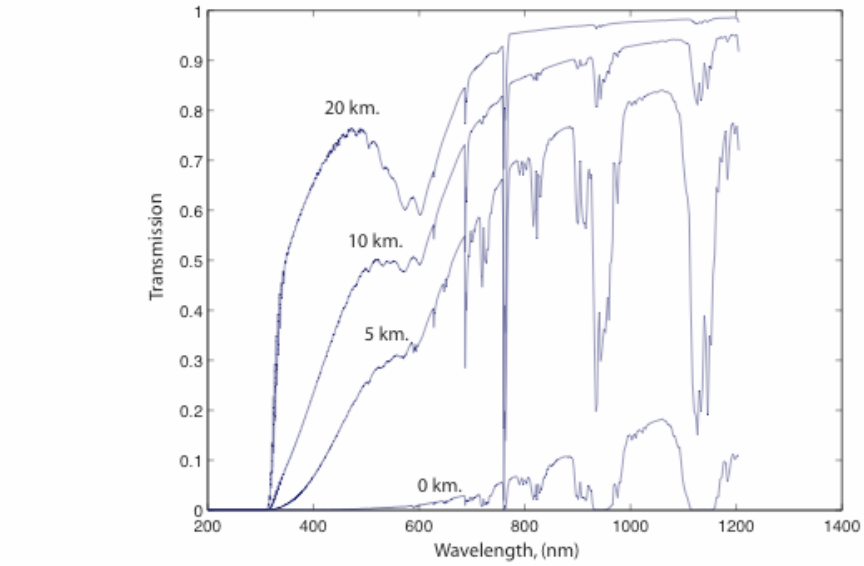

Figure 6: Atmospheric absorption between various altitudes and 65 km along a 500 km path as calculated using the MOSART software package in the present study.

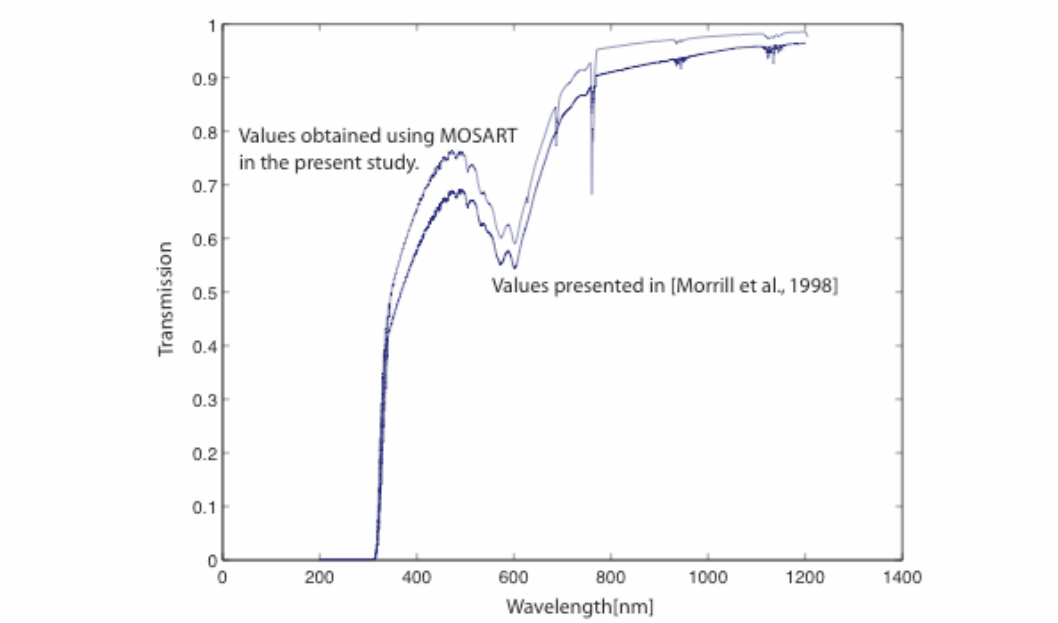

Figure 7: Comparison of predictions of atmospheric transmission between 65 km and 20 km along a 500 km path.

Figure 8 presents the absorption by ozone predicted by the MOSART software package. The ozone density profile used in MOSART extends to 120 km, and thus includes considerably more data than were used in creating Figure 4.

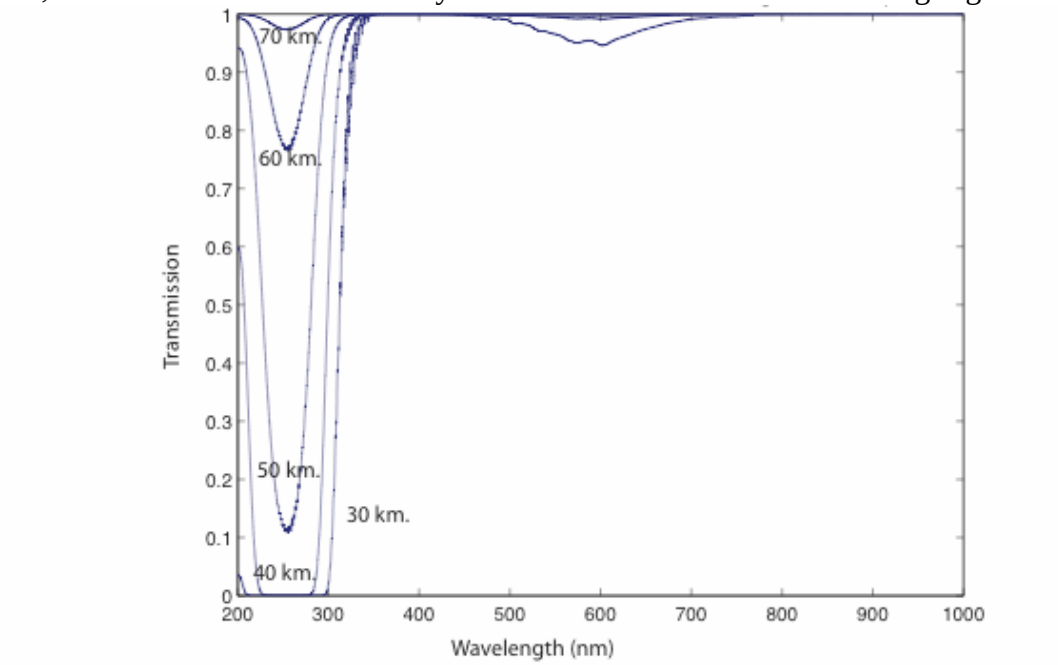

Figure 8: Ozone absorption predicted by MOSART between sprites at various altitudes and a satellite at 891 km along a 2500 km path.

The dissimilarity between Figures 4 and 8 is significant; an assumption was initially made that as ozone densities fell off considerably above 50 km and absorption above 50 km would be insignificant in comparison to that below 50 km. However, as the model that included absorption up to 120 km predicted considerably more absorption than that which only contained data extending to 50 km, this assumption has been shown to be erroneous. Atmospheric absorption models to be used in sprite modeling should therefore consider ozone absorption up to at least 120 km.

Figure 9 presents the total absorption predicted by MOSART for various altitudes.

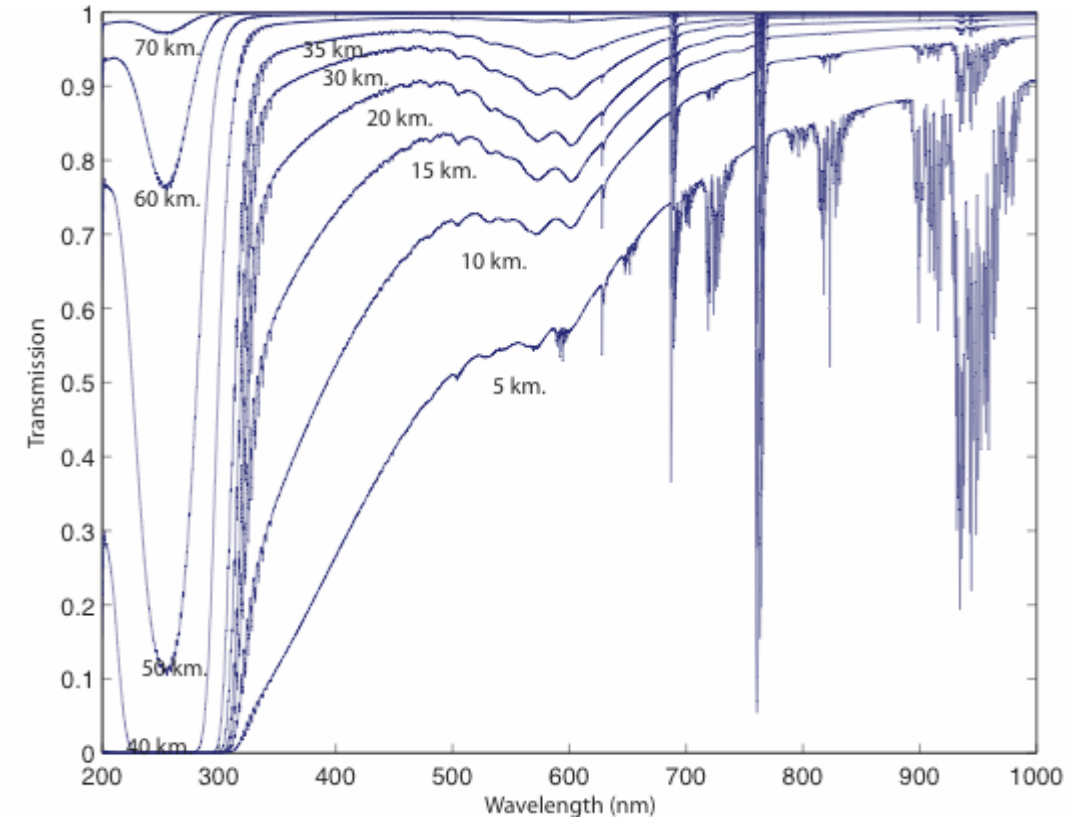

Figure 9: Total atmospheric transmission between sources at various altitudes and a satellite at 891 km along a 2500 km path.

FORMOSAT-2 has been orbiting the Earth for over a year. However, analysis of ISUAL data has thus far not revealed any data that appear to be linked to a blue jet event. The ISUAL filter responsible for blue jet detection is centered on the wavelength 337 nm, a wavelength that is significantly absorbed along emission pathways between 15 km sources and ISUAL as is indicated in Figure 9. It is therefore possible that atmospheric absorption has prevented any observation of blue jet events.

The transmission curves presented in Figure 9 were combined with data representing the relative strength of emissions in the 1st and 2nd positive band systems of N_2 and the 1st negative band system of N^+_2 from [Vallence Jones,1974, p. 80-176], and the Lyman-Birge-Hopfield band system of N_2 from [Liu and Pasko, 2005, and references therein] in order to determine the percentage of the emissions in each band that would be transmitted to the FORMOSAT-2 satellite from various altitudes. All emissions that reach FORMOSAT-2 are not actually detected by the ISUAL spectrophotometer; ISUAL filter data presented in [Mende et al., 2005] were applied to the results to determine the percentage of the emission from each band system that would actually be detected. The fraction of emissions from each band system released by sprites at various altitudes that would be detected by the ISUAL spectrophotometer is presented in Table 1.

The numbers in Table 1 indicate that, for the 1st and 2nd positive band systems of N_2 and the 1st negative band system of N^+_2, there is little difference in the fraction of emissions from 40 km sources that will be detected and the fraction of emissions from70 km sources that will be detected. There is therefore little absorption occurring in these band systems between 40 and 70 km. However, the fact that absorption significantly alters emissions in the Lyman-Birge-Hopfield band indicates that absorption must be taken into account in sprite modeling.

Table 1: Fraction of emissions from various band systems released at various altitudes that would be detected by the ISUAL spectrophotometer.

Emission Altitude	1^{st} positive N_2	2nd positive N_2	Lyman-Birge-Hopfield	1st negative N^+_2
40 km	.11	.27	.01	.63
50 km	.11	.28	.04	.64
60 km	.11	.28	.05	.64
70 km	.11	.28	.05	.64

4. SUMMARY

A simple model of the absorption by ozone of radiation released by sprites and observed by the ISUAL spectrophotometer was developed. Incorporated into the model was the assumption that atmospheric ozone only plays a significant role in absorption at altitudes below 50 km. MOSART software was then applied to standard observation geometries of the ISUAL instruments on the FORMOSAT-2 satellite to generate a more complete absorption model that could account for all major absorbing agents and perform absorption calculations up to altitudes of 120 km. The atmospheric attenuation of radiation released by sprites and other luminous discharges and detected by ISUAL was predicted. Comparisons between MOSART results obtained in this study and MOSART results presented in [Morrill et al., 1998] reveal a difference of about 10% in calculations of ground to sprite atmospheric absorption; an effort should be made to determine the cause of this discrepancy. Comparisons between ozone absorption predicted by the simple model developed in this study and ozone absorption predicted by the

MOSART model indicate that considerable absorption of radiation by ozone occurs in the 50-120 km region; absorption models must therefore include this region in calculations. Total absorption spectra from emission sources at 15 km indicate that atmospheric absorption of radiation released by blue jet and blue starter events may inhibit the ISUAL instrumentation's ability to observe these events.

ACKNOWLEDGEMENTS

This research was supported by the National Science Foundation under Grant No. EEC0244030. Thanks to Dr. Ruyan Guo, Dr. Kenneth Jenkins, and Mrs. Linda Becker for organizing the 2005 Research Experience for Undergraduate program at Penn State University.

REFERENCES

Burrows, J. P., A. Richter, A. Dehn, B. Deters, S. Hmmelmann, S. Voigt, J. Orphal, Atmospheric remote-sensing reference data from GOME-2. Temperature-dependent absorption cross sections of O_3 in the 231-794 nm range, *J. Quant. Spectrosc. Radiat. Transfer*, *61*, no. 4, 509-517, 1999.

Cornette, W. M., P. K. Acharya, G. P. Anderson, Using the MOSART code for atmospheric correction, *IEEE Conf. Proc. Int. Geosci., and Rem. Sens. Sympos*. 1, 215-219, 1994.

Fenn, R. W., S. A. Clough, W. O. Gallery, R. E. Good, F. X. Kneizy, J. D. Mill Lt. Col USAF, L. S. Rothman, E. P. Shettle, F. E. Volz, Optical and Infrared Properties of the Atmosphere, *Handbook of Geophysics and the Space Environment*, edited by A. S. Jursa, pp. 18(1)-18(80), Air Force Geophysics Laboratory, 1985.

Liu, N. and V. P. Pasko, Molecular nitrogen LBH band system far-UV emissions of sprite streamers, *Geophys. Res. Lett.*, Vol. 32, L05104, doi:10.1029/2004GL022001, 2005.

Liu, N., V. P. Pasko, D. H. Burkhardt, H. U. Frey, S. B. Mende, H. T. Su, A. B. Chen, R. R. Hsu, L. C. Lee, H. Fukunishi, Y. Takahashi, Comparison of Results from Sprite Streamer Modeling with Spectrophotometric Measurements by ISUAL Instrument on FORMOSAT-2 Satellite, to be submitted to *Geophys. Res. Lett.* 2005.

Mende, S. B., R. R. Hsu, H. T. Su, A. Chen, L. C. Lee, H. U. Frey, S. Harris, S. P. Geller, H. Heetderks, Y. Takahashi, H. Fukunishi, Spacecraft based studies of transient luminous events, Corsica summer study, *NATO Advanced Study Institute on Sprites, Elves, and Intense Lightning Discharges*, book chapter in press, Kluwer Academic Publishers, 2005.

Mende, S. B., H. U. Frey, R. R. Hsu, H. T. Su, A. B. Chen, L. C. Lee, D. D. Setman, Y. Takahashi, H. Fukunishi, , D region ionization by lightning induced EMP, submitted to *J. Geophys. Res*., 2005.

Molina, L. T. and M. J. Molina, Absolute Absorption Cross Sections of Ozone in the 185 to 350-nm Wavelength Range, *J. Geophys. Res.*, *91*, D13, 14501-14508, 1986.

Morrill, J. S., E. J. Bucsela, V. P. Pasko, S. L. Berg, M. J. Heavner, D. R. Moudry, W. M. Benesch, E. M. Wescott, D. D. Sentman, Time Resolved N2 triplet state vibrational populations and emissions associated with red sprites, *J. Atmos. Solar-Terr. Phys.*, 60, 811-829, 1998.

Pasko, V. P., U. S. Inan, T. F. Bell, Y. N. Taranenko, Sprites Produced by quasi-electrostatic heating and ionization, *J. Geophys. Res.*, 102 (A3), 4429-4561, 1997.

Pasko, V. P. and J. J. George, Three- dimensional modeling of blue jets and blue starters, *J. Geophys. Res.*, 107, A12, 1458, doi:10.1029/2002JA009473, 2002.

Rault, D. F., Ozone profile retrieval from Stratospheric Aerosol and Gas Experiment (SAGE III) limb scatter measurements, *J. Geophys. Res.*, *110*, D09309, doi:10.1029/1004JD004970, 2005.

Vallence Jones, A.K., *Aurora*, First edition, B. M. McCormac Editor, D. Reidel Publishing Company; Dordrecht, Holland; 1974.

ELECTROMETER DESIGN FOR A SOUNDING ROCKET PAYLOAD

Andrew L. Casperson*, John D. Mitchell[#], and Charles L. Croskey[#]

Department of Electrical Engineering
The Pennsylvania State University, University Park, PA 16802

*Undergraduate student of
Department of Electrical and Computer Engineering
University of North Carolina Charlotte
Charlotte, NC 28223

ABSTRACT

This project pertains to the design of a sounding rocket payload that will measure electrical properties of the upper atmosphere. Different probes are used for the detection and collection of charge in the ionosphere. The collected charge is measured as a current by an electrometer. Supporting payload components are data amplifiers and A/D converters, which process the data before transmittal to ground. A telemetry system is used to encode and transmit the data to ground. The transmitter sends the data to ground at a certain frequency. On the ground a receiver picks up the data that is then transferred to a computer for analysis.

The focus of this project is the design of an electrometer circuit. The electrometer is a current-to-voltage converter which performs the important function of precisely measuring very small (pA - mA) currents of charge collected by the probe. For this application, it is critical for the electrometer to be very small, reliable, and accurate under both DC and AC operating conditions.

A logarithmic electrometer can be used to measure small currents over a wide range. It typically consists of an operational amplifier with a parallel combination of diodes placed in the feedback loop. The design of this electrometer circuit involves different variations to get the best results for the application. The analysis and testing of these circuits is contained in this paper.

[#] Faculty Mentor

15

INTRODUCTION

The Earth's upper atmosphere is called the "ionosphere" in reference to the fact that it is an ionized gas, or plasma. Historically, it has been an important region to understand because of its effects on electromagnetic wave propagation, particularly in relation to communications. The ionosphere extends upward from approximately 50 km, which makes it very challenging for measurement investigations.

A variety of rocket probes are presently in use for measuring different electrical properties of the ionosphere. One example, shown in Figure 1, is the DC-biased Langmuir probe, placed at the tip of the nose cone to collect charge as the rocket moves through the upper atmosphere. The collected charge, measured as a very small current (~ nA), can be used to determine the relative plasma number density of the atmospheric region. Further post-flight analysis of the small-scale current fluctuations evident in the data has also led to the evaluation of turbulence parameters for characterizing the region's dynamic processes.

Figure 1: Nose tip probe biased at a DC voltage (typically, +5 V) for electron collection

Whatever the probe geometry happens to be (spherical, cylindrical, or planar), there remains a central need to accurately measure the current of collected charge. Actually, two general kinds of current measurement are necessary: the DC large-signal value and the AC small-signal value. The particular circuit that performs these measurements of very small currents is called an "electrometer."[1]

This investigation considers three different logarithmic electrometer circuits. The evaluation of each of them involves measuring and analyzing both their DC and AC (small-signal) voltage-current response characteristics. The circuits

include a prepackaged electrometer circuit made by Thermoptics,[2] a basic op-amp design using DPAD1 diodes,[3] and another op-amp design using light emitting diodes (LEDs).

LOGARITHMIC ELECTROMETER CIRCUIT

The basic log electrometer circuit, as shown in Figure 2, uses a high-quality op amp having a very small-valued input bias current combined with a feedback element that displays a logarithmic I-V characteristic. The op amp used in our circuit design was the Burr-Brown OPA128LM, which has the specified maximum values $I_B = \pm 75$ fA and $I_{OS} = \pm 30$ fA for input bias current and input offset current, respectively. Also, its maximum input offset voltage is rated to be $V_{OS} = \pm 500$ µV. [4] Clearly, this device is a good one for measuring current levels of 1 pA or greater.

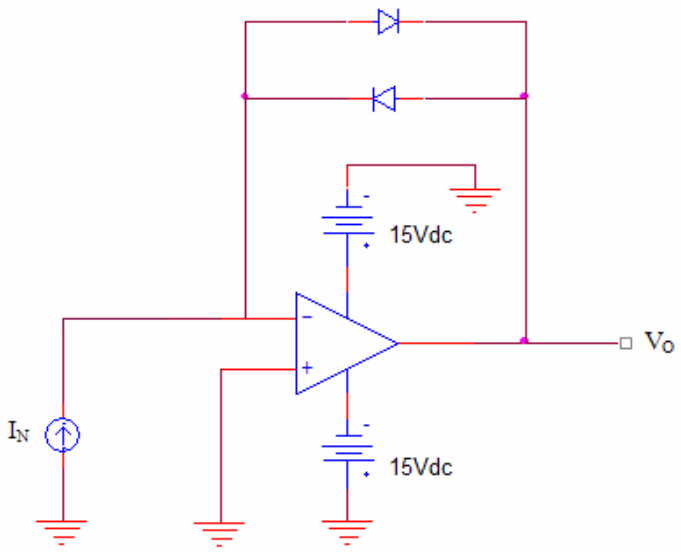

Figure 2: Basic electrometer circuit

A diode is the simplest semiconductor device for producing a logarithmic I-V characteristic:

$$I_D = I_S(e^{V_D/nV_T} - 1) \tag{1}$$

If a matched diode pair is connected in a parallel and back-to back configuration, as shown in Figure 2, the output voltage becomes

$$V_O = nV_T \ln(\frac{I_D}{I_S}) \tag{2}$$

The parameters that describe a diode are its thermal voltage, $V_T = kT/q$, its scale current, I_s, and the constant, *n*, which ranges in value between 1 and 2. Each

diode has different parameter values, and the two diodes in the feedback loop should be closely matched. The basic electrometer designs used two types of diodes: the DPAD1 diode pair manufactured by Vishay Siliconix and a set of two colored LEDs. These diodes provide negative feedback to the op amp as shown in Figure 2.

The DC current source, I_N, in Figure 2 is implemented using a DC power supply in series with a decade resistance box. A multimeter is placed at the output to measure the voltage shown as V_O.

EXPERIMENTAL APPROACH

The electrometers were tested considering two different aspects: DC operation and AC operation. The DC measurements were done to evaluate the circuit's logarithmic behavior and to determine how well the diodes were electrically matched. The AC measurements showed the circuit's linearity and bandwidth for small-signal operation.

The basic DC testing of this electrometer circuit involved the creation of small currents by using a precision decade resistor box and a DC power supply. The experimental setup is illustrated in Figure 3. With the power supply set at 5 V, the resistor box was changed in decades from 10^{12} Ω to 10^4 Ω, resulting in decade increases in input current from 5 pA to 0.5 mA, respectively. This current was then directed into the input of the electrometer, causing it to be converted to small measurable voltages. Each different electrometer circuit was measured using both +5 V and -5V power supply input voltages, except for the Thermoptics circuit which only operated using -5 V.

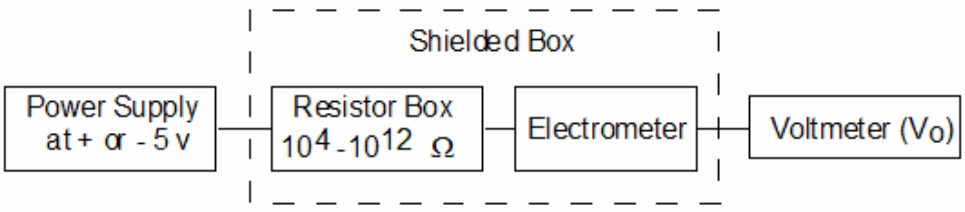

Figure 3: DC current test setup

Another set of measurements involved the evaluation of the AC operation of the aforementioned circuits, as illustrated in Figure 4. This was performed by connecting an AC sinusoidal signal generator in series with an air gap capacitor to the electrometer's input. The series-connected DC power supply and resistor were still needed for biasing purposes. As a result, the total input current to the electrometer included a DC component for biasing and an AC input signal component. The voltmeter was now used to measure the AC RMS voltage at the output of the electrometer.

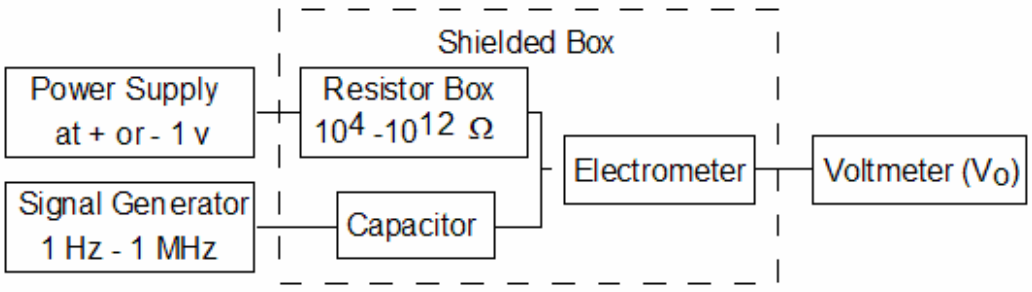

Figure 4: AC current test setup

RESULTS

Using the above methods, large amounts of data were collected for various electrometer setups. Figure 5 displays the DC results for the Thermoptics electrometer circuit, the electrometer circuit using an op amp with a DPAD1 diode pair, and the electrometer circuit using an op amp with an LED pair. The purpose of collecting this data was to display how well each circuit reacted to the various produced small currents, and to show how well the diodes were matched using both polarities of voltage. For the two electrometer circuits that used diode pairs, the diodes were evenly matched as shown by the closeness of each pair of lines. All three circuits displayed very good semilog relationships between current and voltage, as demonstrated by the straight-line behavior of the curves.

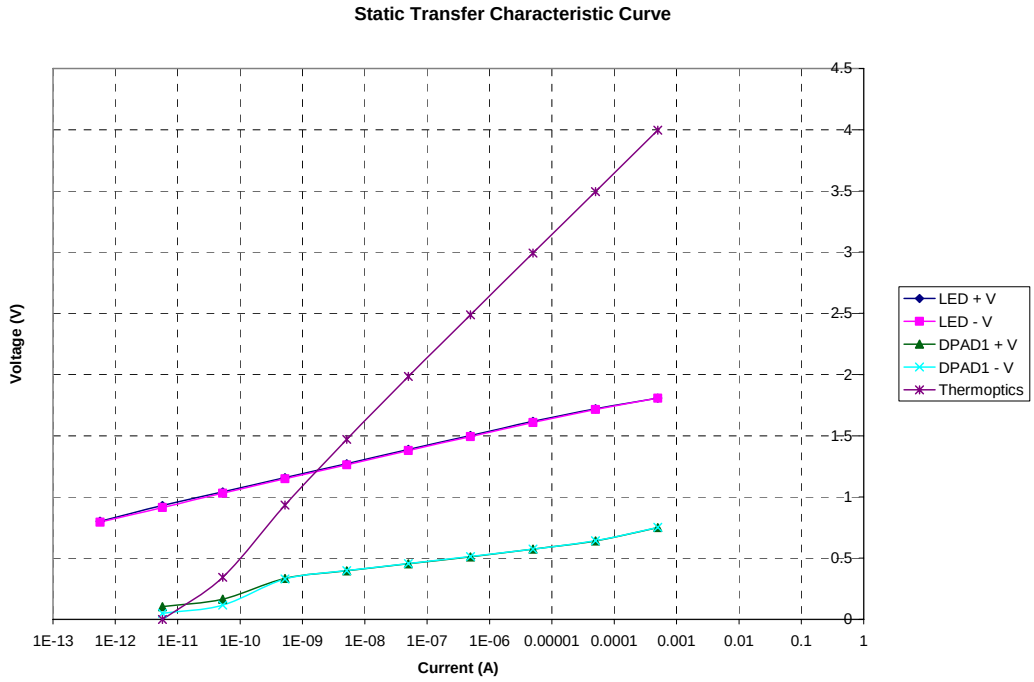

Figure 5: Static transfer characteristics (The negative voltages have been reversed to display the similarity between the lines.)

The semilog relation between output voltage and input current for each electrometer circuit can be expressed by the general equation

$$V_O = A \ln\left(\frac{I_N}{I_S}\right) \tag{3}$$

For the graphs in Figure 5, placing the straight line of best fit to each curve will enable values to be determined for the constants I_S and A given in Equation 3. These values are shown in Table I. For the two electrometer circuits that used diode pairs as feedback elements, the values of A are equal to the nV_T parameter values for the diodes.

Table I. Experimentally determined values for I_S and A

Circuit	I_S (A)	A (V)
DPAD1	1.08315E-13	0.0335
LED	3.52048E-20	0.0493
Thermoptics	7.039E-11	0.2226

An example of the AC small-signal electrometer test measurements is given in Figure 6, in this case for the electrometer circuit using the DPAD1 diode pair as the feedback circuit.

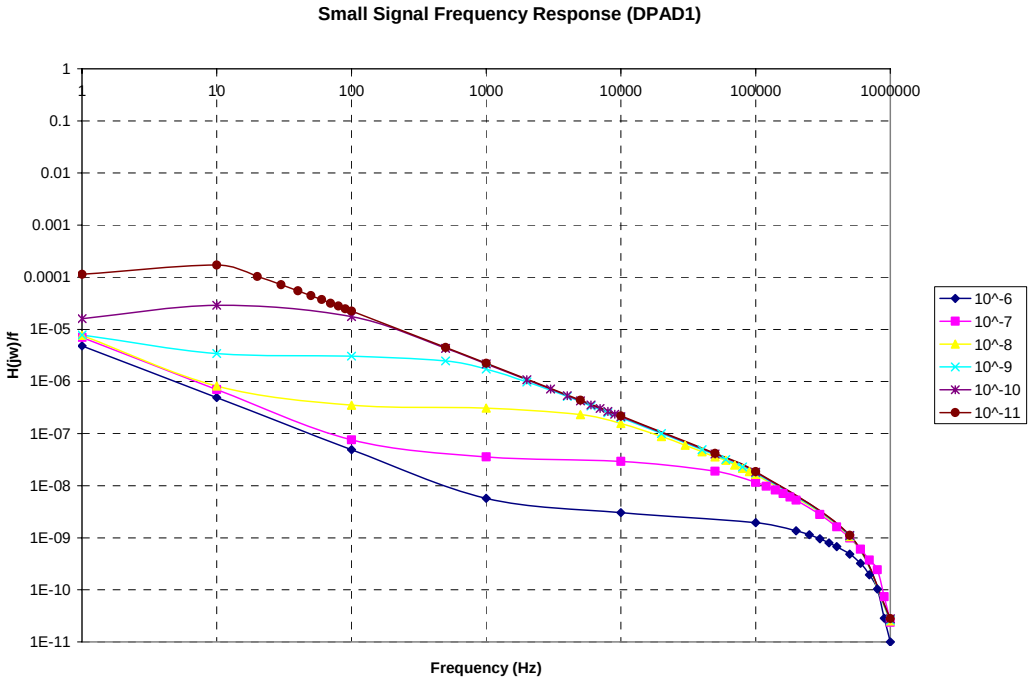

Figure 6: Example small-signal frequency response

In this figure, the vertical axis gives the ratio of the magnitude of the AC small-signal output voltage to input current, which is then normalized to frequency. The displayed bandwidth corresponds to the value where this magnitude is down 3 dB from its perceived midband value. We expect the small-signal bandwidth to be dependent on the electrometer's DC input current level, and thus a series of tests are needed to evaluate this effect. Such an effect is illustrated in Figure 6, where the electrometer's small-signal response has been plotted for decade increments of DC input bias current between 10 pA and 1 μA. As expected, the electrometer's small-signal bandwidth improves (becomes greater) as the bias current increases.

As a summary of the AC test measurements, the determined small-signal bandwidths plotted as a function of DC input bias current are shown in Figure 7 for the three basic electrometer circuits considered in Figure 5. For all three circuits, we observe the general trend of the bandwidth increasing with DC input bias current. All three electrometer circuits display good and relatively comparable bandwidths for larger input bias current values. At smaller current levels, the electrometer using the LED pair has a relatively poorer frequency response, as indicated by the smaller bandwidth.

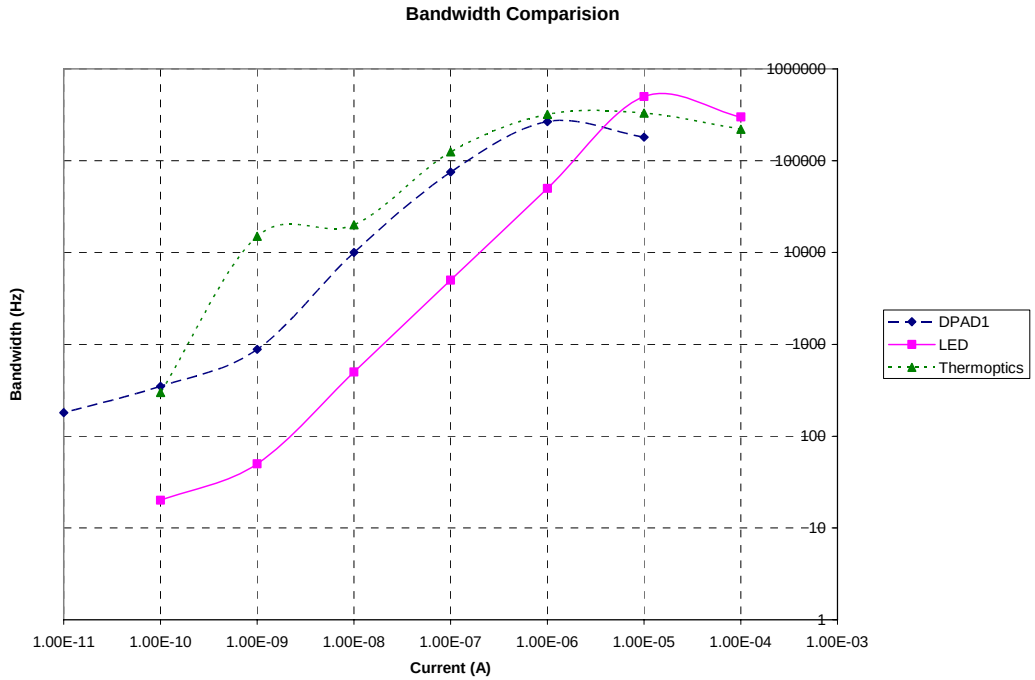

Figure 7: Bandwidth comparison

CONCLUSIONS

In summary, the performance of three logarithmic electrometer circuit designs has been investigated, considering both their DC and AC operation. One circuit was the commercially available Thermoptics electrometer, and the other two used the same type of op amp (OPA128LM) with a different kind of diode pair to provide negative feedback. In one case, the DPAD1 diode pair was used, and the other circuit used a pair of LEDs.

Each of the three circuits showed quite different results for DC test conditions and AC test conditions. As the current values in the atmosphere under investigation are often below 10^{-9} A, the circuit must have a good bandwidth in that range. Both the Thermoptics circuit and the DPAD1 circuit showed relatively good values in this range, except that the Thermoptics circuit at low currents began to get a 10-Hz noise that produced undesirable results, making it useless for this application. The DPAD1 circuit had a relatively good bandwidth over all decades of current, while the LED circuit showed the smallest bandwidth. For the DC results the LED circuit produced the straightest and most accurate line, i.e., it had the best semilog characteristic and current sensitivity, but again, the poorest bandwidth.

The purpose of this experiment was to discover which of the three example electrometers would be most useful for measuring the small currents in the plasma of the atmosphere. Overall, each circuit showed different results, but the one with the superior properties for this application turned out to be the electrometer circuit having the DPAD1 diode pair. It displayed desirable bandwidth and proper functioning diodes for semilog operation. With all these aspects taken into account, this electrometer circuit will most likely be used.

ACKNOWLEDGEMENTS

I would like to thank my faculty mentors Dr. Charles Croskey and Dr. John Mitchell, for their constant help and attention. I would also like to thank PSU for organizing the EEREU and giving me a chance to have this experience.

This material is base upon work supported by the National Science Foundation under Grant No. EEC-0244030.

REFERENCES

[1] W. Liu, "A Logarithmic Electrometer for Rocket Probes," PSU Masters Thesis, 1991.

[2] DN137 Current to voltage converter for pigtailed photodiode fiber optic power monitors. *Thermoptics*. April, 2002 <http://www.thermoptics.com/tcdatasheets.pdf/DN137EVK.pdf>.

[3] DPAD1 Dual Low-Leakage Pico-Amp Diodes. *Vishay.* June 2001. <http://www.vishay.com/docs/70340/70340.pdf>

[4] OPA128LM Difet Electrometer-Grade Operational Amplifier. *Burr-Brown*. May, 1995 <http://focus.ti.com/lit/ds/symlink/opa128.pdf>

ELECTRICAL CHARACTERIZATION OF SILICON NANOWIRE *P-N* JUNCTIONS

Eric Dattoli[1,*], Tsung-ta Ho[2,+], Yanfeng Wang[2,+], K.K. Lew[3,+]
Theresa S. Mayer[2,#], and Joan Redwing[3,#]

[2]Department of Electrical Engineering
[3]Department of Material Science and Engineering
The Pennsylvania State University
University Park, PA 16802

[*]Undergraduate Student of
[1]Department of Electrical and Computer Engineering
University of Florida, Gainesville, FL 32601

ABSTRACT

Silicon nanowire *p-n* junctions were electrically characterized. The nanowire junctions were formed using the vapor-liquid-solid (VLS) method. The dopant gas was varied between *n*- and *p*-type during wire growth so that the junction was formed along the axial direction of the nanowire. Figures of merit (e.g. ideality factor) for I-V curves of *p-n* junctions doped at different concentrations were determined. Junctions passivated with an oxide shell were also characterized. The photodetection properties of the junctions were examined by measuring photogenerated current.

[#] Faculty Mentor
[+] Graduate Mentor

23

INTRODUCTION

The semiconductor industry is facing a predicted ultimate limit to how far conventional CMOS technology can continued to be miniaturized.[1] Research is being carried out into new devices which can one day be used in integrated circuits. One candidate is silicon nanowires (SiNWs), which are circular wires made up of a single crystal of silicon. An attractive feature is that they can be reproducibly grown with substantial uniformity among the parameters: diameter and doping concentration.[2,3] SiNWs are usually grown through the vapor-liquid-solid (VLS) process. This growth procedure is capable of making SiNWs of diameters 45-200 nm[4], while diameters down to 3.5 nm have been demonstrated.[5] A variety of devices have already been constructed using semiconducting nanowires: field-effect transistors,[6] light-emitting diodes,[7] and rectifying diodes.[7,8] The aim of this paper is to characterize the electrical properties of SiNW *p*-*n* junctions fabricated by this group's process.

In the VLS growth procedure used, a ~1 nm layer of gold (Au) is sputtered onto a SiO_2 surface layer on top of a *p*-doped silicon wafer.[9] The diameter of the droplets closely determines the diameter of the grown NW. Silane (SiH_4) gas is introduced into the reactor. The SiH_4 gas decomposes on the Au surface and forms an Au-Si alloy at temperatures greater than 363°C. Once the alloy reaches a large enough percentage of silicon, the silicon crystallizes out of the alloy, and the SiNW starts to grow vertically upwards. Along with silane, dopant gases can be introduced into the chamber during the VLS procedure. The gases phosphine[10] and trimethylboron[3] are used in order to incorporate donor and acceptor atoms, respectively, into the nanowire. If the dopant gas is varied between *p*- and *n*-type during growth, it is possible to form a *p*-*n* junction between *p*- and *n*-type Si along the axial direction of the SiNW. The doping of the nanowire is modulated by this procedure. The ratio of dopant gas to silane can be varied from 0 to 10^{-2} to set the concentration of the dopant atoms. The diameter of the nanowires examined varied between 60 to 140 nm.

The fabrication procedure was modified to produce six different types of silicon nanowire *p*-*n* junctions (Table I). The concentration of the dopant gases was varied in order to produce either highly or lowly doped junctions. The nanowire growth process was varied by either growing the *p* side of a junction first, creating a *p*-*n* configuration, or alternatively growing the *n* side first to create a *n*-*p* junction configuration. Junction type 4 (Table I) was doped in a undoped-*n* configuration. The VLS growth procedure of the NWs introduces light *p*-type background doping into undoped wires. In this configuration, the undoped end of the nanowire served as the *p* doped side of a *p*-*n* junction. Junction type 6 (Table I) was passivated by dry oxidation. The formed SiO_2 shell is about 10 nm thick.

Table I. Types of Nanowire *p*-n Junctions Produced and Characterized

Type No.	Type Name	p doping ratio	N doping ratio	passivation performed?
1	Lowly Doped *p-n* junctions	$2x10^{-3}$ of $TMB:SiH_4$	$2x10^{-4}$ of $PH_3:SiH_4$	no
2	Lowly Doped *n-p* junctions	$2x10^{-3}$ of $TMB:SiH_4$	$2x10^{-4}$ of $PH_3:SiH_4$	no
3	Highly Doped *p-n* junctions	$2x10^{-2}$ of $TMB:SiH_4$	$2x10^{-3}$ of $PH_3:SiH_4$	no
4	Lowly Doped Undoped - *n*, *p-n* junctions	undoped	$2x10^{-4}$ of $PH_3:SiH_4$	no
5	Lowly Doped *n* – Undoped, *n-p* junctions	undoped	$2x10^{-4}$ of $PH_3:SiH_4$	no
6	Highly Doped passivated *p-n* junctions (low on/off ratio)	$2x10^{-2}$ of $TMB:SiH_4$	$2x10^{-3}$ of $PH_3:SiH_4$	yes

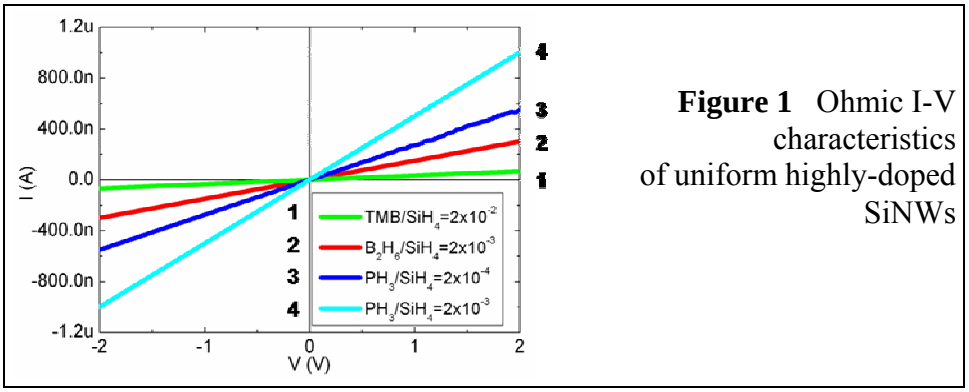

Figure 1 Ohmic I-V characteristics of uniform highly-doped SiNWs

In previous work, uniformly doped *p*- and *n*-type SiNWs were shown to display near ohmic current-voltage characteristics (Fig. 1). This supports the conclusion that the metal-semiconductor junctions at the metal contacts to the NWs were ohmic, instead of Schottky barrier limited. This implies that the rectifying behavior of the modulation-doped *p-n* junctions characterized later in this work can be attributed to the *p-n* junction itself, instead of the metal-semiconductor contacts. Additional evidence supporting this conclusion comes from electrostatic force microscopy (EFM) of a *p-n* SiNW (Fig.2). The EFM image shows a phase contrast difference at the *p-n* junction of the SiNW. The phase contrast indicates a potential difference. One can conclude from the image that the entire voltage drop across the wire occurred at the junction, and not at the contact regions.

In this paper, the current-voltage behavior of SiNW diodes are examined with respect to varied doping concentrations and whether passivation was performed. Figures of merit (e.g. ideality factor) of the current-voltage characteristics of the diodes are inspected. The variability of the nanowire junctions' current-voltage behavior is appraised. It has been shown that uniformly doped silicon nanowires configured as FETs possess photosensitivity.[11] The photodetection properties of the junctions are examined by measuring the photogenerated current of the nanowire junctions.

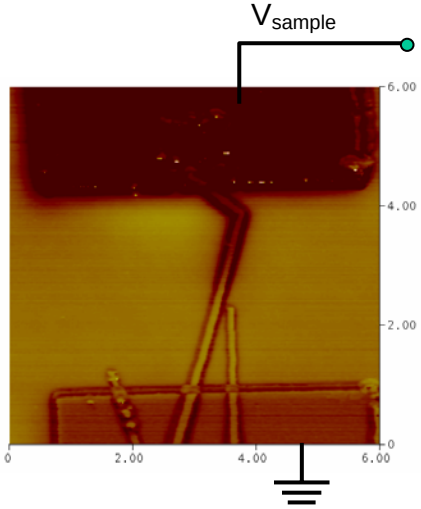

Figure 2 EFM image of a forward biased *p-n* SiNW. Vsample = -2V, Vtip = +2V

EXPERIMENTAL DESCRIPTION

The nanowires were grown in the presence of silane and dopant gases until they reached a desired length. Next, the SiNWs were removed by sonication from the SiO_2 substrate and dispersed into a liquid suspension. Electrical testing of the NWs took place on a test structure fabricated on a Si substrate. The test bed consisted of two Ti/Au metal electrodes connected to each nanowire. These two contacts were 2.2 μm apart. A single NW was aligned between each contact pair through electrofluidic alignment.[12] This procedure takes place by first dispensing a suspension of NWs onto the test beds. An AC voltage is applied between each pair of contacts causing an AC electric field to form. The E field will force the ends of the NWs to shift in position towards the contacts. As soon as one NW makes a connection between a pair of contacts, both contacts will be brought to the same electrical potential and the electric field will cease, leaving a single NW attached to the contacts (Fig. 3). Next, a top metal layer is patterned over the SiNW to obtain good contact.

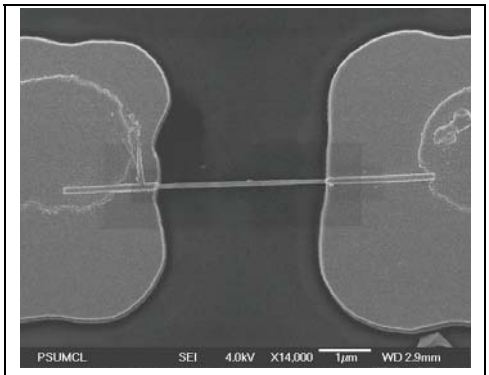

Figure 3. FESEM image of actual test structure

Measuring I-V Behavior

Two-point current-voltage measurements were carried out under a nitrogen gas ambient atmosphere. The samples were purged for at least 8 hours before measurements. Measurements were taken with a Cascade Microchamber probe station and HP semiconductor analyzer 4156B at room temperature.

Measuring response to light

Two-point probe measurements were carried out using the same equipment previously described. A 200 W light source was placed above the cell being examined prior to the start of each measurement. Since the light source was placed manually, it was not in the exact same position for each measurement. The light source was held in place by an apparatus and did not move during a test. The measurements were carried out under the room's atmosphere, and not under nitrogen gas ambient. Ten-minute long transient measurements were performed. The junction was kept in reverse bias at 5 V. The light source was turned on at approximately the 5 minute mark. For nanowires that showed a response to light, the increase in current took place much quicker than the integration time used (1 s).

RESULTS AND DISCUSSION

A summary of the measurement results and yields of the nanowire junctions produced are in Table II. In order to calculate the yield percentages, a rule was placed on which junctions could be considered rectifying. The junctions that were determined to be rectifying possessed on/off ratios greater than 10^2. This rule applied to all the junction types examined except for the passivated junctions. The passivated junctions (type 6) possessed lower on/off ratios, and only junctions with an on/off ratio greater than 10^1 were deemed rectifying.

Table II. Summary of Results for all SiNW junction types

No.	Type of Junction	Average Ideality Factor (0-0.5V)	Yield of Fabrication Process
1	Lowly Doped *p-n* junctions	4.6, $\sigma = 2.81$	25% (23/91)
2	Lowly Doped *n-p* junctions	2.6, $\sigma = 0.69$	43% (16/37)
3	Highly Doped *p-n* junctions	3.9, $\sigma = 1.3$	20% (3/15)
4	Lowly Doped Undoped - *n*, *p-n* junctions	3.4, $\sigma = 1.75$	22% (11/49)
5	Lowly Doped *n* – Undoped, *n-p* junctions	5.5, $\sigma = 6.5$	34% (11/32)
6	Highly Doped passivated *p-n* junctions (low on/off ratio)	4.6, $\sigma = 1.5$	50% (6/12)

In Fig.s 4 and 5 are I-V plots of nanowires that displayed rectifying behavior. These nanowires were considered heavily doped, in terms of this group's fabrication process. The I-V plots in Fig.s 6 and 7 are of lowly doped nanowires. There are two plots shown, corresponding to whether either the *n* or *p* doped end was grown first. In the key to Fig.7 is a schematic of the two nanowires; the Au end represents the place where nanowire growth ceased.

There was a large variability in the current-voltage characteristics of similarly synthesized rectifying junctions. This makes comparison between wires of different doping density and orientation inconclusive. For example, the forward and reverse bias currents (at ± 2V) of all junction types deviated drastically. For every junction type, the average current at forward or reverse bias was surpassed by the standard deviation accompanied with it.

There are some possible factors that account for the variability in the characterization results. The diameter of the nanowires varied between 60 to 140 nm, which directly affected the resistance and surface state of the wires. The nanowire growth procedure produced single crystal nanowires which could take on one of a few different crystal orientations. It is possible that nanowires of different crystal orientations have different electrical behavior. The location of the *p-n* junction was not uniform. The proximity of the junction to the *p* side or *n* side contacts could affect the junction's performance. The grading effect of the junction was unknown. It is not known how the grading of nanowire *p-n* junctions affects their electrical characteristics.

The average ideality factors of the junction types are plotted in Fig. 8. The type of junction with the lowest (2.6, $\sigma = 0.69$) ideality factor is the lowly doped *n-p* junctions (type 2). The ideality factor results for the *n* – undoped (type 5) junctions aren't included since there was a large variance in the sample.

Key for Figures 4 and 5:

- *p* segment is doped at $2x10^{-2}$ of TMB(p acceptor):SiH_4

- *n* segment is doped at $2x10^{-3}$ of PH_3(n donor):SiH_4

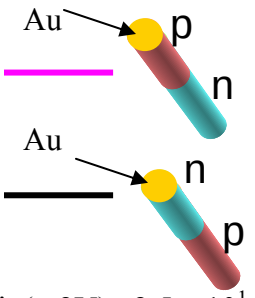

n-p junction Ideality factor: 4.05, on/off ratio(± 2V): 2.5×10^1
p-n junction Ideality factor: 5.46, on/off ratio (± 2V): 1.6×10^1

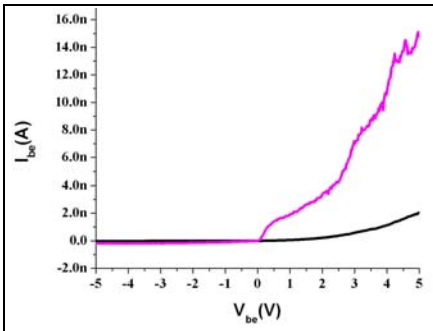

Figure 4. I-V plot of *n-p* and *p-n* highly doped junctions

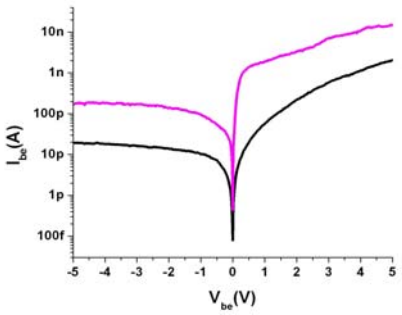

Figure 5. Log I-V plot of *n-p* and *p-n* highly doped junctions

Key for Figures 6 and 7:

- *p* segment is doped at $2x10^{-3}$ of TMB(p acceptor):SiH_4

- *n* segment is doped at $2x10^{-4}$ of PH_3(n donor):SiH_4

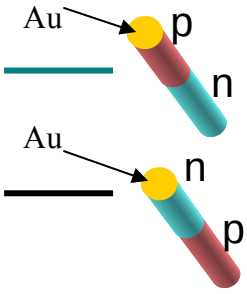

p-n junction Ideality factor: 9.76, on/off ratio (± 2V): 3.7×10^2
n-p junction Ideality factor: 4.5, on/off ratio(± 4V): 11.6×10^2

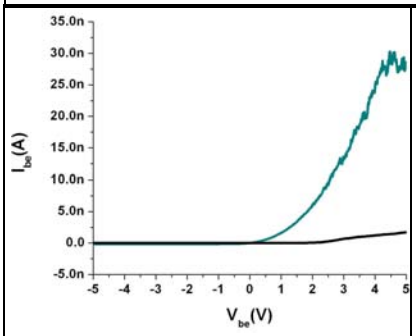

Figure 6. I-V plot of *n-p* and *p-n* lowly doped junctions

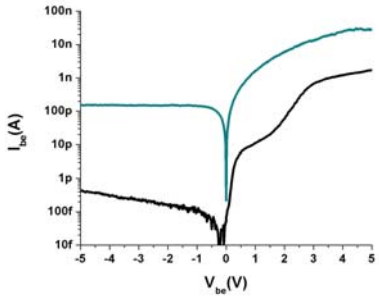

Figure 7. Log Scale I-V plot of *n-p* and *p-n* lowly doped junction

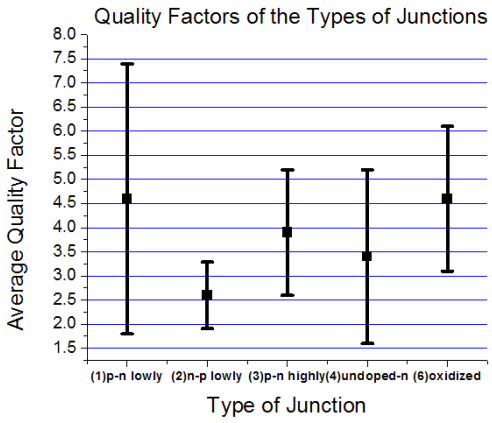

Fig. 8 Average and standard deviations of the quality factors of the junctions. The x-axis lists the types of junctions.

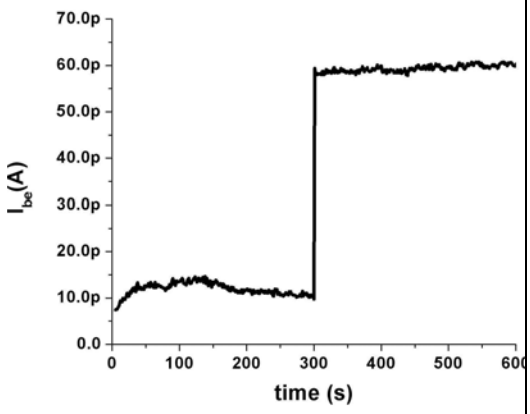

Figure 9. Current vs. time plot. Illumination turned on at 300s. Nanowire junction shows response to light. *P* segment is doped at $2x10^{-3}$ TMB:SiH_4. *N* segment at $2x10^{-4}$ PH_3:SiH_4

As evidenced in Fig.s 5 and 7, the slope of the log scale I-V plots of the junctions displayed a large decrease for applied voltages greater than 0.5 V forward bias. This indicates that a series resistance was present which limited the current conducted at the higher applied voltages. This series resistance can be attributed to the large intrinsic resistance of the nanowires. The small cross-sectional area of the nanowires accounts for the significant intrinsic resistance. The average resistance of a heavily doped *p*-type SiNW (80 nm diameter, 6 μm length) is 3.6 MOhms. This large series resistance causes an increase in the ideality factor of the diode for high voltages. In contrast, conventional diodes, which have series resistances in the low Ohms range, retain their low ideality factors for higher voltages. The ideality factors of the nanowire junctions were determined only for the low voltage range of 0-0.5V forward bias. The large series resistance caused the ideality factor of the junctions to drastically increase for larger forward bias ranges.

38% of the rectifying junctions tested displayed a response to light. An example of a single nanowire responding to light is in Fig. 9. The tests were carried out on lowly doped silicon nanowire junctions (types 1 and 2). The average results showed the dark current was 11.1 pA, and the photogenerated current was 20.6 pA. All of the photosensitive junctions produced a constant photogenerated current while under illumination.

CONCLUSION

Silicon nanowire *p*-*n* junctions were produced which displayed rectifying behavior. Nanowires doped at different concentrations and with or without passivation were found to have rectifying characteristics. The unrefined fabrication process produced junctions with a large amount of variability among their rectifying characteristics. Additionally, it was determined that the junctions could be used as photodiodes. Upon exposure to light, a photogenerated current was measured.

The rectifying silicon nanowire diodes shown in this work are a successful application of the nanowire modulation-doping procedure. This procedure has the ability to produce more complicated nanowire devices, such as *n*-*p*-*n* structures for inversion-type FETs and heterojunctions. The *p*-*n* junctions demonstrated in this paper could one day serve along with other silicon nanowire devices in complex functional structures.[13]

ACKNOWLEDGEMENTS

This material is based upon work supported by the National Science Foundation under Grants No. EEC-0244030 and DMR-0103068 and the Penn State MRSEC, Center for Nanoscale Science (DMR-0213623).

REFERENCES

[1] T. Li, Z. Li, "A discussion on the Extension of Moore's Law," *Solid-State and Integrated Circuits Technology, 2004. Proceedings. 7th International Conference on*, p. 251-254 (2004)

[2] K.K. Lew, C. Reuther, A.H. Carim, J.M. Redwing, "Template-directed vapor-liquid-solid growth of silicon nanowires," *J. Vac. Sci. Tech. B*, **20**, 389 (2002).

[3] K.K. Lew, L. Pan, T.E. Bogart, S.M. Dilts, E.C. Dickey, J.M. Redwing, Y.F. Wang, M. Cabassi, T.E. Mayer, "Structural and electrical properties of trimethylboron-doped silicon nanowires," *Appl. Phys. Lett.*, **85**, 3101 (2004).

[4] S.M. Dilts, A. Mohmmad, K.K. Lew, J.M. Redwing, S.E. Mohney, "Fabrication and Electrical Characterization of Silicon Nanowire Arrays," *Mater. Res. Soc. Symp. Proc.*, **832** (2004)

[5] Y. Wu, Y. Cui, L. Huynh, C. Barrelt, D.C. Bell, C.M. Lieber, "Controlled Growth Structures of Molecular-Scale Silicon Nanowires," *Nano Letters*, **4**, 433 (2004)

[6] Y. Wang, K.K. Lew, B. Liu, J. Mattzela, J. Redwing, T. Mayer, "Electrical Properties of p- and n-type Silicon Nanowires," *Device Research Conference, 2004. 62nd DRC. Conference Digest*, p. 23-24

[7] Y. Cui, C.M. Lieber, "Functional Nanoscale Electronic Devices Assembled Using Silicon Nanowire Building Blocks," *Science*, **291**, 851 (2001)

[8] G. Cheng, A. Kolmakov, Y. Zhang, M. Moskovits, "Current rectification in a single GaN nanowire with a well-defined p-n junction," *Appl. Phys. Lett.*, **83**, 1578 (2003)

[9] K.K. Lew, Y. Wang, B. Lui, S. Mohney, T. Mayer, J. Redwing, "*p-n* Junction in Silicon Nanowires," *Electronic Materials Conference 2005*, presentation

[10] G. Zheng, W. Lu, S. Jin, C.M. Lieber, "Synthesis and Fabrication of High-Performance n-Type Silicon Nanowire Transistors," *Adv. Mater.* 2004, **16**, 1890 (2004)

[11] Y. Ahn, J. Dunning, J. Park, "Scanning Photocurrent Imaging and Electronic Band Studies in Silicon Nanowire Field Effect Transistors," *Nano Lett.,* **5** (7), 1367-1370 (2005)

[12] P.A. Smith, C. D. Nordquist, T.N. Jackson, T.S. Mayer, "Electric-field assisted assembly and alignment of metallic nanowires," *Appl. Phys. Lett.*, **77**, 1399 (2000)

[13] Y. Huang, X.F. Duan, Q.Q. Wei, C.M. Lieber, "Directed Assembly of one-dimensional nanostructures into functional networks," *Science*, **291**, p. 630-633 (2001)

MICROWAVE CHARACTERIZATION OF TRANSMISSION LINES WITH DIELECTRIC THIN FILMS

Kevin Deily*, Lance Haney[+], and Michael Lanagan[#]
Department of Electrical Engineering and Materials Science
Pennsylvania State University, University Park, PA 16802

*Undergraduate student of
Department of Electrical & Computer Engineering and Computer Science
Ohio Northern University
Ada, OH 45810

ABSTRACT

Microwave transmission relies on conductor lines that have low loss and controlled impedance. In addition, novel phase shifters and filters for telecommunications are based on microwave transmission lines with nonlinear dielectric materials. In this study we will explore a ferroelectric polymer PVDF (Polyvinylidene fluoride) as a potential tunable material.

Microstrips, coplanar waveguides (CPW), and ring resonators will be designed, simulated and tested with and without a thin-film layer of PVDF . The electrical characteristics will be measured and compared for both cases using fused quartz as the substrate.

Using the Transmission Line Calculator program, the dimensions for the transmission lines can be found. Following that, a simulation using CST Microwave Studio can be done to acquire the s-parameter graphs. Using the information from those graphs, the effective dielectric constant can be computed using various equations.

The fused quartz substrate will then be placed in the GDK Dielectrometer to determine the dielectric constant of the material. The substrates will then have the microstrip, CPW, and ring resonator patterns screened onto them. After this is completed, the characteristics will be found using the Inter-continental, Cascade Probe Station and the HP8510 Network Analyzer. A thin-film layer will then be placed on the samples and the previous steps will be repeated.

[+] Graduate Mentor
[#] Faculty Mentor

33

INTRODUCTION

Ordinary transmission lines operate normally at low frequencies (typically around 50 to 60 Hz) and function with relatively low power losses. However, at higher frequencies, the radiation losses may be serious and in fact reduce the amount of power carried in the transmission line down to virtually nothing. At these higher frequencies (between 1 GHz and 30 GHz), special low-loss transmission lines must be used to properly transmit the signal.[1]

The way these low-loss transmission lines work is by having a good conductor placed along the surface of a dielectric material. The majority of the energy transmission takes place on the surface of the conductor. This phenomenon is known as the skin effect.[2] Due to the skin effect, the thickness of the conductor can normally be relatively small, since most of the transmission does not occur in the conductor. Also, this will cause some of the electric field lines to go through the dielectric material as well as the material above the conductor (i.e. air). An example of this can be seen in Figure 1.[3]

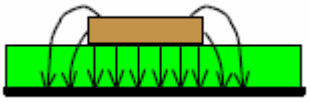

Figure 1. Electric Field Lines

One method of putting the conductor on the dielectric material is to print the conductor onto the material. The conductor can have many different patterns, ranging from a simple straight line (Figure 1) to a coplanar waveguide (Figure 2). In a coplanar waveguide, the signal is transmitted along the middle plane, known as the signal plane, and the electric field lines travel from the signal plane to the two other planes, known as ground planes.

Each pattern has its own characteristics and set of equations to go with it, thus allowing for the low-loss transmission line to be versatile. These transmission lines can be used for many numerous things, including filter design and telecommunications.[4]

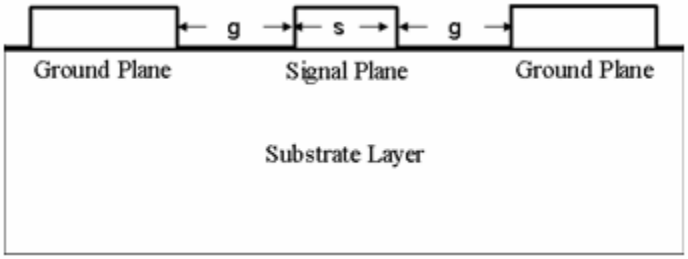

Figure 2. Coplanar Waveguide Pattern

A way to change the dielectric constant would be to add a layer of thin-film to the top of the substrate and on top of the conductor. This is would allow

for more or less of the electric field to transfer through the top and alter the electric field in general. This would theoretically increase or decrease the dielectric constant of the substrate if the top layer had a higher dielectric constant then the substrate.

EXPERIMENT DESCRIPTION

For this experiment, three different patterns were printed onto a fused quartz substrate. Those three patterns were a microstrip, a microstrip ring resonator, and a grounded coplanar waveguide (GCPW), which can be seen in Figure 3. Due to a lack of time, three screens that were already made were used. Taking the dimensions of the screens and using the Transmission Line Calculator (Figure 4), the dimensions for a sample that would be best were found.

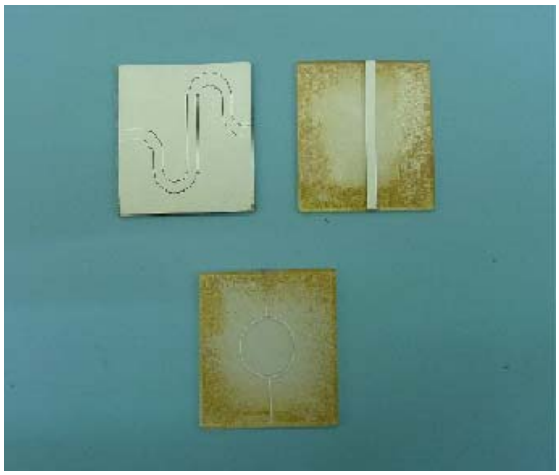

Figure 3. (From Top Left, clockwise) Grounded Coplanar Waveguide, Microstrip and Microstrip Ring Resonator

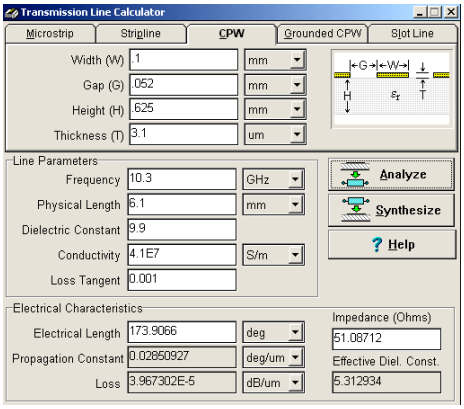

Figure 4. Transmission Line Calculator program

After proper dimensions were decided upon, several fused quartz samples were gathered. Using a GDK Dielectrometer, the dielectric constant (ε_r) the

substrates was calculated. This is done using the software, which calculates ε_r by taking into account the thickness of the sample, the transmission coefficient, and the two 3dB roll-off points. A picture of this device can be seen in Figure 5.

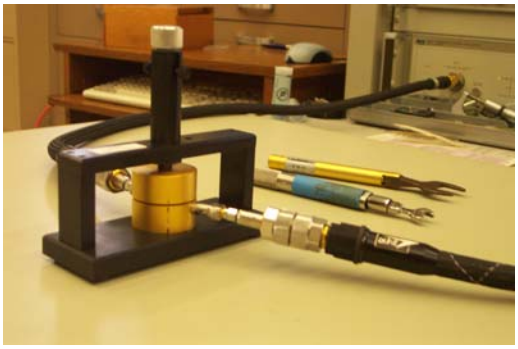

Figure 5. GDK Dielectrometer

After this is completed, the screens for the three different were placed on various samples using a screen-printing method. This method consists of taking a screen mesh and putting the desired pattern onto the mesh. The substrate is then placed under the mesh and the desired ink was poured on the mesh. The ink used in this experiment Silver DuPont 6160 ink was used. A squeegee was then run overtop the screen, and the pattern was transferred to the substrate. Also for all of these samples, a ground plane was placed on the opposite side. To complete the screen-printing method, the substrates were then fired in a furnace for approximately fifteen minutes at 850 ºC.

After the samples were made, the next thing done was the microwave analysis using the Hewlett Packard Network Analyzer 8510 (Figure 6). A network analyzer is a machine that characterizes electric devices by comparing the signal input to it to the signal that is output from it. The HP 8510 has a range of 45 MHz to 26.5 GHz.

Figure 6. Hewlett Packard Network Analyzer 8510

Two different devices were then used to measure the three different samples. The microstrip and microstrip ring resonator were measured using the Inter-Continental Microwave instrument, seen in Figure 7. This instrument is capable of measuring substrates that are between .24" and 4.75" and up to 1.905 mm thick. The device measure the characteristics by having two small points make contact with either end of the microstrip and sending the signal along the conductor. The second device used was the Cascade Microprobe Station, seen in Figure 8. This device measured the characteristics of the GCPW. The microprobe station works by using two probes to provide the signal to the waveguide, in a similar fashion as the Inter-Continental.

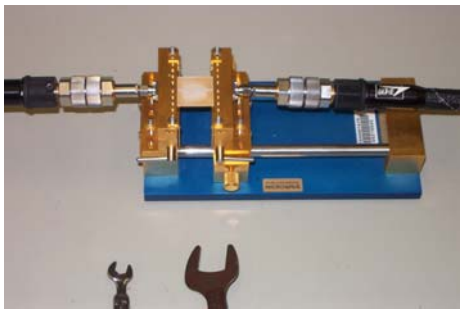

Figure 7. Inter-Continental Microwave

Figure 8. Cascade Microprobe Station

Once all the initial measurements were taken, a layer of the polymer PVDF was applied on top of the samples. Two separate methods were used to place this layer onto the samples. The first method, used on half of the samples, was to spin coat on two layers for approximately a layer of 25 μm thick. The second method was to use a doctor's blade and cast on a layer of approximately .1 mm thick. After this was completed, the measurements were retaken with the new layer on top of the samples.

In addition to the measurements, the samples were simulated using CST Microwave Studio. Using this program, the substrate can be drawn and the conductive pattern and ground plane can be added on top and bottom. Using the transient analysis, the program can simulate what theoretically should occur with the actual samples (Figure 9). Also, markers may be placed at different locations to observer the electronic fields (E-fields).

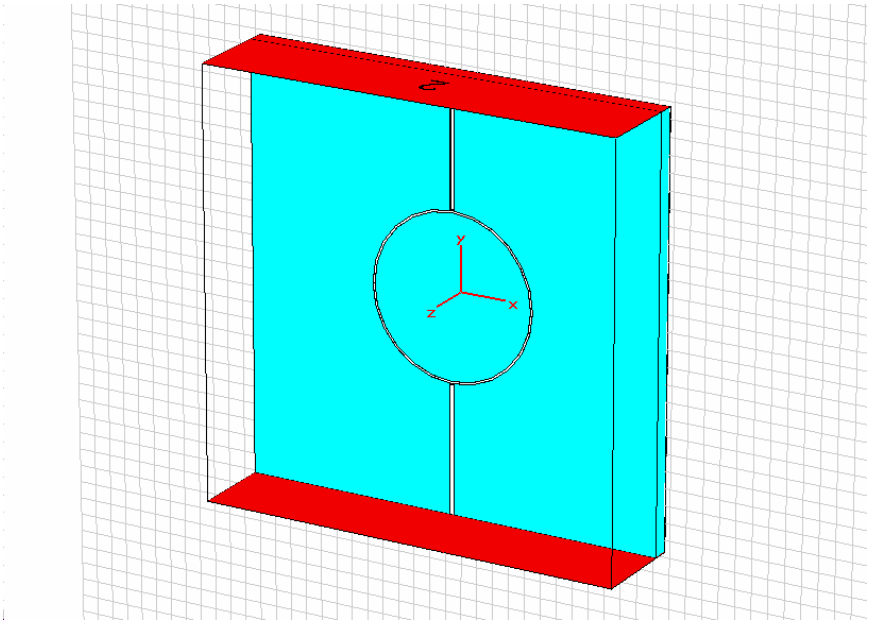

Figure 9. Sample from CST Microwave Studio simulation program

RESULTS AND DISCUSSION

Using the Transmission Line Calculator and the available screens, it was determined that the appropriate dimensions to be used in this experiment were 1 inch by 1 inch by 1 mm. Fifteen samples of fused quartz with those dimensions were ordered. The thickness of the sample is vital in all the measurements, so the thickness was then measured of all the samples. After that was completed, the dielectric constant was measured using the GDK Dielectrometer. The results from this device can be seen in Table I.

The documented value for the dielectric constant of fused quartz is approximately 3.78. The average value taken from the GDK Dielectrometer for the fifteen samples is 3.783. Therefore, the preliminary dielectric values for samples of the fused quartz almost exactly match the accepted value.

Table I. GDK Dielectrometer Measurements

Sample No.	Thickness, cm	Dielectric Constant, ε_r
1	0.1106	3.777
2	0.10942	3.782
3	0.10766	3.785
4	0.10638	3.789
5	0.10596	3.783
6	0.10704	3.785
7	0.10788	3.784
8	0.10514	3.778
9	0.1075	3.778
10	0.10898	3.778
11	0.1068	3.781
12	0.10824	3.784
13	0.10748	3.784
14	0.10524	3.789
15	0.10632	3.786

The measurements for the microstrip ring resonator were done next. Using the information from the network analyzer the effective dielectric constant (ε_{eff}) and real dielectric constant (ε_r) were found using the following equations:

$$\varepsilon_{eff} = \left(\frac{cn}{\pi D f_R} \right)^2 \tag{1}$$

$$\varepsilon_r = \frac{2\varepsilon_{eff} - 1 + \left[1 + 12\left(\frac{d}{w}\right)\right]^{-\frac{1}{2}} + 0.04\left[1 - \left(\frac{d}{w}\right)\right]^2}{1 + \left[1 + 12\left(\frac{d}{w}\right)\right]^{-\frac{1}{2}} + 0.04\left[1 - \left(\frac{d}{w}\right)\right]^2} \tag{2}$$

where c is the speed of light, n is the node number, D is the median ring diameter, f_R is the resonant frequency, d is the thickness of the conductor, and w is the width of the conductor. The calculated values can be found in Table II.

Table II. Initial Ring Resonator Data

Sample No.	Line Width, mm	Sample Thickness, mm	Ring Dia.,mm	node	Frequency, GHz	S_{21} Mag Peak, dB	Δ f, MHz	e_{eff}	e_r
11	0.248	1.068	9.766	1	5.996	-10.0	115.86	2.62	3.79
12	0.244	1.0824	9.792	1	6.003	-9.8	127.79	2.60	3.76
13	0.253	1.0748	9.776	1	6.003	-10.0	119.99	2.61	3.77
15	0.237	1.0632	9.783	1	5.997	-9.8	122.25	2.61	3.78

Next, the values of the microstrip can be found using the following two equations:

$$\varepsilon_{eff} = \left[\frac{\phi c}{360\, fl}\right]^2 \tag{3}$$

$$\varepsilon_r = \frac{2\varepsilon_{eff} \cdot \sqrt{1+12\left(\frac{d}{w}\right)} - \sqrt{1+12\left(\frac{d}{w}\right)} + 1}{\sqrt{1+12\left(\frac{d}{w}\right)} + 1} \tag{4}$$

where φ is the phase angle at a given point, f is the frequency at that point, and l is the length of the conductor. The calculated values for the microstrip are located in Table III.

Table III. Initial Microstrip Measurements

Sample No.	Sample Thickness, mm	Line Width, mm	Phase, degree	Frequency, GHz	e_{eff}	e_r
1	1.106	1.951	360	6.739735	3.0801	4.0635
2	1.0942	1.987	360	6.739375	3.126	4.1206
3	1.0766	1.9415	360	6.72729375	3.126	4.1231
4	1.0638	1.952	360	6.72729375	3.126	4.1169

Following this, the calculations for the GCPW were done using a computer program due to the advanced mathematics required. Those results may be found in Table IV.

Table V. Initial GCPW Measurements

Sample No.	Sample Thickness, mm	Signal Width, mm	Gap Width, mm	Phase, degree	Frequency, GHz	e_{eff}	e_r
10	1.0898	1.75	0.15	180	1.8022125	2.417	3.60
14	1.0524	1.76	0.15	360	3.559425	2.478	3.68

After the PVDF polymer was coated on the samples and the measurements were retaken, the same equations as before (Equations 1-4) were used again for simplicity, due to the fact that the actual equations involved elliptic integrals. Those calculations can be found in Table V.

From the data collected after the coating was placed on the samples, a slight cut through the conductor in sample number 10 was found, which in turn caused the falls to drop dramatically. This caused the dielectric constant to appear much lower than it actually was. The data collected from this sample must be thrown out. Also, the data for the microstrips remained unchanged, showing that almost all of the electric field travels through the substrate and little to none through the air.

Table V. Coated Sample Measurements

Sample No.	Coating	e_{eff}	e_r
1	Thin	3.0801	4.0635
2	Thin	3.126	4.1206
3	Thick	3.126	4.1231
4	Thick	3.126	4.1169
10	Thin	1.33386	1.6
11	Thin	2.65	3.84
12	Thin	2.63	3.8
13	Thick	2.65	3.84
14	Thick	2.72129	4.12
15	Thick	2.65	3.85

After comparing all the data, it was decided to focus on the GCPW with the thicker layer of PVDF. The CST Microwave Studio simulation was run many times changing the dielectric constant of the PVDF to get a range of phase angles which the frequency was 1.6984375 GHz. The reason for doing this was to determine an acceptable range for the dielectric constant of the PVDF and a range of error for the S_{21} phase plot. A graph of this comparison may be found in Figure 10.

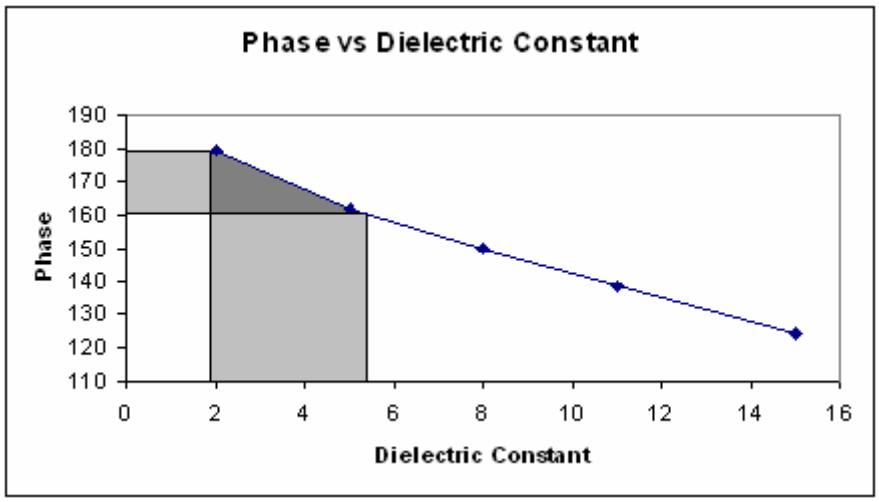

Figure 10. Error Plot for GCPW.

An acceptable range of approximately 10% was given for the simulation. This value was used due to the inaccuracy of the simulation program. As seen in Figure 10, the dielectric constant of the PVDF was roughly between 2 and 6. This is lower than what PVDF is normally reported at, which is between 6 and 12. A possible reason for this could be that the dielectric constant of sample 14 was lower than normally expect, which could in turn affect the calculated value, making it appear as if the layer had a smaller dielectric than normally.

CONCLUSION

It can be seen that by adding the PVDF on top of the sample did increase the dielectric constant for the microstrip ring resonator and the grounded coplanar waveguide. This shows that some of the electric field travels through the medium above the conductor, and that by adding a layer of a material will in fact have an impact. If with more time and money, a better material, with a higher dielectric constant, could be used in place of PVDF causing a much larger change. Also, focusing on the ring resonator and GCPW would be in the best interests, since those two patterns showed the most promise for future studies.

ACKNOWLEDGEMENTS

I would like greatly to thank Dr. Mike Lanagan for giving me support and excellent ideas for my project this summer and Steve Perini for teaching me how to use all the equipment around the lab and making me research go along much smoother. I would also like to thank Amanda Baker for helping me with the screen printing process and Beth Jones for helping with the spinning and coating process of the PVDF layers. Also, I would like to thank Lance Haney for teaching me how to use CST Microwave Studio and for allowing me to use some of his programs to help solve many of more complex mathematical equations. I would finally like to thank the National Science Foundation, the Electro-Optic Center, and Penn State University for allowing me to work on this research project. This material is based upon work supported by the National Science Foundation under Grant No. EEC-0244030.

REFERENCES

[1] D. M. Pozar, "Transmission Lines and Waveguides"; pp. 104-105 in *Microwave Engineering*, 2nd ed. John Wiley & Sons, INC, 1998.

[2] W. H. Hayt Jr. and J. A. Buck, "Propagation in Good Conductors: Skin Effect"; pp. 369-375 in *Engineering Electromagnetics*, 6th ed. McGraw-Hill, 2001.

[3] D. Brooks, "Microstrip Propagation Times Slower Than We Think," UltraCAD Design Inc. 1992.

[4] R. P. Feynam, R. B. Leighton, and M. Sands, "Waveguides"; pp. 24-1 in *The Feynman Lectures on Physics*, Vol II. Addison-Wesley Publishing Company, 1964.

ATMOSPHERIC ABSORPTION OF SPRITE EMISSIONS OBSERVED BY ISUAL INSTRUMENTATION

David H. Burkhardt*, Ningyu Liu+, Victor P. Pasko#

Department of Electrical Engineering
The Pennsylvania State University
University Park, PA 16802

* Undergraduate student of
Department of Physics
Haverford College
Haverford, PA 19041

ABSTRACT

Atmospheric transmission of electromagnetic radiation released by sprites was investigated. Ozone absorption cross-section and density profile data were used to develop a MATLAB script that models the absorption by ozone of radiation traveling from one point in the atmosphere to another as a function of the points' relative locations. MOSART software was then used to develop a model capable of accounting for all major absorbing agents in predicting the transmission of electromagnetic radiation between two points in the Earth's atmosphere. This model was used to determine the atmospheric transmission of radiation between typical sprite altitudes and 891 km, the altitude of FORMOSAT-2, a satellite that includes a set of instruments that observe sprite activity. As the current sprite theory predicts that most transmission comes from the1st and 2nd positive band systems of N_2, the Lyman-Birge-Hopfield band system of N_2, and the 1st negative band system of N^+_2, wavelengths in these bands were considered. The calculations performed indicate that while considerable absorption in the Lyman-Birge-Hopfield band system may occur, only minimal absorption in other band systems occurs. The developed model also indicates that radiation released by a related class of luminous upper atmosphere events known as blue jets may be absorbed by atmospheric ozone.

+ Graduate mentor
# Faculty mentor

1. INTRODUCTION

1.1 Sprite Production Mechanism

Sprites are luminous upper-atmosphere electrical discharges that are induced by cloud to ground lightning strikes. They occur in the mesosphere and lower ionosphere region of the atmosphere, typically between 50 and 90 km. Video of a sprite event was first obtained serendipitously on July 5, 1989 by a low-light level TV camera. Many other video images of sprites have since been captured, and have enabled discussion of sprite production and effects. Several theories explaining sprite production mechanisms have been developed. The theory that will be considered in this paper posits that they are generated by a quasi-electrostatic field that is created by cloud to ground lightning events [Pasko et al., 1997].

According to this theory, charge, both positive and negative, slowly build up in a tropospheric cloud. This accumulation of charge may lead to a lightning event, in which either the positive or negative charges from the cloud are deposited on the ground. This discharge, which transpires on the order of several milliseconds, leaves behind a large concentration of oppositely signed charge in the cloud. The cloud, which was previously an electric dipole, is now a large monopole, and will have associated with it a strong electric field. The field, referred to as a quasi-electrostatic field, will not last long. However, it will be quite strong while it lasts, and it will reach into the atmosphere above the cloud [Pasko et al., 1997].

In the atmosphere above the cloud, optical emissions may now occur through a mechanism that is comprised of several steps. The electric field causes electrons in the air to move, leading to collisions between these electrons and other air molecules. These collisions can excite and ionize the neutral particles in the air. When excited particles return to their unexcited state, they emit energy in the form of electromagnetic radiation. Emissions predicted by the model occur primarily in the 1st and 2nd positive bands of N_2, the Lyman-Birge-Hopfield band system of N_2, and the 1st negative bands of N^+_2 [Pasko et al., 1997].

Not all cloud to ground lightning events will instigate sprites. For a sprite to be initiated at any given point in space, the quasi-electrostatic field at that point must exceed a value known as the breakdown threshold. As the breakdown threshold falls off more rapidly with increasing altitude than the quasi-electrostatic field does, there is a greater chance of a sprite forming at higher altitudes. It is for this reason that sprites typically begin in the 70-80 km region [Pasko et al., 1997].

1.2 Blue Jet Generation

Blue jets and blue starters are another breed of luminous electrical discharge that occur above cloud level. Blue jets, so named for the blue light that they emit, are lightning-like events that begin at cloud tops and develop upwards, typically reaching altitudes of around 40 km. Blue starters are similar to blue jets

save for the fact that they terminate at an altitude of at most 25.5 km. Blue jets and blue starters events occur over volumes of space on the order of thousands of cubic kilometers, which is much greater than the volume of space associated with typical cloud to ground lightning events [Pasko and George, 2002].

Unlike sprites, blue jet and blue starter events are not instantiated by cloud to ground lightning. Their development, which is discussed more fully in [Pasko and George, 2002], is thought to be the result of the electric field within a cloud exceeding a certain threshold field value. When this level is approached, a leader-type discharge occurs, eventually transforming into a blue jet or a blue starter.

1.3 ISUAL Instrumentation

The scientific investigation of sprites consists of observing the electromagnetic radiation released by them. From these observations the identity of the molecules that emitted the radiation as well as their temperature and other characters can be inferred. Early sprite data were collected from land-based observation points, airplanes, and balloons. Now, the Imager of Sprites/Upper Atmospheric Lightning (ISUAL), a set of instruments on the FORMOSAT-2 satellite, is a major source of sprite data [Mende et al., 2004].

ISUAL is the product of a collaboration between the National Cheng Kung University, Taiwan, Tohoku University, Japan, and the University of California, Berkeley, and was sponsored by the National Space Program Office of Taiwan. ISUAL consists of a visible wavelength intensified CCD imager, a bore-weighted six wavelength channel spectrophotometer, and a two channel Array Photometer with 16 vertically spaced horizontally wide sensitive regions. Together, this instrumentation is capable of observing and recording electromagnetic radiation from the far ultraviolet to the near infrared regions of the visible spectrum. ISUAL is part of the payload of FORMOSAT-2, a satellite that was launched by Taiwan on March 20, 2004. FORMOSAT-2 orbits the earth at an altitude of 891 km with a periodicity of exactly 1/14 of a day, and is expected to gather data until 2009 [Mende et al., 2004].

Four of the channels of the spectrophotometer are designed to conform with the four major emission band systems that are associated with sprite events: the 1st and 2nd positive bands of N_2, the Lyman-Birge-Hopfield band system of N_2, and the 1st negative bands of N_2^+. By comparing the total intensities of radiation measured by these channels one can infer the relative significance of the band systems in sprite emissions [Mende et al., 2004].

ISUAL has several advantages over ground-based sprite observation systems. ISUAL's high altitude allows it to monitor a large portion of the Earth's surface at any given time. As sprite events are currently non-predictable, a system that is able to monitor a large area is seen as advantageous because it has a greater chance of observing a sprite when one does happen. Because the atmosphere is more dense below 50 km than it is above 50 km, there is considerably less atmospheric attenuation of radiation between ISUAL and sprite events than there is between ground based observation points and sprite events,

enabling ISUAL to detect a greater percentage of the radiation released by sprites than a ground-based system would be able to detect [Mende et al., 2004].

Thus far, ISUAL has monitored and reported data from many sprite events. However, ISUAL has not yet recorded a blue jet event [Mende et al., 2005]. As ISUAL has been orbiting the earth for over a year, this suggests that some atmospheric factor may be influencing the observation of blue jet and blue starter events by ISUAL.

1.4 Atmospheric Attenuation Considerations

As was mentioned in Section 1.3, atmospheric attenuation of radiation transmitted from sprite events to ISUAL is considerably less than the absorption that would be anticipated during the transmission of radiation from sprite events to ground-based observation points. However, attenuation still does occur and must be accounted for in any complete sprite model.

Several attenuating mechanisms exist in the atmosphere. One such mechanism is absorption. Molecules of any given species selectively absorb photons that have energy exactly equal to the energy difference between one of their occupied electron orbitals and one of their higher energy unoccupied orbitals. Molecules allow the transmission of photons whose energies do not match any orbital energy difference, meaning that some wavelengths will be heavily absorbed while other wavelengths will not be absorbed at all. The wavelengths that a given species absorbs are referred to as that species absorption lines. Absorption lines can be theoretically predicted, but because of the complexity of multi-atomic systems it is easier to measure them experimentally [Fenn et al, 1985].

When data regarding the strength of absorption lines is known, predicting atmospheric absorption along a pathway is not difficult; it can be performed by utilizing Lambert's Law:

$$dI_\lambda / I_\lambda = -n\sigma_{a\lambda} ds \qquad (1)$$

where I_λ is the intensity of radiation at wavelength λ, n is the number density of the molecule in question, $\sigma_{a\lambda}$ is the absorption cross-section of the molecule in question, and ds is an infinitesimal distance along the absorption pathway. Integrating both sides of this equations along a path of length s yields:

$$I_\lambda(s) = I_\lambda(0) e^{-\int_0^s n\sigma_{a\lambda} ds} \qquad (2)$$

where $I(0)$ is the initial intensity and $I(s)$ is the intensity transmitted across paths [e. g. Liu et al., 2005].

Molecular scattering is another mechanism that contributes to attenuation of radiation traversing the atmosphere. When a photon collides with a particle, it is possible that the oscillating electric field associated with the photon may

influence the electron distribution of atoms within the particle, causing them to oscillate and interact with the incident photon, effectively altering its trajectory. Molecular scattering refers only to scattering caused by interactions between photons and molecules with dimension on the same order as the wavelength of the photons [Fenn, 1985].

Larger particles suspended in air known as aerosols are also responsible for scattering photons that collide with them. Aerosol absorption is similar to molecular scattering except that it occurs with particles that are orders of magnitude larger than the wavelength of the radiation. These particles interfere with photons, causing them to change trajectory [Fenn, 1985].

These effects make the observed spectrum considerably different from the spectrum that is released by the sprite. Before radiation predicted by a sprite model can be compared to data gathered by ISUAL, this interference must be accounted for.

2. EXPERIMENTAL METHODS

Initially, a model for ozone absorption was generated. Data describing the cross-sectional absorption of ozone and its atmospheric density profile were obtained, and MATLAB technical computing software was used to incorporate these data into a script capable of determining absorption by ozone between two points in the atmosphere. These calculations were performed using equation (2). This script was used to predict the atmospheric absorption by ozone of radiation released by sprite events.

In order to simulate actual situations that might occur during ISUAL observations, absorption between the satellite altitude, 891 km, and altitudes at which sprites are expected to occur, 40, 50, 60, and 70 km, was calculated. The distance between sprite and satellite was set to be 2500 km. The geometry described is depicted in Figure 1.

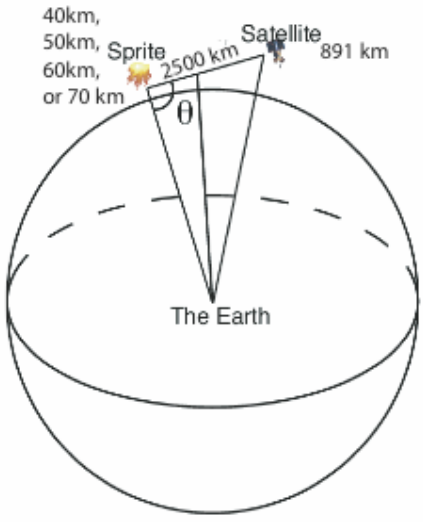

Figure 1:
ISUAL observation geometry [Liu et al., 2005].

A more complete absorption model was then developed using the Moderate Spectral Atmospheric Radiance and Transmittance Program (MOSART). MOSART is an atmospheric modeling program that combines atmospheric data from many sources in order to compute the transmission of radiation along pathways through the atmosphere. The user gives MOSART a list of geometrical situations describing lines through the atmosphere and a range of wavelengths and returns the fraction of radiation intensity at each wavelength that will be transmitted along the pathway described [Cornette et al., 1994]. Prior to the execution of this project, MOSART software had not been compiled for the Macintosh OS X operating system; considerable effort was therefore invested in determining and documenting the method for doing so.

MOSART software was used to generate Figure 1(b) presented in [Morrill et al., 1998] to insure that the software was correctly compiled. The geometry presented in Figure 1 was then entered into MOSART to determine absorption that will occur while radiation released by sprites travels to ISUAL.

These results were used to predict the absorption of radiation in the four bands that are considered in the current sprite model.

3. RESULTS AND DISCUSSION

Figure 2 shows the ozone cross-sectional data that was compiled from data presented in [Molina and Molina, 1986] and [Burrows et al., 1999]. Figure 3 displays the ozone vertical density profile, obtained through correspondence with Dr. Didier Rault and used in [Rault, 2005]. These data only represent ozone concentrations up to 50 km; it was initially assumed that because ozone density in the atmosphere falls off considerably above this altitude it does not play a significant role in absorption of radiation. Figure 4 presents the absorption of radiation by ozone predicted by the MATLAB script produced using these data.

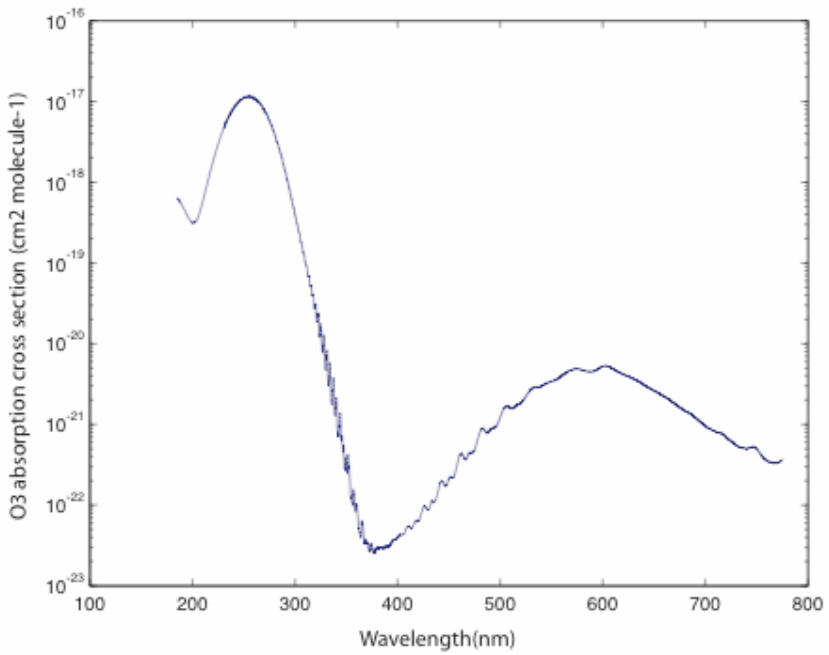

Figure 2: Ozone absorption cross-section obtained from [Molina and Molina, 1986] and [Burrows et al., 1999].

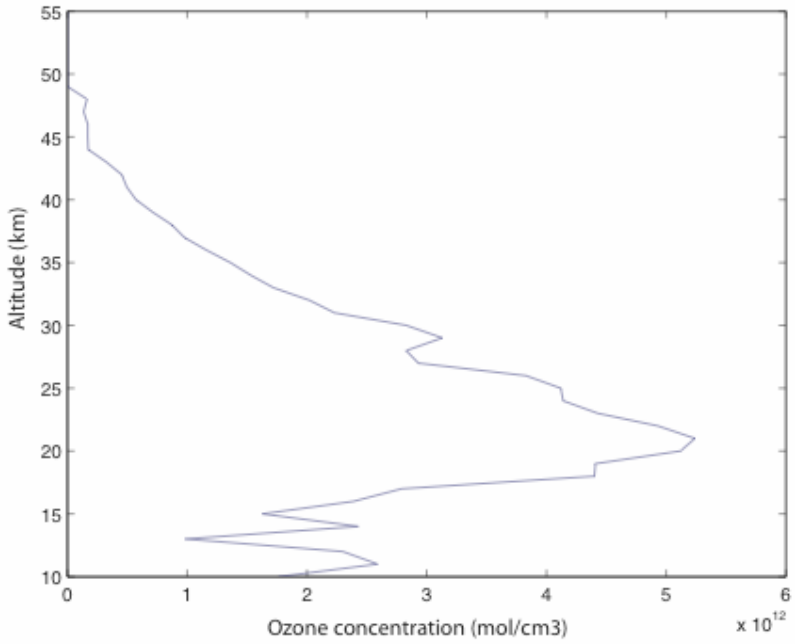

Figure 3: Ozone density profile obtained from [Rault, 2005].

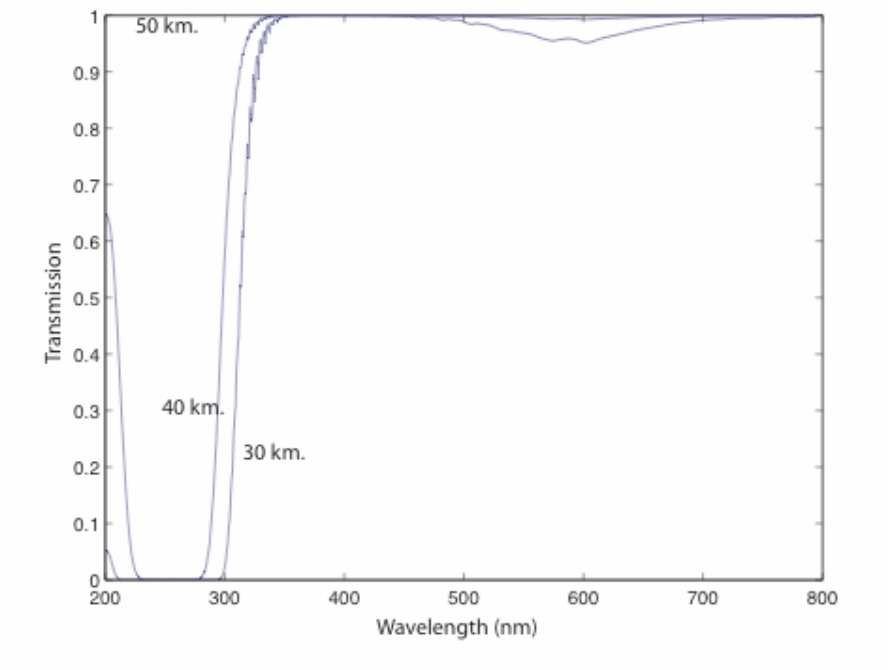

Figure 4: Ozone absorption between sprites at various altitudes and a satellite at 891 km along a 2500 km path predicted using ozone cross-section presented in Figure 2 and ozone density profile presented in Figure 3.

Several results were obtained with the software package MOSART. Figure 5 presents the absorption between sprite events at 65 km and observers at 0, 5, 10 and 20 km as presented by Morrill et al. [1998]. Figure 6 represents an attempt at the re-creation of this figure using MOSART. This figure is similar in shape to that of [Morrill et al., 1998], but the two differ in most places by approximately 10%. Several attempts were made to obtain closer values by altering the time of day, location of observer, and other calculation parameters. Altering the latitude of the observation point provided a noticeable change, but no location tested produced values similar to the results presented in [Morrill et al., 1998]. Figure 7 demonstrates the difference in the absorption between 20 km and 65 km along a 500 km path way presented in [Morrill et al., 1998] and the values obtained using MOSART. The cause of this discrepancy has not yet been discerned.

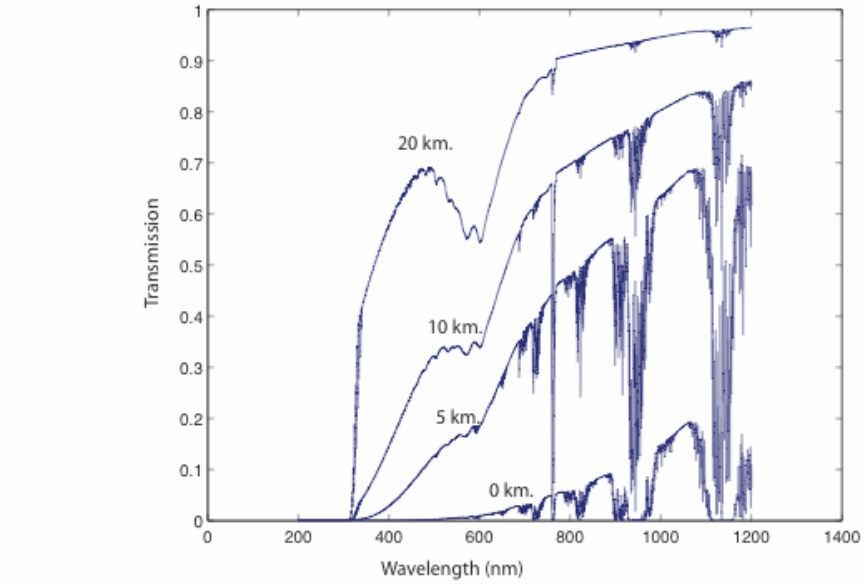

Figure 5: Atmospheric transmission between various altitudes and 65 km along a 500 km path as presented in [Morrill et al., 1998]

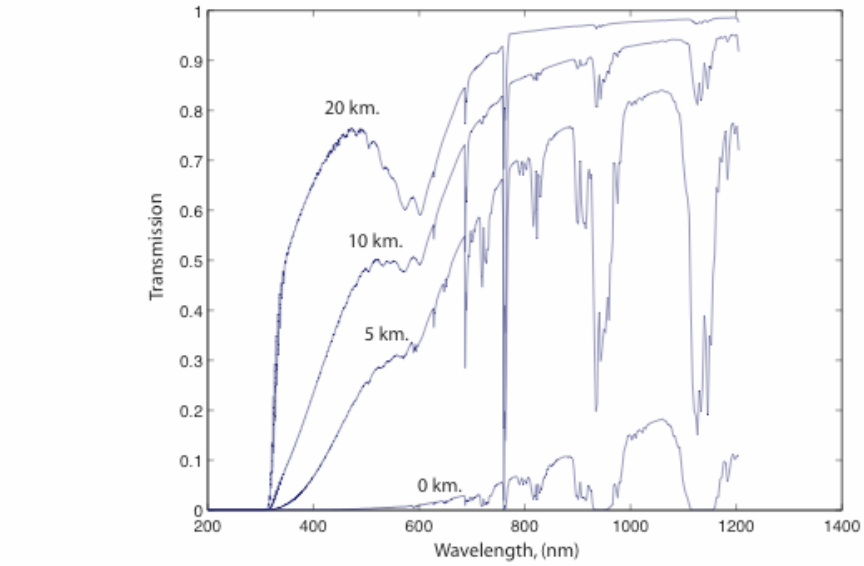

Figure 6: Atmospheric absorption between various altitudes and 65 km along a 500 km path as calculated using the MOSART software package in the present study.

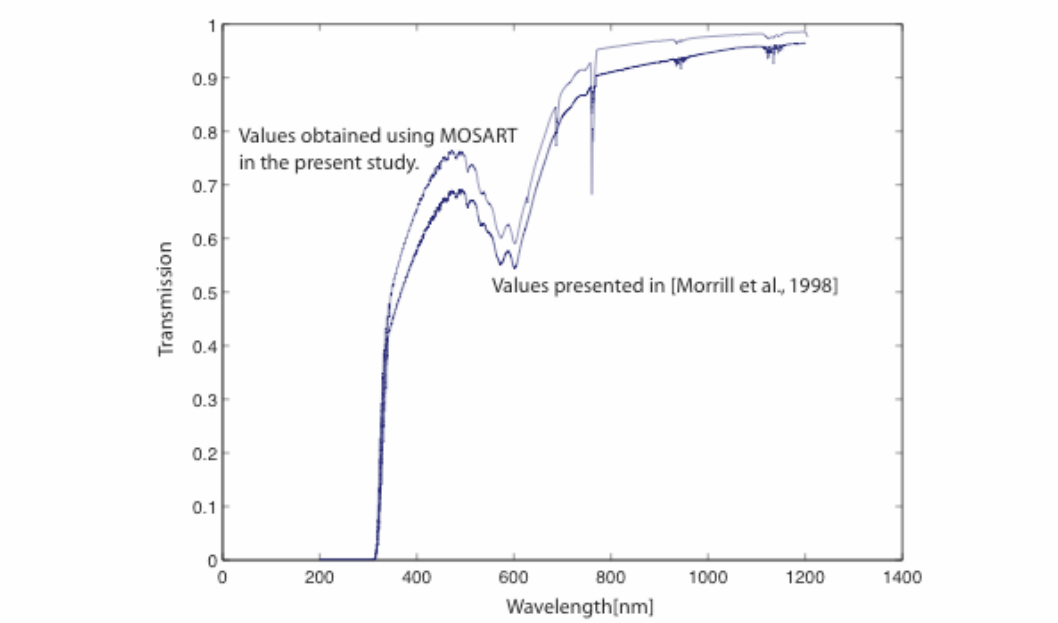

Figure 7: Comparison of predictions of atmospheric transmission between 65 km and 20 km along a 500 km path.

Figure 8 presents the absorption by ozone predicted by the MOSART software package. The ozone density profile used in MOSART extends to 120 km, and thus includes considerably more data than were used in creating Figure 4.

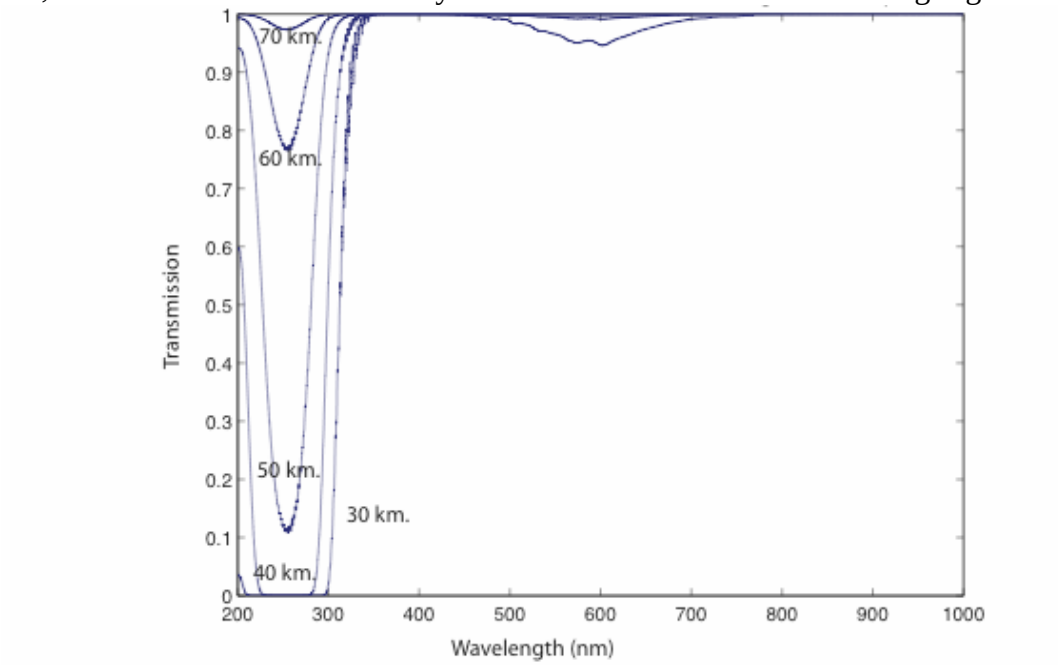

Figure 8: Ozone absorption predicted by MOSART between sprites at various altitudes and a satellite at 891 km along a 2500 km path.

The dissimilarity between Figures 4 and 8 is significant; an assumption was initially made that as ozone densities fell off considerably above 50 km and absorption above 50 km would be insignificant in comparison to that below 50 km. However, as the model that included absorption up to 120 km predicted considerably more absorption than that which only contained data extending to 50 km, this assumption has been shown to be erroneous. Atmospheric absorption models to be used in sprite modeling should therefore consider ozone absorption up to at least 120 km.

Figure 9 presents the total absorption predicted by MOSART for various altitudes.

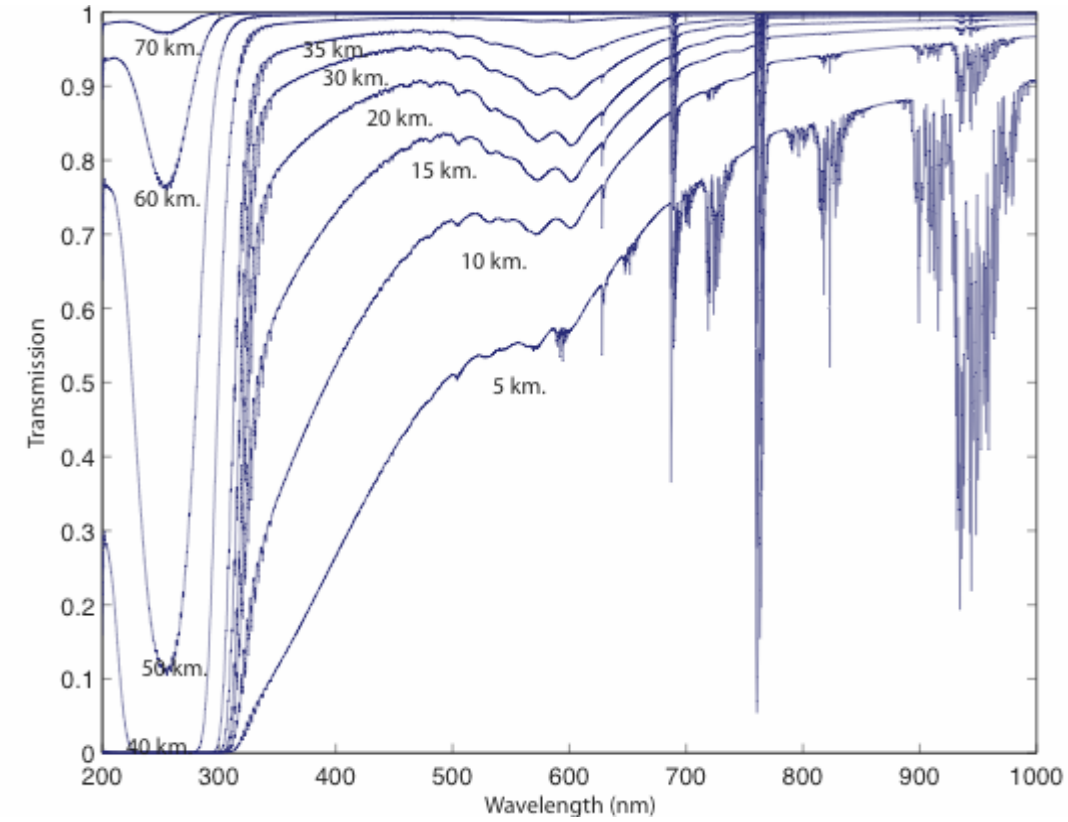

Figure 9: Total atmospheric transmission between sources at various altitudes and a satellite at 891 km along a 2500 km path.

FORMOSAT-2 has been orbiting the Earth for over a year. However, analysis of ISUAL data has thus far not revealed any data that appear to be linked to a blue jet event. The ISUAL filter responsible for blue jet detection is centered on the wavelength 337 nm, a wavelength that is significantly absorbed along emission pathways between 15 km sources and ISUAL as is indicated in Figure 9. It is therefore possible that atmospheric absorption has prevented any observation of blue jet events.

The transmission curves presented in Figure 9 were combined with data representing the relative strength of emissions in the 1st and 2nd positive band systems of N_2 and the 1st negative band system of N^+_2 from [Vallence Jones,1974, p. 80-176], and the Lyman-Birge-Hopfield band system of N_2 from [Liu and Pasko, 2005, and references therein] in order to determine the percentage of the emissions in each band that would be transmitted to the FORMOSAT-2 satellite from various altitudes. All emissions that reach FORMOSAT-2 are not actually detected by the ISUAL spectrophotometer; ISUAL filter data presented in [Mende et al., 2005] were applied to the results to determine the percentage of the emission from each band system that would actually be detected. The fraction of emissions from each band system released by sprites at various altitudes that would be detected by the ISUAL spectrophotometer is presented in Table 1.

The numbers in Table 1 indicate that, for the 1st and 2nd positive band systems of N_2 and the 1st negative band system of N^+_2, there is little difference in the fraction of emissions from 40 km sources that will be detected and the fraction of emissions from70 km sources that will be detected. There is therefore little absorption occurring in these band systems between 40 and 70 km. However, the fact that absorption significantly alters emissions in the Lyman-Birge-Hopfield band indicates that absorption must be taken into account in sprite modeling.

Table 1: Fraction of emissions from various band systems released at various altitudes that would be detected by the ISUAL spectrophotometer.

Emission Altitude	1^{st} positive N_2	2nd positive N_2	Lyman-Birge-Hopfield	1st negative N^+_2
40 km	.11	.27	.01	.63
50 km	.11	.28	.04	.64
60 km	.11	.28	.05	.64
70 km	.11	.28	.05	.64

4. SUMMARY

A simple model of the absorption by ozone of radiation released by sprites and observed by the ISUAL spectrophotometer was developed. Incorporated into the model was the assumption that atmospheric ozone only plays a significant role in absorption at altitudes below 50 km. MOSART software was then applied to standard observation geometries of the ISUAL instruments on the FORMOSAT-2 satellite to generate a more complete absorption model that could account for all major absorbing agents and perform absorption calculations up to altitudes of 120 km. The atmospheric attenuation of radiation released by sprites and other luminous discharges and detected by ISUAL was predicted. Comparisons between MOSART results obtained in this study and MOSART results presented in [Morrill et al., 1998] reveal a difference of about 10% in calculations of ground to sprite atmospheric absorption; an effort should be made to determine the cause of this discrepancy. Comparisons between ozone absorption predicted by the simple model developed in this study and ozone absorption predicted by the

MOSART model indicate that considerable absorption of radiation by ozone occurs in the 50-120 km region; absorption models must therefore include this region in calculations. Total absorption spectra from emission sources at 15 km indicate that atmospheric absorption of radiation released by blue jet and blue starter events may inhibit the ISUAL instrumentation's ability to observe these events.

ACKNOWLEDGEMENTS

This research was supported by the National Science Foundation under Grant No. EEC0244030. Thanks to Dr. Ruyan Guo, Dr. Kenneth Jenkins, and Mrs. Linda Becker for organizing the 2005 Research Experience for Undergraduate program at Penn State University.

REFERENCES

Burrows, J. P., A. Richter, A. Dehn, B. Deters, S. Hmmelmann, S. Voigt, J. Orphal, Atmospheric remote-sensing reference data from GOME-2. Temperature-dependent absorption cross sections of O_3 in the 231-794 nm range, *J. Quant. Spectrosc. Radiat. Transfer*, *61*, no. 4, 509-517, 1999.

Cornette, W. M., P. K. Acharya, G. P. Anderson, Using the MOSART code for atmospheric correction, *IEEE Conf. Proc. Int. Geosci., and Rem. Sens. Sympos*. 1, 215-219, 1994.

Fenn, R. W., S. A. Clough, W. O. Gallery, R. E. Good, F. X. Kneizy, J. D. Mill Lt. Col USAF, L. S. Rothman, E. P. Shettle, F. E. Volz, Optical and Infrared Properties of the Atmosphere, *Handbook of Geophysics and the Space Environment*, edited by A. S. Jursa, pp. 18(1)-18(80), Air Force Geophysics Laboratory, 1985.

Liu, N. and V. P. Pasko, Molecular nitrogen LBH band system far-UV emissions of sprite streamers, *Geophys. Res. Lett.*, Vol. 32, L05104, doi:10.1029/2004GL022001, 2005.

Liu, N., V. P. Pasko, D. H. Burkhardt, H. U. Frey, S. B. Mende, H. T. Su, A. B. Chen, R. R. Hsu, L. C. Lee, H. Fukunishi, Y. Takahashi, Comparison of Results from Sprite Streamer Modeling with Spectrophotometric Measurements by ISUAL Instrument on FORMOSAT-2 Satellite, to be submitted to *Geophys. Res. Lett.* 2005.

Mende, S. B., R. R. Hsu, H. T. Su, A. Chen, L. C. Lee, H. U. Frey, S. Harris, S. P. Geller, H. Heetderks, Y. Takahashi, H. Fukunishi, Spacecraft based studies of transient luminous events, Corsica summer study, *NATO Advanced Study Institute on Sprites, Elves, and Intense Lightning Discharges*, book chapter in press, Kluwer Academic Publishers, 2005.

Mende, S. B., H. U. Frey, R. R. Hsu, H. T. Su, A. B. Chen, L. C. Lee, D. D. Setman, Y. Takahashi, H. Fukunishi, , D region ionization by lightning induced EMP, submitted to *J. Geophys. Res*., 2005.

Molina, L. T. and M. J. Molina, Absolute Absorption Cross Sections of Ozone in the 185 to 350-nm Wavelength Range, *J. Geophys. Res.*, *91*, D13, 14501-14508, 1986.

Morrill, J. S., E. J. Bucsela, V. P. Pasko, S. L. Berg, M. J. Heavner, D. R. Moudry, W. M. Benesch, E. M. Wescott, D. D. Sentman, Time Resolved N2 triplet state vibrational populations and emissions associated with red sprites, *J. Atmos. Solar-Terr. Phys.*, 60, 811-829, 1998.

Pasko, V. P., U. S. Inan, T. F. Bell, Y. N. Taranenko, Sprites Produced by quasi-electrostatic heating and ionization, *J. Geophys. Res.*, 102 (A3), 4429-4561, 1997.

Pasko, V. P. and J. J. George, Three- dimensional modeling of blue jets and blue starters, *J. Geophys. Res.*, 107, A12, 1458, doi:10.1029/2002JA009473, 2002.

Rault, D. F., Ozone profile retrieval from Stratospheric Aerosol and Gas Experiment (SAGE III) limb scatter measurements, *J. Geophys. Res.*, *110*, D09309, doi:10.1029/1004JD004970, 2005.

Vallence Jones, A.K., *Aurora*, First edition, B. M. McCormac Editor, D. Reidel Publishing Company; Dordrecht, Holland; 1974.

INTERPOLATION OF WIND DATA FOR THE ANALYSIS OF DUCTED GRAVITY WAVE VERTICAL STRUCTURE

Liang Di*, Jonathan B. Snively[+], and Victor P. Pasko[#]

Department of Electrical Engineering,
The Pennsylvania State University, University Park, PA 16802

*Undergraduate student of
Department of Electrical Engineering
The Pennsylvania State University, University Park, PA 16802

ABSTRACT

Gravity waves are buoyant atmospheric wave motions that carry energy and momentum throughout the atmosphere. Gravity wave vertical structure is described by the Taylor-Goldstein equation, which is a second order linear differential equation that relates the vertical velocities of gravity waves to the altitude, given various parameters, and assuming time-harmonic solutions. The Taylor-Goldstein equation contains a term dependent on the second order derivative of horizontal background wind velocity with respect to altitude, which is known as the curvature term. Often times, the curvature term is neglected in the study of gravity waves when it is considered to be insignificant when compared with the other terms. In this study, vertical wavenumbers for a simulated gravity wave are calculated using an analytical wind profile. The analytical wind profile is taken using points at every 4 km, 2 km, and 1 km, and interpolated to every 0.25 km, after which vertical wavenumbers are calculated using the interpolated wind profiles. The error introduced by interpolating the wind profile is compared to the error introduced by neglecting the curvature term.

INTRODUCTION

Gravity Waves

Gravity waves are an atmospheric wave motion excited by a number of sources including storms in the troposphere [1], flow over mountains, and the breaking of other gravity waves [2]. The periods of gravity waves typically range

[+] Graduate Mentor
[#] Faculty Mentor

from 5 minutes to one hour, and their horizontal wavelengths range from tens to hundreds of kilometers.

When a parcel of air is displaced in a statically stable atmosphere, the buoyant restoring force and the force of gravity lead to an oscillation with a characteristic frequency known as the Brunt-Väisälä frequency; the Brunt-Väisälä frequency depends on atmospheric parameters such as pressure, density, and temperature. It is energy from oscillations at or below the Brunt-Väisälä frequency that gives rise to propagating gravity waves. The Brunt-Väisälä frequency N is given as a function of potential temperature θ (for the case of a compressible atmosphere) or density ρ_0 (for the case of an incompressible atmosphere) by [2]:

$$N^2 = \frac{g}{\theta}\frac{\partial \theta}{\partial z} \cong -\frac{g}{\rho_0}\frac{d\rho}{dz} \tag{1}$$

Note that the density ρ_0 is given by:

$$\rho_0 = \rho_g e^{-\frac{z}{H}} \tag{2}$$

where ρ_g is the density at ground level, H is the density scale height (usually 6-8 km), and z is the altitude. Propagating gravity waves have frequencies lower than the local Brunt-Väisälä frequency [3]. Gravity waves will be reflected if their frequencies become equal to the local Brunt-Väisälä frequency as they propagate vertically, and gravity waves with frequencies above the local Brunt-Väisälä frequency are evanescent.

In certain wind conditions, the Doppler shifted frequency of propagating gravity waves becomes equal to the local Brunt-Väisälä frequency. Since gravity waves can only propagate at frequencies below the Brunt-Väisälä frequency, the Doppler-shifted gravity wave becomes reflected downwards or upwards. When gravity waves are reflected at certain altitudes, "ducts" may result in regions where waves can propagate, trapped by levels of reflection above and below. Waves trapped in these ducts may propagate over large horizontal distances with little attenuation. Since these ducts may result from background winds that Doppler shift the gravity waves, background winds are extremely important in the study of gravity wave ducting and propagation [3]. Ducted waves may be excited by breaking gravity waves [4], or by energy leaking from other ducts [5].

The Taylor-Goldstein equation is a second-order linear differential equation for the vertical velocity field associated with gravity waves; it may be used to determine the vertical velocities of gravity waves as a function of altitude, given the Brunt-Väisälä frequency (N), horizontal phase speed ($c=\omega/k_x$) and wavenumber (k_x), and the horizontal wind velocities (u). The equation may be

derived by combining equations of motion assuming a two-dimensional nonrotating, inviscid, Boussinesq fluid and linearizing small perturbations about a basic steady state. The Taylor-Goldstein equation is given by [2, 5, 8]:

$$\frac{\partial^2 W_z}{\partial z^2} + \left[\frac{N^2}{(u-c)^2} - \left(\frac{\partial^2 u}{\partial z^2} \frac{1}{u-c} \right) - k_x^2 \right] * W_z = 0 \tag{3}$$

where W_z is the vertical velocity, normalized as

$$W_z = V_z \left(\frac{\rho_0}{\rho_g} \right)^{1/2} e^{j(\omega t - k_x x)} \tag{4}$$

Assuming that the horizontal wind and Brunt-Väisälä frequency vary slowly and smoothly with altitude, the vertical wave number k_z may be expressed as [2]:

$$k_z^2 = \frac{N^2}{(u-c)^2} - \left(\frac{\partial^2 u}{\partial z^2} \frac{1}{u-c} \right) - k_x^2 \tag{5}$$

This leads to a linear dispersion relation for gravity waves for an incompressible atmosphere, filtering high frequency acoustic wave solutions, while retaining lower frequency gravity wave solutions [2]. The dispersion relation allows the phase velocity and group velocity in the horizontal and vertical directions for a gravity wave to be determined. The dispersion relation may be derived by setting $\partial^2 u / \partial z^2$ equal to zero in the expression for vertical wave number above and solved for frequency ω, is given by [3]:

$$\omega = k_x u \pm N \left(\frac{k_x^2}{k_x^2 + k_z^2} \right)^{1/2} \tag{6}$$

where k_x is the wavenumber in the horizontal direction, k_z is the wavenumber in the vertical direction, N is the Brunt-Väisälä frequency, and u is the constant horizontal background wind velocity. Phase and group velocity can then easily be calculated from ω / k_x or ω / k_z, and $\partial \omega / \partial k_x$ or $\partial \omega / \partial k_z$, respectively [3].

Observations of Gravity Waves

Gravity waves are studied experimentally with the help of airglow imagers [1, 6], meteor wind radar, lidar, and various radar technologies [7]. Propagating gravity waves cause temperature and density perturbations throughout the atmosphere, which may be monitored by observing airglow modulation due to these effects. This results in alternating bands of enhanced and depleted optical

emissions traveling slowly across the mesopause. These emissions, due to excitation of background species often resulting from recombination of atomic oxygen (including OH near-infrared and OI 557.7nm), are observed by ground based imagers. Airglow imagers, consisting of all-sky, wide angle lens systems, filters, and low-light CCD cameras, are used to record airglow emissions modulated by gravity waves. Observing several airglow emissions of known height simultaneously (in particular, OI and OH emissions, at ~96 km and ~87 km, respectively) yields insight into the vertical structure and propagation of gravity waves [1, 6]. Meteor wind radar is used to determine wind speeds as a function of altitude; it does not reproduce small scale gravity waves, capturing only large scale background winds. Pulsed radio waves are transmitted to detect meteor trails, and the motions of the meteor trails are used to compute wind speeds over a large period of time [7]. These wind speeds are important in identifying gravity wave ducts using solutions for k_z^2 in the Taylor-Goldstein equation, as mentioned in the previous section, and in calculating wave dispersion properties. Meteor wind radar has limitations to its resolution, however, often providing 3-4 km altitude resolution and hourly time measurements.

Significance of the curvature term

Note that in the Taylor-Goldstein equation, there is a term containing the second order derivative of horizontal wind velocity with respect to altitude. Often times in the study of gravity waves, this term (referred to as the curvature term since it deals with the curvature of wind velocity) is neglected, when the effects of the term are considered to be negligible compared to the Brunt-Väisälä term. At other times, the effects of the term are included for only limited wind data. Isler et al. notes that the overall effect of the curvature term is to decrease k_z^2 in the center of the duct and to increase k_z^2 near the edge of the duct, however, these effects vary greatly with wind structure and magnitude [8].

In this report, the significance of the curvature term in affecting the vertical wavenumber of gravity waves is investigated. Specifically, cases in which there are few wind data points in the 80 kilometers-100 kilometers range are considered (for example, 3-4 km. resolution). Since only several data points are available, additional data points are obtained using cubic spline interpolation. The error due to interpolating curvature from the limited data points is compared with the error due to neglecting the curvature term, to determine when it is reasonable to neglect it in the study of gravity waves. This allows us to estimate how much data is necessary before it may be included to accurately reflect wind properties, and to explore the numerical limitations of cubic spline interpolation for this application.

EXPERIMENTAL DESCRIPTION

Finite Difference Method for Taking Second Order Derivatives

When calculating the curvature term, it is necessary to obtain second order derivatives of the horizontal wind profile. This is accomplished using a finite

difference solution. In finite difference derivative calculations, the area of interest is defined by a mesh of points separated by a distance Δz. For any given point f_j on the mesh, a first order derivative may be computed using either a forward difference approximation:

$$f_j^{'} = \frac{f_{j+1} - f_j}{\Delta z} \tag{7}$$

or a backward difference approximation:

$$f_j^{'} = \frac{f_j - f_{j-1}}{\Delta z} \tag{8}$$

Since the second order derivative is defined as the change in the first order derivative at a given mesh point, a good approximation of the second order derivative is given by taking the difference between the forward difference approximation and the backward difference approximation of first order derivatives:

$$f_j^{''} = \left(\frac{f_{j+1} - f_j}{\Delta z} - \frac{f_j - f_{j-1}}{\Delta z} \right) / \Delta z = \frac{f_{j+1} - 2 * f_j + f_{j-1}}{\Delta z^2} \tag{9}$$

The expression above is used in calculating second order wind profile derivatives throughout this paper [9].

Polynomial Interpolation

Cubic spline interpolation is used to interpolate wind profiles for the results presented in this paper. Cubic spline interpolation is an example of piecewise polynomial interpolation, in which, for each subinterval between sets of data points, a different interpolating polynomial is used. Piecewise polynomial interpolation eliminates unwanted oscillatory behavior, but tends to lack smoothness in the interpolating function.

Cubic spline interpolation uses values of the function to be interpolated, first derivatives, and second derivatives [10]. It is important to note that cubic splines are twice continuously differentiable polynomials, and tend to be closer to the original data than Hermite cubic polynomials in interpolation [11].

Experimental Process

An analytical horizontal wind model given by:

$$u(z) = 50\cos(k_z(z - 90\text{km}))e^{\frac{z-90\text{km}}{2H}} \quad [\text{m/s}] \tag{10}$$

was utilized, where scale height H was taken to be 6 km, wavenumber $k_z = 2\pi/\lambda_z$ was taken to correspond to a wavelength of λ_z=20 km, and the horizontal phase speed of the gravity wave was taken to be c=75 m/s. The region of interest for the wind model was taken to be 80-100 km, since ducting is likely to be observed in this region. The second order derivative of $u(z)$ was found using a central difference approximation with a mesh length of 0.25 km, and the values obtained in this way were graphed alongside the second order derivative values found by analytically solving for the second order derivative of the horizontal wind model; the results are shown in Figure 1 below. It can be seen that the second order derivatives found by using a central difference approximation are very close to the analytical values, indicating that, for the given model, the central difference approximation is appropriate for finding second order derivatives.

Next, using equation (5) above, the vertical wavenumber, was found both with and without the curvature term. The vertical wavenumber plots were compared, and differences were noted. Cubic spline interpolation using points spaced at 1 km, 2 km, and 4 km on the analytical wind model are then used to arrive at new wind profiles. A central difference approximation was used to find the second order derivatives of these interpolated models. The results were compared with the second order derivatives of the original model, and absolute error of the interpolated second order derivatives was calculated and plotted.

The second order derivatives of the interpolated models were then used in calculating new values of the vertical wavenumber. These interpolated vertical wavenumbers were plotted with the original vertical wavenumber to determine whether the error introduced by neglecting the curvature term is significant with respect to the error introduced by interpolation.

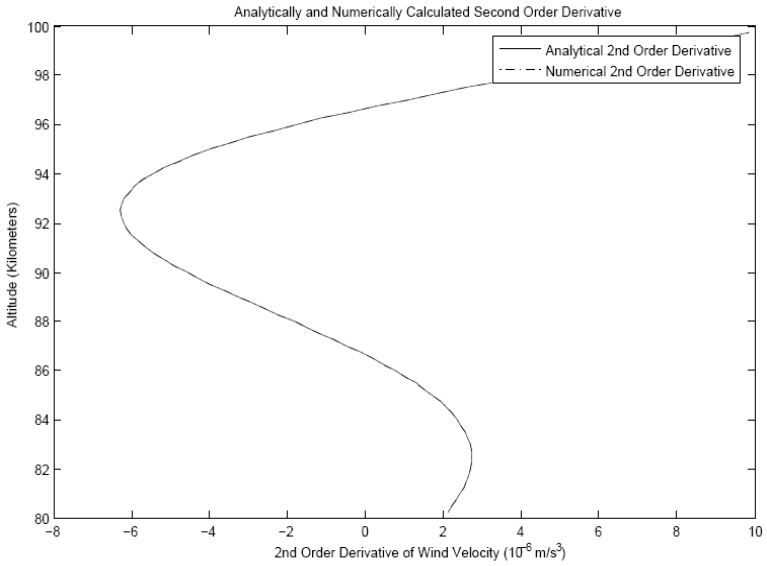

Figure 1.

Comparison of analytically and numerically computed second order derivative of wind profile.

RESULTS

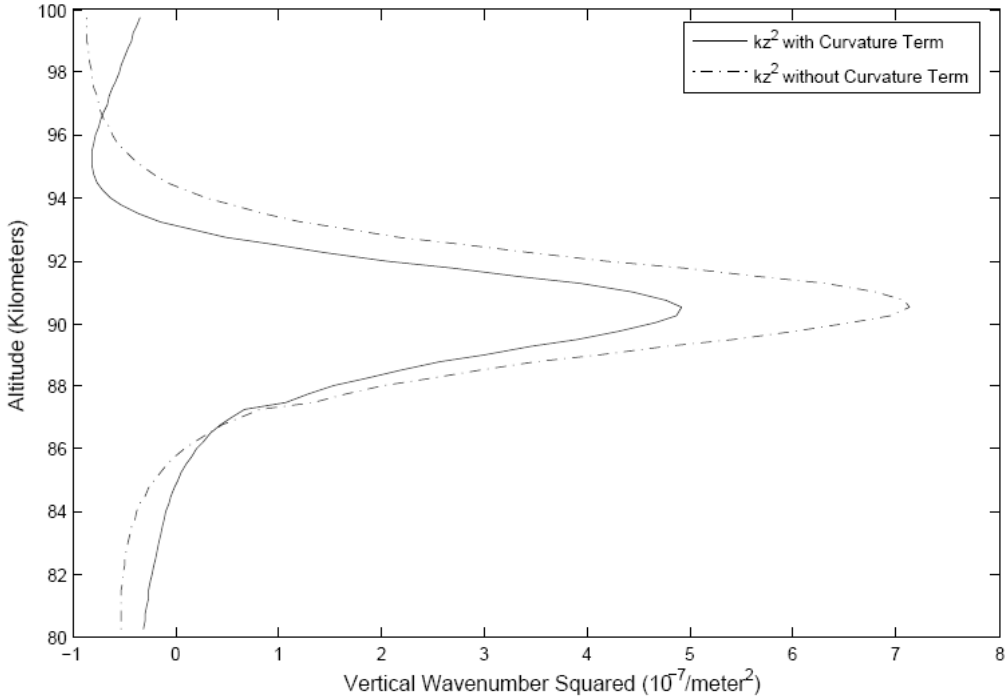

Figure 2. Comparison of vertical wavenumber squared (k_z^2) with and without curvature term.

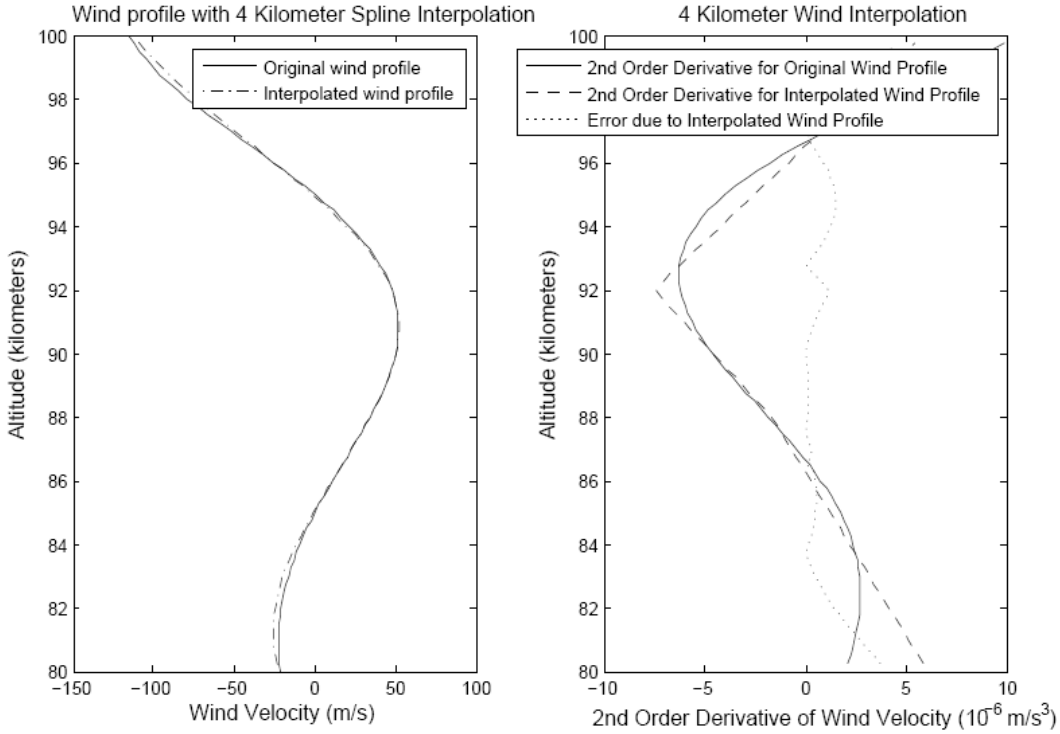

Figure 3. Original wind profile and wind profile interpolated every 4 km.

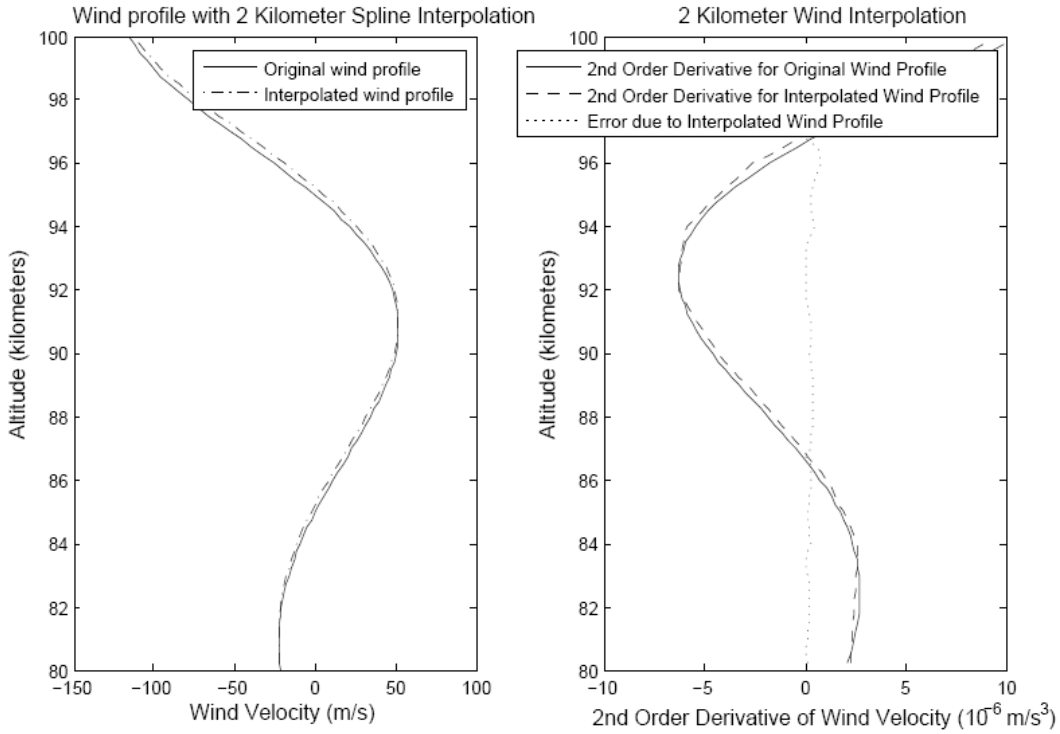

Figure 4. Original wind profile and wind profile interpolated every 2 km.

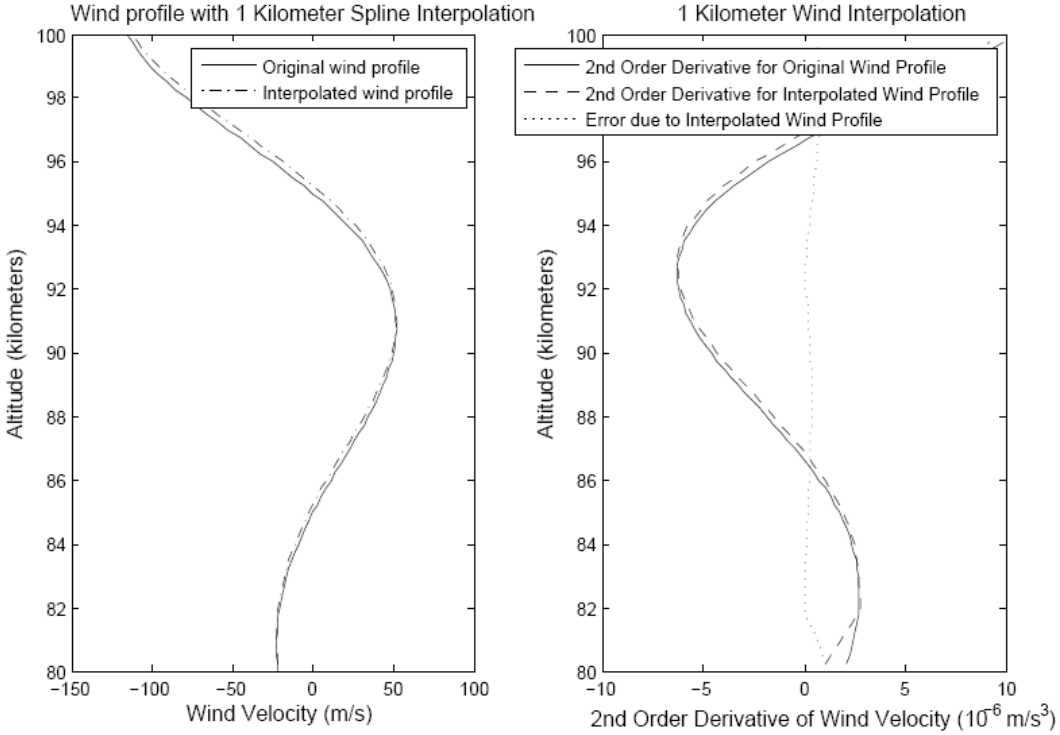

Figure 5. Original wind profile and wind profile interpolated every 1 km.

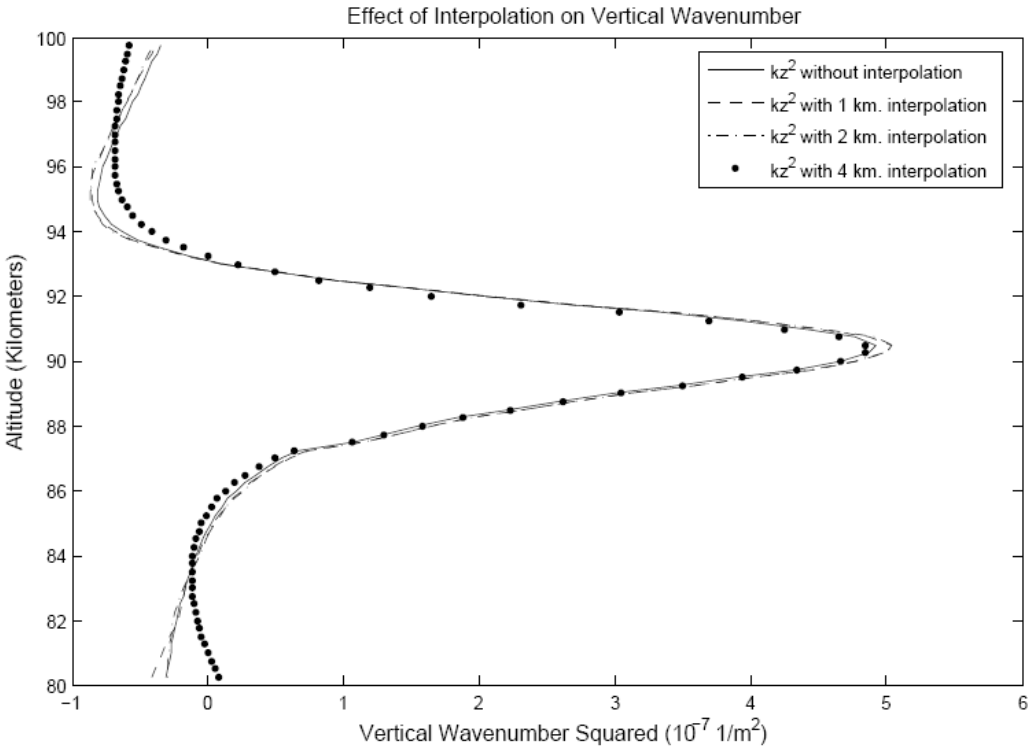

Figure 6. Vertical wavenumber squared (k_z^2) calculated using interpolated wind profiles.

DISCUSSION

It is clear from Figure 2 that the inclusion of the curvature term has a significant effect on the vertical structure of the hypothetical ducted gravity wave. As Ishler et al. noted, there is a decrease in vertical wavenumber squared (k_z^2) near the center of the duct and an increase in vertical wavenumber squared near the edges of the duct, as well as an overall narrowing of the duct [7]. The effect of the curvature term is less pronounced at lower altitudes (altitudes less than 88 kilometers) than at higher altitudes, due to the lower magnitude of wind flow at lower altitudes. The vertical wavenumbers with and without the curvature term differ by a maximum of roughly $2*10^{-7}$ m^{-1}, near the center of the duct. The width of the duct becomes narrower by roughly 1 km after inclusion of the curvature term. The modeled case is consistent with simple typical conditions that may be observed in the Earth's atmosphere and may support Doppler-ducted propagation.

Figure 3 shows the second order derivative calculated from the wind profile interpolated at every 4 kilometers, as well as the non-interpolated second order derivative and the absolute error between the original and interpolated second order derivatives. It can be seen that interpolating every 4 kilometers leads to a considerable amount of error in the second order derivative, and that the second order derivative has a number of "jagged" edges. This is due to the condition that second order derivatives must be continuous in cubic spline

interpolation, and that the second derivative of a cubic polynomial is a line, resulting in clearly identifiable discrete segments when too few points are used. Comparison of Figure 3 with Figure 4 and Figure 5 indicates that with an increase in the number of points used for interpolation, the second order derivative of the interpolated wind profile becomes considerably closer to the non-interpolated second order derivative. The effect arising from cubic spline interpolation is negligible for interpolation at every 1 and 2 km. Comparison of Figures 3, 4 and 5 further indicates that the interpolated wind profile itself also becomes closer to the non-interpolated wind profile with an increase in the number of points used. Figure 6 shows the vertical wavenumbers calculated with interpolation of wind profile at various points. It is apparent that the 1 kilometer interpolation performs best, and at times is visually indistinguishable from the non-interpolated wavenumbers. The 4 kilometer interpolation performs poorly near the edges of the duct, differing significantly from the non-interpolated wavenumbers at roughly 82 kilometers and 98 kilometers, with an absolute error on the order of 10^{-8} m^{-1}. However, the error due to the 4 kilometer interpolation is never more than $1*10^{-7}$ m^{-1}, which is less than the error introduced by neglecting the curvature term. The width of the duct is unchanged by the interpolation. The maximal error introduced by neglecting the curvature term is more significant than the error introduced by interpolation, however, neglecting the curvature term serves to widen the duct while interpolation with limited data points serves to narrow the duct.

CONCLUSIONS

It was found that the curvature term has a significant effect on the vertical structure of gravity waves. The curvature term was seen to have an overall effect of narrowing the duct, and, in particular, the curvature term significantly decreased the wavenumbers near the center of the duct, increased the wavenumbers near the top of the duct, and did not have a significant effect near the bottom of the duct where wind velocities were weaker. It was also found that using cubic spline interpolation with a limited number of points may not always be optimal in calculating the curvature term, due to the nature of second derivatives of cubic splines as connected lines, although in some cases the error introduced may be negligible. In cases where the wind profile varies only negligibly, the curvature term is indeed negligible, whereas in cases where the wind profile varies rapidly (i.e., near the center and top of the duct), the curvature term may not be neglected. It is convenient that, for most large scale wind structures capable of both being captured by meteor wind radar and supporting ducted gravity wave propagation, simple spline interpolation should be sufficient for determining vertical gravity wave structure. Deviations from such simple wind structure would either be poorly described by the limited resolution of radar, be unable to support ducted wave modes, or be unsuited for analysis via interpolation.

ACKNOWLEDGEMENTS

This material is based upon work supported by the National Science Foundation under Grants ATM-01-34838 and ATM-04-37140 to The Pennsylvania State University.

REFERENCES

[1] Taylor, M.J., and M. A. Hapgood, Identification of a thunderstorm as a source of short period gravity waves in the upper atmospheric nightglow emissions, *Planetary Space Science*, 36, 975-985, 1988.

[2] Gossard, E.E., and W.H. Hooke, *Waves in the Atmosphere*, Elsevier Scientific, 1975.

[3] Taylor, L. L., Mesospheric heating due to intense tropospheric convection, *NASA Contractor Report*, 3131, 2-5, 1979.

[4] Snively, J. B., and V. P. Pasko, Breaking of thunderstorm-generated gravity waves as a source of short-period ducted waves at mesopause altitudes, *Geophysical Research Letters*, 30(24), 2254, 2003.

[5] Fritts, D. C., and L. Yuan, An analysis of gravity wave ducting in the atmosphere: Eckart's resonances in thermal and doppler ducts, *Journal of Geophysical Research*, 94, 18455-18466, 1989.

[6] Chisolm, R., J.B. Snively, and V. P. Pasko, Study of atmospheric gravity waves. NSF EE REU Penn State, Annual Research Journal, 2, 18-29, 2004.

[7] "Meteor Wind Radar." *Space Dynamics Laboratory*. 2003. Utah State University. 15 July 2005 <http://www.sdl.usu.edu/products-capabilities/bearlake/meteor-radar/index>.

[8] Isler, J. R., M. J. Taylor, and D. C. Fritts, Observational evidence of wave ducting and evanescence in the mesosphere, *Journal of Geophysical Research*, 102, 26301-26313, 1997.

[9] Potter, D., *Computational Physics*, Ann Arbor: UMI, 1973.

[10] Heath, M. T., *Scientific Computing*, 2nd ed. New York: McGraw Hill, 2002.

[11] "Interpolation." MATLAB Central. 11 Dec. 2002. Mathworks. 14 July 2005 <http://www.mathworks.com/matlabcentral/link_exchange/MATLAB/Mathematics/Fitting_and_Interpolation/>.

PIEZOELECTRIC MULTILAYER ACTUATOR WITH "FLEX" ENDCAP

Daniel Gallagher*, Hyeoungwoo Kim[+], Kenji Uchino[#]

Department of Electrical Engineering and
International Center for Actuators and Transducers
The Pennsylvania State University, University Park, PA 16802

*Undergraduate student of
Department of Electrical Engineering
Cedarville University, Cedarville, OH 45314

ABSTRACT

This paper describes the process of designing, producing, and testing a new metallic endcap to be fitted onto a standard rectangular multilayer piezoelectric actuator. The purpose of this is to increase the low displacement of the multilayer actuator into a higher displacement without excessively decreasing the generative force available. We found the Flex endcap produced up to 60 microns of displacement at resonance given an applied voltage of 20 Vpp. This greatly increases the displacement compared to the ceramic without the endcap, which gave approximately 10 microns displacement [1]. The Flex endcap increased off-resonance displacement similarly to 0.6-0.7 microns at 10 Vpp. These endcaps are designed to be integrated onto a microrobot "Nano Factory" being developed by ICAT/Penn State University. Simulations show that they increase the robot's rotational motion to over 0.005 degrees/step and its translational motion to over 1.05 microns/step.

[+] Graduate Mentor
[#] Faculty Mentor

INTRODUCTION

Certain materials demonstrate a relationship between their electrical and mechanical properties. For instance, a voltage applied across some ceramics will induce a certain amount of strain within the ceramic. This particular example demonstrates the converse piezoelectric effect. These materials are labeled "piezoelectric" and are proving themselves to be a top choice for micro actuators and other small-scale devices. [2]

Currently, a "Nano Factory" program is being developed by ICAT/Penn State University in a joint effort with Micromechatronics Inc (MMI), State College and Applied Micro Systems (AMS), Japan using these piezoelectric materials (K. Uchino, unpublished data). Its purpose is to develop a system able to manipulate and machine components with nanometer accuracy for medical purposes [3] as well as a variety of other applications [4]. The nano factory is composed of various microtools mounted on multiple piezoelectric microrobot platforms.

Currently, each robot platform is composed of four electromagnets, four piezoelectric ML actuators, and two metal legs as shown in Figure 1(a). By various patterns of clamping the electromagnets to a steel bench and expanding or contracting the actuators, the robot can perform rotation, translation, or orbital motion, also shown in Figure 1(a). Figure 1(b) shows a picture of the robot. Both images are available online from the Applied Micro Systems website.

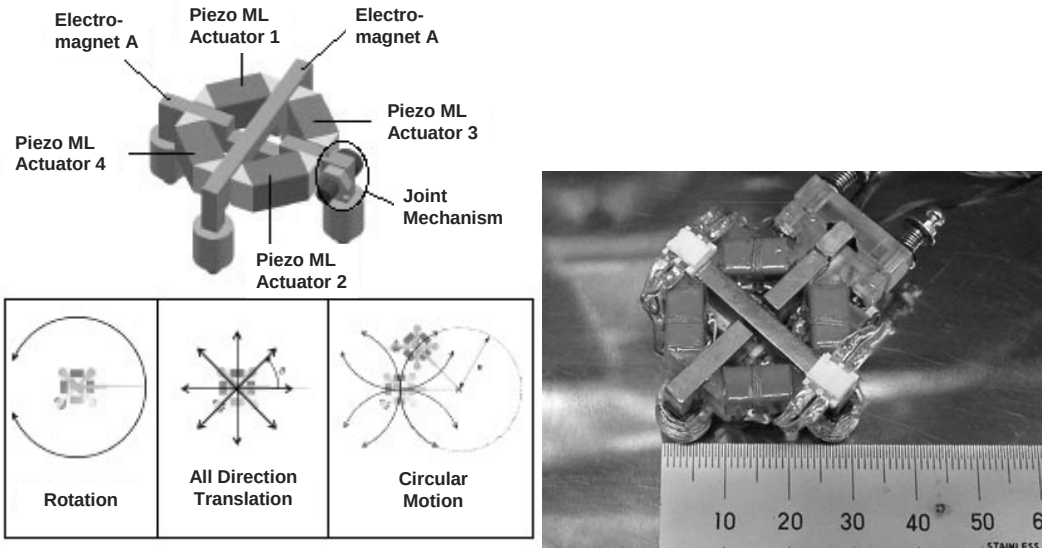

(a) (b)

Figure 1: (a) Structure of micro robotic platform developed by Applied Micro Systems. It is able to perform several types of motion. (b) Photograph: the robot measures 30mm x 30mm x 20mm.

The purpose of this study is to improve the agility of the micro robot. We propose (1) enhancement of the actuator displacement and (2) the inclusion of a monolithic hinge. A Flex ML actuator is proposed as an alternative to the

conventional multilayer actuator to increase the available displacement while keeping enough driving force to still move the robot. It consists of a metallic endcap designed to fit around the original rectangular multilayer ceramic. This is an attractive alternative to the similar "cymbal" structure, where an endcap is mounted on the top and bottom of a circular ceramic [1]. A monolithic hinge is then designed between the Flex ML actuator and its adjoining legs due to the decreased width of the new actuator in the direction of displacement. Compared to the conventional plastic triangular spacer, the displacement loss should be dramatically minimized. Figure 2 shows the proposed replacements.

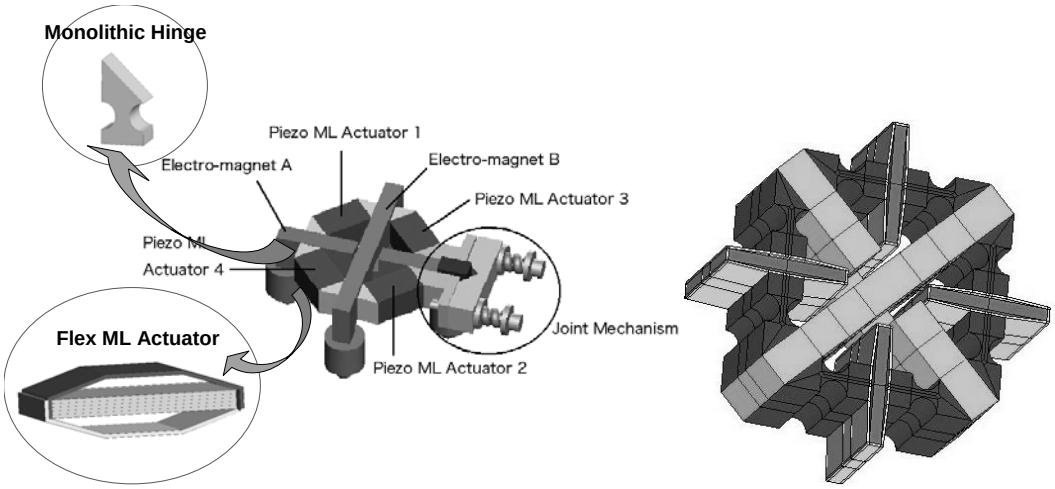

Figure 2: Improvement of the micro robot platform. Flex ML actuators and Monolithic Hinges will replace the ML actuators and triangular spacers.

This specific study accomplished several things. First it attempted to optimize the dimensions and material of the endcap for the Flex endcap using ATILA/GID computer simulation [5]. A variety of different dimensions were examined, such as thickness, cavity depth, and apex length. The materials considered for the endcap are listed in Table I. Optimal designs are those that display highest displacement only, since we are not currently able to test generative force. Stresses induced were also recorded. Second, it determined the best manufacturing process with respect to cost and accuracy. Next, it physically tested the endcap design chosen to determine its actual displacement. Finally, it returned to ATILA/GID simulation to model and test the full robot design.

In computer simulation and testing, it is important to find the resonance frequency of the design, below which the actuator can be operated. This is a driving voltage frequency at which the admittance spikes up dramatically, leading to higher displacement. Several of these may occur within a certain design as is shown in Figure 3, known as the first harmonic, second harmonic, etc. The mode of bending is different near each harmonic, thus we want to test the first harmonic

only, since the actual operating frequency is lower than any of the resonance frequencies.

Table I: Materials considered for Flex endcap

Material	Young's Modulus	Poisson's Ratio	Density (Kg/m^3)
Brass	92 e9	0.33	8270
Steel 1	210 e9	0.285	7800
Steel 2	215 e9	0.33	7900

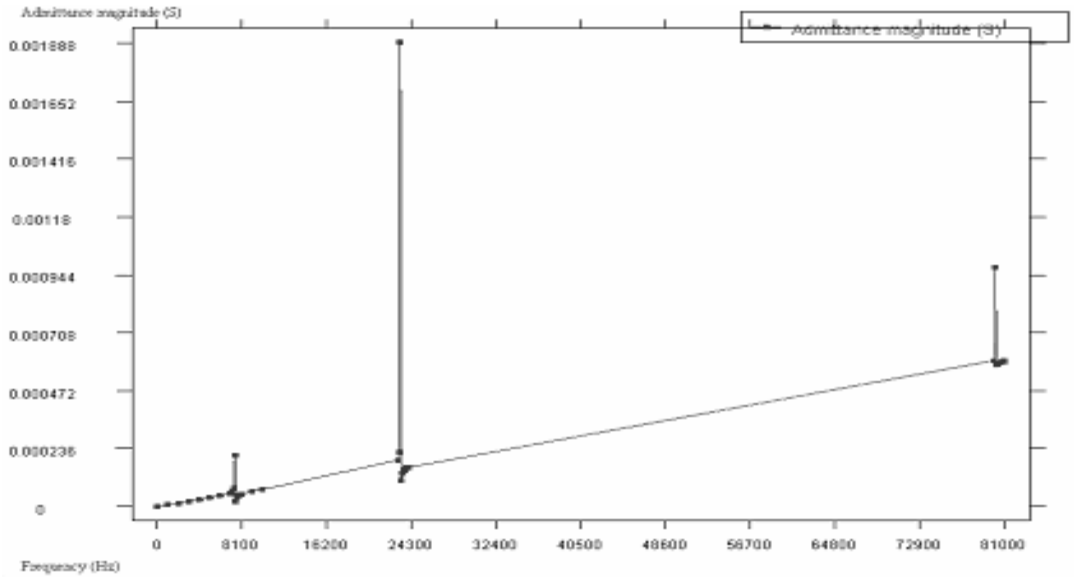

Figure 3: Typical admittance spectrum of the Flex endcap showing 3 separate resonance frequencies

EXPERIMENTAL DESCRIPTION

Computer Simulated Endcap Optimization

The Flex endcap and ML actuator were modeled using ATILA version 5.2.4 and GID version 7.2 software. The dimensions and material of the ML actuator were already known (10mm x 10mm x 1mm and PZT D140 respectively) as well as the general shape of the endcap. Many different designs were modeled by varying the exact dimensions of the endcap as well as its material. Designs were simulated with a 100 Vpp signal over a single layer ceramic, being equivalent to a 10 Vpp signal using a multilayer ceramic. This decision was made both for ease of design and to keep the mesh size and calculation times reasonable. Once a design was modeled, ATILA was able to determine the resonance frequency of the endcap. We also simulated the displacement and stress at 100 Hz, since the

robot is designed to operate off-resonance. By recording and comparing the results of these simulations, we were able to determine how to adjust the parameters to optimize the endcap.

Manufacture

Initial plans called for the Flex endcap to be manufactured in two pieces using sheet metal and a metal bender. These would then be matched for closest resonance frequencies and bonded together with epoxy. This is shown in Figure 4. Pressure would then be applied to deform the endcap to allow ceramic insertion.

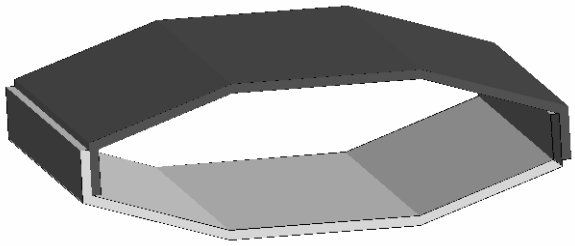

Figure 4: Initial plans called for two endcaps bonded together to form the full Flex design.

Since we did not have the proper machinery available to make precise metal bends, we decided to manufacture the endcap in one piece using Wire Electron Discharge Machine (EDM) cutting. This gave accuracy to approximately 70 microns. The ceramic pieces were found to be approximately 0.2 mm larger in every dimension than specified, while the endcaps were approximately 5 microns smaller. To fit the ceramic inside the endcap, it became necessary to polish the ceramics down to size. Great care was needed, since polishing too much causes the ceramic to fit loosely or not at all. Also, the sides must stay perpendicular and of uniform width throughout polishing (note that even on a single ceramic piece, there will likely be a initial width variation of as much as 20 microns, usually bulging out in the center). In addition, we did not want to expose the multilayer metallic leads by polishing too much. Ideally, once the ceramic is very close to fitting (within 20-30 microns) one should apply a small amount of force to deform the endcap enough to accept the ceramic piece, thus providing a bias stress point. Once an endcap and ceramic pair is able to fit together, one can apply a very thin epoxy layer before insertion to secure the bond.

Testing

Once we had several endcap/ceramic pairs completed, we performed a frequency sweep on an Agilent 4194 Impedance Analyzer to confirm the simulation's impedance spectrum.

We then set up equipment to test the displacement of each pair. This involved generating a small control signal using a waveform generator and sending it through a NF Electronic Systems 4010 Power Amplifier to bring the signal up to a

useful level. The output of the amplifier was connected to the contact points on the ceramic and measured using an oscilloscope so that we could know exactly how much voltage we were applying. The pair being tested was mounted by its electrical contact points to allow the endcap to expand and contract freely. We mounted a tiny white sticker to the center of the endcap to increase its reflectivity, thus allowing a laser sensor to "see" it. The output of the laser ran into a Polytec OFV 511 Fiber Interferometer/ Polytec OFV 3001 Vibrometer Controller setup, which converted the velocity of the endcap vibration into a voltage signal. This signal was read on a second oscilloscope. It is then easily integrated to give the displacement of the endcap if the original control signal is sinusoidal.

Computer Simulated Hinge Optimization

We proceeded to model the Flex endcap within the full robot using ATILA. This included optimizing the monolithic hinge to transfer the displacement of the endcap to the "legs" of the robot. We designed the basic monolithic hinge to fit the Flex endcap, then modified and simulated the design several times to find an optimum solution. This included fixing one of the legs of the robot in place, then determining the linear displacement of the other for both rotational and translational motion. Linear displacement could then be used to calculate angular displacement for rotational motion. The variables tested were material used and the radius of the hinge cuts.

RESULTS AND DISCUSSION

Computer Simulation Endcap Optimization

We began simulation by sweeping for the first harmonic resonance frequency, corresponding to the first admittance spike in Figure 3. We found this to be in the range from 5-15 kHz for all of the designs simulated. We also simulated the different designs at 100 Hz to simulate the off resonance application of the actuator better. The results are summarized in Figures 6-9.

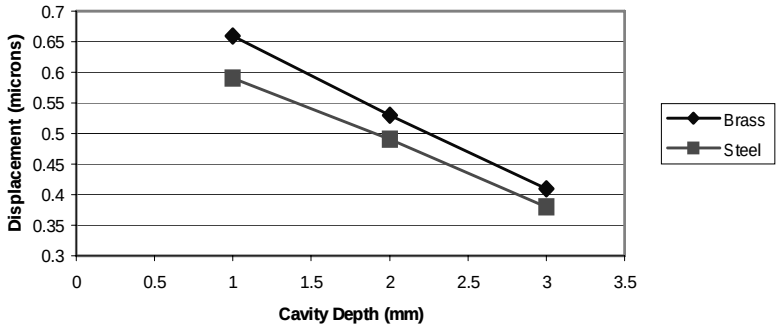

Figure 6: Comparison of different materials tested over several designs. Endcap thickness and cavity apex length were held constant at 0.1 mm and 3.5 mm respectively. The two varieties of steel performed identically at off-resonance.

Figure 6 shows that brass outperforms steel, providing approximately 10% higher displacement for the higher displacement designs. For this reason, brass was chosen as the optimum material. Note that Figures 7-9 show only the results for the brass endcaps.

As can be seen from Figure 7, maximum displacement occurs with the thinnest endcaps possible. We chose not to experiment with 0.1 mm endcaps, since we do not want only the highest displacement, but also high generative force. Since we expect the force to increase with thicker endcaps, we chose to experiment with 0.2 and 0.3 mm endcaps as a compromise between the two parameters. This would also allow easier manufacture and handling of the part.

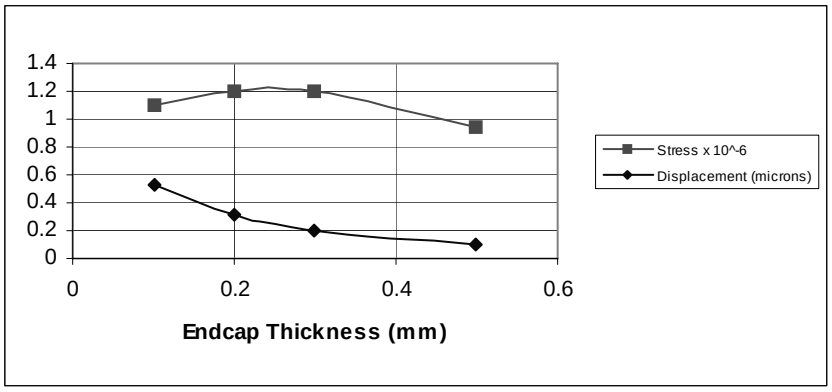

Figure 7: Simulated displacement and stress curves with varying endcap thickness using a brass endcap. Cavity depth and cavity apex length were held constant at 0.2 mm and 3.5 mm respectively.

Figure 8 shows that maximum displacement would occur with zero cavity apex length (i.e. a triangular cavity apex). Since we wanted both high displacement and a fair amount of surface area in contact with the monolithic hinges, we decided to test using a 3 mm cavity apex length.

Figure 9 shows the large influence of cavity depth upon displacement. We chose to experiment initially with a 0.2 mm cavity depth. While still on the high end of the curve, this design would allow easier manufacture. We eventually decided to test other depths as well due to unexpectedly low manufacturing cost.

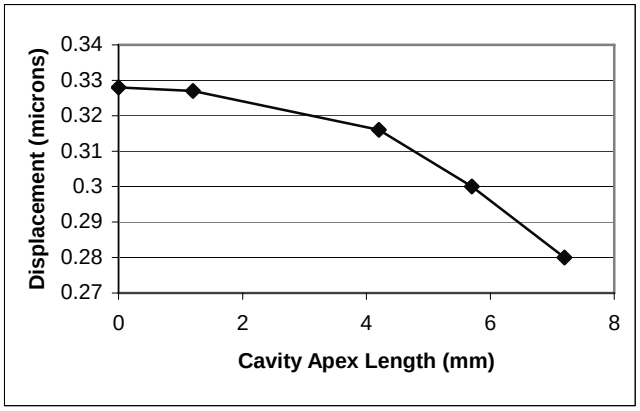

Figure 8: Simulated displacement curve with varying cavity apex length for brass endcap. The thickness and cavity depth were both held constant at 0.2 mm.

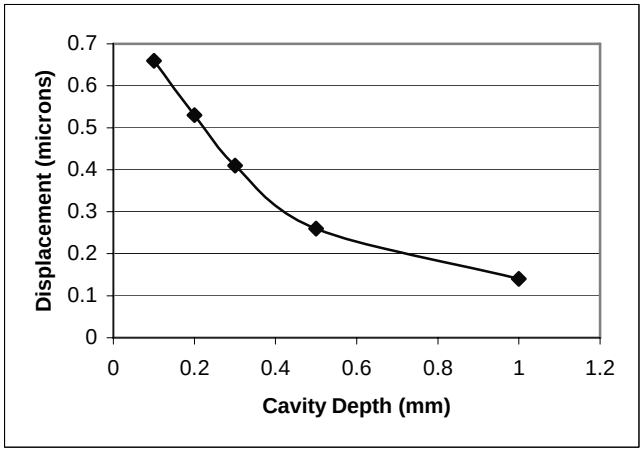

Figure 9: Simulated displacement curve with varying cavity depth for brass endcap. The thickness and cavity apex length were held constant at 0.1 mm and 3.5 mm respectively.

Manufacturing Process

We found difficulty during the process of fitting the endcap onto the ceramic piece. Due to difficulties inherent in the procedure outlined above (see Experimental Description: Manufacturing Process), the fitting process took much more effort and skill than expected. Each attempt averaged around an hour or more of work, with an overall success rate of only 30%. This was very much a skill procedure, since with practice both the time required and success rate improved. We estimate that with practice, one could succeed 80-90% of the time and take about 20-30 minutes per fitting. This does not seem very efficient for

high-volume devices. A benefit to this method is that no specialized equipment is necessary to purchase, such as a mold.

Even if we had known the exact dimensions of the ceramic ahead of time, it would still have been necessary to order the endcaps slightly smaller and polish the ceramics down to fit. This is due to the variance in both the width of the ceramics (up to 100 microns), the inaccuracy of the endcaps (up to 75 microns), and the need for a very tight fit.

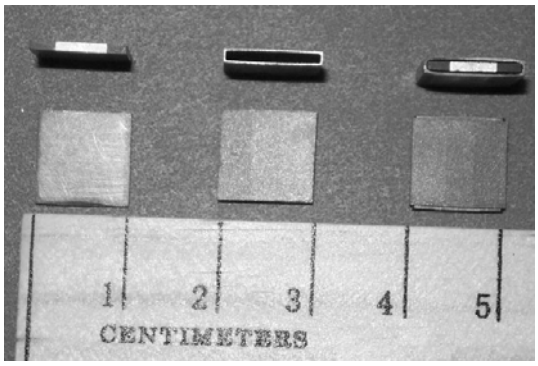

Figure 10: The polished ceramic (left) is inserted into the brass endcap (center) to form the full Flex ML Actuator (right).

Testing

The impedance analyzer revealed resonance peaks at somewhat lower than the simulated values, but still within a reasonable range. These results are shown in Table II. Several of the endcaps produced split resonance peaks, likely due to slightly uneven gaps between the ceramic and the endcap in the finished product. Both a normal and split resonance peak are shown in Figure 11.

Table II: Resonance frequencies as given by Impedance Analyzer. (Designs have variable thickness, 3 mm cavity apex length, and 0.2 mm cavity depth. The endcap material is brass.)

Thickness = 0.2 mm					
Model	Simulated	Part #21	Part #22	Part #23	
Resonance Frequency (kHz)	9.95	*8.24 9.43	**	**	
Thickness = 0.3 mm					
Model	Simulated	Part #31	Part #32	Part #33	*Split Resonance Peaks
Resonance Frequency (kHz)	12.39	12.12	10.56	*10.39 12.54	** Damaged during manufacture

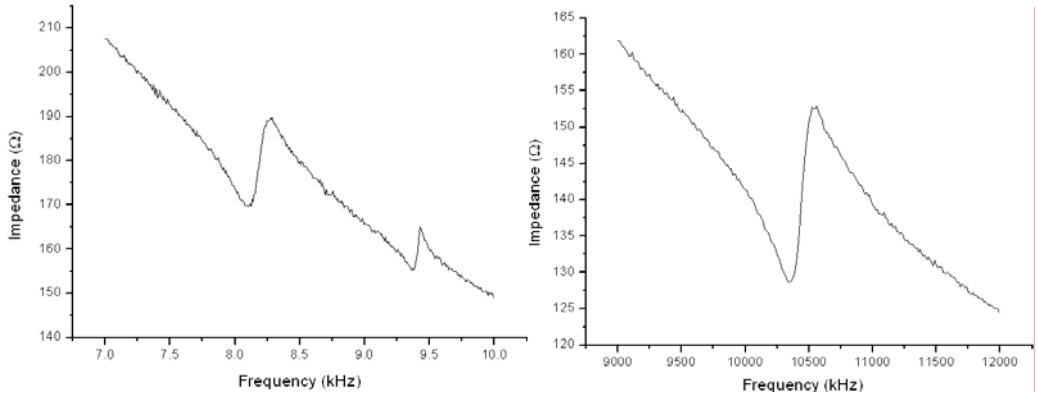

a) Part #21 b) Part #32

Figure 11: Pair of graphs showing both a) split and b) normal resonance peaks

During resonance displacement testing, we found that the 0.3 mm thick Flex endcaps produced a single-sided displacement around 20 microns, while the 0.2 mm thick endcaps increased the displacement to 30 microns. This ratio was predicted by low-frequency simulation. Table III shows these results. Note that the actual useful displacement of the endcap will be twice as large, since we were only testing one surface of the endcap.

Table III: Results of resonance peak testing at 20 Vpp.

Thickness = 0.2 mm				
Model	Part #21	Part #22	Part #23	
Displacement (Microns)	29.8	**	**	
Thickness = 0.3 mm				
Model	Part #31	Part #32	Part #33	*Visible gap after manufacture
Displacement (Microns)	8.9*	22	20.7	**Damaged during manufacture

Note that in Table III the split resonance peaks of part 33 did not seriously impact its displacement compared to the normal resonance peak of part 32. Cavity depth and apex length were constant at 0.2 mm and 3 mm respectively. The endcap material was brass.

We found that both the 0.3 mm and 0.2 mm thick endcaps showed similar off resonance displacement to the computer simulation, though some variation is expected. Table IV summarizes these results for the brass endcap at 10 Vpp. The cavity depth and apex length were constant at 0.2 mm and 3 mm respectively. Note that the displacement shown in Table IV is only that for a single side of the endcap; full displacement will be approximately twice as much.

Table IV: Comparison of off-resonance displacement testing to simulation results.

Thickness = 0.2 mm					
Model	Simulated	Part #21	Part #22	Part #23	
Displacement (Microns)	0.31	0.33	**	**	
Thickness = 0.3 mm					
Model	Simulated	Part #31	Part #32	Part #33	*Visible gap after manufacture
Displacement (Microns)	0.21	0.14*	0.22	0.28	**Damaged during manufacture

Computer Simulated Hinge Optimization

ATILA simulations predict that integrating the Flex endcap into the entire robot will lower the resonance frequency dramatically to around 2 kHz. This seems reasonable, as the endcap now has to move more mass. The simulated robot has proper rotational or translation motion, depending on the relative phase of the individual ceramics and which legs are clamped. Figure 12 shows that plastic outperforms both brass and steel for rotational motion, with an optimum minimum thickness of 0.4 mm. Figure 13 shows that plastic performs best for translational motion as well and that displacement increases slightly with decreasing minimum thickness. Figure 14 shows our recommendation for the hinge dimensions. The 0.4 mm minimum thickness was chosen according to the results of Figure 12 as well as considerations that the thinner the hinge, the more likely it will be to fail due to wear and tear.

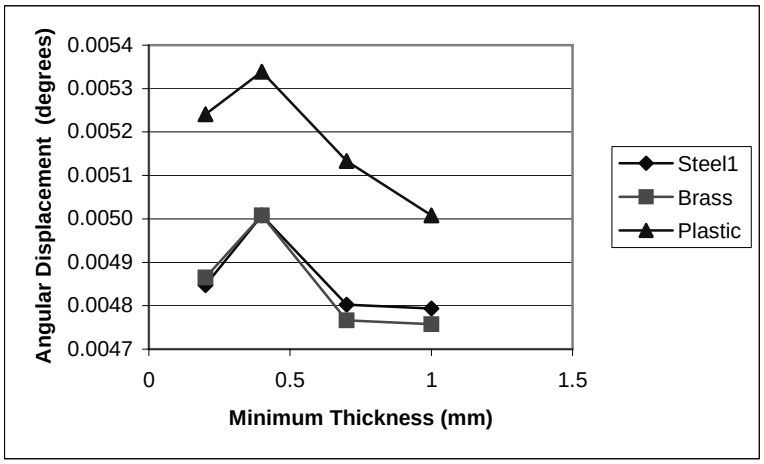

Figure 12: Comparison of different hinge designs during computer simulation of the rotational motion of the full robot.

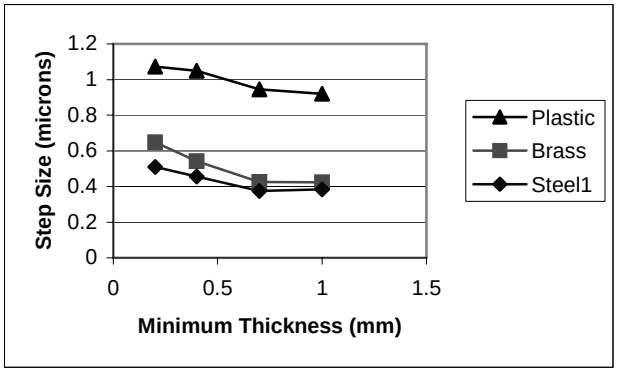

Figure 13: Comparison of different hinge designs during computer simulation of the translational motion of the full robot.

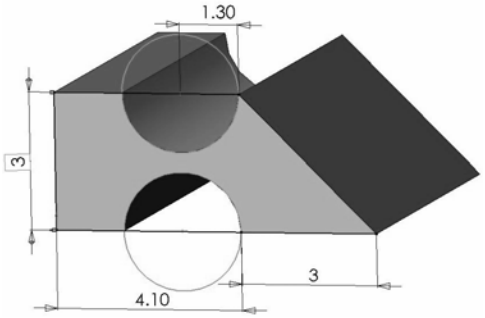

Figure 14: Optimum hinge dimensions according to ATILA simulations. The 1.3 mm radius cuts correspond to a 0.4 mm minimum thickness. The part is extruded 10 mm to fit with the endcap. It should be made of plastic (Young's Modulus = 4.1e9, Poisson's Ratio = 0.4, Density = 1400 kg/m^3).

ACKNOWLEDGEMENT

I would like to thank Ken Biddle and the Earth and Mineral Sciences Machine Shop, State College for assistance in manufacturing the endcaps. I would also like to thank Dongil Tech, Korea for supplying the multilayer actuators. Special thanks go to Professor Ruyan Guo and Professor Ken Jenkins for organizing the Research Experience for Undergraduates program. This material is based upon work supported by the National Science Foundation under Grant No. EEC-0244030.

REFERENCES

[1] A. Dogan and K. Uchino, "Composite Piezoelectric Transducer with Truncated Conical Endcaps 'Cymbal'"; *IEEE Transactions on Ultrasonics, Ferroelectrics, and Frequency Control*, **44** (3), pp. 597-605 (1997).

[2] K. Uchino and J.R. Giniewicz, "Current Trends for Actuators and Micromechatronics and A Theoretical Description of Field-Induced Strains," pp. 1-101 in *Micromechatronics*, Marcel Dekker, New York, 2003.
[3] H. Aoyama and H. Takubo, "Automatic Insemination and Incubation by Male and Female Micro Robots"; *Journal of Robotics and Mechatronics,* **15** (6)**,** pp. 596-601 (2003).
[4] O. Fuchiwaki and H. Aoyama, "Micromanipulation by Miniature Robots in a SEM Vacuum Chamber"; Journal of Robotics and Mechatronics, **14** (3), pp. 221- 226 (2002).
[5] R. Ribo, M. Pasenau, E. Escolano, J. Ronda, L. Gonzalez, and E. Rosa, "GID User Manual," Version 7. CIMNE, Barcelona, Spain.

DETECTING TOUCH-TONE FREQUENCY IN TELEPHONE SYSTEMS USING ADAPTIVE FILTERING AND CLASSIFICATION OF SPEECH SIGNALS

Navjit S. Grewal[*], William K. Jenkins,[#] Robert Nickel[#], Siddharth Pal[+]

Department of Electrical Engineering
The Pennsylvania State University, University Park, PA 16802

[*]Undergraduate Student of
Department of Electrical and Computer Engineering
University of Rhode Island
Kingston, RI 02881

ABSTRACT

In telephone systems, Dual-Tone Multi-Frequency (DTMF also known as touch-tone) is a standard set of two specific voice band frequencies, one from a group of lower frequencies and the other from a group a higher frequency. A touch-tone signal sometimes has a varying frequency and consists of noise, hence a normalized least mean squares (LMS) algorithm was implemented to detect and smooth these signals to identify which button was pressed.

A comparative analysis between System Identification and Linear Predictor was performed to find an optimal solution to tone detection. Finally pattern recognition of speech for the ten digits was carried out which has the capability to identify the digits from various people. The task was carried out using power spectral densities in MATLAB.

[#]Faculty Mentor
[+]Graduate Mentor

67

1. INTRODUCTION

1.1 Touch-tone

Dual-tone multi-frequency was developed at Bell Labs in order to allow dialing signals to dial long distance numbers, potentially over non-wire links such as microwave links or satellites [1]. DTMF is used for telephone signaling over the line in the voice frequency band to the call switching center. Today it is used for most call setup to telephone exchange and trunk signaling so that they can pass through the entire connection to the destination user.

The DTMF keypad with 12 keys is laid out in a matrix as shown below in Table 1. Each key corresponds to a different pair of frequencies, consisting of one low (rows) one high (columns). The symbols '*' and '#' are reserved for special purposes.

The tone frequencies are selected in such a way that their harmonics do not overlap any given set of other frequencies causing an unreliable signal. Overlapped harmonics are linearly dependent sinusoidal signals. For example, pressing a single key such as '0' will send a sinusoidal tone of two frequencies 941 Hz and 1336 Hz which are not linear combinations of other frequencies.

Table 1. DTMF Keypad Frequencies

1	2	3	**697 Hz**
4	5	6	**770 Hz**
7	8	9	**852 Hz**
*	0	#	**941 Hz**
1209 Hz	**1336 Hz**	**1477 Hz**	

Often during transmission there are variations in the frequencies of the tone which may consist of noise, making it harder for the system to determine which key was pressed. In the current systems, the frequencies may not vary more than 1.5% from their center frequency; otherwise the switching center will ignore them. The high frequency component of the tone may be the same or greater amplitude as the low frequency component when transmitted, but the difference in amplitude between the high and low frequency can be only as large as 3dB which is refereed to as twist [1].

Hence an adaptive system was implemented to compensate for the conditions mentioned above in order to determine which key was pressed. This system is suitable for a potential application in some environments where a varying set of frequency is required to keep the tone identification a secret.

1.2 Spoken Digit Recognition

Speech processing has been an active area for a wide variety of applications ranging from communications to automatic reading machines [2]. With the innovation of faster digital computers there was a natural tendency to experiment with more sophisticated algorithms. As the field of digital signal processing developed, both in terms of digital hardware capabilities and the development of new signal processing algorithms, it became increasingly clear that these algorithms developed would have a significant impact on the area of speech processing [2].

The basic techniques for speech analysis and synthesis can be viewed in terms of a model of the speech waveform as the response of a slowly time varying system to either a periodic or noise like excitation. The speech production mechanism consists of an acoustic tube, the vocal tract, excited by an appropriate source to generate the desired sound. The sounds are generated by forcing the air through the vocal tract, thereby creating a turbulence, which produces a source of noise to excite the vocal tract [2].

The purpose of this experiment is to use the algorithms such as a Fourier transform and smoothing by windows to identify spoken digits by a random user. For example, for an automatic speech-recognition system, one begins from the speech waveform to the desired result in an action based on recognition of speech.

2. EXPERIMENTAL DESCRIPTION

2.1 Touch Tone Detection

The objective of the experiment is to train the system to a given set of frequencies using Liner Predictor (LP) and System Identification (SI) as shown in Figure 1, and perform a comparative analysis to determine the optimal solution. The task was accomplished using MATLAB as the software tool to simulate the results.

The system will be trained for the given set of frequencies, one at a time on normalized LMS adaptive filtering algorithm which consist of a finite impulse response (FIR) filters. The adaptive filter sets its parameters such as step size and filter lengths in such a way that its output tries to minimize a meaningful objective function involving the reference signal in System Identification or input signal in Linear Predictor [3]. The meaningful objective function in this experiment is the error signal denoted as e(n) in the Figure 1. The parameter list for each is given below.

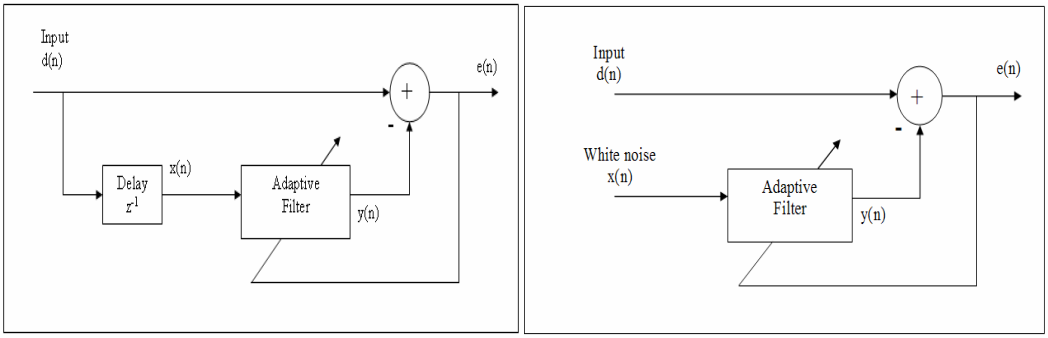

Figure 1. Linear Predictor (left) and System Identification (right)

Then an unknown tone signal contaminated with noise and non-linear varying frequency was passed through each of these trained FIR filters, followed by the Fast Fourier Transform (FFT) analysis on each of the filter outputs. Therefore, by comparing the FFT of the trained filters and filter outputs, the two key frequency components from the outputs that resemble the filters as close as possible will be mapped to the right key that was pressed.

Table 2. I/O parameter list for System Identification and Linear Predictor

Inputs	
$d = \mathrm{s} + \mathrm{n}_o = [d(0)\, d(1).....d(N)];$	N is the number of samples and n_o is the noise.
$s(n) = \sin\left[\left(\frac{2\pi}{N} + \frac{\pi}{\eta}\sin\left(\frac{2\pi k}{N}\right)\right)\cdot k\right]$	where η is a variation parameter $\eta = \infty$ for fixed sinusoid
$\vec{x} = [0\, d(0)\, d(1).....d(N-1)]$	Linear Predictor
$\vec{x}$	White noise for System Identification
Outputs	
$y(n) = \vec{W}(n)\cdot\vec{x}(n)$	$y(n)$ is the filter output and $\vec{W}(n)$ is the filter coefficients
$e(n) = d(n) - y(n)$	

The derivation steps to minimize the error for normalized LMS algorithm as seen at the summing junction in Figures 1 and 2 is as follows:

$$\begin{cases} e(n) = d(n) - y(n) \\ \\ e(n) = d(n) - \vec{W}(n)\cdot\vec{x}(n) \end{cases} \tag{1}$$

Squaring both sides yields

$$e^2(n) = \left[d(n) - \vec{W}(n) \cdot \vec{x}(n) \right]^2 \tag{2}$$

To minimize the error the resulting gradient estimate is given by

$$\begin{cases} \dfrac{\partial e^2(n)}{\partial \vec{W}} = \vec{g}_w(n) \\ \vec{g}_w(n) = 2 \cdot \left[d(n) - \vec{W}(n) \cdot \vec{x}(n) \right] \cdot \vec{x}(n) = 2 \cdot e(n) \cdot \vec{x}(n) \end{cases} \tag{3}$$

Hence the updating equation for the coefficients of the FIR filters in each of the two systems is given in equation 4, where the μ is step size for the convergence to mean squared error (MSE).

$$\vec{W}(n+1) = \vec{W}(n) + 2\mu \, e(n) \cdot \vec{x}(n) \tag{4}$$

The updating coefficients of the adaptive filter in the feedback loop converge to the input signal, depending upon the step size and number of taps. The normalized LMS algorithm is a simplification of the gradient vector computation or steepest descent method. The LMS algorithm is the most widely used because of its low computational complexity and unbiased convergence to achieve the desired goal [2].

2.2 Spoken Digit Recognition

The objective for secondary part of the experiment is to identify the ten digits spoken by various people. Each individual has unique speech characteristics given by their vocal tract, making it extremely challenging to detect the digits. Especially, the pitch differences in male and female voices further add to the complications.

The methodology followed is first to train the system with eight male and female utterances, for each digit spoken several times. Following an unknown user speaks a digit which is compared to all the utterances in the database from training and matched to the one that fits the closest by extracting meaningful information.

Extracting the meaningful information is done by removing the phase by transforming the signal into the frequency domain by taking the discrete-time Fourier Transform (DTFT) of the spoken digit. Since the signal is non-periodic and consists of various frequencies a discrete Fourier transform (DFT) is not applicable however with a slight transformation to the DTFT, a DFT can be applied for a finite length as given below. The DFT of an N-point sequence and DTFT are given by

DTF: $$S[k]=\sum_{n=0}^{N-1} s[n]\cdot e^{-j\frac{2\pi mk}{N}} \quad (5)$$

DTFT: $$S[\omega]=\sum_{n=-\infty}^{\infty} s[n]\cdot e^{-j\omega n} \quad (6)$$

With a transformation of $\omega=\frac{2\pi k}{N}$ $k=0,...,N-1$ and breaking the signal in to N blocks of p elements over total length of m given by $n=mN+p$ where $m=-\infty,...,\infty$ and $p=0,...,N-1$ the DTFT can be written as follows

$$S[k]=\sum_{m=-\infty}^{\infty}\sum_{p=0}^{N-1} s[mN+p]\cdot e^{-j\frac{2\pi k(mN+p)}{N}} \quad (7)$$

$$S[k]=\sum_{p=0}^{N-1}\left[\sum_{m=-\infty}^{\infty} s[mN+p]\right]\cdot e^{-j\frac{2\pi kp}{N}}. \quad (8)$$

The equation (8) is analogous to the DFT and enables storing the data for shorter lengths without loosing its original spectrum. After performing the DFT each utterance of train sample is given a shape by performing smoothing with a triangle window or hamming window shown in Figure 2. The hamming window is given by

$$w(k+1)=0.54-0.46\cos\left(2\pi\frac{k}{n-1}\right),\ k=0,...,n-1 \quad (9)$$

and the triangle window is formed by convolving two rectangular boxes of the same size.

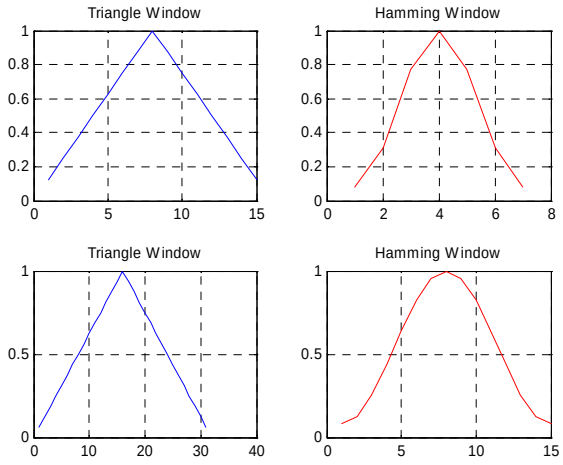

Figure 2. Smoothing windows

The comparative analysis is done by summing up the difference of log of trained utterance spectra and the test sample given by equation (10), sample with the least error is selected.

$$Error = \sum_{k=0}^{N-1} \left| \log[S_{Train}(k)] - \log[S_{Test}(k)] \right| \quad (10)$$

3. RESULTS AND DISCUSSION

3.1 Touch-tone Detection

Touch-tone detection was implemented using normalized LMS algorithm for both System Identification and Linear Predictor. The length of the adaptive filter used was 128. Figures 3 and 4 show the single tone detection (1336 Hz) for both System Identification and Linear Predictor. On comparing both the figures it is observed that Linear Predictor obtains a lower mean-squared error.

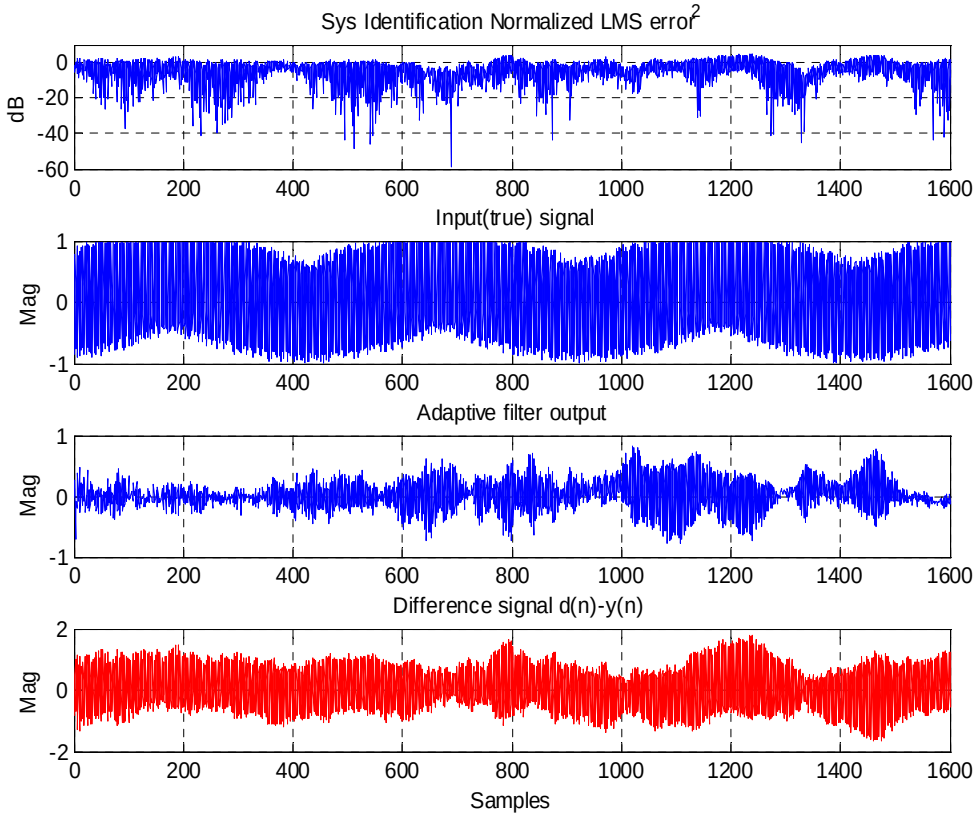

Figure 3. System Identification mean squared error plot

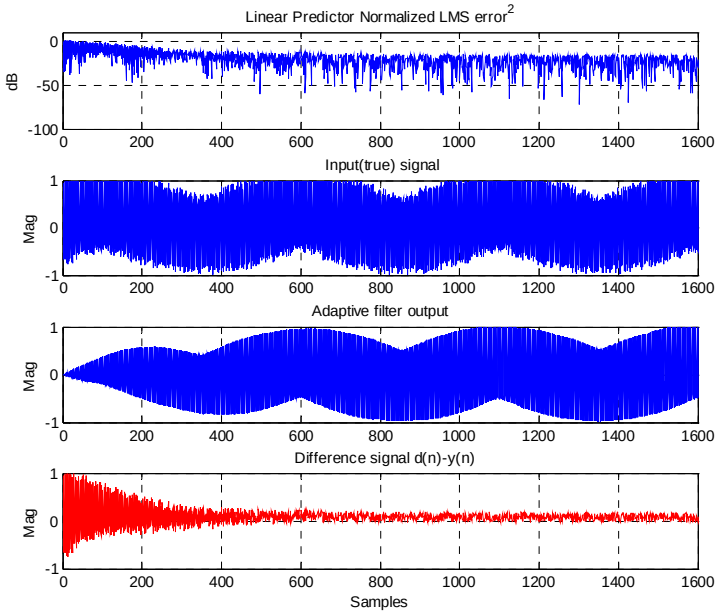

Figure 4**.** Linear Predictor mean squared error plot

The Fourier transform of the signal, reconstructed signal and filter coefficients for both the System Identification and Linear Predictor are shown in Figures 5 and 6 respectively.

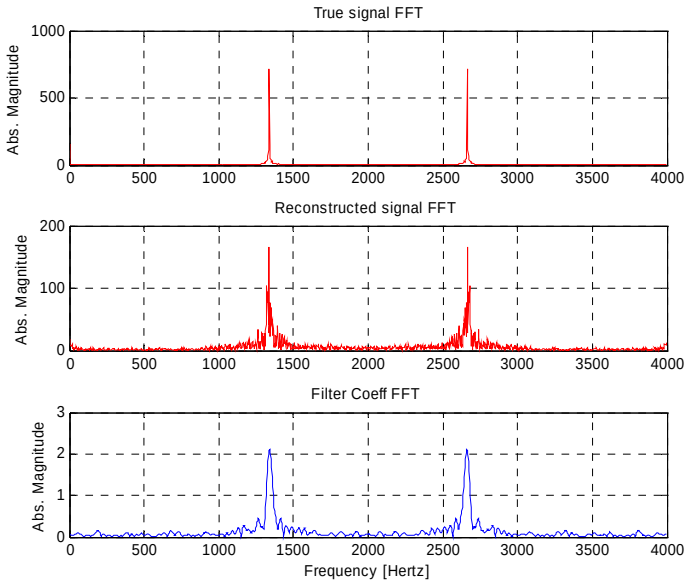

Figure 5. Fourier transforms for the signal, reconstructed signal and filter coefficients using System Identification

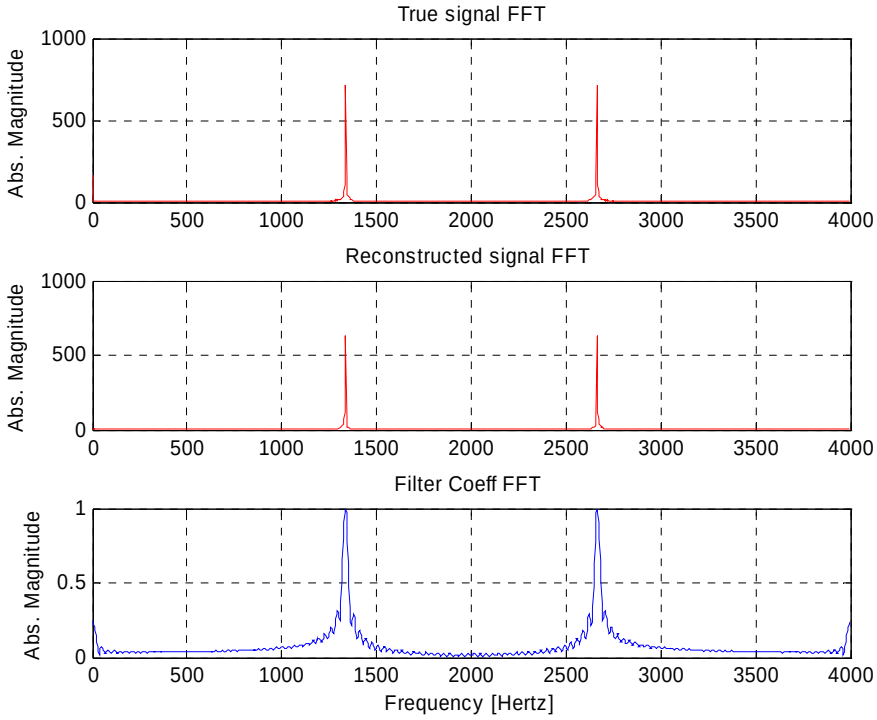

Figure 6. Fourier transforms for the signal, reconstructed signal and filter coefficients using Linear Predictor

In Figure 7 the Fourier transform of the trained filter coefficients (Linear Predictor) for all the 7 frequencies are shown.

Another thing to note is that the filter magnitude in the Linear Predictor is between 0 and 1, whereas for System Identification it varies from 0 and 2. This makes touch-tone detection difficult in case of System Identification. This is illustrated in Figure 8.

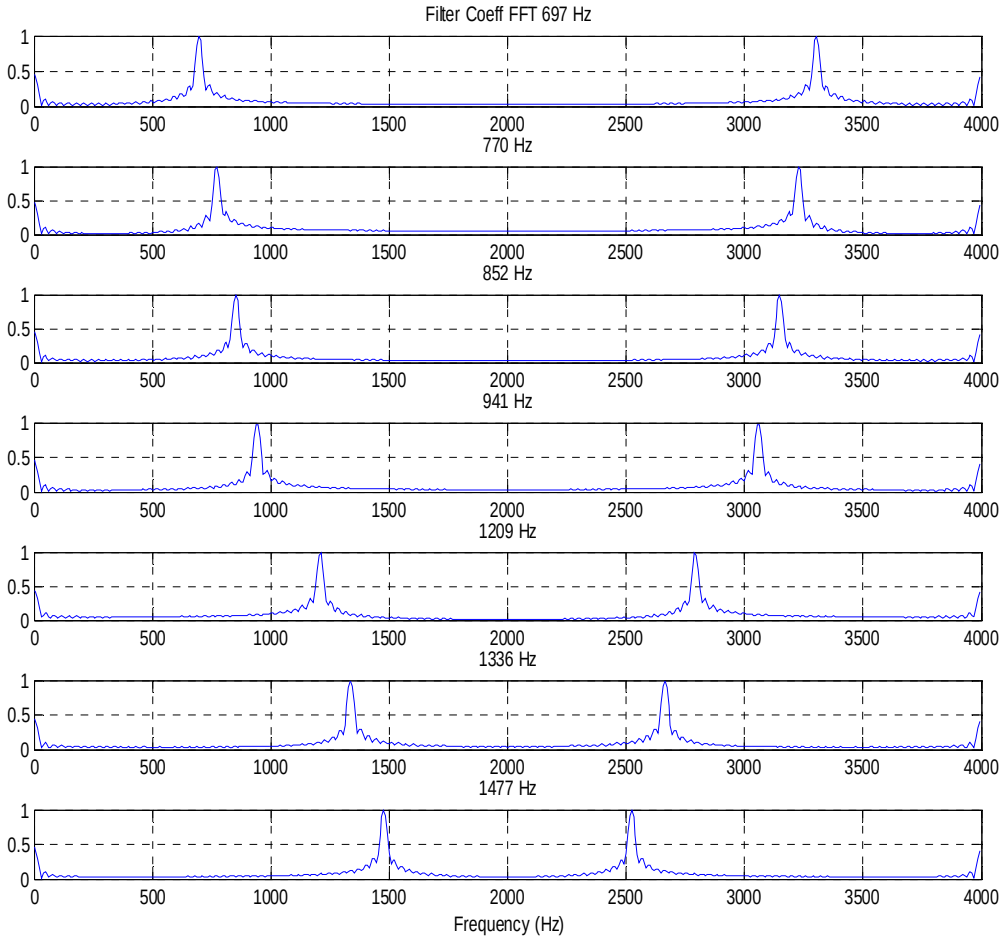

Figure 7. Filter coefficients Fourier transform for all 7 filters using Linear Predictor

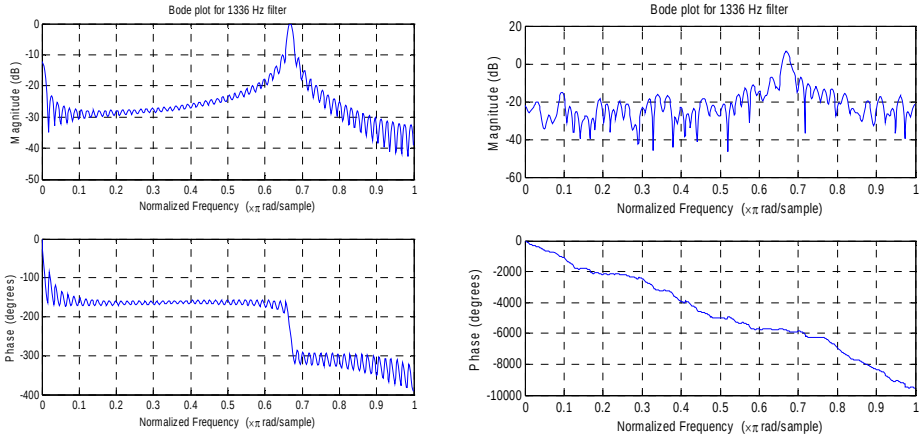

Figure 8. Bode and phase plot for 128 tap FIR filter Linear Predictor (left) and System Identification (right)

The filter convergence coefficients are shown in Figure 9 for both Linear Predictor (upper) and System Identification (lower). It can be seen that Linear Prediction is a better approach than System Identification as the convergence is faster.

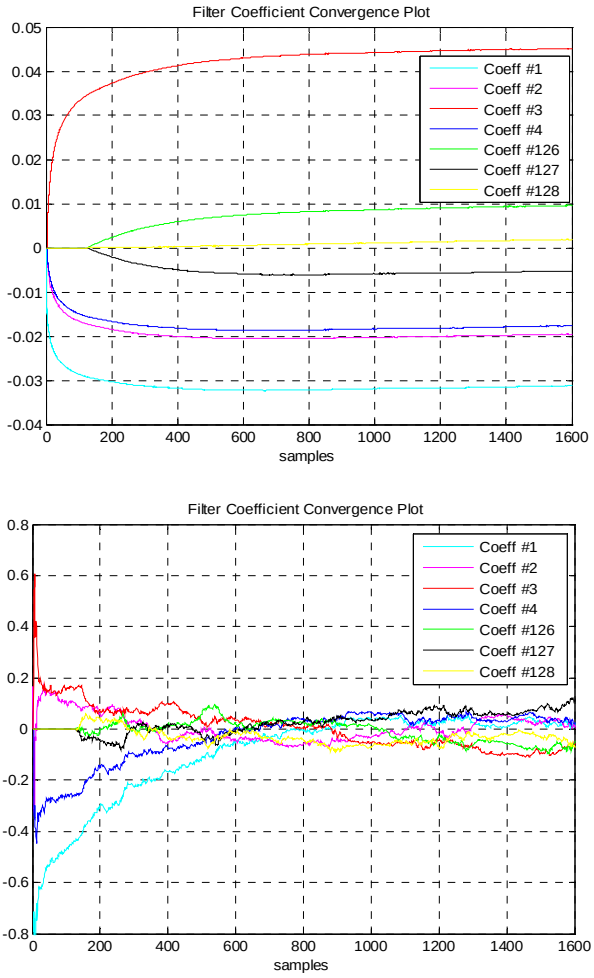

Figure 9. Filter coefficients convergence for Linear Predictor (upper) and System Identification (lower)

Experiments were also performed with noise and non-linear variation in the touch-tone. Figure 10(left) shows the FFT of the filter output for all 7 trained adaptive filters. The input to the system was a touch-tone of digit '6' with sinusoidal sweeping frequency and noise. It is observed that only 2 adaptive filters corresponding to frequencies 770 Hz and 1477 Hz allow signal to pass through, indicating that the tone was that of digit '6'. Figure 10(right) shows the similar same case as Figure 10(left) but the input to the system was a touch-tone of digit '6' without a sinusoidal sweeping frequency.

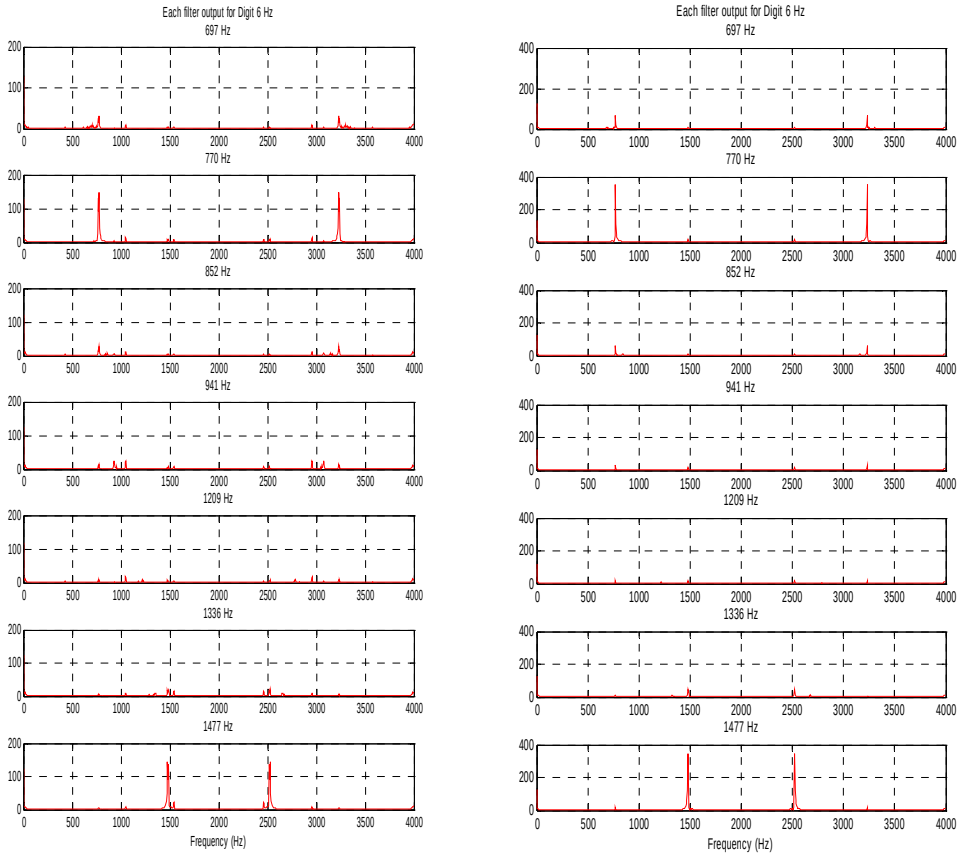

Figure 10. Filter outputs of fixed frequency (right) and varying frequency (left) for digit 6 consisting of 770 Hz and 1477 Hz

The results observed are dependent on how much variation there is and signal to noise ratio (SNR) [4], which given by

$$SNR = \frac{\sigma^2_{signal}}{\sigma^2_{noise}}, where \;\; \sigma^2_{signal} = E\left\{ |s(n)|^2 \right\} and \;\; \sigma^2_{noise} = E\left\{ |n(n)|^2 \right\} \qquad (11)$$

Under simulations correct results were found for variation of +/-5 Hz i.e. η=10 with SNR as low as 31 whereas, for a fixed frequency SNR was as low as 10.

Table 3. Results for Touch-tone

Frequency	Variations +/-(Hz)	SNR
Fixed	0	10
Variable	5	31

3.2 Speech for Spoken Digit Recognition

Detecting the speech for digit recognition, various methods with subtle variations were performed. Specifically, the spectrum was limited to 256, 512 and 1024 sample length and a smooth spectrum was evolved from various triangular and hamming windows. Smooth spectra for the digit '5' are given in Figures 11, 12 and 13.

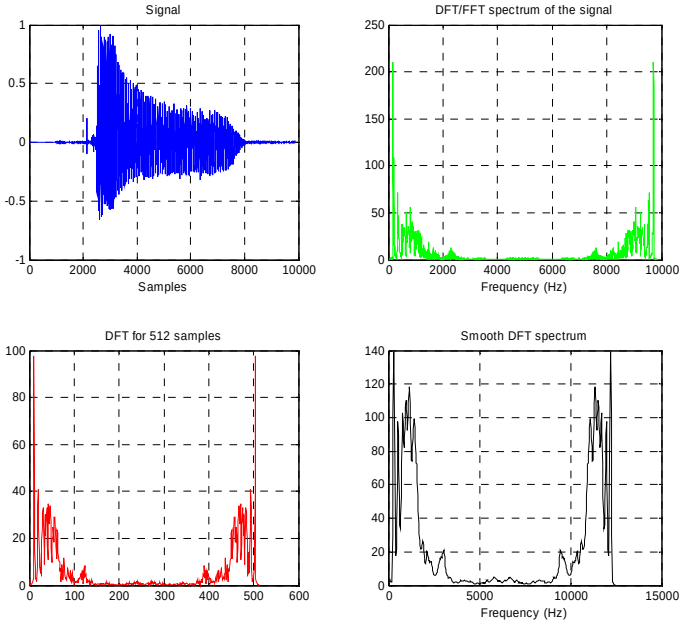

Figure 11. Female spoken digit '5' Fourier transform

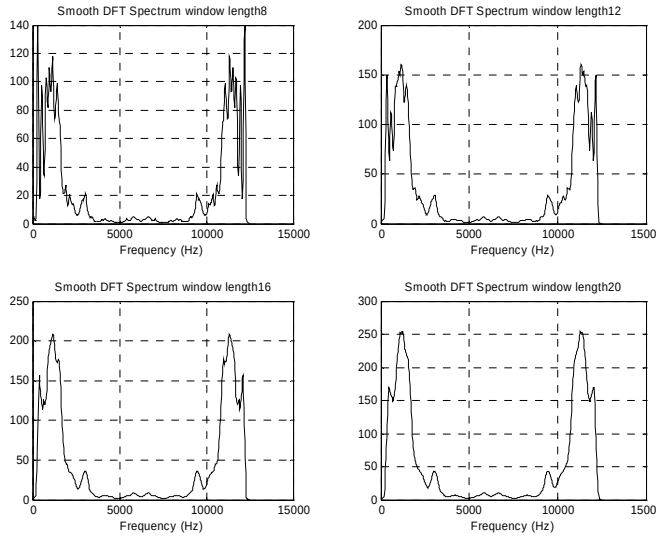

Figure 12. Smooth spectra for triangular window of different lengths

for digit ‘5’

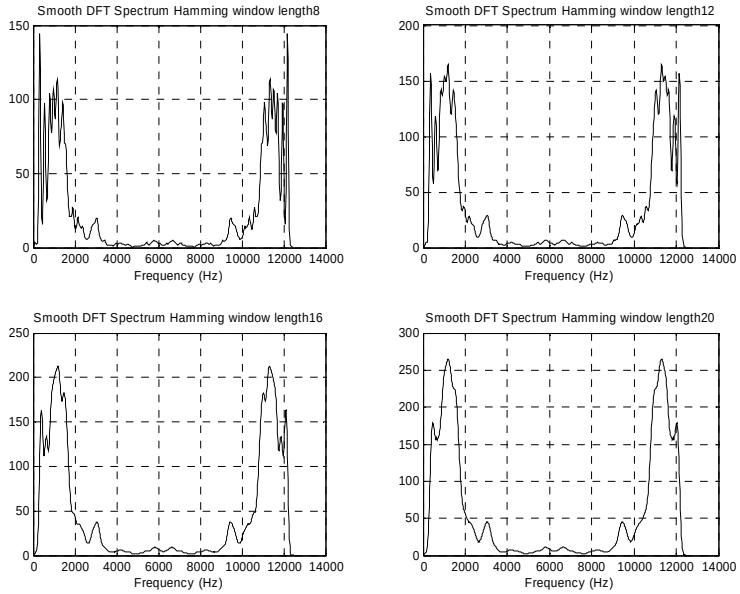

Figure 13. Smooth spectra for hamming window of different lengths for digit ‘5’

It can be noted that there is subtle difference in hamming and triangular window, however increasing the window length further smoothes the spectra but looses key features which are present in the lower frequencies, hence making the detection harder. Figures 14, 15 and 16 show that for similar speech of digits ‘5’ and ‘9’ there is no difference in time domain but Fourier transform yields a noticeable difference.

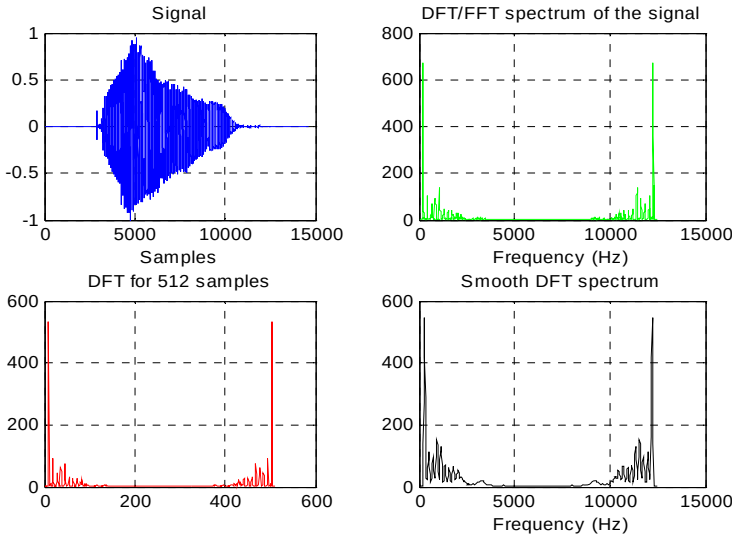

Figure 14. Female spoken digit ‘9’ Fourier transform

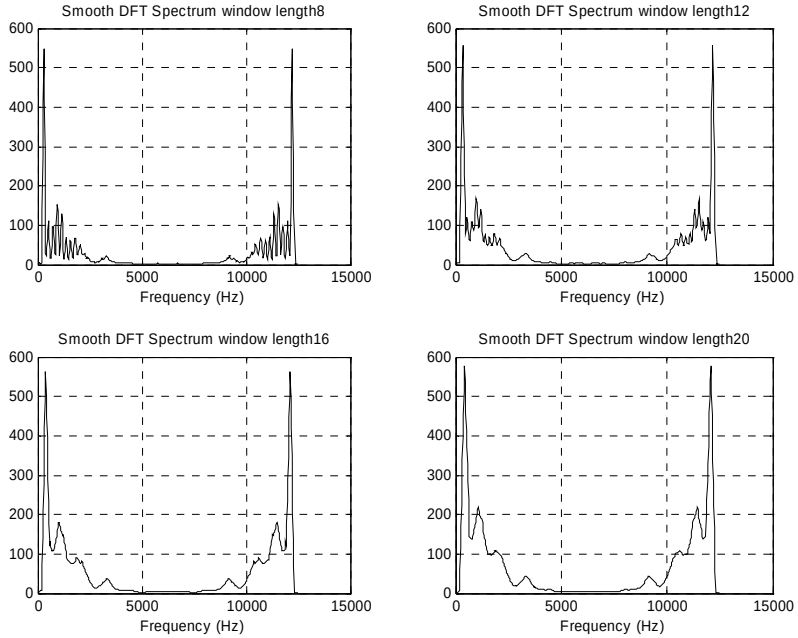

Figure 15. Smooth spectra for triangular window of different lengths for digit '9'

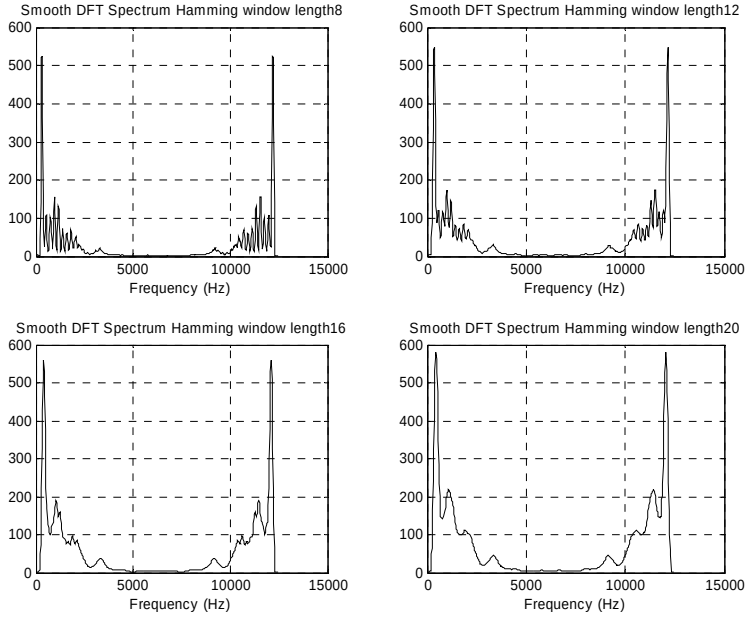

Figure 16. Smooth spectra for hamming window of different lengths for digit '9'

The overall best result found for 2,560 simulations from 8 different male and female utterances of all the ten digits was 90.31% accurate with a DFT window of 1024 samples. However, the ideal solution was a DFT with a hamming size window of 6 samples and an accuracy of 87.66%. A problem with larger DFT length was the large file size of the trained utterances and a longer computational time to detect a digit. A detailed accuracy for variations is given in Table 4.

Table 4. Result accuracy for 2560 utterances

	FFT Length→	256	512	1024
Triangular Window Length	7	82.60%	87.58%	88.48%
	11	80.74%	87.58%	89.94%
	15	77.38%	86.00%	90.31%
	19	73.05%	85.70%	89.65%
Hamming Window Length	4	82.89%	87.66	86.17%
	6	83.24%	87.27%	87.46%
	12	80.94%	87.00%	89.53%

Overall the results can further be increased by using the mel frequency cepstral coefficients (MFCC) which use a logarithmic spacing of windows as more information lies in lower frequencies than at higher frequencies [5]. Another factor that will significantly enhance the accuracy rate would be normalizing the power of the test and train samples being compared.

4. CONCLUSION

The testing for detection of the Touch-tone frequencies yielded that Linear Predictor is better fit than System Identification approach. The system has capabilities of detecting frequency for a SNR as low as 10 for a fixed frequency simulation and as low as SNR of 31 for a non linear +/- 5 Hz variations. The system will prompt an error if the frequencies lie outside the limited bandwidth. This system has the capabilities of adapting to various sets of frequencies without any changes in design as oppose to block filter design and can be used in an environment where digit recognition is kept a secret.

Speech recognition of the digits from various users was successful with a highest success rate of 90.31% with a FFT window of 1024 samples and fixed triangular smoothing window of 15 samples. However, the computational time and storing file size of the training samples were comparatively high when compared to a FFT window of 512 which yielded an accuracy of 87.66% with a hamming window of 4 samples. Achieving 100% accuracy still remains a challenge for speech recognition.

ACKNOWLEDGEMENTS

I would like to thank those involved in the Penn State EEREU program, especially Prof. William K. Jenkins, Prof. Ruyan Guo, Linda Becker, Amanda Skrabut and Andrew Fontanella for organizing a superb program by providing an educational and motivating nine weeks of research experience.

I would also like to thank the National Science Foundation for funding the research and the Pennsylvania State University for organizing and supplying facilities to conduct the research. Lastly, I would like to thank Prof. William Ken Jenkins, Prof. Robert Nickel and Siddharth Pal a graduate mentor for their guidance and ideas in accomplishing the goals of this research. This material is based upon work supported by the National Science Foundation under Grant No. EEC-0244030.

REFERRENCES

[1] Wikipedia, *Dual-tone Multifrequency (DTMF) signaling* <http://en.wikipedia.org/wiki/Dual-tone_multi-frequency>, 12 June 2005

[2] Alan V. Oppenheim, *Applications of Digital Signal Processing,* Prentice-Hall, Englewood Cliffs, N.J, 1978

[3] Paulo S. R. Diniz, *Adaptive Filtering Algorithms and Practical Implementation,* Second Edition, Kluwer Academic Publishers, Norwell, MA, 2002

[4] Dimitris G. Manolakis, Vinay K. Ingle, Stephen M. Kogan, *Statistical and Adaptive Signal Processing,* Artec House, Norwood, MA, 2005

[5] John R. Dellar, John G. Proakis, John H. L. Hansen, *Discrete-Time Processing of Speech Signals*, Macmillan Publishing Company, New York, NY, 1993

HIGH SPEED ANISOTROPIC INDUCTIVELY COUPLED PLASMA (ICP) ETCHING OF GLASS

Vincent Hood[*], Abhijat Goyal[+], and Srinivas Tadigadapa[#]

Department of Electrical Engineering
The Pennsylvania State University, University Park, PA 16802

*Undergraduate Student of
Department of Mechanical, Aerospace, and Nuclear Engineering
Rensselaer Polytechnic Institute
Troy, NY 12180

ABSTRACT

We have achieved high speed dry anisotropic etching of Pyrex substrates with the optimization of Inductively Coupled Plasma Reactive Ion Etching (ICP-RIE) process using an SF_6/Ar based chemistry. Optimization of the etching process was accomplished through Design of Experiment (DOE) involving variation of substrate temperature, substrate distance to source, ICP power, substrate power, vacuum level and flow rates of the etching gases. To prepare the Pyrex substrates a seed layer of Cr/Au was ebeam evaporated and delineated using standard lithography and wet etching techniques. This was followed by electroplating a patterned layer of Ni on the seed layer to act as a hard mask. Process optimization yielded an etch rate greater than .5 mm/min with a root mean square (rms) surface roughness of less than 2 nm.

INTRODUCTION

Conventional requirements on the etching processes for silicon dioxide involved optimization and characterization of sidewalls such as its angel, roughness and also selectivity of masking material with respect to silicon dioxide enabling. However with the advent of Microelectromechanical Systems (MEMS), the dielectric etch process has to deliver in terms of high etch rate, high selectivity of masking material, low surface roughness and uniformity of the etched membranes, in addition to the requirements listed above.). Due to this

[+] Graduate Mentor
[#] Faculty Mentor

shift in constraints on the features being etched in dielectric materials, this paper aims to develop etching recipes enabling fabrication of such MEMS as quartz based microsensors and implementation of the idea of a "laboratory on a chip." To create these MEMS based microsystems, an etch depth of at least 100 μm is needed. Additionally, it is desirable that stringent control over the rms surface roughness of the etched features is maintained, with a surface roughness of less than 5 nm. In order to achieve such high and anisotropic etch rates as well as such a smooth surface with mirror finish, an ICP-RIE system must be used. Due to the fact that the two power sources, the substrate power source and the ICP power source, are not directly coupled to each other a more uniform and higher density plasma can be achieved. Due to decoupling between the ICP and substrate power, primarily because of use of different RF generators as source, the plasma can be generated at pressures as low as less than a mTorr. Plasmas in conventional systems is not stable at such pressures. These factors allow excellent control over the surface roughness of the etched structures for Microsystems fabrication while maintaining a relatively fast etch rates. In this paper, through the variance of ICP power, substrate power, distance from source, gas flow rates, operating process pressure, ratio of gas flows and substrate temperature we were able to optimize the etch rate and surface roughness of silicon dioxide.

EXPERIMENTAL DESCRIPTION

The basic preparation of the four-inch Pyrex wafers involved cleaning then first with Acetone and Isopropyl Alcohol proceeded by cleaning the wafer in a piranha solution (1:1 H_2SO_4:H_2O_2). Next a 200 nm seed layer of gold with a 20 nm adhesion layer of chromium, were e-beam evaporated onto the cleaned wafer. Using standard lithography and wet etching steps the etch patterns where delineated onto the seed layer. The four-inch wafers where then diced into one-inch samples using a commercial dicing saw. Each sample was then coated with approximately 5-10μm of nickel. During the electroplating process the electroplating solution was stirred constantly and the electricity pulsed to create a uniform electroplating. An SF_6/Ar based chemistry was used in the current run of experiments. The standard run time for a sample was one hour. The sample temperature was controlled by using a He cooling system which cooled the back of the substrate holder, which was made of aluminum and the one inch samples were physically clamped onto it. To determine the etch rate, a stylus profilometer was used to measure the step height of the etched feature.

RESULTS AND DISCUSSION

A scientific method to find the optimum etch recipe was used. A four point design of experiment (DOE) was used involving a simple 2^k factorial method. The trends in the process were eliminated by completely randomizing the order of the runs. The variables used in the DOE where ICP power (500W-2000W), substrate power (100W-475W), distance from source (100mm-200mm), gas flow rates (5sccm-50sccm, SF_6, Ar), operating process pressure (5mTorr-

30mTorr), ratio of gas flows and substrate temperature ($10C^{o}$-$30C^{o}$). Through the variance of these factors we were able to achieve an etch rate of 0.536 micron/minute at a rms surface roughness of 1.97 nm at a ICP power of 2000W, substrate power of 475 W, SF_6 flow rate of 5 sccm and Ar flow rate of 50 sccm. If the SF_6 flow rate is increased, the etch rate also increases to 0.75 µm/min. The tradeoff for this increase in etch rate is that the surface roughness increases significantly as well.

Figure 1

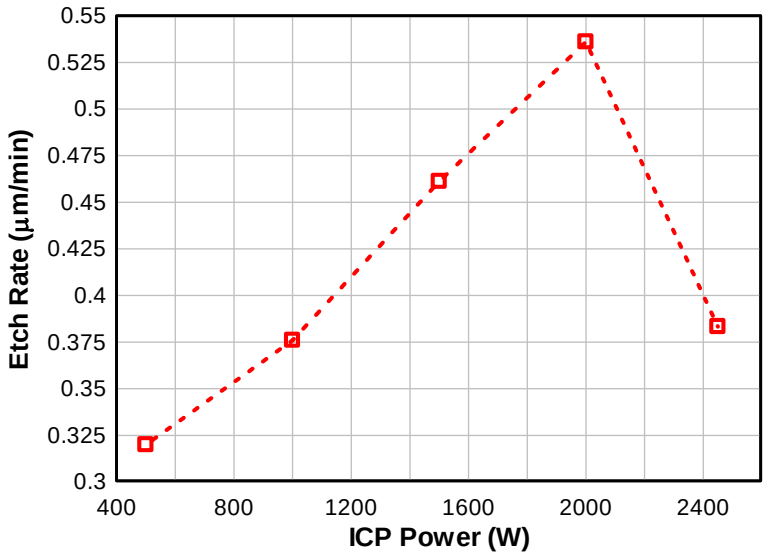

Figure 1: ICP power is varied, all other variables held at optimum values.

Effect of ICP Power

ICP power is directly linked to the plasma density, a higher plasma density increases the number of dissociated and ionized SF_6 and Ar molecules, thus resulting in the formation of a much more dense plasma. With a greater number of dissociated and ionized molecules, a higher etch rate is achieved,as shown in Figure 1.

As we can see from Figure 1, use of a very high ICP power of 2450W, the maximum ICP power that our machine could generate, there is actually a decrease in etch rate. This can be accounted by the fact the as the ICP power increases so do the amount of ionized Ar molecules. With a large increase of ionized Ar molecules, the sputtering of SiO_2 overtakes that of the chemical etch rate of the SF_6 on the SiO_2. This was verified when the ICP power was held constant at 2450W but the Ar flow rate is decreased from 50sccm to 40sccm, resulting in the optimum etch conditions once again.

Effect of Substrate Power

Substrate power is in direct correlation to speed at which the dissociated and ionized particles are attracted to the substrate itself. As we increased the

substrate power the the acceleration dissociated Ar and SF_6 molecules towards the substrate increases, which in turn resulted in an increase of the etch rate, Figure 2. Due to increased energy of the incident ions on the substrate, an increase in the creation and removal of reactants results that eventually resulted in a higher etch rate.

Figure 2

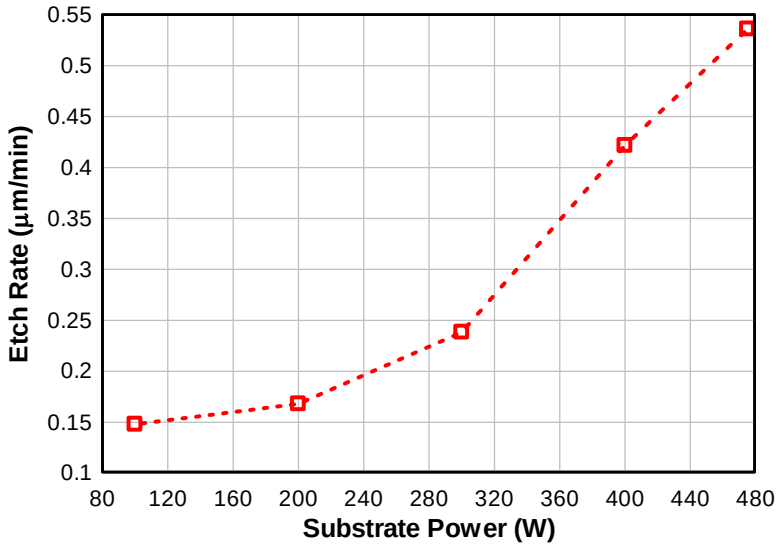

Figure 2: Substrate power is varied, all other variables held at optimum values.

Effect of Chemistry

Optimizing the relative amounts and ratio of flow rates of SF_6 and Ar is vital to the creation and removal of reactants. While fluorine radicals generated from SF_6 helps in creation of reaction products at the surface of the substrate, the Ar ions incident on the substrate surface help in removal of these reaction products and also the stray particles generated from (a) walls of the etching chamber, and (b) hard mask on Nickel. By finding an optimal ratio we are able to have nearly the exact amount of particles created by the chemical reaction and other stray particles removed quickly so as not to interfere with the etching process. The optimum ratio that we found to be is 10 to 1 of Ar to SF_6. As seen in Figure 3, as we decrease the flow of Ar we get a decrease in etch rate.

This can be attributed to the fact that there isn't enough Ar to carry away the particles due to the chemical reaction produced by SF_6. If you increase the SF_6 you will notice that the etch rate increases, as shown in Figure 4. This is because at higher flows of SF_6, more and more number of fluorine ions and radicals are generated, which accelerates the isotropic chemical etching at the surface, thus resulting in higher etch rates with increasing flow rates.

Figure 3

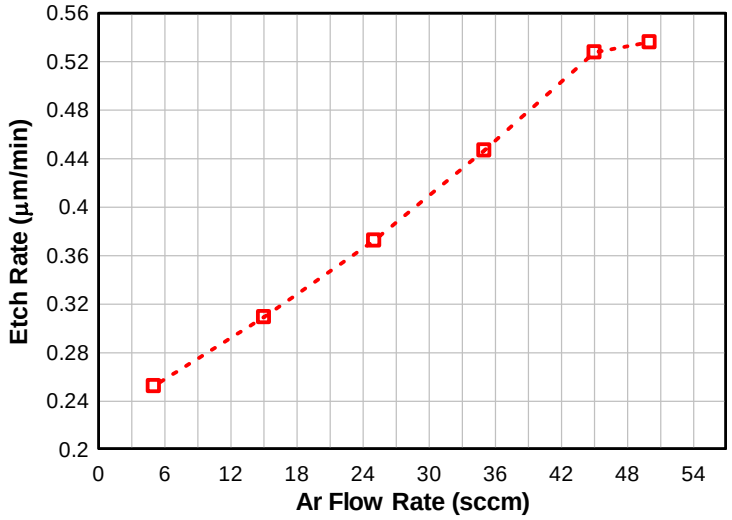

Figure 3: Ar flow rate is varied, all other variables held at optimum values.

Figure 4

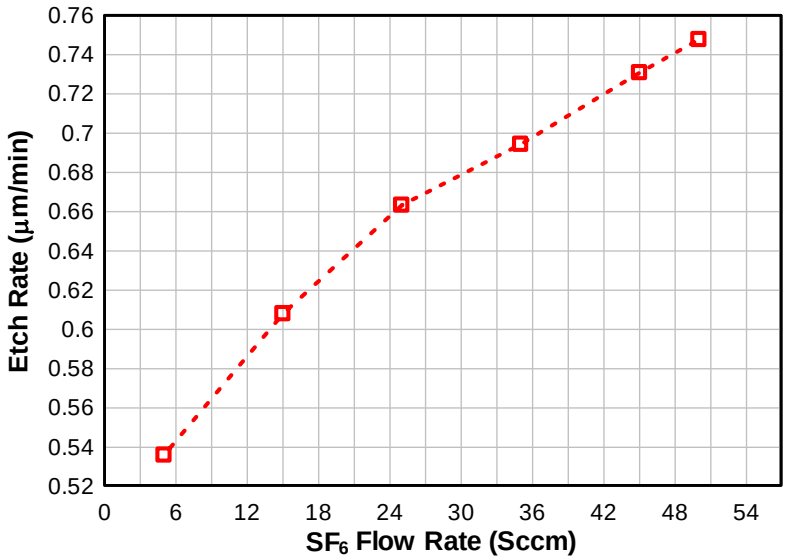

Figure 4: SF_6 flow rate is varied, all other variables held at optimum values.

Now if we could keep our optimum ratio of 10:1 we should be able to achieve even faster etch rates; the only problem with this is that we are limited by the amount of gas that our system can supply. Also as we increase the flow rate of both chemicals our turbo pump can not sustain our optimum pressure of 2 mTorr; therefore it is unable to remove the reaction products and particles off the surface of the sample fast enough. This is verified when we allow the pressure to rise

above 5 mTorr, as shown in Figure 5, where we see a dramatic decrease in the etch rate.

Figure 5

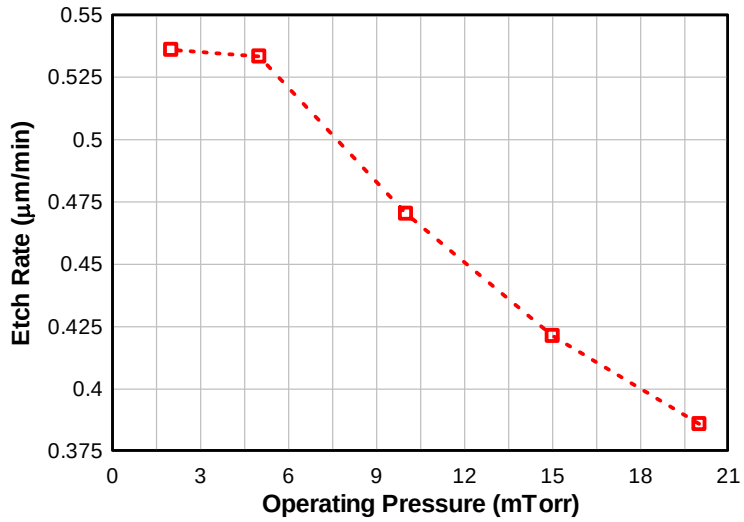

Figure 5: Operating pressure is varied, all other variables held at optimum values.

Effect of Substrate Temperature and Distance from Source

The effects of temperature are rather minimal on the etch rate. As you increase the temperature you do see an increase of etch rate, Figure 6.

Figure 6

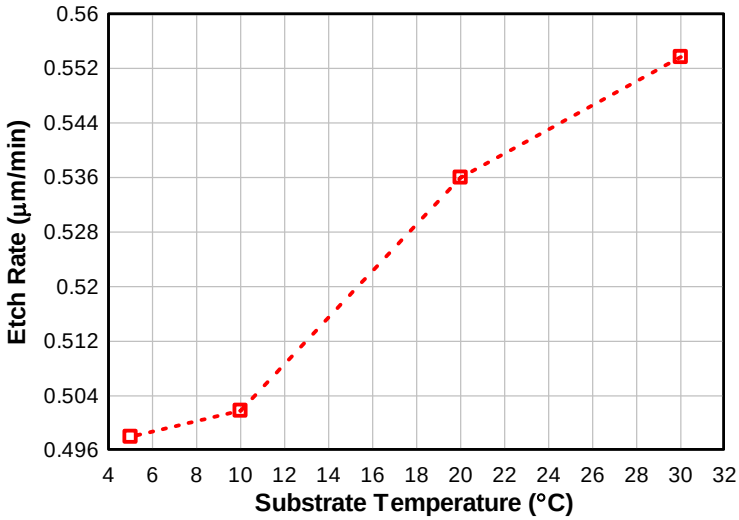

Figure 6: Substrate Temperature is varied, all other variables held at optimum values.

This can be attributed to the fact that the increase in temperature increases the rate of the chemical reaction on the sample which in turn leads an increase of etch rate. But according to the Arrhenius law, the etch rate should increase

exponentially with temperature. This difference can be explained by the fact that there is poor contact between the sample and the sample holder. Because of this the helium back cooled sample holder doesn't conduct the proper amount of heat away.

Distance of sample holder from the ICP source has a profound effect on the etch rate, Figure 7.

Figure 7

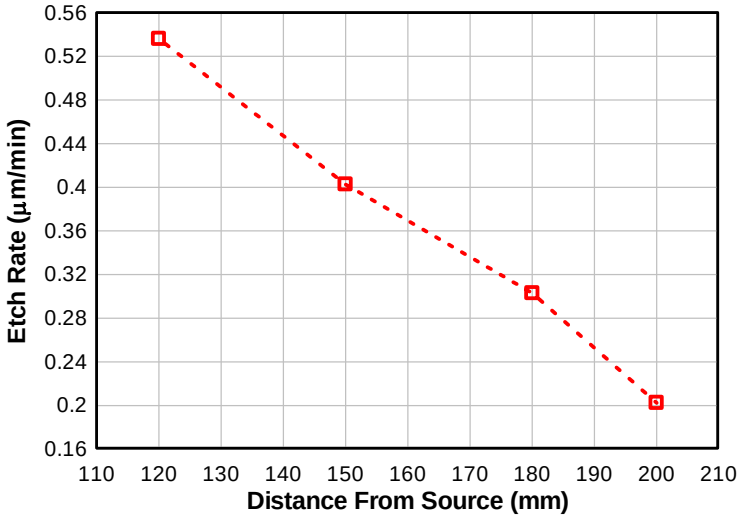

Figure 7: Distance from source is varied, all other variables held at optimum values.

This can be explained by the fact that as the distance away from the source increases, the sample is exposed to plasma which is less dense, more non-uniform with lower concentration of ionic particles and reactive species resulting in lower etch rates.

CONCLUSION

Through the optimization of an Inductively Coupled Plasma Reactive Ion Etcher (ICP-RIE) using SF_6 and Ar based chemistry we were able to achieve an etch rate of 0.536 µm/min and a surface roughness of 1.97 nm. The optimum recipe was 475 W of substrate power, Argon flow rate of 50 sccm, SF_6 flow rate of 5 sccm, substrate temperature of 20ºC, distance from source 120 mm and ambient pressure of 2 mTorr. We were also able to achieve an etch rate of 0.75 µm/min if we supplied a maximum flow of SF_6 and Ar that our machine could; but it resulted in a terrible surface roughness because of an elevated ambient pressure and also because of predominance of isotropic chemical etching effect from chemistry provided by SF_6.

ACKNOWLEDGEMENT

This material is based upon work supported by the National Science Foundation under Grant No. EEC-0244030.

REFERENCES

[1] M. Madou, "Fundamentals of Microfabricatoin"; pp. 53-87 in *Pattern Transfer with Dry Etching Techniques*, Edited by M. Madou and P. Gottehrer, CRC Press, Florida, 1997.

[2] "Plasma Technology, Fundamentals and Applications"; pp. 93-107 in *Plasma EtchingProcesses and Diagnostics*, Edited by M. Capitelli and C. Gorse, Plenum Press, New York, 1992.

[3] M.A. Liberman and A.J. Lichtenberg, "Principles of Plasma Discharges and Materials Processing"; pp. 472-510 in *Etching and Deposition and Implantation*, John Wiley and Sons, Inc., New York, 1994.

[4] "Handbook of Advanced Plasma Processing Techniques"; pp. 33-60, Edited by R.J. Shul and S.J. Pearton, Springer, Berlin, 2000.

[5] B. Wu and D. Chan, "Cr Photomask Etch," *J. Microlitho. Microfadr. Microsyst.*, 2 (3) 200-209 (2003).

[6] B. Wu, "Quartz Etch Optimization," Research and Development Div., Photoronics Inc.

[7] K.J. An, H.S. Kim, J.B. Yoo, G.Y. Yeom, "A Study of the Characteristics of Inductively Coupled Plasma using Multidipole Magnets and its Application to oxide etching," *Elsevier Thin Solid Films*, 341 176-179 (1999).

[8] A. Goyal, V. Hood, S. Tadigadapa, "High Speed Anisotropic Etching of Glass for Microsystems Applications"; to appear in *Journal of Non Crystalline Solids*

LOW VOLTAGE BEHAVIOR AND ELECTRO-OPTICAL SWITCHING PROPERTIES OF DUAL-FREQUENCY NEMATIC LIQUID CRYSTALS

S. Jobling*, Y. Williams[+], J. Liou[+], I. C. Khoo[#]

Department of Electrical Engineering
The Pennsylvania State University, University Park, PA 16802

*Undergraduate Student of
Department of Electrical and Computer Engineering
University of Massachusetts, Lowell
Lowell, MA 01854

ABSTRACT

We investigate the behavior and switching times of the dual-frequency liquid crystal (DFLC) MLC-2048 under various applied AC voltages. The DFLC response time as well as the applied voltage can be minimized under appropriate conditions. DFLC have natural tendencies to turn on and off in response to both a strong enough applied DC field similar to standard nematic liquid crystals (NLC), as well as to an AC field. The critical frequency of this AC field changes with respect to its amplitude and visa versa. In the case of a DFLC the switching time of this change can be greatly reduced in comparison to standard NLC systems which rely on natural alignment times. The change can range from the order of 10ms in NLC to <1ms in DFLC.

INTRODUCTION

I. Electro-optics, Non-linear Optics and Liquid Crystals

Liquid crystals (LC) are some of the most unique and dynamic materials in existence today. Like the name suggests, these materials exhibit an interesting intermediate state in which both liquid and crystalline properties can be observed. Although three types of liquid crystals have been discovered[1], thermotropic, and in particular nematic thermotropic LC have been extensively studied and will be the concentration of this report.

Nematic Liquid Crystals (NLC) in general exhibit a general directional orientation along a so-called director axis; however, there is no positional ordering among molecules[1]. The director axis can be reoriented by an electric,

[+] Graduate Mentor
[#] Faculty Mentor

magnetic, or optical field depending on strength and frequency of the field. When aligned, LC can be treated as a uniaxial crystal. The principle property of LC's that enable directional orientation is their birefringence – they exhibit two separate indices of refraction parallel, $n_{e,}$, and perpendicular, n_o, to the director axis. This birefringence is of great importance due not only to its potential for optical control systems, but for its wideband potential as well. Many NLC possess large birefringence properties throughout the entire UV-infrared spectrum.

NLC systems in existence include active and passive matrix LC display monitors, optical retarders, and optically controlled projectors, to name a few. These systems all rely on the reaction speed of the liquid crystal being implemented, and all NLC systems have serious speed limitations due to their physical properties. The switching times of NLC can be described by[1]

the free relaxation time,
$$\tau_0 = \frac{(\gamma_1 d^2)}{(K_{11}\pi^2)} \tag{1a}$$

the rise time,
$$\tau_{rise} = \frac{\tau_0}{\left[\left(\frac{V}{V_{th}}\right)^2 - 1\right]} \tag{1b}$$

and the decay time,
$$\tau_{decay} = \frac{\tau_0}{\left|\left(\frac{V_b}{V_{th}}\right)^2 - 1\right|} \tag{1c}$$

where V and V_b are the final voltages applied to the LC, V_{th} is the threshold voltage, γ_1 is the rotational viscosity, K_{11} is the splay (bend parallel to the director axis) elastic constant, and d is the sample thickness. A developing field within liquid crystal science in response to the need to shorten these times is the investigation into the dual frequency properties of liquid crystals. That is, the reaction of a liquid crystal to reorient its director axis in two different directions in reaction to two different excitations, usually low and high frequency.

II. Dual Frequency Nematic Liquid Crystals

While the dual frequency properties of liquid crystals have been known for years, much of the work that has involved them has been in an impractical high voltage domain. Knowledge of the behavior of such dual frequency liquid crystal (DFLC) systems in a low voltage (less than ten volts RMS) domain is essential to the practical implementation of these systems in modern technology. The properties of liquid crystals to exhibit dual frequency behavior is inherent in many NLC, however the phase retardation, δ, described by Eqns. (2a) and (2b)[2] is much more greatly effected by voltage than frequency ($(\partial\delta)/(\partial V) \gg (\partial\delta)/(\partial f)$) often. Newly manufactured materials have combined multiple NLC components

together to increase the impact of frequency changes ($(\partial\delta)/(\partial V)\sim(\partial\delta)/(\partial f)$) and emphasize these dual frequency properties as a primary use.

$$\delta=\delta(\lambda,T,V,f)=\frac{(2\lambda d\,\Delta n(\lambda,T,V,f))}{\lambda} \tag{2a}$$

$$\Delta n=\frac{(\Delta\epsilon)}{(2\sqrt{\epsilon})} \tag{2b}$$

Studies investigating the response times of DFLC systems in a higher voltage (ten volts plus RMS) domain have shown superior speeds when compared to standard nematic liquid crystal systems due to their stronger orientational forces[3, 4]. DFLC systems have also proved superior to NLC systems in phase modulation setups as a more effective material due to their larger birefringence properties [5,6]. This larger birefringence comes about as a result of DFLC systems manipulating the LC to orient along two strongly defined directions. This compared to NLC systems which only take advantage of one defined orientation, while the other comes about as a result of natural alignment. The switching times of such DFLC systems take on the general form[1]:

$$\tau_{rise}=\frac{\gamma_1}{\left[\Delta\epsilon_l E_l^2-\Delta\epsilon_h E_h^2-K_{11}\left(\frac{\pi}{d}\right)^2\right]} \tag{3a}$$

$$\tau_{decay}=\frac{\gamma_1}{\left[K_{11}\left(\frac{\pi}{d}\right)^2+\Delta\epsilon_h E_h^2\right]} \tag{3b}$$

where $\Delta\varepsilon_{l,\,h}$ and $E_{l,\,h}$ represent the respective low and high frequency dielectric anisotropy and applied field strength, $K_{11,}$ γ_1, d are the same as with the NLC case. Immediately it can be seen that with any positive anisotropy at a high frequency there will be a faster decay time in DFLC than in NLC. Other studies have made use of the variable dielectric constant for voltage and frequency controlled capacitors[5, 6], as well as a detector in closed-loop adaptive optics[6].

Dual frequency systems can be implemented in such a way as to dramatically improve the response time and lower the required power needed to obtain equally reliable results when compared to equivalent NLC systems. These new systems will operate in a practical (less than ten volts) range and respond very quickly (less than one millisecond) to changes in the control parameters.

EXPERIMENTAL SETUP

The setup designed to investigate the low voltage behavior of the DFLC system is depicted in Fig. 1. The components are a Uniphase 543.5nm He-Ne laser, a pair of Newport LM-1R cross polarizing lenses, a Newport 6619 photodetector, a Newport 1825-C Power meter, as well as a Wavetek 188 function generator. Various width planar DFLC samples (240nm - 25um) were created in

the lab by distributing MLC-2048 from Licristal© (Germany) on conductive TiO slides with a surface coating of rubbed polyvynil-alcohol (PVA). The PVA was used to create a grating surface for each sample to align with.

The transmittivity through the system is governed by Eqns. (4a) and (4b). Each sample was placed in the beam path of the He-Ne laser at an angle $\theta = 45°$ from the vertical to maximize the perpendicular transmission through the system.

$$T_{\perp} = \sin^2 2\theta \sin^2(\delta/2) \tag{4a}$$

$$T_{\parallel} = 1 - \sin^2 2\theta \sin^2(\delta/2) \tag{4b}$$

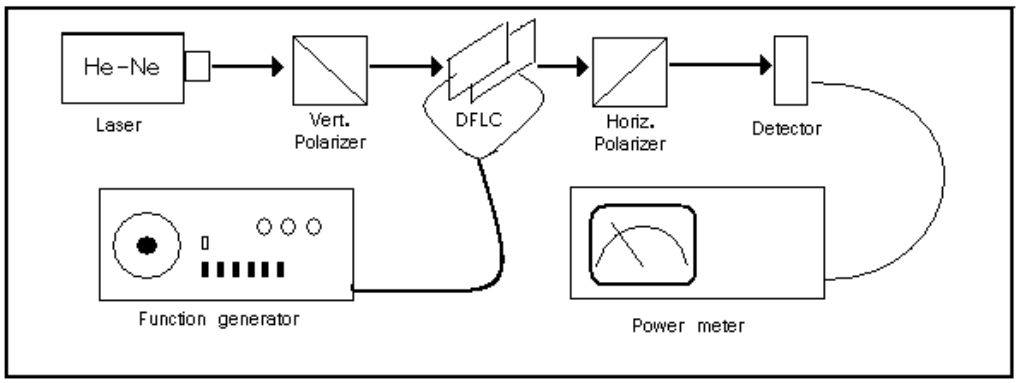

Figure 1: Experimental setup for low voltage DFLC behavior.

The Wavetek was used to generate a controlled applied voltage and frequency on the sample. The natural birefringence, Δn, of the LC causes a normal incident beam to be divided into polarized ordinary and extraordinary components. This difference in refractive indices creates a phase shift between the two components of the polarized beam within the LC, and upon exit of the LC the two components recombine into an elliptically polarized beam (black trace in Fig. 2b).

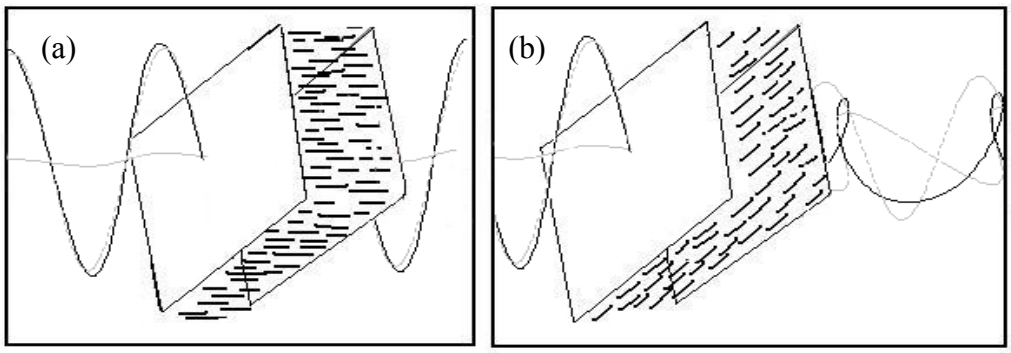

Figure 2: Incident beam through DFLC with (a) Low frequency field on (b) No field or high frequency field on

When a low frequency electric field is applied to the cell the director axis of the LC reorients parallel to the field, and in this case perpendicular to the surface of the sample. When an incident beam passes through a LC parallel to the director axis there are no extraordinary components and the beam passes without any change (shown in Figure 2a). As the frequency increases above a critical value the director axis starts to oscillate for a certain frequency range before again orienting itself along the natural alignment.

By using two cross polarizing lenses this effect can be observed by measuring the output. If the LC has no effect (Fig. 2a) there is no output due to the cross polarizers. However, if the LC reorients the incident beam (Fig. 2b) there is a measurable output after the second polarizing lens. For each sample we recorded the output at the detector while varying both the applied RMS voltage as well as the frequency of the field.

In order to measure the response time of each sample a new setup was used as shown in Fig. 3. Equipment used in addition to that which was used in measuring the low voltage behavior is one Tektronix TDS 360 oscilloscope as well as an additional Wavetek function generator. We measured rise and decay times (10%-90% and visa versa) as the excitation of the system switched between a low and a high frequency.

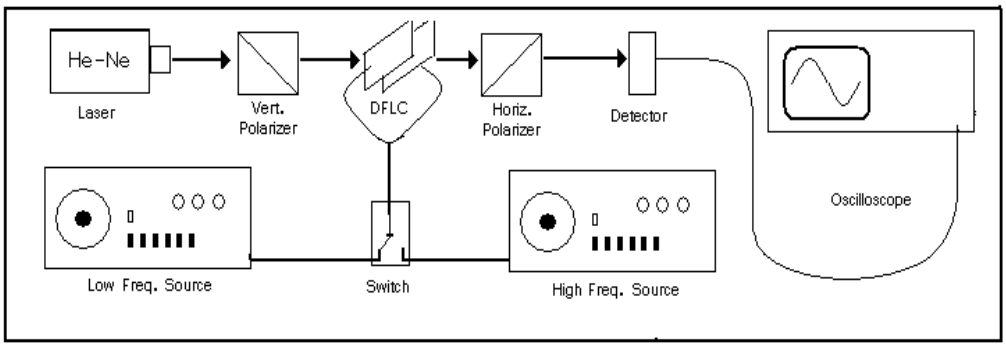

Figure 3: Experimental setup for DFLC response time

RESULTS & DISCUSSION

I. Low-Voltage Behavior

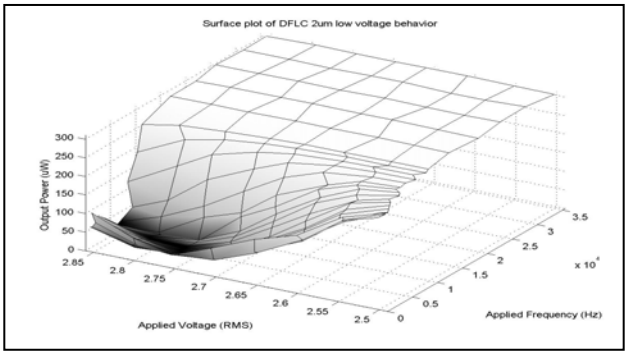

Figure 4: General low-voltage trend

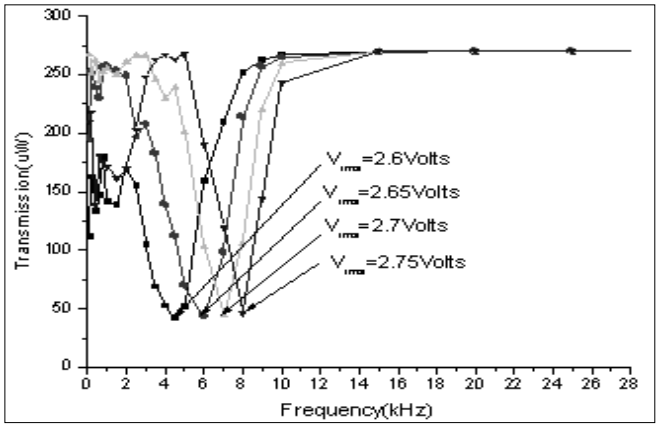

Figure 5: Low-voltage behavior of 240nm sample

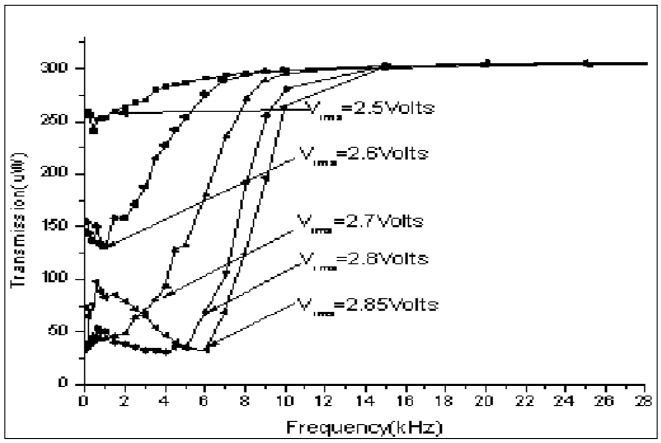

Figure 6: Low-voltage behavior of 2um sample

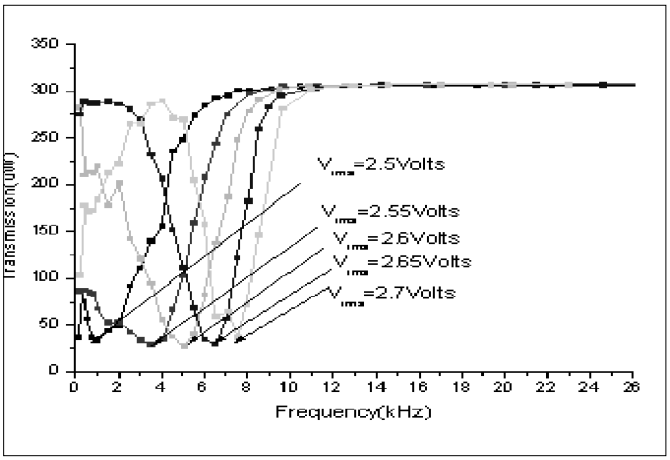

Figure 7: Low-voltage behavior of 5um sample

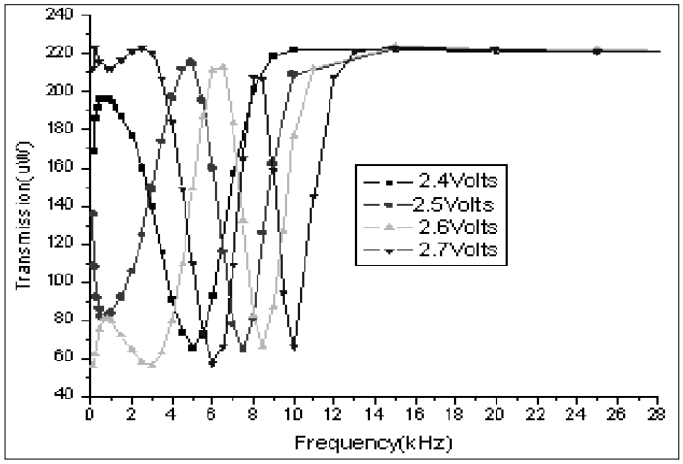

Figure 8: Low-voltage behavior of 10um sample

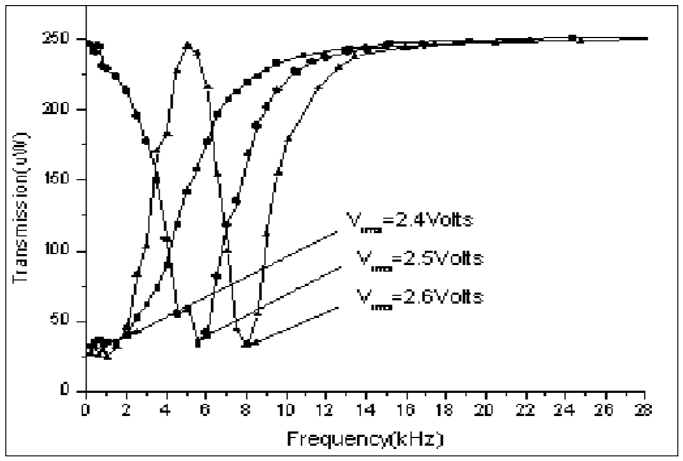

Figure 9: Low-voltage behavior of 25um sample

For each sample there is a clear trend close to the threshold voltage to develop a single minimum transition point when the sample has reached its critical frequency. This signifies the liquid crystal's first non-natural alignment in the direction of the applied electric field (Fig. 2a). The light passes unchanged through the LC and is then near totally attenuated by the cross polarizing lens. This point corresponds to the point at which the dielectric anisotropy is equal to zero[2] shifting from $\Delta\varepsilon>0$ *to* $\Delta\varepsilon<0$, as shown by the point f_0 in Fig. 10.

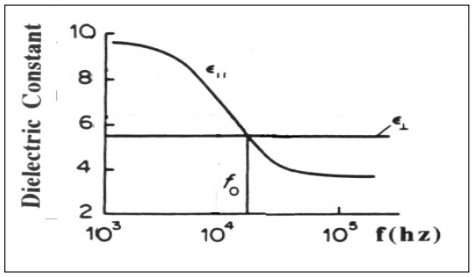

Figure 10: Dielectric constants, $\varepsilon_{\perp}$ and $\varepsilon_{\parallel}$, versus frequency (constant voltage)

As the applied voltage is increased, the point at which this alignment occurs begins to shift to a higher and higher frequency. If the voltage is increased enough a second peak will occur at low frequencies when the LC overcomes the forces associated with the applied field, and the LC will once again align along its director axis. As stated earlier, when aligned forty-five degrees shifted from the incident beam there will be maximum transmission through the second polarizer.

The cleanest results obtained were at lower voltages and are shown above. When the applied RMS voltage continues to increase there will be more and more of these oscillations as δ changes, see Eqn. (4a). With many maxima and minima at higher voltages there is also a definite correlation between higher frequencies and shorter frequency differences between maximum and minimum points. This effect can be seen weakly occurring in Figs. 7 and 8 at the higher voltages.

II. Dual Frequency Response Behavior

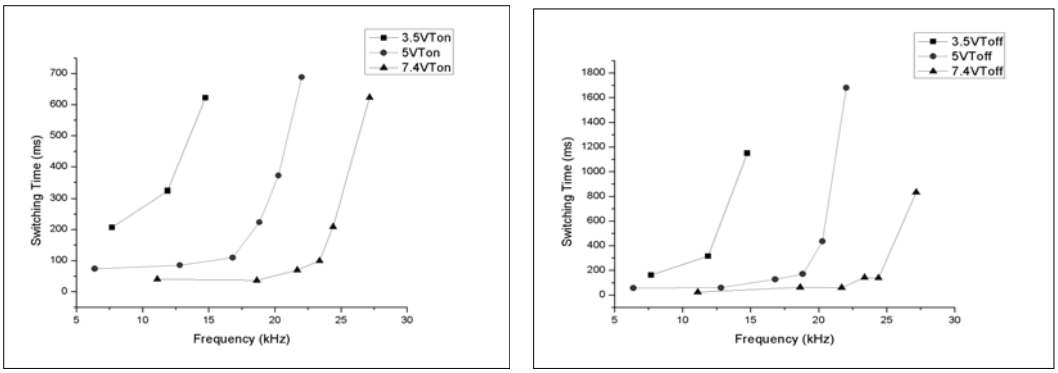

Figure 11: Response times of 2um sample vs average switching frequency

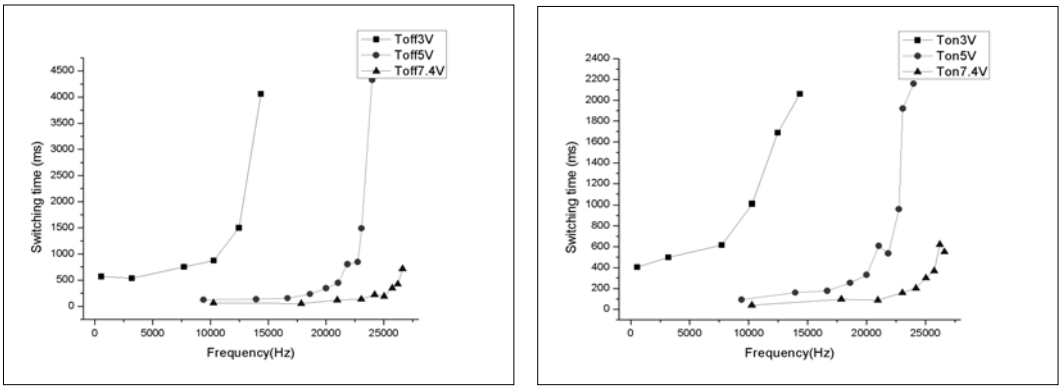

Figure 12: Response times of 5um sample vs average switching frequency

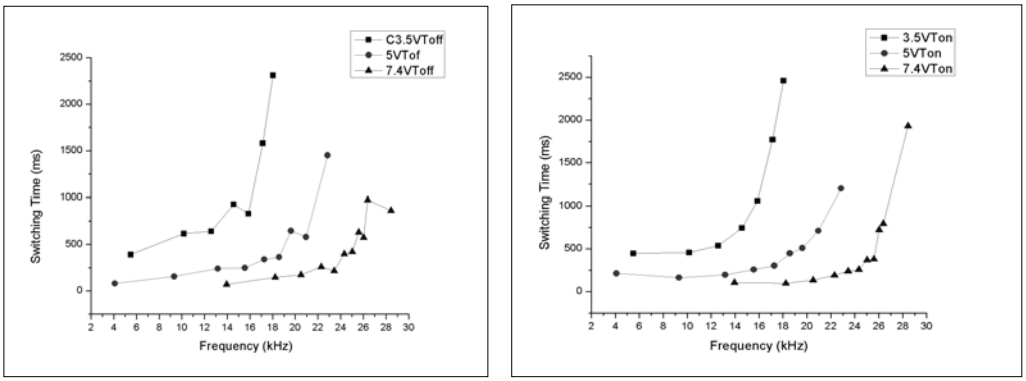

Figure 13: Response times of 25um sample vs average switching frequency

Each of the samples tested demonstrated very good results and repeatability for Figs. 11-13. At the time of this writing no 10um samples had been evaluated. The 240nm sample was not included in the figures due to its few maxima and minima resulting in only 3 data points per plot. The 240 did however match the trend of being faster than any thicker slide with its fastest rise and decay times both below 10ms (compared to around 25 and 40 on the 2 and 5 um samples), and also had faster switching times at higher voltages.

Given a fixed voltage applied to the DFLC sample, the rise and decay times of each sample were fastest at the lowest average frequency. Average frequency was used to plot the data due to the confusing nature of plotting two frequencies on one axis. As an example, the rise and decay times shown in Fig. 12 are given below with all the frequency data for five volts.

Table 1: Rise and Decay Times of 5um Sample at $5V_{RMS}$

Frequencies switched between:		Freq Avg	τ_{on}	τ_{off}
Frequency at T_{max} (Hz)	Frequency at T_{min} (Hz)	(Hz)	(ms)	(ms)
6520	12280	9400	92	125
15560	12350	13955	160	136
15560	17780	16670	177	156
19310	17920	18615	253	234
19310	20700	20005	330	345
21380	20700	21040	608	448
21380	22320	21850	535	805
23100	22400	22750	961	846
23100	23050	23075	1920	1490
24400	23600	24000	2160	4330

From the table one may note a couple additional points. First, notice how that despite the smaller and smaller frequency change between maximum and minimum transmission points there are larger and larger switch on and switch off times. Second, it is interesting to see a second trend within this set of data. Not only do the switching times increase with frequency, but they also change with respect to the direction of switching. For example, when switching from a high to

low frequency there is a faster decay time than rise time, and visa versa for low to high frequencies. There are two exceptions in the data set shown, and five exceptions in all the 5um data taken. Three of those five points have near equal rise and fall times.

CONCLUSIONS

We have presented a thorough analysis of the low voltage characteristics and switching properties of a DFLC system. The DFLC domain of electro-optics is certainly very far from being fully classified. However the results presented here show quite high potential for MLC-2048 and other DFLC systems to dramatically improve upon modern technology. Not only could these operate significantly faster, but also at lower power. As a further note, the samples used were all created in lab by hand and tested by hand, which most always leaves more than plenty of room for improvement though machining and automation.

ACKNOWLEDGEMENTS

Firstly, I would like to extend my gratitude to the organizers of this summer REU program that I've been lucky enough to participate in. Dr. Ruyan Guo, Mrs. Linda Becker, Dr. Ken Jenkins, Prof. Andy Lau, Prof. John Mitchell, as well as all of the faculty that have worked together to make this a possibility. You've all certainly created an outstanding program! And of course this list wouldn't be complete without mentioning the hard work put in by both Amanda Skrabut and Andrew Fontanella, who have helped to make all the students feel comfortable and welcome at our new home this summer. Lastly, I would like to thank Mike Stinger, Andres Diaz, and Kan Chen for all the assistance and explanations they have provided me in the past two months, without all their help and counseling I would certainly have been lost in an utter world of confusion for 9 weeks straight. Well, that and I'd probably have no idea where all the great places to eat are.

This material is based upon work supported by the National Science foundation under Grant No. EEC-0244030.

REFERENCES

[1] I. C. Khoo, S. T. Wu, Electro-Optical Properties of Liquid Crystals, pp139-163, 107-110, and 194-196, Optics and Nonlinear Optics of Liquid Crystals, Volume 1, World Scientific, Singapore, 1993.

[2] I. C. Khoo, Dielectric Constants and Refractive Indices, pp. 39-45, Liquid Crystals: Physical Properties and Nonlinear Optical Phenomena, John Wiley & Sons, Inc., New York, 1995.

[3] Y. H. Fan, H. Ren, X. Liang, Y. H. Lin, and S. T. Wu, "Dual-frequency liquid crystal gels with submillisecond response time", *Appl. Phys. Lett.* **85**, 2451 (2004).

[4] A. B. Golovin, S. V. Shiyanovskii, and O. D. Lavrentovich, "Fast switching dual-frequency liquid crystal optical retarder, driven by an amplitude and frequency modulated voltage", *Appl. Phys. Lett*. **83**, 3864 (2003).

[5] A. K. Kirby, and G. D. Love, "Fast, large and controllable phase modulation

using dual frequency liquid crystals", *Optics Express* **12** 1470 (2004).
[6] Y. Q. Lu, X. Liang, Y. H. Wu, F. Du, and S. T. Wu, "Dual-frequency addressed hybrid-aligned nematic liquid crystal", *Appl. Phys. Lett.* **85**, 3354 (2004).
[7] H. K. Bücher, R. T. Klinbiel, and J. P. VanMeter, "Frequency-addressed liquid crystal field effect", *Appl. Phys. Lett.* **25**, 186 (1974).
[8] S. R. Restaino, D. Dayton, S. Browne, J. Gonglewki, J. Baker, S. Rogers, S. McDermott, J. Gallegos, and M. Shilko, "On the usage of dual frequency nematic material for adaptive optics systems: first results of a closed-loop experiment", *Optics Express* **6** 2 (1999).
[9] M. Schadt, and W. Helfrich, "Voltage-dependent optical activity of a twisted nematic liquid crystal", *Appl. Phys. Lett*. **18**, 127 (1971).
[10] I. C. Khoo, M. Y. Shih, M. V. Wood, B. D. Guenther, P. H. Chen, F. Simoni, S. S. Slussarenko, O. Francescangeli, and L. Lucchetti, "Dye-Doped Photorefractive Liquid Crystals for Dynamic and Storage Holographic Grating Formation and Spatial Light Modulation", *Proceedings of the IEEE* **87**, 11, 1897-1911 (1999).
[11] I. C. Khoo, "Orientational Photorefractive Effects in Nematic Liquid Crystal Films", *IEEE Journal of Quantum Electronics* **32**, 3, 525-534 (1996).

DEVELOPMENT OF A CONSTANT LEVEL OSCILLATOR CIRCUIT FOR DYNAMIC MONITORING OF RESONANCE FREQUENCY AND QUALITY FACTOR OF A QUARTZ CRYSTAL MICROBALANCE (QCM)

Timo R. Mechler*, Abhijat Goyal[+], Srinivas Tadigadapa[#]

Department of Electrical Engineering
The Pennsylvania State University, University Park, PA 16802

*Undergraduate Student of
Computer Science, Math, and Physics Departments
Luther College
Decorah, IA 52101

ABSTRACT

A Quartz Crystal Microbalance is a type of mass sensor that can be used for specific analyte detection and has been actively deployed in industry and in research labs. Due to ongoing advances in MEMS (Micro Electro Mechanical Systems) technology, an ultra-sensitive QCM has been developed requiring less of the unknown substance (from nanograms to femtograms) in question for sufficient Signal to Noise ratio of the output signal. Because of the reduced size, the resonance frequency of the QCM is expected to increase requiring development of oscillator circuits operating at radio frequencies (RF). To date, analysis of the resonance spectra of these ultra-sensitive QCM's has been done with an impedance analyzer. This has proven to be expensive and also prevented use of the device into a handheld diagnostic and sensory tool. To combat these challenges, a novel circuit topology has been developed using an automatic gain controller, operational amplifiers, and other common circuit elements. This paper presents results on design, analysis and testing of the circuit and its components.

[+] Graduate Mentor
[#] Faculty Mentor

 103

INTRODUCTION

Quartz is an abundantly available material that exhibits piezoelectric properties. This means that when a potential difference is applied to a quartz crystal, the electric field causes the crystal to distort physically and this distortion causes a voltage to be developed across the surface of the crystal. The AC signal hence applied across the electrodes of the QCM causes the crystal to resonate at a characteristic frequency called as the resonance frequency. Quartz crystals are widely deployed in today's high-speed electronic devices. Applications range from simple timer/oscillator circuits operating in the kilohertz range to more advanced applications such as filters for cellular telephones that operate on the order of a few gigahertz. Due to the high frequency stability of these crystals, there is also suitability for applications as gravimetric and temperature sensors.

A Quartz Crystal Microbalance (QCM) is a gravimetric sensor that is being actively used in commercial and research applications. The resonance frequency of a QCM shifts when a mass is deposited on its electrodes, accompanied with a decrease in the Q, which is the amount energy dissipated per cycle. For the oscillator circuit to be able to drive the crystal effectively, it should be able to dynamically adjust to the change in Q by changing the amplitude of the feedback signal. Hence, by monitoring the value of this feedback signal an estimate of the Q of the crystal can be obtained. The goal of this research project has been to develop an oscillator circuit topology for real-time monitoring of the resonance frequency and quality factor of the QCM, which can dynamically adjust its gain to compensate of the decrease in Q of the crystal under conditions of viscous mass loading.

Butterworth Van Dyke Model of a QCM

An equivalent circuit for the QCM based on the Butterworth Van Dyke model is as shown in Figure 1:

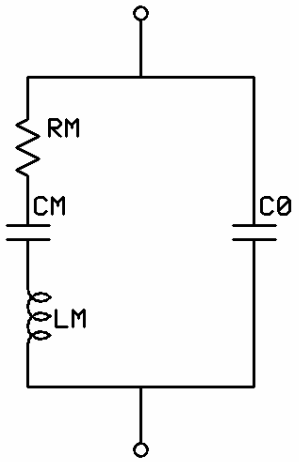

Figure 1: Quartz Crystal Microbalance Equivalent Circuit

The value of inductor L_M depends on the initial mass of the crystal; capacitor C_M depends on the stiffness and resistor R_M accounts for the energy loss in the crystal and its mounting structures. All of the above factors are motional components and dominate near resonance. Capacitor C_0 is the static capacitance and determines the impedance of the QCM away from resonance. All quartz crystals exhibit two types of resonances, a series resonance, and a slightly higher parallel resonance. When oscillating at the series resonance frequency, f_s, the crystal has very low resistance. Using Figure 1 as reference, the series resonance frequency f_s can then be calculated as follows,

$$f_s = \frac{1}{\sqrt{2\pi L_M C_M}} \tag{1}$$

Between the series and parallel resonance frequencies the crystal acts like an inductor, i.e. it has a high inductive reactance. At the parallel frequency f_p, the crystal has a very high resistance. Again, using Figure 1 as a reference, the parallel resonance f_p frequency can be determined readily if the series resonance f_s is known using the following formula,

$$f_p = \frac{f_s}{\sqrt{1 + C_M / C_0}} \tag{2}$$

A graph of the Reactance vs. Frequency of a crystal oscillator, and its series and parallel resonance frequency can be seen in Figure 2:

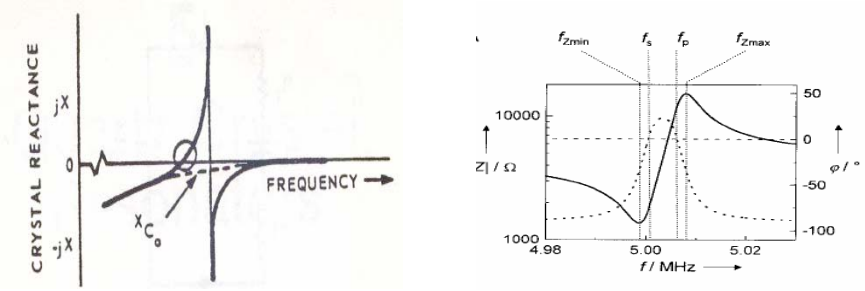

Figure 2: (a) Reactance vs. Frequency plot of a Quartz Crystal[1], (b) Diagram showing series and parallel resonance frequency of the crystal.

By looking at the Figure 2, it can be seen that the series resonance and inductive reactance are only exhibited over a small range of frequencies, making a quartz crystal oscillator frequency very stable due to the high quality factor of the resonance. Since a very stable and accurate frequency is needed for a QCM, it is important that the proposed oscillator circuit be able to operate at the series resonance of the QCM.

Oscillator Circuit Theory

The fundamental components of an oscillator circuit include an amplifier and feedback network, which are illustrated in Figure 3:

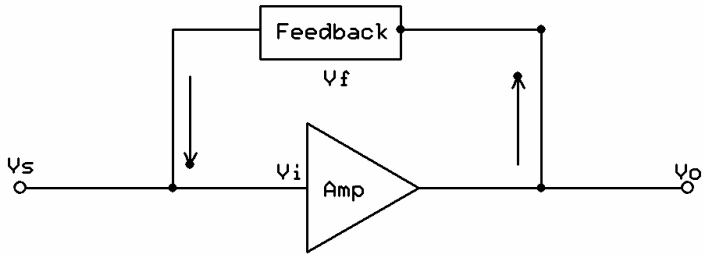

Figure 3: Basic Feedback Circuit Topology

Two main criteria exist[2] that must be met so that a circuit can freely oscillate:

1) The feedback must be positive (i.e. it must aid the original input signal).
2) The Barkhausen criterion for oscillation must be met. This basically states that the gain of the amplifier multiplied by the feedback factor of the feedback network must be greater than or equal to unity.

Once both these conditions are met, oscillation of the circuit can be sustained. Several circuit designs have been readily developed to be used with a quartz crystal oscillator, e.g. the Clapp, Colpitts and Pierce oscillator circuits. A simplified circuit schematic[3] that is applicable to all three can be seen in Figure 4:

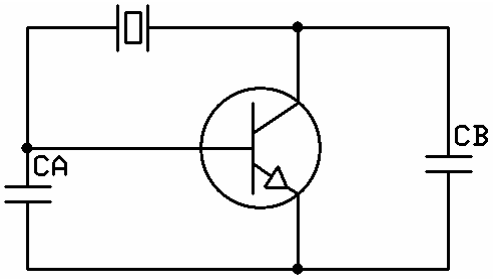

Figure 4: Simplified Crystal Oscillator Circuit Schematic

The above circuit contains a transistor, two capacitors, C_A and C_B, and a quartz crystal oscillator connected in series with both capacitors. These three components will make up the feedback network. C_A and C_B are usually chosen to be large and the quartz crystal operates at its series resonance frequency with C_A and C_B. There will be a 180-degree phase shift due to capacitors C_A and C_B, and the transistor will provide another 180 degrees of shift, resulting in a positive feedback and meeting the first criteria for oscillation. With the proper values of

C_A and C_B it can also be ensured that the loop gain of the circuit will be unity or greater for satisfying the Barkhausen criterion and allowing oscillation to be self-sustaining.

PIERCE OSCILLATOR

Of the three designs introduced in the previous section, a Colpitts oscillator is different in that it uses a pair of capacitors which are in series connected with the crystal oscillator and act as a voltage divider[4]. The advantage of this is that then frequency of the oscillator circuit is very stable and furthermore the circuit performs well at high frequencies and thus is suitable for the application of this project. A Pierce oscillator is really nothing more than a modified Colpitts oscillator. The main difference between the two is that the AC ground is at the emitter of the transistor in the Pierce oscillator and in the Colpitts at the collector of the transistor. Furthermore, the advantage of the Pierce oscillator is that it is very easy to construct and scales easily to 30 MHz for higher frequency crystals, while the Colpitts is more challenging to build and tune.

Practical Implementation

To monitor the output frequency of a QCM that has a resonance frequency of about 6 MHz, a Pierce oscillator whose operating range is between 1 to 10 MHz was constructed[3]. A detailed circuit schematic including components used can be seen in Figure 5:

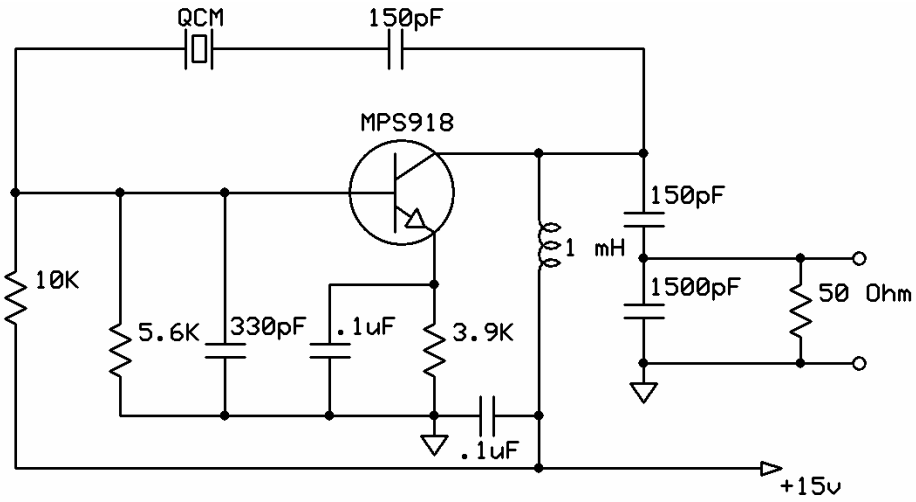

Figure 5: 1-10 mhz Pierce Oscillator Circuit Schematic

Analyzing the circuit in detail, it can be seen that the 10K and 5.6K resistors serve to bias transistor. The 150pF capacitor in series with the QCM is used to fine tune the frequency and can be exchanged for different values depending on the crystal implemented. The 330pF and second 150pF capacitor act as C_A and C_B

referenced in Figure 4. The inductor in the schematic acts a finite load at radio frequencies, and otherwise as a DC short.
Before the circuit was powered up, the resonance frequency of the QCM used was precisely determined using an Impedance Analyzer (Agilent 4294A). Figure 6 shows the output of the impedance analyzer with the QCM connected across the test terminals.

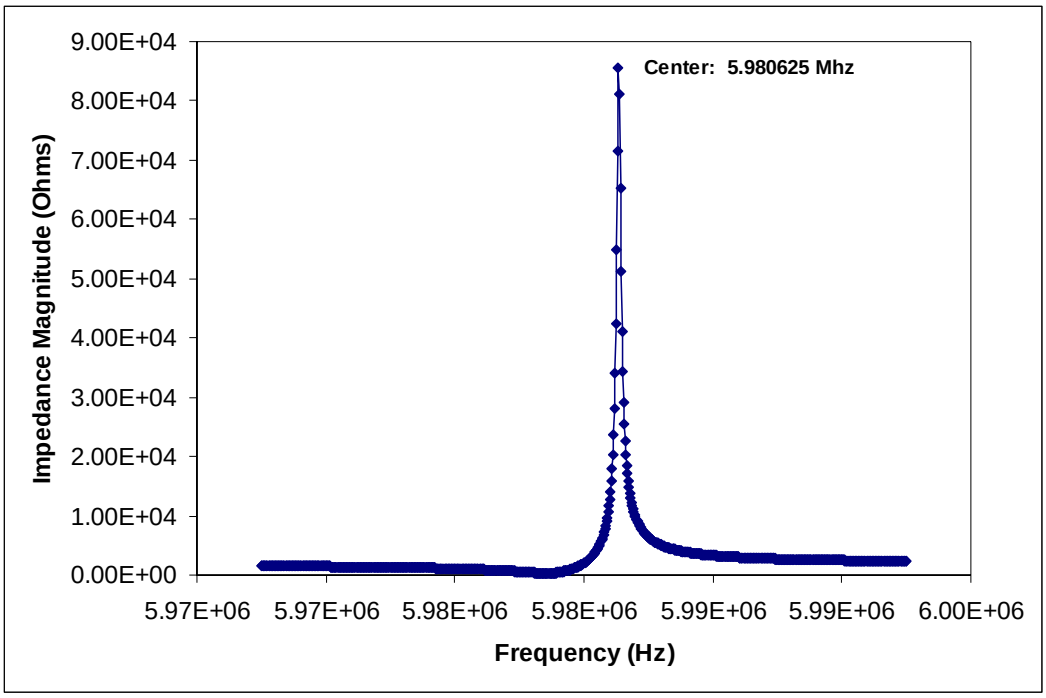

Figure 6: Impedance Analyzer Output Displaying Resonance Frequency

As can be seen from the figure, the maximum of the resonance, which corresponds to the resonance frequency of the QCM, is 5.980625 MHz. After getting a quick precise estimate of the resonance frequency using an impedance analyzer, the QCM was inserted into the constructed Pierce oscillator circuit, and the circuit was powered on. Figure 7 shows the output that was observed on the oscilloscope (Tektronix TDS714L):

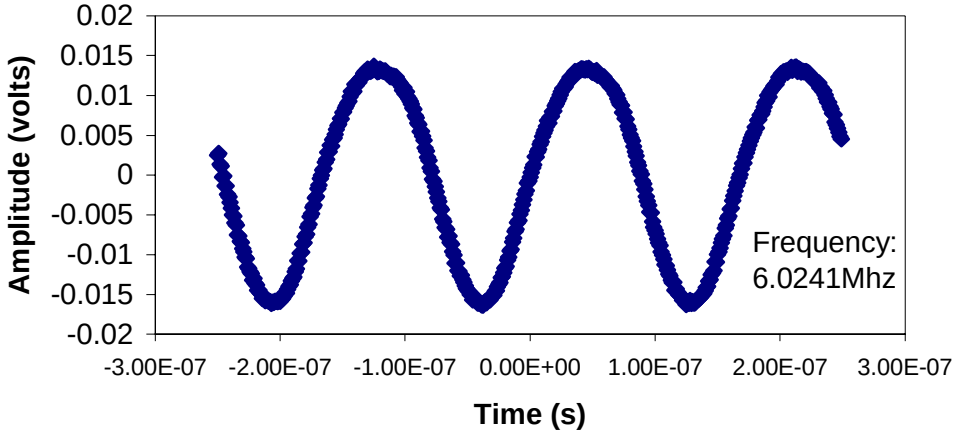

Figure 7: Oscilloscope output of Pierce oscillator circuit

The resonance frequency, calculated from the output of the oscilloscope turned out to be approximately 6.0241 MHz. This is an error of .8% from the value of the resonance frequency as obtained from the impedance analyzer and can be attributed to the error in estimation of the time period from the output of the oscilloscope. Apart from the measurement errors, the Pierce oscillator circuit was able to drive the QCM into oscillation.

Dextrose Water Experiment

To further test the QCM and the oscillator circuit, it was decided to conduct a mass loading experiment on the QCM. The mass loading solution was prepared by dissolving 18 grams of Dextrose ($C_6H_{12}O_6$) into 500grams of water (H_2O). This solution was then diluted 1000 times to ensure mass loading in the nanogram range on the QCM. One microlitres of the solution, containing approximately 36 ng of the sugar dissolved in it, was then dispensed on the QCM surface. The water was allowed to evaporate leaving behind sugar on the electrode. The resonance frequency was measured using a frequency counter (HP 53181 A) for greater accuracy. The resonance frequency was first observed and recorded for the unloaded QCM and then for the QCM with mass on it. This process was then repeated, thus depositing a total of 72 ng of sugar on the electrode of the QCM. Frequency readings were taken all the way to 218ng of mass loading. Figure 8 shows the QCM's resonance frequency as a function of the amount of Dextrose present on its surface:

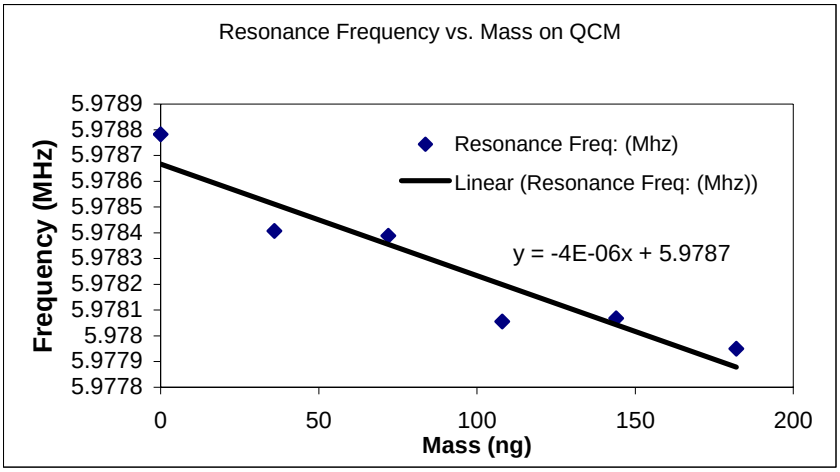

Figure 8: Plot of Resonance Frequency vs. Mass present on QCM

The shift in resonance frequency of a QCM with mass deposition on its electrode is given according to Sauerbrey as –

$$\Delta f = -\frac{2 f_0^2 \Delta m}{A_{piezo}\sqrt{(\mu_q \rho_q)}} \tag{3}$$

where, Δm is the mass loading, A_{piezo} is the area defined by the electrodes, μ_q is the shear modulus, and ρ_q is the density of quartz. Here the negative sign indicates that the resonance frequency decreases as mass is added onto the electrodes of the QCM. The dependence between mass and frequency is linear as predicted by the equation 3, and the slope is about –4e-6, which is line with the sensitivity of the QCM used.

Drawbacks of the Pierce Oscillator

While Pierce Oscillator is extremely accurate at monitoring the frequency of a QCM, there are some major drawbacks to its operation. To begin, there is currently no means to monitor the quality factor of the microbalance. Further, while the resonance frequency can be monitored, it cannot be monitored real-time as the QCM is mass loaded. This is because the oscillator circuit could not drive the QCM when a drop was added on the electrode. In other words, the Pierce oscillator cannot compensate for reduction of quality factor of the QCM and hence cannot drive the crystal under condition of viscous mass loading, which is the case when the QCM is operated in the liquid media. For example, in the case of the Dextrose experiment, the oscillator circuit could drive the QCM only when all the water had evaporated and hence it was only then that the resonance frequency measurement could be recorded. An ideal oscillator circuit should be able to control the gain allowing for real-time monitoring of the mass deposited on the QCM, even for operation in liquid ambient. This gain control would furthermore be tunable so that the QCM can be operated in different environments

(for example, water and extremely viscous glycerin). It would also be wise to move away from having to use inductors in the circuit to prevent unnecessary parasitics and reduce unwanted effects on the resonance frequency of the QCM.

AN OSCILLATOR CIRCUIT WITH VARIABLE GAIN

Literature survey for such a circuit revealed presence of a patent[5] , describing an automatic gain control (AGC) circuit for driving a QCM, thus enabling real time monitoring of both resonance frequency and quality factor using inexpensive frequency counters and multi-meters rather than an impedance analyzer.

Overview

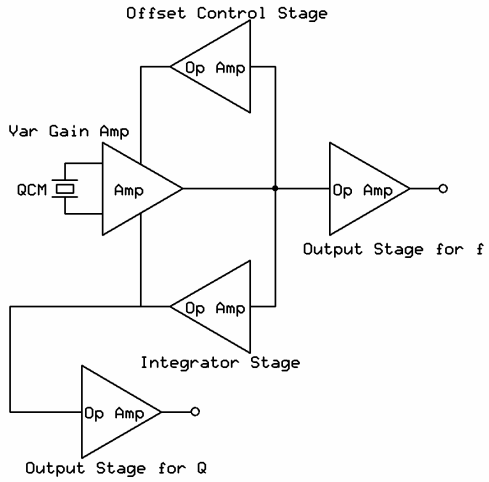

Figure 9: Block Diagram of Circuit from Patent

Looking at the block diagram in Figure 9, the patent suggests the use of a variable gain amplifier with built-in AGC to be to connected to four operational amplifiers; two that will act to amplify the resonance frequency and quality factor, one to act as a comparator/integrator to control the gain, and one to act as a lowpass filter/offset control in the positive feedback loop back to the amplifier input. The QCM is connected to the variable gain amplifier where it will begin to start oscillating and produce an AC signal. This signal will pass through the variable gain amplifier, at which point it will be amplified by an operational amplifier that is internal to the chip package before reaching the output. At the output, part of the signal is amplified by an output stage consisting of an op-amp before being read off. The signal also gets fed back positively to the input of the variable gain amplifier and to the internal op amp via the offset control stage. Part of the AC signal also becomes rectified and gets fed into the integrator/comparator stage where it is compared to a reference voltage. Depending on the size of the incoming signal, the outgoing DC signal will either tell the AGC by means of the variable gain amplifier to increase the resonance frequency signal or attenuate it. This output signal is also split off and directed into the output stage for Q where it will be amplified before being read out.

Circuit Modules

In the following section the main components of the circuit will be described in more detail and more information will be given regarding their operation. These parts will be the variable gain amplifier, integrator/comparator stage, and also the offset stage that's present in the feedback loop.

Variable Gain Amplifier

The patent suggests the use of the National CLC 520/522 integrated circuit package. Since this package is no longer manufactured, it was replaced by the CLC 520/522's successor, the LMH6502/6503. Figure 10 shows a picture of the LMH6502 connected to an evaluation board provided by National Semiconductor.

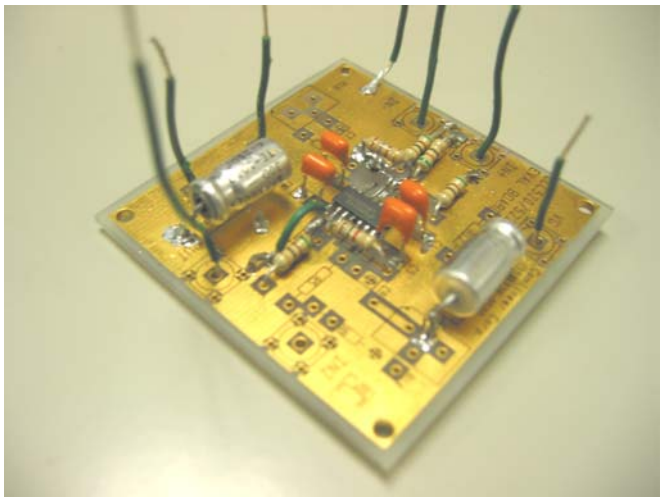

Figure 10: Evaluation Board for LMH6502

A setup as shown in the evaluation board in Figure 10 sets the amplifier up with a maximum gain of approximately ten[6]. Using a DC voltage, the input to the chip was varied from 0 to 400mV (limited by LMH6502 specifications[7]) and a corresponding gain of ten was observed at the output. The same is true if an AC signal is used instead of DC, however, if the frequency goes up into the tens of megahertz, the amplifier maximum gain begins to drop of from ten to about two or three.

Integrator/Comparator Stage

To be able to adjust the gain voltage dynamically depending on what the output of the QCM coming from the variable gain amplifier is, an integrator/comparator stage is necessary. Figure 11 shows a schematic of this stage as suggested by the patent with an added 1 Megaohm resistor in parallel with the capacitor located in the amplifier feedback loop:

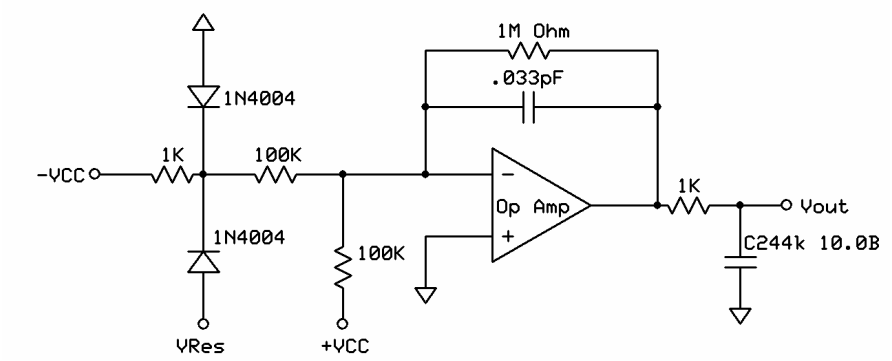

Figure 11: Circuit Schematic of Integrator

In the above schematic, V_{CC-} and V_{CC+} represent input voltages of 5V each, and V_{res} is the output signal coming from the LMH6502 variable gain amplifier. Both diodes serve to rectify V_{res} before this signal is passed onto the integrator. V_{CC+} is adjusted (usually via a Potentiometer) to change the output characteristics of the integrator. Figure 12 shows a plot of various V_{CC+} measurements and the corresponding voltage outputs:

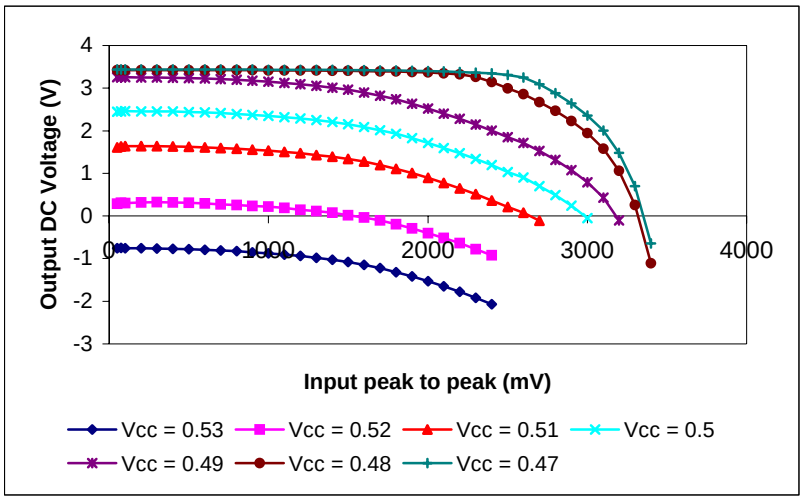

Figure 12: DC Bias Curves for Integrator/Comparator Stage

When the output signal from the variable gain amplifier, or equivalently, the amplitude of the QCM's resonance frequency decreases, the output of the integrator begins to increase, telling the gain control in the amplifier (LMH 6502) to amplify the output signal. The output of the integrator increases rapidly as output voltage (peak to peak of AC signal) coming from QCM decreases, suggesting that even with tiny changes in the amplitude of the QCM's resonance frequency the integrator will continue to pass a positive DC voltage to the gain control of the amplifier, increasing the output. Hence, due to the integrator the amplitude of the resonance spectrum will stay mostly constant, allowing for real-

time monitoring during mass loading of the QCM. Since the input gain voltage of the LMH6502 is limited from 0 to 2V as given by the data sheets, a $+V_{CC}$ setting of approximately .51 volts works out quite well in the present case.

Offset Control Stage

The output signal of the operational amplifier gets passed into an offset control means shown in Figure 13:

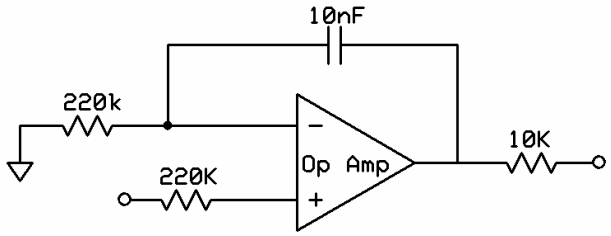

Figure 13: Schematic of Offset Control Stage

Located in the feedback loop of the operational amplifier that is internal to the variable gain amplifier (LMH6502), the offset control varies the voltage going back into this operational amplifier between 0 and 1 volts thus preventing a DC offset in the output coming from the LMH6502.

Detailed Implementation

Having tested the individual modules in the circuit and quantitatively estimating their input/output characteristics, the design given forth in the patent was implemented in a circuit board. The circuit first had to be laid out in CAD software, and then fabricated.

Circuit Design

Layout of the traces and components was initially done by hand to maximize efficiency in design and to minimize the amount of wire jumps on the circuit board. The design was then taken and drawn up in the AutoCAD 2005 software. After having completed this step, the circuit design was first checked for consistency and then stored to be used on the circuit fabrication machine.

Fabrication and Assembly

The circuit traces were fabricated on high frequency copper laminates (Rogers 5870) which consist of two copper planes separated by a thin dielectric layer. The bottom copper layer serves as the ground plane and the top layer is where the traces are defined. The circuit fabrication machine is router-like in nature and mills away the unnecessary copper using an ultra-fine drill bit spinning at high speeds. Once the excess copper was removed, the op amps, variable gain amplifier, resistors, capacitors, and other common circuit elements were soldered onto the board. The finished board (fully assembled) can be seen Figure 14. The circuit currently being tested for driving a QCM and bugs introduced due to

integration of different circuit components are being ironed out at the time of this writing.

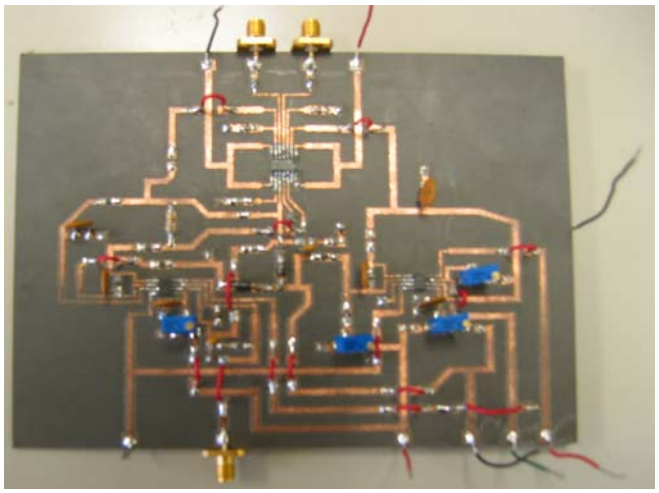

Figure 14: Completed Oscillator Circuit with Components

SUMMARY

QCM's are versatile sensor platforms used in both industry and research labs. With miniaturization, it has been possible to realize these sensors in array formats, necessitating the use of oscillator circuits for monitoring the resonance frequency and the quality factors of individual pixels of the array. The miniaturized sensors, with high resonance frequencies, find increasing applications requiring their operation in liquid ambient. Under such conditions, the common oscillator circuits cannot drive the QCM since they are not able to compensate for the reduced Q of the crystal. In this project, the operation of the QCM was understood. Its description in terms of a BVD equivalent circuit was studied and a Pierce oscillator circuit was constructed for monitoring the resonance frequency. Mass loading experiments using Dextrose solution were conducted, confirming the Sauerbrey equation. A variable gain oscillator topology was found using literature search, and was implemented in a circuit board. The individual components of the circuit were implemented and their input/output characteristics were recorded indicating the feasibility of such an Automatic Gain Control Circuit capable of dynamically adjusting to the Q of the crystal thereby enabling real time monitoring of the resonance frequency and quality factor of the QCM.

ACKNOWLEDGEMENT

This material is based upon work supported by the National Science Foundation under Grant No. EEC-0244030. A special thank you also goes out to Professor Lynn Carpenter, Nathan Curtis, and Bruce Knoll for their assistance with circuit design and fabrication.

REFERENCES

[1] M.E. Frerking, "Quartz Crystal Resonators"; pp. 20-22 in *Crystal Oscillator Design and Temperature Compensation,* Litton Educational Publishing, Inc., New York, 1978.

[2] B. Davis, "Positive Feedback and Oscillator Fundamentals"; pp. 220-227 in *Understanding DC Powersupplies & Oscillators,* Prentice Hall Australia Pty Ltd, Australia, 1996.

[3] M.E. Frerking, "Oscillator Circuits"; pp. 56-78 in *Crystal Oscillator Design and Temperature Compensation,* Litton Educational Publishing, Inc., New York, 1978.

[4] I.M. Gottlieb P.E., "Some practical aspects of various oscillators"; pp.151-152 in *Practical Oscillator Handbook*, Newnes, Oxford, 1997.

[5] F. Paul, K. Pavey, and R.C. Payne, "Quartz Crystal Microbalance with Feedback Loop for Automatic Gain Control", U.S. Patent 6,848,299 B2, Feb. 1, 2005

[6] Author Unknown, "CLC73003 Evaluation Boards", National Semiconductor, 2004.

[7] Author Unknown, "LMH6502 Wideband, Low Power, Linear-in-dB Variable Gain Amplifier", Product Data Sheet, National Semiconductor, 2004.

FABRICATION OF IRON (III) OXIDE NANOSTRUCTURES BY POTENTIOSTATIC ANODIZATION

Brian J. Park*, Haripriya E. Prakasam[+], Craig A. Grimes[#]

Department of Electrical Engineering
Department of Materials Science and Engineering
Pennsylvania State University, University Park, PA 16802

*Undergraduate student of
Department of Engineering
Swarthmore College
Swarthmore, PA 19081

ABSTRACT

Iron (III) oxide (Fe_2O_3) is an excellent material for absorbing visible light from the solar spectrum because of its suitable band gap. However, due to low mobility and high bulk carrier recombination, the photoconversion efficiency of iron (III) oxide has been proven to be very poor. Fabrication of nanostructured iron oxide can potentially compensate for the material's poor properties. In this work, iron (III) oxide nanostructures were fabricated by potentiostatic anodization of iron foils in various electrolytes. The structures were characterized using Field Emission Scanning Electron Microscopy (FESEM). The architectures of the nanostructures were dependent on the anodization parameters. Successful fabrication of Fe_2O_3 nanopillars, nanopores, and nanoleaflets were achieved and described.

[+] Graduate Mentor
[#] Faculty Mentor

 117

INTRODUCTION

With the ongoing growth in global population and rise in the demand for energy, there is a race to find new sources of energy to meet future expectations and alleviate the depletion of oil reserves. Lately, solar energy has been receiving tremendous amounts of attention. Semiconductors under solar illumination are capable of splitting water and generating hydrogen[1], which can be used in fuel cells and other applications. Stable semiconductors under illumination are typically metal oxides.[2] Many studies have delved into finding the optimal semiconductor material and properties for efficient hydrogen generation.

Most stable, semiconductor oxides are photochemically active in the ultraviolet spectrum. Since only a very small fraction of the solar spectrum is absorbed, the photoconversion efficiencies of these oxides are very low. Commercial single-crystalline solar cells have efficiencies ranging from 12-16%.[1] Although non-oxide material architectures have better efficiencies than semiconductor oxides, oxide materials are attractive for their ability to withstand corrosion, wide-spread availability, and affordability.[3] Much emphasis has been placed on improving the efficiency of semiconductor oxides by shifting the absorption spectra into visible light, where the majority of the solar spectrum resides.

Iron (III) oxide (Fe_2O_3) is a promising material for direct water splitting due to its small band gap, high corrosion resistivity, and low cost. The band gap determines the amount of solar energy absorbed and available for conversion. Crystalline silicon has a band gap of 1.1eV, but the solar spectrum covers a range from 0.5eV to 2.9eV.[4] Iron oxide has a band gap of 2.1eV, which is sufficient to split water and absorb a large portion, including visible light, of the solar spectrum. Iron oxide semiconductors are able to capture 40% of incident solar radiation.[5]

However, due to the inherent, poor semiconductor properties of iron oxide, the photoconversion efficiency is actually very low. The low conversion efficiency is attributable to high recombination losses and slow charge transfer kinetics.[6] Carrier recombination from trapping electrons by oxygen deficiency sites and low mobility of the holes give rise to low conductivity and a poor photoresponse.[5] Studies of nanostructure arrays have shown enhancement of electron percolation pathways, light conversion, and improved ion diffusion at the semiconductor-electrolyte interface.[3] Therefore, an array of iron oxide nanostructures can reduce the recombination rate, minimize the diffusion length of the holes, and provide a larger surface area for more efficient light harvesting.

This study investigates the fabrication of suitable iron oxide architectures for photoelectrochemical use. The present work focuses on synthesizing iron oxide nanostructures by anodization of pure iron foils using various electrolytes, and characterization of the samples through electron microscopy. Although much research has been conducted on synthesizing iron oxide nanostructures through thermal oxidation[7], few if any have studied synthesis using anodization

techniques. Anodization of titania nanotube arrays for photocleavage of water have shown promising results with overall conversion efficiencies of 12.3%.[8,3] With success, anodizing Fe_2O_3 nanostructured arrays may unfold the pathway to a low cost, highly efficient way of using the Sun's energy.

EXPERIMENTAL DESCRIPTION

Thin iron (III) oxide (Fe_2O_3) layers were fabricated by potentiostatic anodization.[9] Pure (99.9+ %) iron foils, 0.1 mm thick, were anodized using various electrolytes (Fig. 1). The anodization current was monitored with a computer-controlled Keithley 2000 multimeter. Electrolytes used in this investigation involved the chemicals: oxalic acid ($H_2C_2O_4$), hydrochloric acid (HCl), potassium fluoride (KF), nitric acid (HNO_3), and water (H_2O). Various combinations and concentrations of the chemicals were prepared and tested until iron (III) oxide nanostructures were synthesized with success and repeatability. All anodizations were performed under room temperature conditions. The Fe_2O_3 samples were characterized and imaged using Field Emission Scanning Electron Microscopy (FESEM).

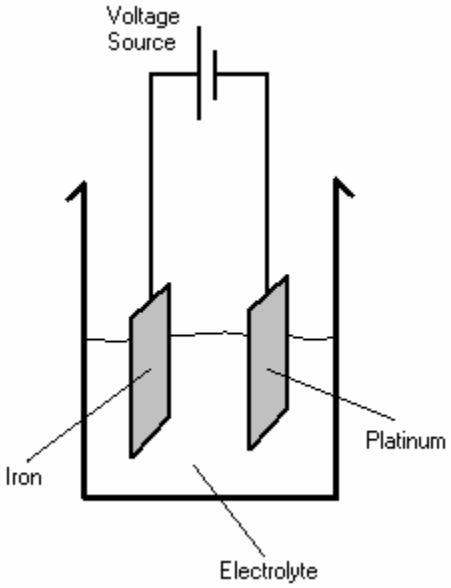

Figure 1. Iron (III) oxide fabrication of pure iron foils through potentiostatic anodization.

RESULTS & DISCUSSION

Nanopillars and Nanopores

Iron (III) oxide nanopillar and nanoporous structures were formed using an electrolyte comprised of 5ml of 0.1M HNO_3, 2ml of 1M KF, and 93ml of 0.3M oxalic acid. The anodizations were carried out at a potential of 2.9V; the anodization current behavior suggests oxide pore formation (Fig. 2). During

Stage I, oxide growth on the iron foil causes a steep decrease in current of 100-150mA. The current increase in Stage II is due to pore initiation. In Stage III, oxidation balances dissolution of the oxide, causing the current to remain relatively constant. With the absence of KF or HNO_3 in the electrolyte, the current behavior failed to show this general trend of pore formation.

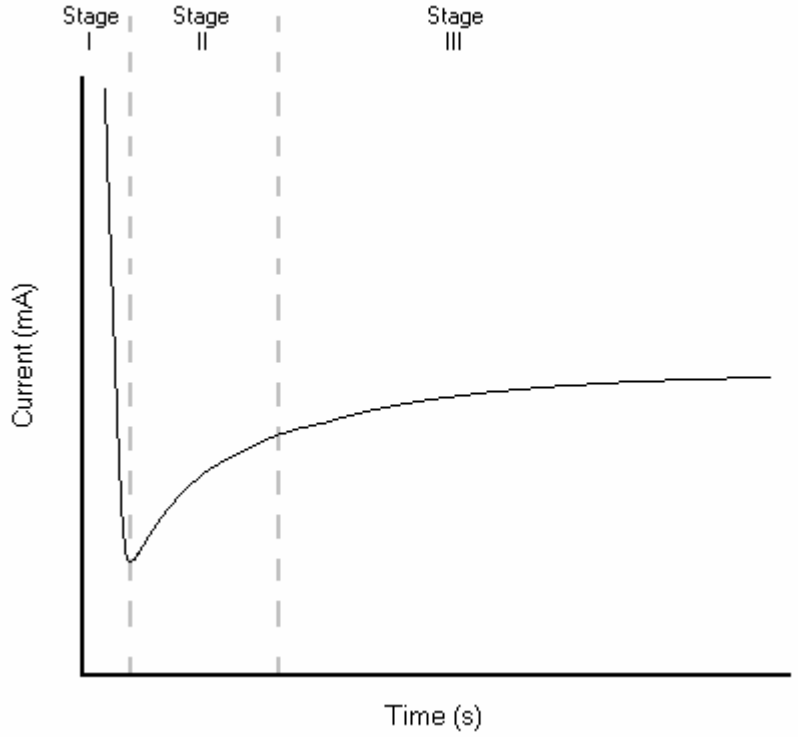

Figure 2. General current behavior of iron (III) oxide nanopillar/porous structures during potentiostatic anodiztion of pure iron foils in an electrolyte with nitric acid (HNO_3), potassium fluoride (KF), and oxalic acid ($H_2C_2O_4$).

The anodizations resulted in the growth of cubic, pillar structures above an underlying layer of pores (Fig. 3a). The pillars typically ranged from 300-800nm in length and 50-200nm in width. The density of the pillars was controlled by the anodization time and concentration of oxalic acid. The pillar density decreased as the anodization time prolonged (Fig. 3b). This phenomenon agrees with the current behavior mentioned previously. As the anodization current approached steady-state, the majority of the pillars dissolved unveiling a layer of nanopores (Fig. 3c). In addition, a lower concentration of oxalic acid, 0.1M, resulted in a greater density of pillars with larger dimensions (Fig. 4). Therefore, a positive correlation exists between the pH of the electrolyte and pillar size.

a.

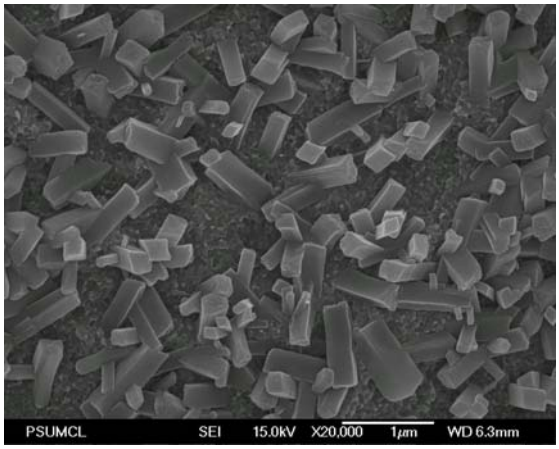

b.

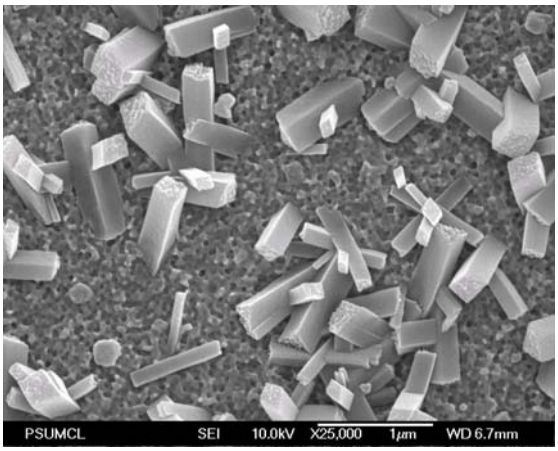

c.

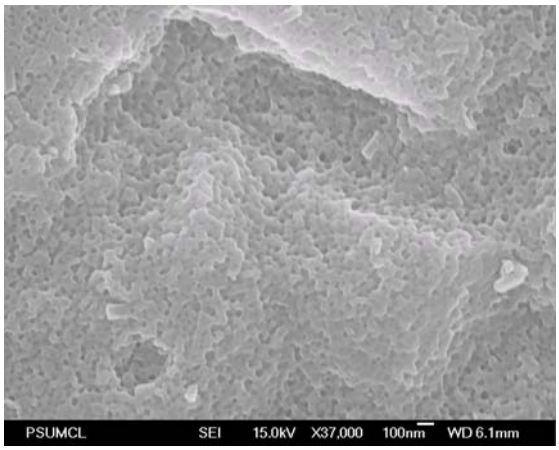

Figure 3. FESEM images of iron (III) oxide nanopillars/pores prepared by anodic oxidation of iron foil in an electrolyte containing 5ml of 0.1M HNO_3, 2ml of 1M KF, and 93ml of 0.3M oxalic acid at 2.9V. (a) Anodization time of 5 minutes. (b) Anodization time of 15 minutes. (c) Anodization time greater than 45 minutes.

a.

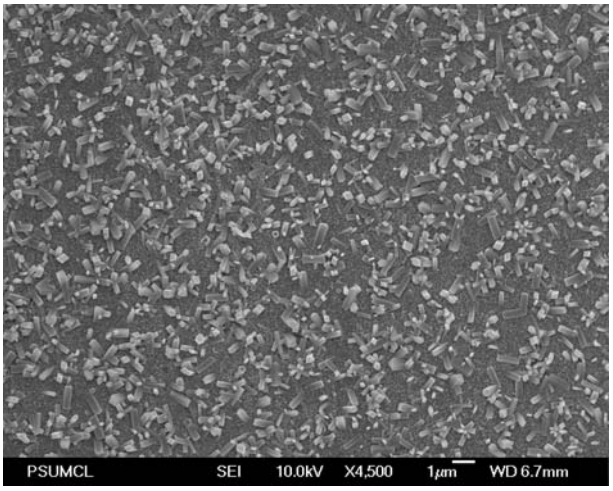

b.

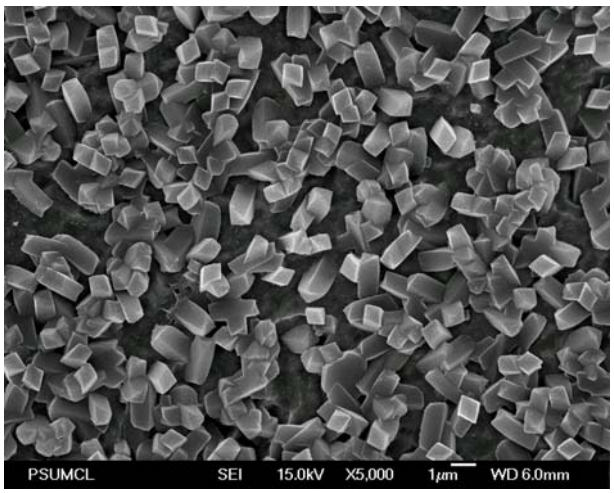

Figure 4. FESEM images of iron (III) oxide nanopillars anodized using different molarities of oxalic acid and time durations. (a) 5ml of 0.1M HNO_3, 2ml of 1M KF, and 93ml of 0.3M oxalic acid at 2.9V for 15 minutes. (b) 5ml of 0.1M HNO_3, 2ml of 1M KF, and 93ml of 0.1M oxalic acid at 2.9V for 10 minutes.

Although iron (III) oxide nanopillars were successfully synthesized, the structures are not suitable for photocurrent generation. The nanopillars do provide a greater surface area for harvesting more light, but the pillars themselves are too large to aid charge transport in the material. The electron mobility of iron (III) oxide is low and the diffusion length of the holes is only 2-4nm.[5] The nanopillars are 50-200nm in width, which is too thick for the holes to diffuse to the electrolyte.[3] On the other hand, the nanopores show more promise for photocurrent generation. The nanopores provide shorter diffusion lengths for minority carriers. But depending on the thickness of the oxide layer, grain

boundaries will inhibit electron transport to the back contact, or conductive substrate.[10]

Nanoleaflets

Iron (III) oxide nanoleaflet structures were synthesized using an electrolyte containing 4ml of 0.1M hydrochloric acid (HCl), 2ml of 1M potassium fluoride (KF), and 94ml of deionized water (H_2O). The anodizations were performed at a potential of 6V. The general, observed anodization current behavior is different compared to the current behavior for the nanopillars/pores. Instead of an initial current drop, the current rises indicating etching of the iron foil. The rise is followed by a slow, progressive decrease in the current which represents growth of a thin, oxide layer.

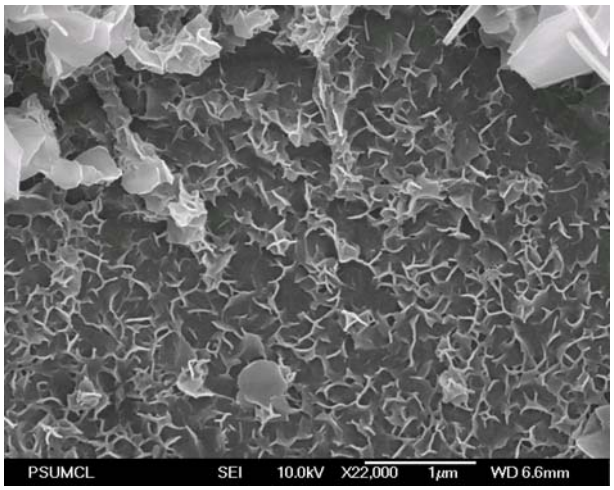

Figure 6. FESEM images of iron (III) oxide nanoleaflets prepared by anodic oxidation of iron foil in an electrolyte containing 4ml of 0.1M HCl, 2ml of 1M KF, and 94ml of water at 6V.

Iron (III) oxide nanoleaflets are an optimal structure for photocurrent generation. The thin oxide layer facilitates electron transport in the material to the back contact. The leaflets compensate for the small diffusion length of the minority carriers, while providing a greater surface area for more efficient light harvesting. As a result, the nanoleaflets are a solution to high recombination losses and slow charge transfer kinetics of iron oxide. Further investigation on the photoelectrochemical properties of Fe_2O_3 nanoleaflets may have a significant impact on the advancement of solar cell technology.

CONCLUSION

Iron (III) oxide nanostructures were fabricated by potentiostatic anodization. The architectures of the nanostructures were dependent on the anodization

parameters. Nanoporous and nanopillar structures were synthesized in an electrolyte comprised of nitric acid (HNO_3), potassium fluoride (KF), and oxalic acid ($H_2C_2O_4$). Nanoleaflet structures were synthesized in an electrolyte containing hydrochloric acid (HCl), potassium fluoride (KF), and water (H_2O). All of the anodized Fe_2O_3 samples were amorphous. Grain boundaries and defects in the iron oxide act as charge recombination centers.[10] Subsequent study of crystallizing the reported nanostructures by annealing may reveal improvement in charge transport and further lower the carrier recombination rate. In effect, anodization of Fe_2O_3 nanostructures advances the movement to find the optimal semiconductor for water photoelectrolysis and efficient hydrogen generation.

ACKNOWLEDGMENT

I would like to thank my faculty mentor, Professor Craig Grimes, for giving me this opportunity to become involved with and conduct in this area of cutting-edge research. I would especially like to thank my graduate mentor, Haripriya Prakasam, for all of her guidance and support. My gratitude also extends to Gopal K. Mor and Maggie Paulose for their advice and assistance in the laboratory. This material is based upon the work supported by the National Science Foundation under Grant No. EEC-0244030.

REFERENCES

[1] Bard, Allen J., and Marye Anne Fox, "Artificial Photosynthesis: Solar Splitting of Water to Hydrogen and Oxygen," *Accounts of Chemical Research*, **28** 141-45 (1995).

[2] Grätzel, Michael, "Photoelectrochemical Cells," *Nature*, **414** 338-44 (2001).

[3] Varghese, Oomman K., Maggie Paulose, Kathik Shankar, Gopal K. Mor, and Craig A . Grimes, "Photoelectrochemical and Water-Phtoelectrolysis Properties of Micron-Length Highly-Ordered Titania Nanotube-Arrays," *Journal of Nanoscience and Nanotechnology*, **5** 1-8 (2005).

[4] "Bandgap Energies of Semiconductors and Light." *Solar Energy Technologies Program*. 10 Feb. 2004. U.S. Department of Energy. 10. Jul. 2005 <http://www.eere.energy.gov/solar/bandgap_energies.html>.

[5] Lindgren, Torbjörn, Heli Wang, Niclas Beermann, Lionel Vayssieres, Anders Hagfeldt, and Sten-Eric Lindquist, "Aqueous Photoelectrochemistry of Hematite Nanorod Array," *Solar Energy Materials & Solar Cells*, **71** 231-43 (2002).

[6] Sartoretti, C. Jorand, M. Ulmann, B.D. Alexander, J. Augustynski, and A. Weidenkaff, "Photoelectrochemical Oxidation of Water at Transparent Ferric Oxide Film Electrodes," *Chemical Physics Letters*, **376** 194-200 (2003).

[7] Fu, Yunyi, Jing Chen, and Han Zhang, "Synthesis of Fe_2O_3 Nanowires by Oxidation of Iron," *Chemical Physics Letters* **350** (2001) 491–94.

[8] Mor, Gopal K., Kathik Shankar, Maggie Paulose, Oomman K. Varghese, and Craig A . Grimes, "Enhanced Photocleavage of Water Using Titania Nanotube Arrays," *Nano Letters*, **5** (1) 191-95 (2005).
[9] Alwitt, Robert S. "Anodizing." *Electrochemistry Encyclopedia*. Dec. 2002. Case Western Reserve University. 10 Jul. 2005 <http://electrochem.cwru.edu/ed/encycl/art-a02-anodizing.htm>.
[10] Beerman, Niclas, Lionel Vayssieres, Sten-Eric Lindquist, and Anders Hagfeldtz, "Photoelectrochemical Studies of Oriented Nanorod Thin Films of Hematite," *Journal of The Electrochemical Society*, **147** (7) 2456-61 (2000).

RESEARCH AND DEVELOPMENT OF LIONSAT SENSOR BOARD HARDWARE

Thomas R. Riccobono* and Sven G. Bilén[#]

Department of Electrical Engineering
The Pennsylvania State University, University Park, PA 16802

*Undergraduate student of
Department of Electrical and Computer Engineering
New Jersey Institute of Technology
Newark, NJ 07102

ABSTRACT

The LionSat nanosatellite requires a means of monitoring various sensor measurements distributed throughout the satellite. Data such as voltages, temperatures, and currents must be constantly reviewed to ensure mission success. A sensor board will be the central location for collecting and digitizing all of these measurements. It is necessary for this board to take in the analog signals, buffer them, and convert them to digital signals so that the information can be communicated to the flight computer. This article will discuss the debugging, development, and testing of a sensor board for LionSat. Various techniques for noise reduction and power requirements will be examined. Lastly, design testing and overall system operation will be discussed.

INTRODUCTION

LionSat, which stands for Local Ionospheric Measurements Satellite (Figure 1), is a two-year-old project at Penn State, on which students from diverse backgrounds and technical fields take part in an opportunity to develop a small satellite. The mission of the program is to apply classroom education to

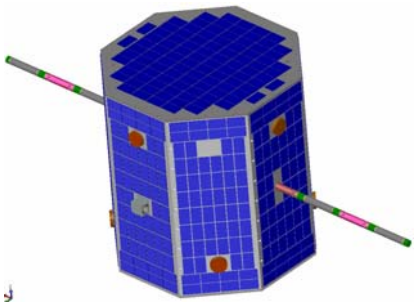

Figure 1. LionSat CAD drawing

[#] Faculty Mentor

126

design a flight-worthy spacecraft that has the capability of taking measurements in the ionosphere. The ionosphere is the part of the upper atmosphere where free electrons are found in a density that is sufficient enough to have a substantial effect on the propagation of radio frequency electromagnetic waves.[1]

While in space, LionSat will be making many measurements; this data must be collected, buffered, and digitally converted so that it can be communicated back to earth. Work on part of the hardware known as a sensor board is discussed in this paper. This work includes the design, troubleshooting, and testing of certain aspects of the sensor board as individual parts and as a whole. The use of Orcad Capture and Orcad Layout Plus has aided in the troubleshooting and redesign of the printed circuit board (PCB). While a new sensor board has not been produced, improvements to the design of the board have been made.

Redesigning the sensor board took into part the overall layout of the satellite. Connectors, wires, and power must be placed on the board in such a way to most efficiently utilize space within the satellite. Work with other members of the LionSat team has provided an overall understanding of the satellite as well as provided the ability to organize the layout of the sensor board. It is necessary to understand what typical ranges of measurements the various sensors will be making in order to accurately choose sensors and their buffering circuits.

While many integrated circuits exist to do the necessary tasks, it is an objective of this project to find the optimal parts that have been approved for use in space. Utilizing databases that have been provided by NASA, it is possible to cross reference desired design parts with approved parts. It is necessary to use parts that have been approved for use in conditions of greater than 5 krads and able to face temperature ranges from –20 to +80°C. Appropriate parts selection is necessary due to the conditions LionSat will be facing in orbit.

One of the first steps in beginning the redesign of the sensor board was to look into what work had been done previously on the board. The original layout was produced on a four-layer PCB and some problems were found when attempting to power the digital portion. After populating a certain part of the analog section of the board and populating all of the digital section of the board, programming of CPLD (Complex Programmable Logic Device) was not possible. It was understood that there were grounding issues on the PCB and initial testing did not find the problem. Some testing on the individual analog circuitry also did not turn up any signs of problems with the circuit designs.

EXPERIMENTAL DESIGN

One of the first steps in pursuing the identification of the problem was to make a list of possible errors in design or part failures. At first, it was necessary to look for shorts between analog ground and digital ground. Since the problem was that both ground and power were displaying five volts, this was the first issue to look into. Another problem could have been with a failed CPLD. If all of the pins on the CPLD were showing five volts, it could be a sign that the integrated circuit was not performing the way it should. After doing a visual inspection for

any solder bridges that could cause shorts, the PCB was powered up. Noticing that the current draw on the power supply was not excessive, this was an indicator that there was no short between ground and power.

The conclusion from this initial investigation was that the digital ground was not grounded at all. An oversight during the layout of the PCB had occurred and the digital ground was not connected to the ground layer of the PCB. Therefore, none of the digital parts were grounded to the power ground. Once this oversight was fixed, the CPLD was able to be programmed and a look into each part of the circuit board was taken. Each section of the sensor board was examined to be sure that it worked individually as well as part of the whole board. In order to do this, it was necessary to gather information on the types of sensors to be used, the ranges of measurements to be taken, and the specifications that are needed for the overall satellite.

The sensor board basically collects data from three types of sensors: current, voltage, and temperature sensors. During the experimental stages, it was necessary to design and build each of these circuits and test them with conditions that the circuits would face in the finished satellite. Besides looking into each of the sensor circuits, a look into the buffer circuits as well as the analog to digital converter circuit was necessary. Figure 2 shows a block diagram of the overall sensor board as well as the setup used in order to make sure the individual parts of the board worked.

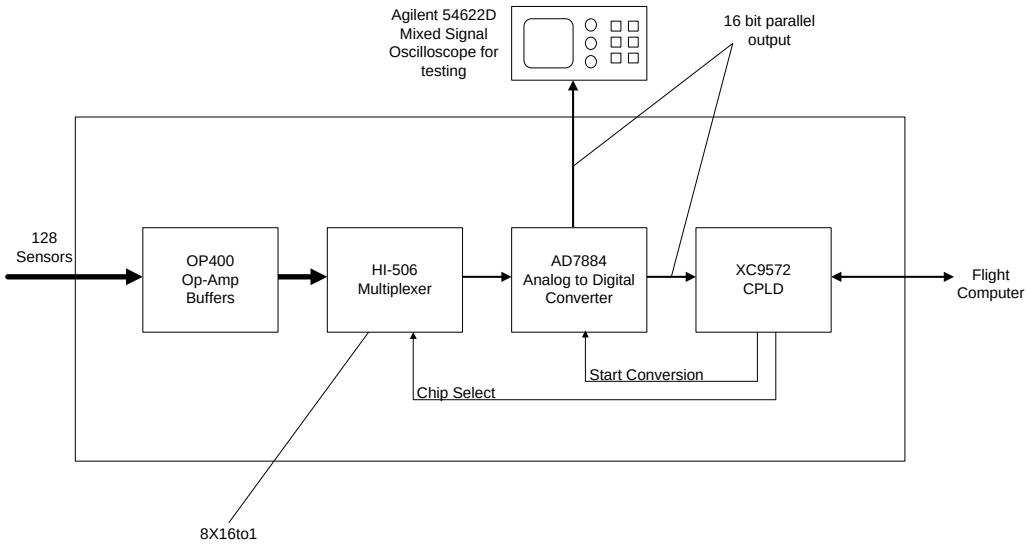

Figure 2. Sensor board block diagram

An important portion of the sensor board is the analog-to-digital converter (ADC). As noted in Figure 2, the ADC used in the design is the AD7884. This 16-bit parallel output ADC is known for high speed conversion and low power consumption.[2] Without this part, the flight computer would not be able to read any measurements. With this in mind, it was decided to take a close look into all aspects of the ADC. One of the necessary tasks was to compare specifications of

different candidate parts for signal conditioning. While the AD817 is the operational amplifier recommended in the ADC data sheet, it was necessary to look into op-amps with better noise ratings. Several op-amps, including the AD8608, OP484, and OP467, were promising. These are all high speed op-amps with very good noise ratings.

The analog-to-digital (A/D) test board that was previously used (shown in Figure 3) was not ideal since it only utilized a single-sided copper board. Figure 4 shows the schematic of the A/D test board circuit used in this work in order to test the new operational amplifier. As opposed to the initial A/D, the new test circuit is on a two layer board with the bottom layer being divided into a digital ground and analog ground. The addition of the second layer provides for better grounding and greater noise reduction. The main reason for the new board is to test a new op-amp before placing it into the final design, as well as to generate a design that will provide low noise at its output. Figure 5 shows the second A/D test board. It is possible to see that an effort has been made to reduce the area of the board and create a layout that is similar to the end result.

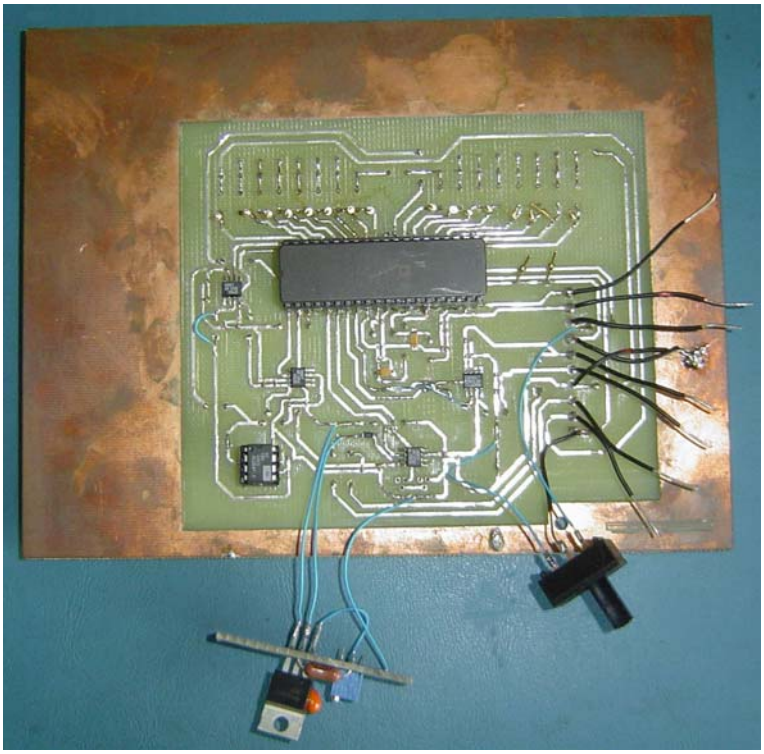

Figure 3. First analog-to-digital test board

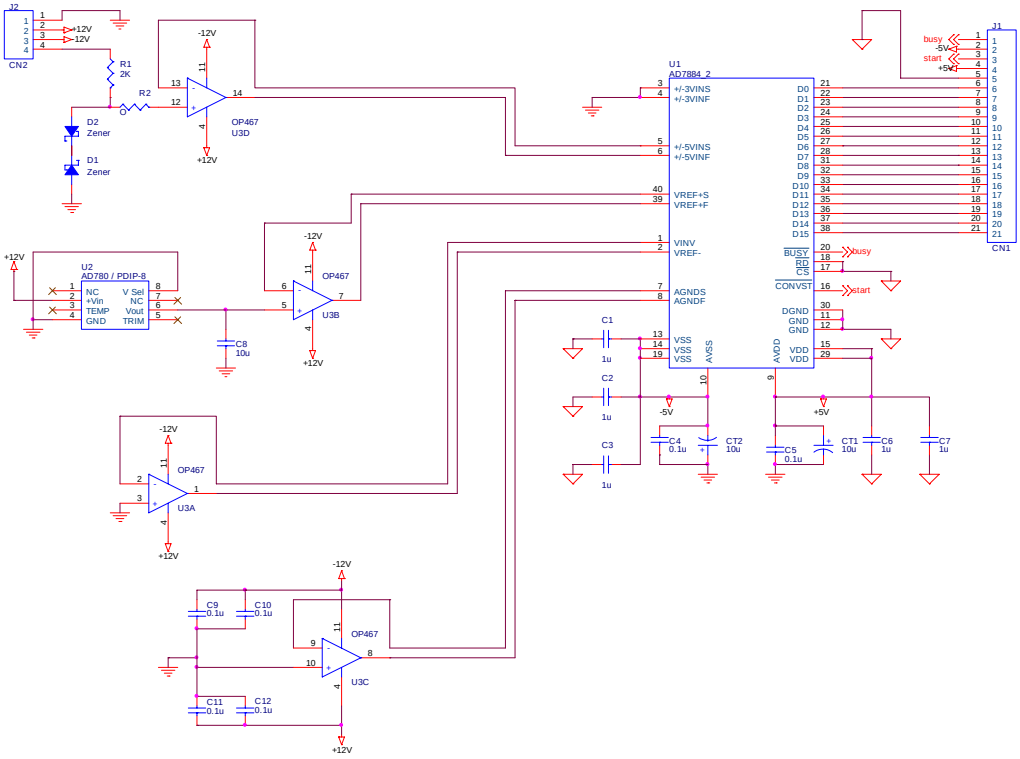

Figure 4. Second analog-to-digital test circuit schematic[#]

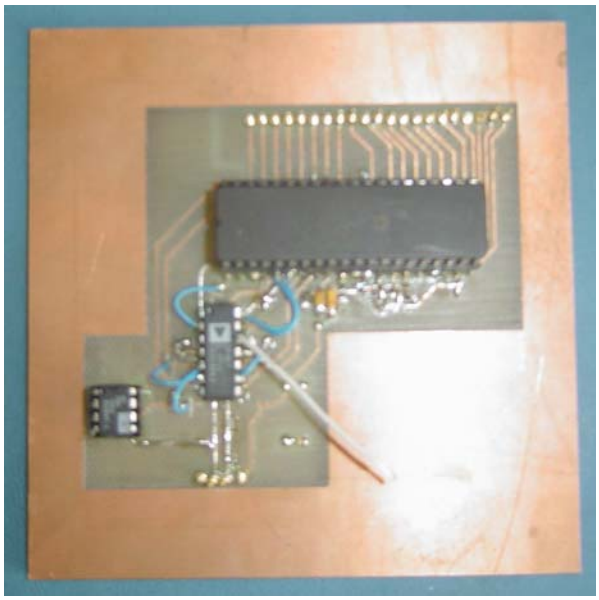

Figure 5. Analog-to-digital test board used in this work

[#] This revision based on work done by LionSat member Yashar Fakhari

RESULTS

As a result of searching for an op-amp with a better noise rating, it was discovered that the AD817, which was used in the first design of the sensor board, is not space rated. Upon examining several candidate op-amps, it was possible to select one that appeared to be best suited and do practical testing with it. Another advantage of looking into other op-amps was different package types. Table I shows the various specifications that were considered while trying to choose an op-amp.

Table I. Comparing possible operational amplifiers

Op-Amp	Noise	# of Amplifiers	Space Rated	Temp. Range
AD817[3]	15 nV/rtHz	single	no	-40 to +85°C
OP467[4]	6 nV/rtHz	quad	yes	-55 to +125°C
AD8608[5]	8 nV/rtHz	quad	no	-40 to +125°C
OP484[6]	3.9 nV/rtHz	quad	no	-40 to +125°C

After gathering information on a few low noise op-amps, it was evident that the OP467 was the only one that should be investigated further. The OP467 satisfies the requirements of radiation testing as it has been tested by the NASA Goddard Space Flight Center.[7] The selected op-amp also has very good noise and temperature ratings. From the design point of view, since the OP467 is available in a quad package, the new op-amp also utilizes less space than the previously used AD817.

Testing of the OP467 using the A/D test board (Figure 5) provided promising results. Testing done with the AD817 showed seven bits of noise on the output of the ADC, while using the OP467 only two bits of noise were apparent on the output of the 16-bit ADC. Realizing that a single bit represents 0.153 mV, the fluctuation of only the last two bits is negligible.[2] With these results, it was possible to proceed with developing new schematics and designing a new board layout for the sensor board as a whole.

By working with another member of the LionSat team, it was possible to redesign the overall layout of the sensor board for noise reduction, space savings, and efficiency. It became clear that there was more to consider than placing parts randomly. In order to make everything work, it was necessary to find a place for each of the three-hundred-plus wires that would be coming to the sensor board. Realizing that structure design would ultimately dictate where parts could be placed, a new layout beginning with placing connectors was started. Utilizing the exploded CAD view of LionSat, shown in Figure 6 above, it was possible to realize where wires should be routed and where parts should be placed. Table II shows where different sensors are coming from as well as how many wires are needed for each of those areas. While the final layout is not complete, it is

completely organized and the schematics drawn. The final layout will be a four layer board: two routing, one power, and one ground layer.

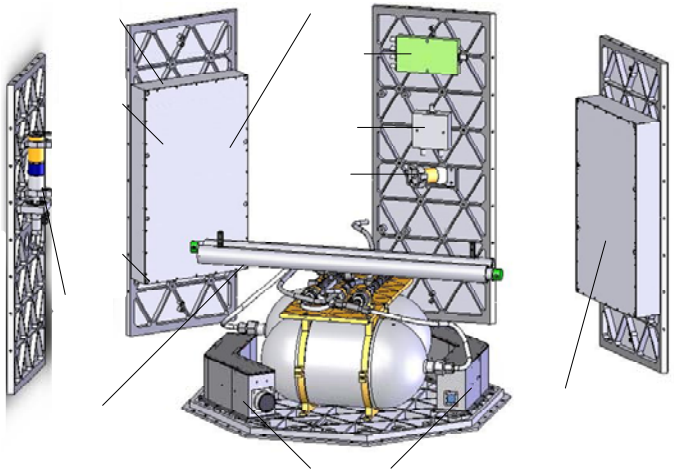

Figure 6. Exploded view of half of LionSat

Table II. Sensor measurements distribution

Sensor	# of pins	Location
Batteries	31	Bottom
Booms	14	Front
Flight Computer	49	Front
GPS	8	Top
Gyro	9	Top
Hybrid Plasma Probe	14	Bottom
Magnetometer	16	Top
Power Box	13	Top
Solar Panels	80	Top
Thruster	13	Bottom
Torque Rods	23	Top
Transceiver	16	Top
Voltage Buses	26	Top
Xe Tank	15	Bottom
Total:	327	

CONCLUSION

While the original goal of completing a new layout of a sensor board was not met, various obstacles that will aid in the final design have been overcome. Grounding and programming issues of the CPLD have been solved. The general layout of sensors, connectors, op-amps, and various parts has been planned. New parts that meet specifications such as noise reduction and radiation survivability have been selected and will go into the new board design. These results, along

to

with further planning, will provide the LionSat team with a flight-worthy sensor board.

ACKNOWLEDGEMENTS

I would like to thank my faculty mentor, Professor Sven Bilén for constant guidance and assistance throughout the entire nine weeks. I would also like to thank Brendan Surrusco, LionSat Project Manager, and the entire LionSat team for their patience in answering my endless questions and for their assistance in my work. Thank you to Professor Mark Wharton for meeting with me to discuss the A/D on such short notice. Thank you to Bruce Knoll for bending over backwards to get me the tools and the help I needed to get my test board milled out.

I would also like to thank those involved with the Pennsylvania State EEREU program, specifically Linda Becker, Amanda Skrabut, Professor Andy Lau, Professor Ken Jenkins, and Professor Ruyan Guo. The preceding provided for a great educational and research experience.

This material is based upon work supported by the National Science Foundation under Grant No. EEC-0244030.

REFERENCES

1 LionSat Website. Pennsylvania State University. July 2005. <http://www.courses.psu.edu/ee/lionsat/LionSat_files/SubPages/about.htm>

2 LC^{2}MOS 16-bit, High Speed Sampling ADC Rev E. AD7884. *Analog Devices*. February 2003. <http://www.analog.com/UploadedFiles/Data_Sheets/49198388AD7884_5_e.pdf>

3 High Speed, Low Power, Wide Supply Range Amplifier Rev B. AD817. *Analog Devices.* June 1995. <http://www.analog.com/UploadedFiles/Data_Sheets/289066266ad817.pdf>

4 Quad Precision, High Speed Operational Amplifier Rev E. OP467. *Analog Devices.* March 2004. <http://www.analog.com/UploadedFiles/Data_Sheets/711197792OP467_e.pdf>

5 Precision Low Noise CMOS Rail-to-Rail Input/Output Operational Amplifier Rev D. AD8608. *Analog Devices*. May 2004. <http://www.analog.com/UploadedFiles/Data_Sheets/141253328AD8605_6_8_d.pdf>

6 Precision Rail-to-Rail Input and Output Operational Amplifiers Rev B. OP484. *Analog Devices*. September 2002. <http://www.analog.com/UploadedFiles/Data_Sheets/390492658OP184_284_484_b.pdf>

7 NASA Goddard Space Flight Center radiation test data. July 2005. <http://radhome.gsfc.nasa.gov/radhome/RadDataBase/RadDataBase.html>

PIEZOELECTRIC ENERGY HARVESTING USING DIFFERENT APPROACHES INCLUDING CONTROL SYSTEM

Mintiwab Sahele*, Yiming Liu+, Heath F. Hofmann#

Department of Electrical Engineering
Pennsylvania State University
University Park, PA 16802

*Undergraduate Student of
Department of Electrical Engineering
New Jersey Institute of Technology
Newark, NJ 07102

ABSTRACT

There is an interest in developing electronic devices which do not require wires, such as wireless sensors. However, powering these devices wirelessly is a big challenge. Batteries are one solution to power these devices, except that the energy stored in batteries is not infinite. Current research if focused on extracting electrical energy from the force exerted on a piezoelectric device, placed under a shoe during walking or running or from mechanical vibrations, and supply it to the battery. This paper presents an energy harvesting comparison between full-bridge and half-bridge diode rectifiers, and also an energy harvesting technique with active power electronic circuitry which will control the voltage across the piezoelectric device. In the active approach the piezoelectric device is connected to the half bridge transistor circuit. The circuit will be controlled using a pulse-width modulation approach to generate higher power levels.

+ Graduate Mentor
# Faculty Mentor

 134

INTRODUCTION

Piezoelectric materials, such as PZT (lead-zirconate-titanate), have the ability to change mechanical energy into electrical energy. Because of this characteristic of the material, researchers have found it applicable to extract electrical energy from the force exerted on a piezoelectric devise placed under a shoe during walking, running or from vibration structures. Since technology is providing more and more portable electronic devices which we can take anywhere, it would also be desirable to power them without running out of electrical energy. The objective of energy harvesting is to create an alternative power source which will replace batteries, or at least to prolong the battery life. An example of an application that would benefit from this supply is a foot-powered radio-frequency identity tag[1].

Before 1881 the Curie brothers were able to demonstrate extracting electricity by applying stress to a piezoelectric device. Since then the piezoelectric device has gone through many significant developments in terms of its strength, flexibility and other qualities. This smart material has been a common choice to harvest energy. The piezoelectric device can be modeled as a voltage or current source with internal impedance. Assuming a resistive load is connected in parallel with the PZT device, to assure a maximum power output the resistive load should be set to equal the magnitude of the internal PZT impedance. This method is often used to evaluate the energy conversion capability of the PZT material. Kasyap et al[5,] attached a PZT to a vibrating beam and collected the energy harvested by using a fly back converter by running the piezo at resonance to get 20% efficiency. Other researchers proposed to optimize the power level by connecting an AC-DC rectifier that will convert the AC voltage coming from the PZT and directly charging a battery that needs a DC signal. However, this method is non-optimal. Placing a DC-DC converter between the rectifier out put and the battery would be able to optimize the charging process.[3.] A control algorithm was created to achieve a maximum current flow into the battery. This method reveals that a DC-DC converter results in more than four times the amount of power level than with direct charging of a battery across the rectifier circuit.

The purpose of this paper is to compare the performance of half-bridge and full-bridge diode rectifiers in electrical energy harvesting, and to develop a control algorithm to generate higher power levels using a half-bridge transistor circuit. This circuitry will be connected to the piezoelectric device. The purpose of this circuit is to control the voltage across the piezoelectric device. This can be done by controlling the MOSFETs inside the circuit by turning them “on” and “off”, like a switch. This approach is known as “Pulse-Width Modulation.” It is a powerful technique for controlling analog circuits with a processor’s digital outputs. PWM works by making a square wave with a variable on-to-off ratio. In a controllable switch we desire a small leakage current in the off-state and a small on-state voltage to minimize on-state power losses, and short turn-on and turn-off times will allow the device to be used at high switching frequency.

EXPERIMENTAL DESCRIPTION

Mathematical Model

The fundamental property of piezoelectric materials is their ability to generate charge from an applied stress. The constitutive equations are as follow

$$q = Cv + df_p \tag{1}$$

$$x = \frac{f_p}{k} + dv \tag{2}$$

Where q is the charge displaced across the piezoelectric element v is the voltage across the terminals of the piezoelectric device, x is the displacement of the device, and f_p is the total force on the piezoelectric element. The parameter C is the electrode capacitance of the device, d is the piezoelectric coefficient, and k is the mechanical stiffness of the device. The open-circuit voltage across the device (assuming q=*0*) is therefore given by:

$$v = \frac{-d}{C} f_p \tag{3}$$

Physical Experiment

Since the magnitude of the voltage generated by the PZT is dependent upon the force applied on it, we started our experiments by testing the piezoelectric composite, with properties listed in table I, by applying different amounts of mechanical forces with a frequency of 10Hz.

Table I. Properties of piezoelectric element

Material	PZT 5A1
PZT fill factor	Approx. 50%
Thickness	250 μm (6MHz)
Usable area	20mm x 20mm

The piezoelectric element was modeled as a current source in parallel with its internal capacitor and connected to a full bridge and half bridge rectifiers, as shown in figures 1(a) and 1(b) respectively, to compare the energy harvesting power level. Both circuits were built by using a 10μF capacitor to filter the output of the rectifier, a 21.77 K Ω resistor to measure the current passing to the battery, and IN 914 type diodes. By applying different levels of forces with frequency of 10 Hz, the out put power flow was compared.

A half-bridge transistor circuit, consisting of an inductor, two MOSFETs, capacitors, and resisters, was built to compare the power level with the half-bridge diode rectifier.

The control code for this active circuit was developed in MATLAB. See figure 2 for a block diagram. The force input signal was filtered by an analog filter to get a DC component. This signal was multiplied by a phase-locked loop, which is a closed loop frequency control system. Their product was blocked by a switch which has a 0.9 and -0.9 threshold levels for the upper and lower one respectively. The output signal was checked using an oscilloscope.

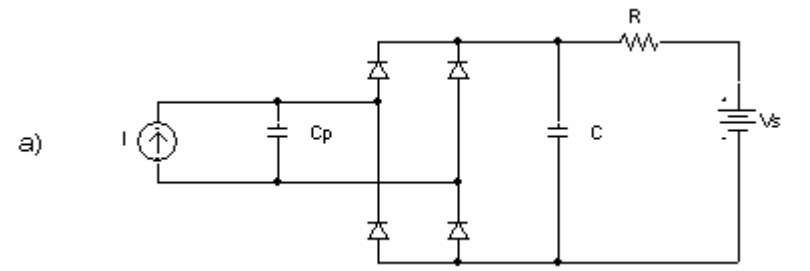

Figure 1(a): Full bridge rectifier in parallel with PZT

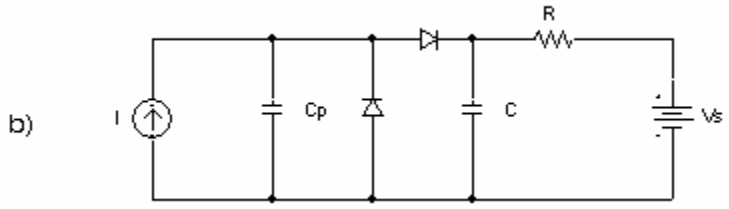

Figure 1(b): Half-bridge rectifier in parallel with PZT

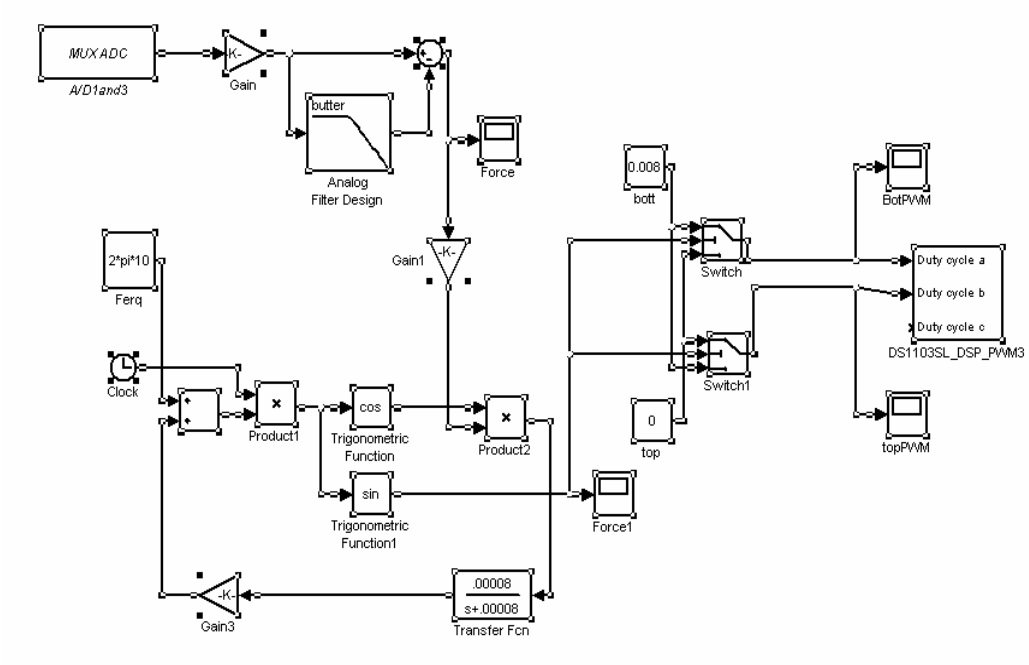

Figure 2: Controller implementation in Simulink.

RESULTS

The piezoelectric device open-circuit voltage was measured for seven different values of mechanical forces. As expected, the PZT output voltage was roughly proportional to the force applied. The result is shown in figure 3.

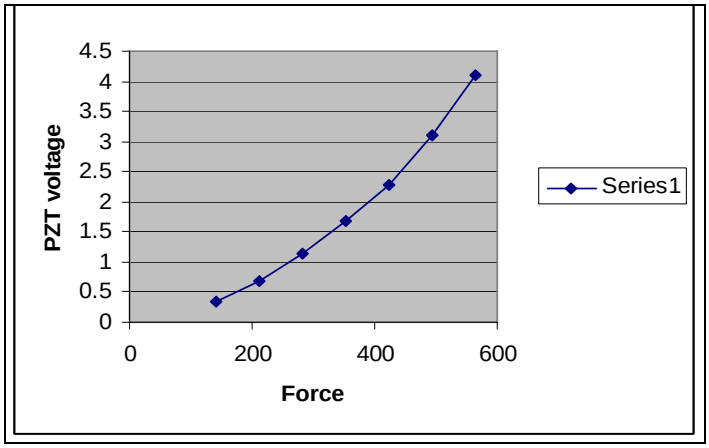

Figure 3: Force vs. PZT voltage.

The half-bridge and full-bridge diode rectifiers were tested with RMS values of 400 Lb f and 250 lb f force, with a frequency of 10Hz. The half-bridge diode rectifier showed a better performance for energy harvesting power levels

because of the decrease of voltage drops on the additional two diodes in the full-bridge diode rectifier. The comparison is shown in figure

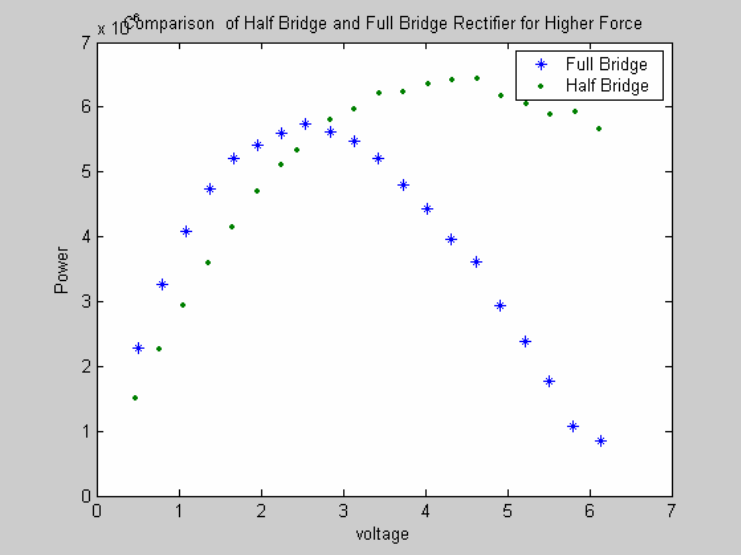

Figure 4: Comparison of half bridge and full bridge rectifier for higher force.

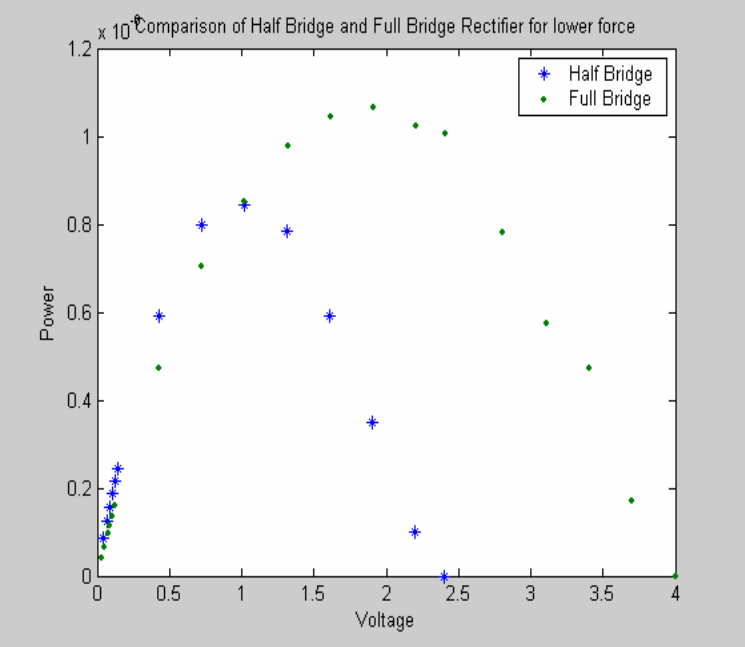

Figure 5: Energy harvesting Comparison between half bridge and full bridge circuits

A PZT composite device was used to test the active circuitry. This device has an open-circuit output voltage of 1.72V RMS for a peak-to- peak force of 64lbf with a frequency of 10 Hz. The same composite was connected to the half bridge to compare its energy harvesting power level with the active circuitry. The experimental result shows that the active power electronic circuitry increases the harvested power level by 4.5 times the rate of the half-bridge diode rectifier alone. Figure 6 illustrates the result.

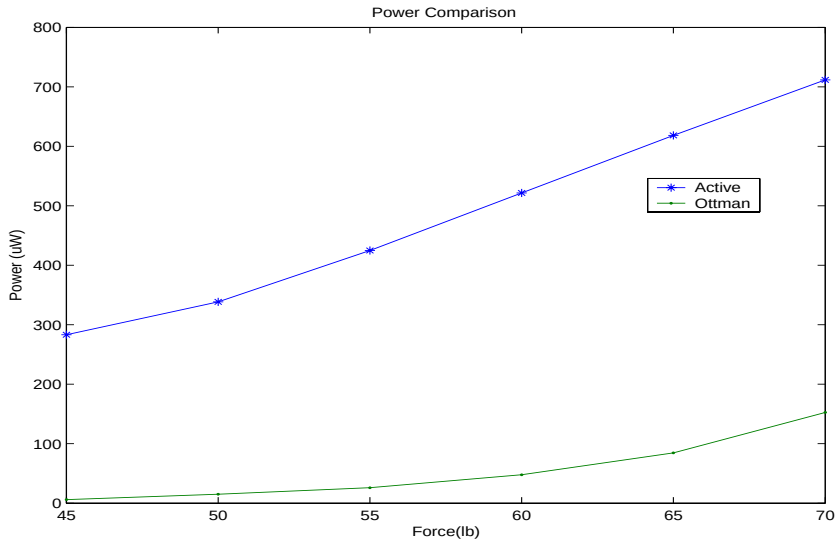

Figure 6: Power comparison result.

DISCUSSION

It can be noted that the voltage generated by the PZT device is directly proportional to the force applied on it. The observed result also confirm the theory. Since the Piezoelectric material has a considerable impact on achievable performance of energy harvesting, effort should be made to improve its voltage level for less force.

The half-bridge diode rectifier was preferable compared to the full-bridge diode rectifier due to the reduction of voltage drops due to diodes. However, the active circuitry harvested the most power. The harvested power level was 4.5 times better than a half bridge rectifier alone.

CONCLUSION

This research presents energy harvesting comparisons between a full-bridge diode rectifier, a half-bridge diode rectifier, and active circuitry which consists of a control system and a half-bridge transistor circuit has been investigated. The comparisons were performed experimentally by applying a mechanical force to a piezoelectric composite device. Comparing the two diode rectifiers, a better power level has been achieved by using the half bridge rectifier. When it comes to the comparison between the half bridge rectifier with the active

circuitry , the half bridge active circuitry with control algorithm harvested energy at 4.5 times bigger than a half bridge rectifier alone.

ACKNOWLEDGEMENT

I would like to thank Dr. Heath Hofmann for his guidance, help and patience. This material is based upon work supported by the National Science Foundation under Grant No. EEC-0244030.

REFERENCES

[1] Geffrey K. Ottman, Heath F. Hofmann and George A. Lesieutre, "Optimized Piezoelectric Energy Harvesting Circuit Using Step-Down Converter in Discontinuous Conduction Mode," *IEEE Transactions on Power Electronics*, **18**(2) 696-703(2003).

[2] Daniel Guyomar, Adrien Badel, Elie Lefeuvre, and Claude Richard, "Toward Energy Harvesting Using Active Materials and Conversion Improvement by Nonlinear Processing" *IEEE Transactions on Ultrasonics, Ferroelectrics, and Frequency Control, 52(4) 584-595(2005).*

[3] Geffrey K. Ottman, Heath F. Hofmann and George A. Lesieutre, "Adaptive piezoelectric energy harvesting circuit for wireless remote power supply," *IEEE Transactions on Power Electronics*, **17** (5) 669–676 (2002).

[4] P. Glynne-Jones, S.P. Beeby and N.M. White, "Towards a piezoelectric vibration-powered microgenerator," IEEE Proceedings-Science, Measurement and Technology, **148**(2) 68-72 (2001)

[5] Niell G Elvin, Alex A Elvin and Myron Spector, "A Self-Powered Mechanical Strain Energy Sensor," Institute of Physics Publishing <http://ej.jop.org/links/942/dbcqrKCVFXK4Vg,OVG70GA/Sm1214.pdf>

[6] Timothy Eggborn, "Analytical Models to Predict Power Harvesting with Piezoelectric Materials," Virginia Polytechnic Institute and State University <http://Scholar.lib.vt.edu/theses/available/etd-o5192003-150202/unrestricted/EggbornThesis1.pdf>

NITROGEN DOPING OF TITANIUM OXIDE VIA ANODIC OXIDATION

Kong C. Tep*, Karthik Shankar[+], Craig A. Grimes[#]

Department of Electrical Engineering
Pennsylvania State University, University Park, PA 16802

*Undergraduate Student of
Department of Electrical Engineering
Michigan State University
East Lansing, MI 48823

ABSTRACT

Titanium Oxide (TiO_2) is a large band gap semiconductor whose catalytic properties, relatively low cost and chemical inertness render it suitable for use in solar photoelectrochemical cells.[1] However, attaining useful energy conversion efficiencies requires a reduction in the electronic band gap of TiO_2. This work investigates ways to incorporate nitrogen atoms into titanium oxide nanotubes and studies the resulting effect on the band gap and the photoelectrochemical properties. The incorporation of nitrogen on titania (TiO_2) is accomplished during the anodization process by introducing nitrogen ion bearing species into the electrolyte such as nitric acid (HNO_3), ammonium hydroxide (NH_4OH), ammonium fluoride (NH_4F), and triethylamine ($C_6H_{15}N$). The presence of nitrogen was verified by X-Ray Photoelectron Spectroscopy (XPS).

In nitric acid bearing electrolytes, XPS revealed shorter anodization periods to result in greater nitrogen incorporation. Meanwhile, Scanning Electron Microscopy (SEM) showed formation of an interesting nanotubular structure in $C_6H_{15}N$ and NH_4F anodization bath. Nitrogen was successfully introduced into the TiO_2 lattice replacing oxygen atoms. As a result, a significant shift of TiO_2 band edge was seen by Ultraviolet-Visible (UV-Vis) Spectroscopy, and change in photocurrent generated upon solar illumination was observed.

[+] Graduate Mentor
Faculty Mentor

INTRODUCTION

In search of better semiconductors for application in photochemical cells, many have been focusing on transition metal oxides such as Tungsten oxide (WO_3), Zinc oxide (ZnO), titanium oxide (TiO_2), iron oxide (Fe_2O_3),[2] etc. Of these, TiO_2 offers great promise – it has been shown that TiO_2 is very stable and corrosive resistant, perfectly suitable as a photochemical cell electrode.[1] While TiO_2 is an N-type material, it could be used to convert photons into chemical/electrical energy by generating electrons and holes under the presence of UV light.[3] The holes perform work at the semiconductor-electrolyte interface by oxidizing suitable redox species in the electrolyte while the electrons flow to the back contact through the external circuit. In a solar cell, the redox reaction is a reversible one and no net chemical change occurs so that the photocurrent generated by the cell is available as electricity. In a photoelectrochemical cell, the photogenerated charge carriers convert solar energy directly into chemical energy by conducting an irreversible chemical reaction such as the splitting of water into oxygen and hydrogen.[4] In a water-splitting cell, Oxygen is generated at the TiO_2 semiconductor anode while Hydrogen is generated at the platinum cathode.[5]

However, TiO_2 is still far from becoming a practical semiconductor for photovoltaic cell surpassing mono and poly crystalline silicon. Despite its cost, making highly efficient photochemical cells using TiO_2 is a challenge unless two issues are addressed. The achievement of high-efficiency requires a suitable architecture that minimizes the recombination of the photogenerated electron-hole pairs by separating them quickly. Such architecture ought to have a high surface area in contact with the electrolyte species and a structure whose dimensions are smaller than the recombination length of the charge carriers.[6] The second issue involves the large band gap of Titania (3.0-3.2 eV) compared to other oxides mentioned above.[4] This means that only about 5% of the sunlight (UV wavelengths) can be absorbed by TiO_2 and converted into useful chemical and electrical energy.

Many research groups are engaged in efforts to find an optimal architecture for TiO_2 photoelectrodes. Since the recombination length of holes in titania is about 100 nm, an optimal architecture has to possess critical dimensions in the same length range and needs to be nanostructured by definition.[7] Titania nanopores, nanowires, nanorods, and nanotubes have been fabricated via different methods by the Grimes Research Group. In 2004, they reported on TiO_2 with regular ordered nanotubular architecture, fabricated through anodic oxidation, with less than 20% of the photogenerated carriers being lost to recombination (quantum efficiency greater than 80%) under the exposure of monochromatic UV light at 337 nm.[3] Since the absorbed spectrum is very limited to the UV wavelengths, the overall efficiency is relatively low compared to the conventional silicon oxide (SiO_2). Now, it is apparent that the remaining challenge is to lower the band gap of TiO_2, hence increase the photon absorption.

According to a recent article in Science,[8] nitrogen doping of TiO_2 narrows its optical band gap thus enhancing the absorption of visible light. Our work

emphasizes on the techniques of nitrogen incorporation of TiO_2 and the investigation of its photoresponse to visible light spectral irradiation.

EXPERIMENTAL DESCRIPTION

Two methods were carried out in this experiment, the incorporation of nitrogen into titanium foil while fabricating oxide nanostructure and the incorporation directly on pre-fabricated titanium nanotubes. Both methods were done via anodic oxidation.

Method One: Nitrogen incorporation into TiO_2 while fabricating nanostructures

Titanium foil (0.25 mm thick, 99.7% purity purchased from Aldrich Corporation, Milwaukee, WI) was prepared by rinsing it in acetone and water. The anodization was carried out potentiostatically using a platinum counter electrode (99% purity Alfa-Aesar Corporation, Ward Hill, MA). The titanium foil was attached to the anode as seen in **Figure 1**; hence it is called anodic oxidation.

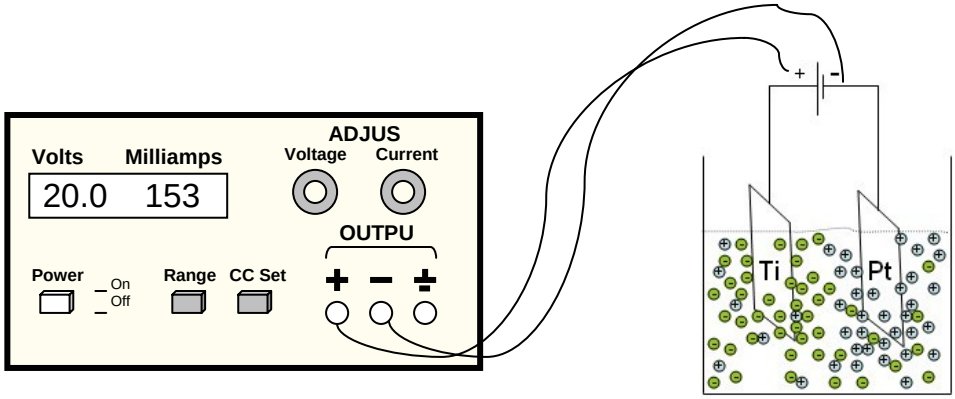

Figure 1 Schematic of the anodization experiment setup.

The electrolyte (Potential of Hydrogen [pH] = 4.5) was made out of acid and base solutions, containing fluoride ions which are essential for the development of any porous structure. For purposes of nitrogen doping, suitable nitrogen bearing ionic species were included in the anodization bath. The species used included triethylamine ($C_6H_{15}N$), nitride (NO_3^-) and ammonium (NH_4^+) both individually and in combination. Among these ions, NO_3^- ions resulted in the highest amount of nitrogen incorporation.

After the anodization was completed, the N-doped TiO_2 sample was annealed at 500^{o}C-600^{o}C in an oxygen ambient furnace as illustrated in **Figure 2**. XPS and SEM were used to confirm the presence of nitrogen in TiO_2 lattice and nanostructures respectively. Verifying these results, recorded Ultraviolet-Visible spectrum and tested photocurrent were compared to the normal TiO_2 photoresponse.

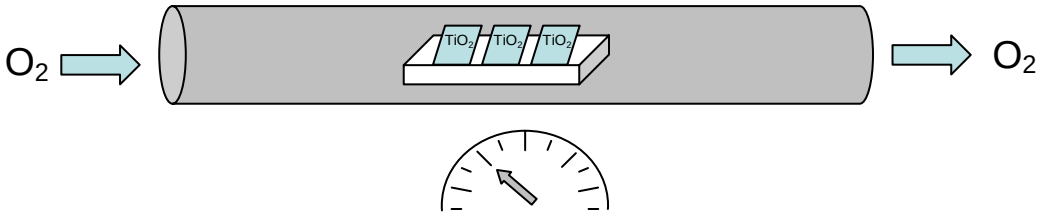

Figure 2 Oxygen ambient furnace setup.

Method Two: Nitrogen incorporation into pre-fabricated titania nanotubes

Prior to the nitrogen incorporation, titania nanotubes were fabricated via techniques as described by Gong and co-worker.[9] The anodic oxidation was conducted via constant voltage across the platinum and titanium electrodes. The photocurrents of the nanotubes before and after nitrogen doping were compared.

RESULTS AND DISCUSSION

Method One

XPS showed that the greatest amount of doped nitrogen into TiO_2 was 7.7% when anodized for 2 minutes at 20V. **Figure 3** underlines the importance of the anodization period versus the amount of nitrogen incorporated. Longer anodization periods yielded less incorporated nitrogen. Nitrogen concentration decreases rapidly as the depth of TiO_2 increases (see **Figure 4**). Although nitrogen was clearly incorporated, the amount of nitrogen was still rather moderate in comparison to the desired amount of approximately 10%.

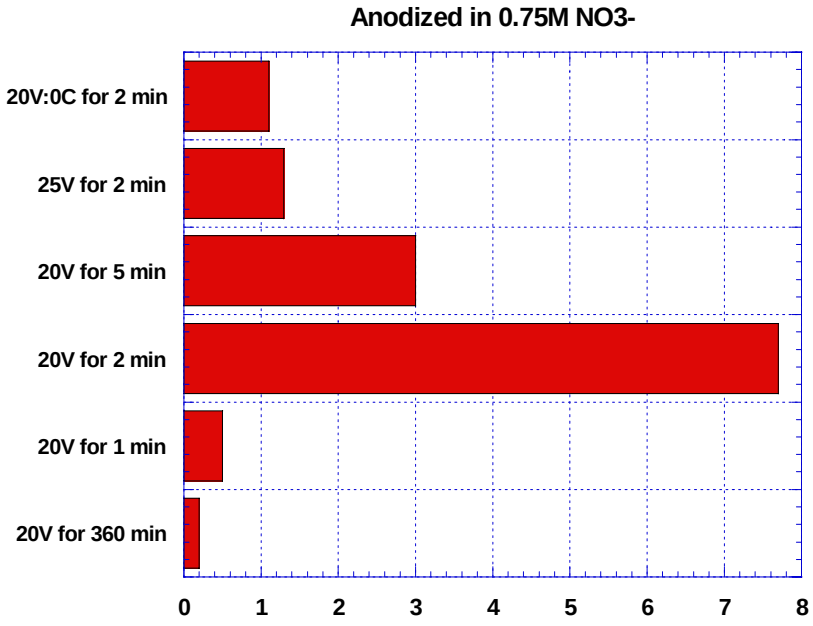

Figure 3 Nitrogen incorporated 10 nm from the surface (at %).

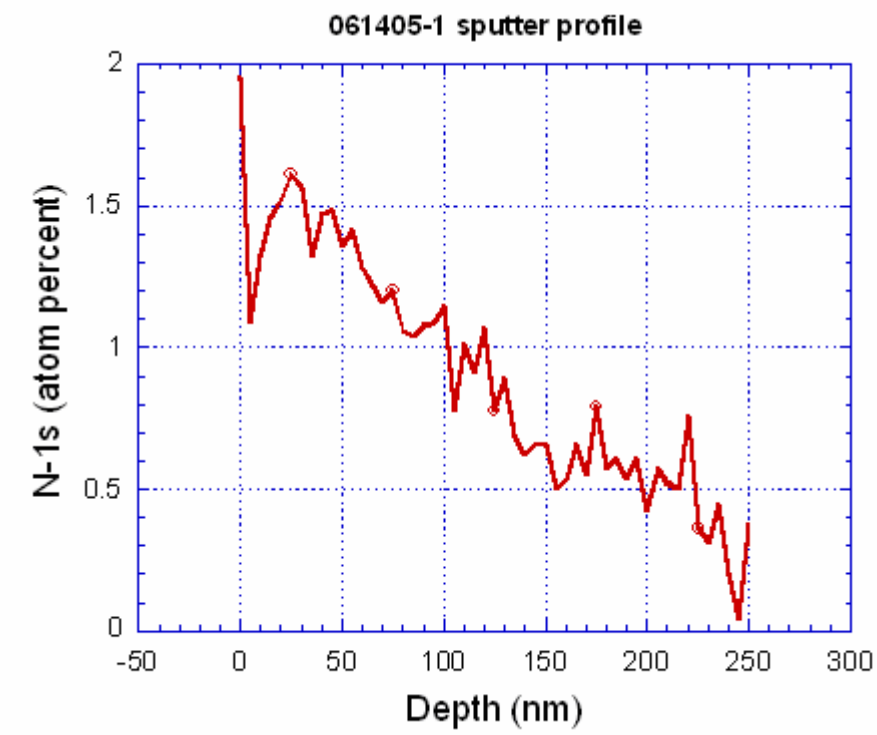

Figure 4 Distribution of nitrogen atom percent (%).

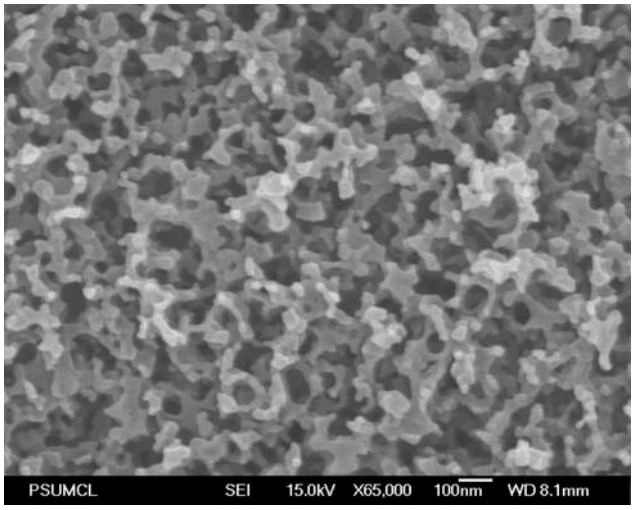

Figure 5 SEM image of the titania surface anodized in (NH_4F) electrolyte.

Meanwhile, nanostructures were studied using SEM after anodization. **Figure 5** shows the nanoporous structure with an average diameter of about 100 nm, attained by anodizing titanium foil at 60V for 17 hours in NH_4F electrolyte. Similarly, other electrolytes mentioned above showed comparable surface nanostructure. In particular, the nanotubular structure was observed after 1 hour

of anodization at 15V in $C_6H_{15}N$ plus hydrofluoric acid (HF). As seen in **Figure 6**, the average inner diameter of the tubes is approximately 30 nm.

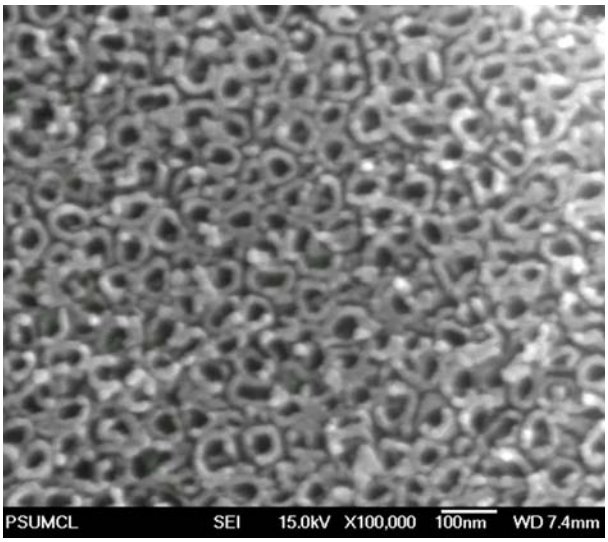

Figure 6 Titania nanotube arrays anodized in $C_6H_{15}N$.

Results from the NO_3^- electrolyte propounded another interesting concept – a combination of oxide layer and nanostructure could be accomplished by varying the pH concentration during anodization period. A steady change in pH concentration from 2 to 5 was observed during the 6 hours anodization. Consequentially, nanotube arrays were formed on top of a thick oxide layer (see **Figure 7**).

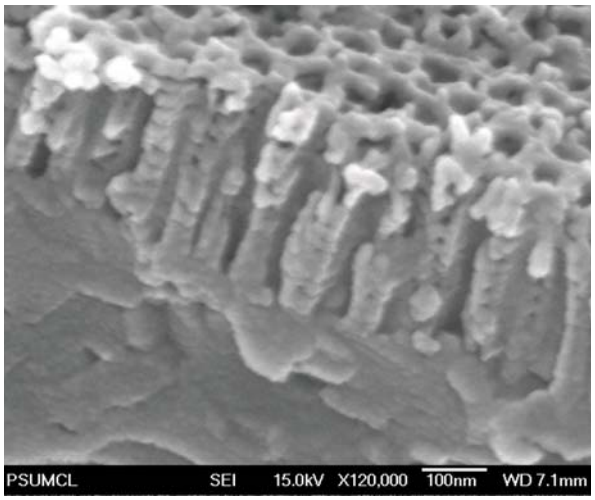

Figure 7 TiO_2 nanotubes fabricated in (NO_3^-) electrolyte.

According to XPS results, nitrogen atoms were mostly within nitride bonds (Ti-N). This bond is the primary factor for the increased visible spectrum photoelectrochemical activity[10] as illustrated in **Figure 8.** The band edge of TiO_2 was shifted to the right by 25 nm. **Figure 9** shows the dark and illumination currents of the sample whose sputter profile seen in **Figure 4**.

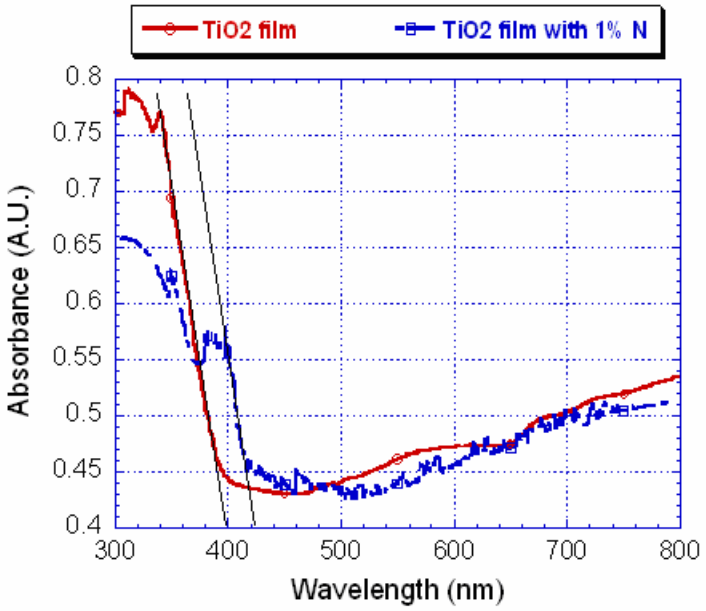

Figure 8 UV-Vis absorbed spectrum of TiO_2 and N-doped TiO_2

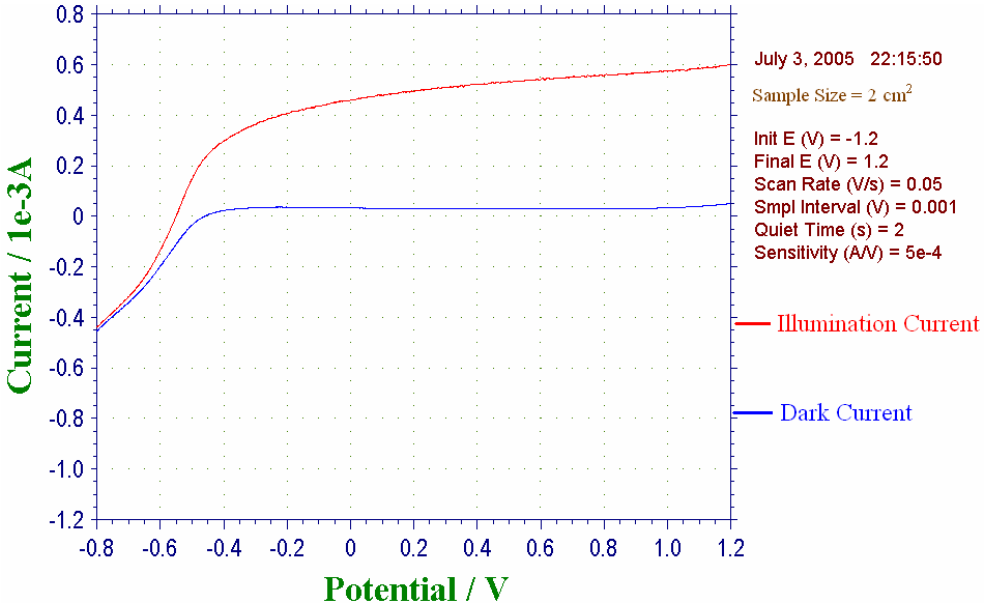

Figure 9 Photocurrent generated by N-doped TiO_2

Method Two

The photoresponse of titania nanotubes before and after the anodization are shown below in **Figure 10.** The difference between dark and illumination current is the photocurrent generated due to the light. As seen in the graph, it doubled after the anodization.

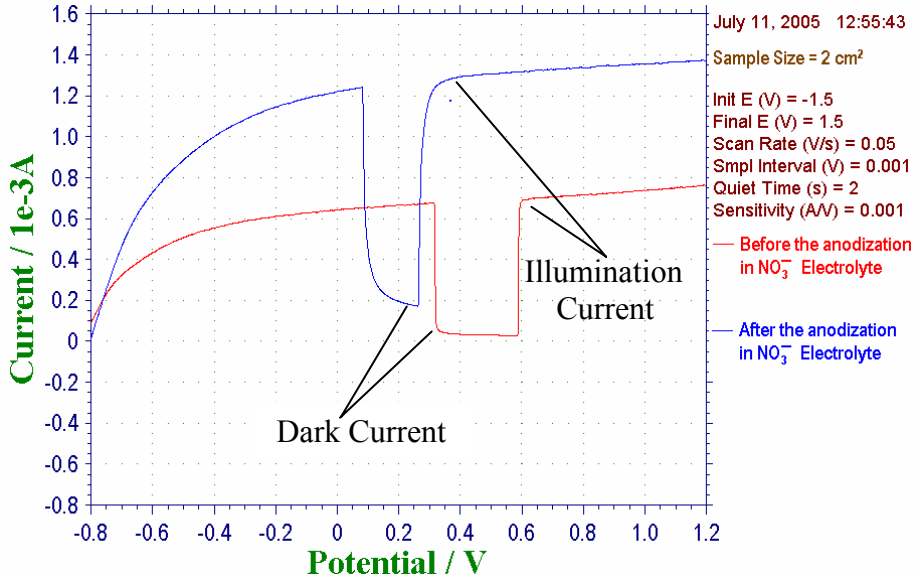

Figure 10 Photocurrent of before and after the anodization in NO_3^-

CONCLUSION

Nitrogen was successfully incorporated into titania nanotubes and thin films by use of nitrogen bearing species in the anodization bath. A bath containing NO_3^- ions was found to incorporate the largest amount of nitrogen into the TiO_2 lattice. This incorporation of nitrogen reduced the bandgap of TiO_2 as measured by Ultraviolet-Visible absorption spectroscopy and extended the photoresponse of titania into the visible by 25 nm. However, the length of the titania nanotube arrays fabricated in NO_3^- containing electrolytes was shorter due to the vigorous etching reaction of this ionic species. The flux of NO_3^- ions impinging on the electrode surface during the anodization process is directly proportional to the anodization current. As observed, the anodization current is largest at the beginning of the process and decreases exponentially with time. As a result, the greatest amount of nitrogen incorporation occurs in the first minute of the reaction.

In method two, the nitrogen incorporation improved the photocurrent by a factor of 2. However, the nanotubes were usually destroyed by the etching action of NO_3^- ions if kept too long in the electrolyte, limiting our effort to incorporate more nitrogen. Furthermore, nitrogen concentration at the surface saturates at the end of the anodization process. Addressing this hindrance, Rapid Thermal

Annealing (RTA) was exploited to help distribute newly incorporated nitrogen atoms, but this technique has a tendency to damage the sample. Hence, the resulting change in photocurrent was unremarkable.

In order to achieve greater improvement in photocurrent, a higher concentration of nitrogen in TiO_2 with longer nanotubular structures are necessary. Fulfilling these two competing factors still remains to be a challenge.

ACKNOWLEDGMENTS

This material is based upon work supported by the National Science Foundation under Grant No. EEC-0244030. The assistance of Dr. Mor with this project is gratefully acknowledged. Special thanks go to Dr. Grimes, Dr. Guo, Dr. Jenkins, and the Electrical Engineering Department of Pennsylvania State University for providing this research opportunity.

REFERENCES

1. T. Umebayashi, T. Yamaki, H. Itoh, K. Asai, "Band Gap Narrowing of Titanium Dioxide By Sulfur Doping," *Appl. Phys. Lett.* **81** (3) 454-456 (2002)
2. M. Yang, T. Yang, M. Wong, "Nitrogen-Doped Titanium Oxide Films As Visible Light Photocatalyst By Vapor Deposition," *Thin Solid Films* **1** (5) 469-470 (2004)
3. A. Fujishima and K. Honda, "Electrochemical Photolysis Of water At A Semiconductor Electrode" *Nature* **238**, 37, (1972)
4. M. Grätzel, "Photoelectrochmical Cells," *Nature* **414**, 338-344 (2001)
5. G. Mor, K. Shankar, M. Paulose, O. Varghese, C. Grimes, "Enhanced Photocleavage Of Water Using Titania Nanotube Arrays," *Nano Letters* **5** (1) 191-195 (2005)
6. J. Van de lagemaat, M. Plakman, D. Vanmaekelbergh, J. Kelly, "Enhancement Of The Light-to-current Conversion Efficiency In An n-SiC/solution Diode By Porous Etching," *Appl. Phys. Lett.* **69** (15) 2246-2248 (1996)
7. W.H. Lubberhuizen, D. Vanmaekelbergh, E. Van Faassen, "Recombination Of Photogenerated Charge Carriers In Nanoporous Gallium Phosphide," *Journal of Porous Materials* **7** (1-3) 147-152 (2000)
8. R. Asahi, T. Morikawa, T. Ohwaki, K. Aoki, Y. Taga, "Visible-Light Photocatalysis In Nitrogen-Doped Titanium Oxides," *Science* **293** (5528) 269-271 (2001)
9. Q. Cai, M. Paulose, O. Varghese, C. Grimes, "The Effect Of Electrolyte Composition On The Fabrication Of Self-Organized Titanium Oxide Nanotube Arrays By Anodic Oxidation," *J. Materials Res.* **20** (1) 230-236 (2005)
10. Y. Nosaka, M. Matsushita, J. Nishina, A. Nosaka, "Nitrogen-Doped Titanium Dioxide Photocatalysis For Visible Response Prepared By Using Organic Compounds," *Science and Technology of Advanced Materials* **6**, 143-148 (2005)

LOSS & DIELECTRIC PERMITTIVITY OF SMALL SAMPLES OF MATERIALS IN THE C BAND OF MICROWAVE FREQUENCIES

Stephen Tomko*, Shashnk Agrawal[+], and A. S. Bhalla[#]

Department of Electrical Engineering and Materials Research Institute
The Pennsylvania State University, University Park, PA 16802

*Undergraduate Student of:
Department of Computer Engineering
The Pennsylvania State University McKeesport
McKeesport, PA 15132

ABSTRACT

In trying to find suitable materials for the transmitting and receiving of microwave frequencies, useful for communications and data transfer, the dielectric permittivity of samples of varying composite ratios of BST to MgO are measured. The objective is to study these electrically tunable materials such that the loss of microwave energy due to absorption in the material and its transfer into a wasteful byproduct of heat is minimal. Also, variations in the orientation of the samples are examined to determine any noticeable changes in the dielectric properties of theses relatively isotropic composites. The method used is the cavity perturbation technique, based on the principles of the scattering effect, in a modified rectangular waveguide. These complex dielectric properties are measured in the 3GHz to 6 GHz range, under normal temperature and atmospheric conditions. Additionally, the technique is modified to make the measurement of an anisotropic dielectric material in the GHz range. A crystalline rod of SBN nonlinear material is used to test the modified waveguides capabilities of measuring the dielectric permittivity.

[+] Graduate Student
[#] Faculty Mentor

 151

INTRODUCTION

With the ever increasing amounts of data and communication applying more demand on the gradually decreasing quantity of open radio and microwave frequencies, new methods and materials are being studied to try reducing this problem. One idea is to use better, low-loss materials that will allow for greater accuracy, therefore reducing the amount of electromagnetic bandwidth per channel and freeing more of the electromagnetic spectrum. However, a more applicable approach is to use electrically tunable dielectrics, which have similar low-losses but with the added benefit of being adjustable to several clear and sharp frequencies.

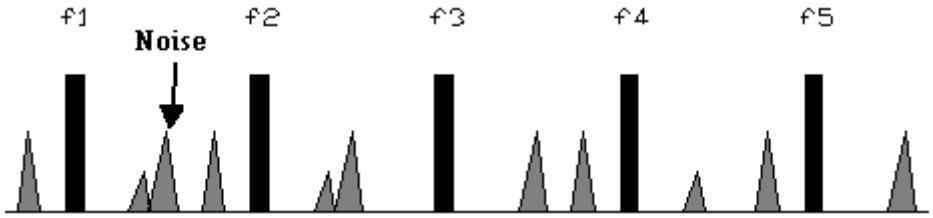

Figure 1: Real World Spectrum Band – At any given time, there can be multiple frequencies in a relatively narrow range of the electromagnetic spectrum in use. In addition, there is also useless noise generated from natural phenomena to stray electromagnetic radiation from electronic devices. In order to transmit or receive at a given frequency (for example, f3), there are two methods that can be taken:

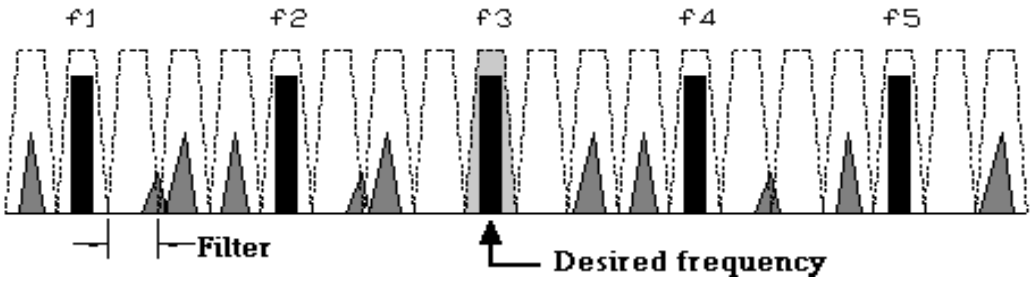

Figure 1a: Switched Filter Bank - In this manner, multiple filters would be required to cover the desired spectrum. In order to tune to a desired frequency, the appropriate filter would need to be turn on while the remaining turned off. This process can be very accurate but is not very practical.

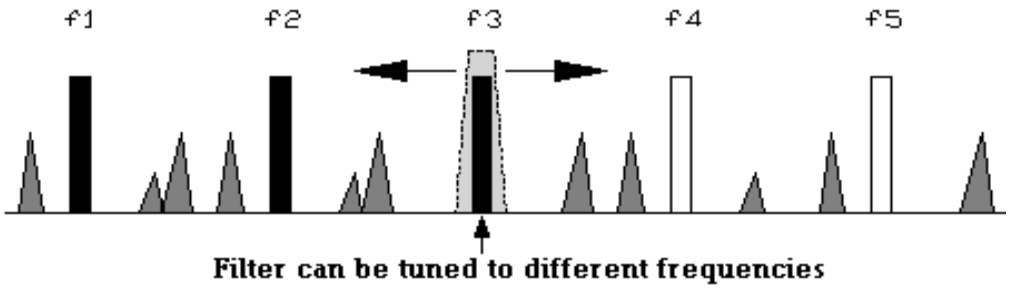

Figure 1b: Single Tunable Filter – Using an electrically tunable dielectric, a single filter can be made such that by applying different electric fields across the dielectric, the filter can be tuned to different frequencies. This process can offer comparable accuracy to that of a switch filter bank but is much more economically efficient.

The tunable dielectric material studied is $(BaSr)TiO_3$ (or BST). The high dielectric constant of these samples is reduced to approximately one hundred by the composite processing route of combining it with MgO. This not only decreases the dielectric constant of pure BST and the composite but also results in the composite maintaining similar losses as just BST due to the low losses associated with MgO. The resulting BST+MgO composite's dielectric constant now makes it useful in devices operating at microwave frequencies while still remaining electric field tunable; their dielectric constants can be varied by applying specific electric fields across the samples surface. Therefore, each tunable dielectric constant value corresponds to a specific resonant frequency, i.e. one resonator can efficiently be used different frequencies.

Since the composition of BST and MgO is, more or less, like an isotropic material, the dielectric constant of the sample is dependent on the ratio of the two composites, i.e. each different ratio should result in one and only one dielectric constant. The same method that can be used to test the dielectric of isotropic materials can also be extended to measure that of an anisotropic or nonlinear material. In this case, the dielectric constant can be changed by simply altering the orientation of the sample to the electromagnetic wave. The anisotropic material studied for testing this approach is $(SrBa)Nb_2O_5$ (or SBN).

The cavity perturbation theory using rectangular waveguides is a very simple method used to measure the dielectric permittivity of materials at microwave frequencies. By placing a sample at some known position within the specially designed cavity, applying a set range of microwave frequencies, and measuring the perturbation or changes in the resonant frequency and quality factor of the cavity, the dielectric properties of the sample can easily be calculated [2]. For measuring the dielectric constant of a nonlinear material, the cavity design is modified as shown in the following figure:

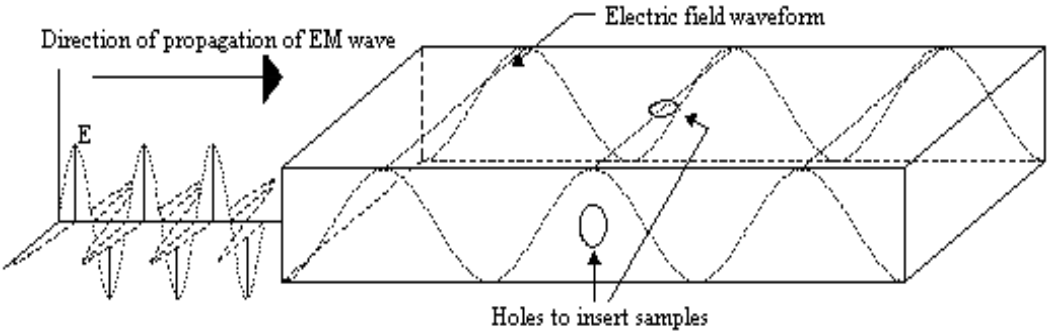

Figure 2: The direction of propagation of the electromagnetic wave through the cavity is parallel to the length and width of the waveguide. Even though an electromagnetic wave contains both an electric and magnetic field component, only the electric field is used in this experiment. A maximum electric field will always occur where the sample is inserted, in either one of the two holes.

The purpose of a waveguide is to allow for accurate measurement of electromagnetic frequencies (in this case, microwaves) by placing the wave in a controlled environment. The waveguide restricts the three-dimensional propagation of the wave to one dimension and does so with minimal losses to the energy of the wave. By introducing a sample material in the path of this controlled electromagnetic wave, three atomic level interactions can occur between the two elements: reflection, absorption, or transmission [1].

Reflection occurs at the surface of the material and is affected by the surface roughness or smoothness of the material at the microscopic level and also by its physical characteristics. As an electromagnetic wave comes into contact with a new medium, the frequency of the wave has an impact on the electrons of the material causing them to vibrate. If the frequency of the electromagnetic wave is not the natural frequency of the electrons, the electrons may only vibrate for a short period of time and with small magnitude. Also, if these vibrations are not passed through a large portion of the material, this energy will be reemitted as electromagnetic energy; hence, it will be reflected.

Absorption is the process by which a material turns electromagnetic energy into another form of energy, usually as heat. Similar to reflection, it is largely dependent on the frequency of the electromagnetic wave. If the wave has the same frequency as the natural frequency of the electrons of the material, it will cause the electrons to vibrate with their maximum amplitude. These energized electrons are now more likely to come into contact with neighboring atoms (as compared to the reflection process). This interaction converts the vibration energy of the electron into thermal energy.

Transmission is very similar to reflection in that the frequency of the electromagnetic wave cannot be the natural frequency of the electrons of the material. Because it is not this frequency, the electrons only vibrate for short

periods of time and with small degree. The difference between transmission and reflection is that these vibrations are passed on to other electrons in the material. When this "wave" of vibrations is passed through the material, the vibration energy is then converted back to electromagnetic energy and emitted out of the other side.

These three interactions are important concepts when looking for the permittivity of materials. Also, these interactions are all related by the conservation of energy such that:

$$R + A + T = E_{in} \tag{1}$$

where R is the energy reflected from the material, A is the energy absorbed, T is the energy transmitted, and E_{in} is the energy of the electromagnetic wave before it comes into contact with the material. This principle is crucial when trying to find low loss materials because it implies that if the energy of the incoming electromagnetic wave is constant, then the alteration of at least one of energies of an interaction will influence the other(s). The ideal low loss material is one in which R=A=0 (the electromagnetic energy leaving the material is equal to the energy that entered it), meaning that no energy is scattered or dissipated respectively by the material. This ideal situation is only possible in a vacuum, which finds little use in practical applications. Therefore, if one considers the reflected energy to be relatively the same across a range of materials (esp. at microwave frequencies), then by finding materials with lower absorption rates, one can decrease the amount of energy dissipated as wasteful heat all the while increasing the amount of energy that passes through the material; this is the basis for this experiment.

A common approach to categorizing materials and their properties concerning the previously mentioned interactions with electromagnetic waves is in the form of complex dielectric permittivity [3]:

$$\varepsilon = \varepsilon' - j\,\varepsilon'' \tag{2}$$

where ε' (real part) is the ability of the dielectric material to store electric energy and ε'' (imaginary part) is the dielectric losses that occur in the material. Usually, materials with a negative ε' are metals, where no propagating electromagnetic waves exist, and positive ε' are dielectrics. This permittivity is rarely ever a constant value as such parameters as position of medium, frequency of the applied field, temperature, and humidity can all have an impact on this property of the material. An important relation used in this experiment is the dissipation factor or loss tangent:

$$\tan\delta = \frac{\varepsilon''}{\varepsilon'} \tag{3}$$

which is the ratio of power lost to heat to the energy stored per cycle. This is a good measure of how "lossy" or how much of the energy the material is absorbing. The lower the loss tangent, the less electromagnetic energy is converted to heat which is used to observe which samples waste the least amount of energy as a thermal byproduct.

For most materials, the dielectric permittivity is a relatively constant value throughout the composition of the material regardless of its orientation to the incoming electromagnetic wave, as long as all other variables are held constant. These are classified as isotropic because from any particular point in the material, the physical properties are the same in all directions. Since there is no change in the physical properties and all other variables are held constant, there is no reason for the dielectric permittivity to change. However, if there are variations in the homogeneity of the structural composition of the material, it will most likely have a range of different dielectrics depending on its orientation. The electromagnetic wave will interact differently with each variation in its composition as if it is a different substance. This behavior is known as anisotropic and is examined with the help of the modified waveguide.

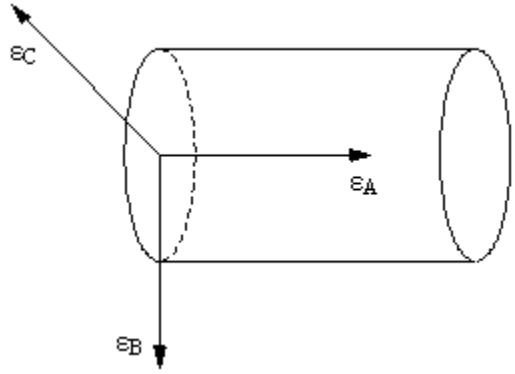

Figure 3: Using a cylindrical example: if the material is isotropic then the dielectric permittivity would be equal in all directions ($\varepsilon_A = \varepsilon_B = \varepsilon_C$), if it is anisotropic then in at least two directions, the dielectric constants are not equal (ε_B and ε_C are considered as the major dielectric axes and any direction in between is simply an average related by the cosine factor of the two)

EXPERIMENTAL DESCRIPTION

Waveguide

A standard rectangular C-band waveguide (inner dimensions 4.74 cm x 2.21 cm x 18.2 cm) uses a thin slit to insert the sample into the cavity, this approach limits the sample material in such a way that it must be rather thin yet also have a relatively large surface area compared to the thickness (thin to fit through the slit while long enough to fill the dimensions of the waveguide). The modified waveguide that is used for this experiment allows for much smaller sample sizes to be measured [4]. It employs two holes (inner diameter 8.2 mm) cut

out of the walls of the waveguide at the center. A hollow metal tube (length 3 cm) is welded to each of these holes to prevent excess losses of energy from the cavity. The sample is then placed in a quartz tube (outer diameter 8 mm, inner 6 mm) and the tube is inserted through the holes, placing the sample in the maximum electric field.

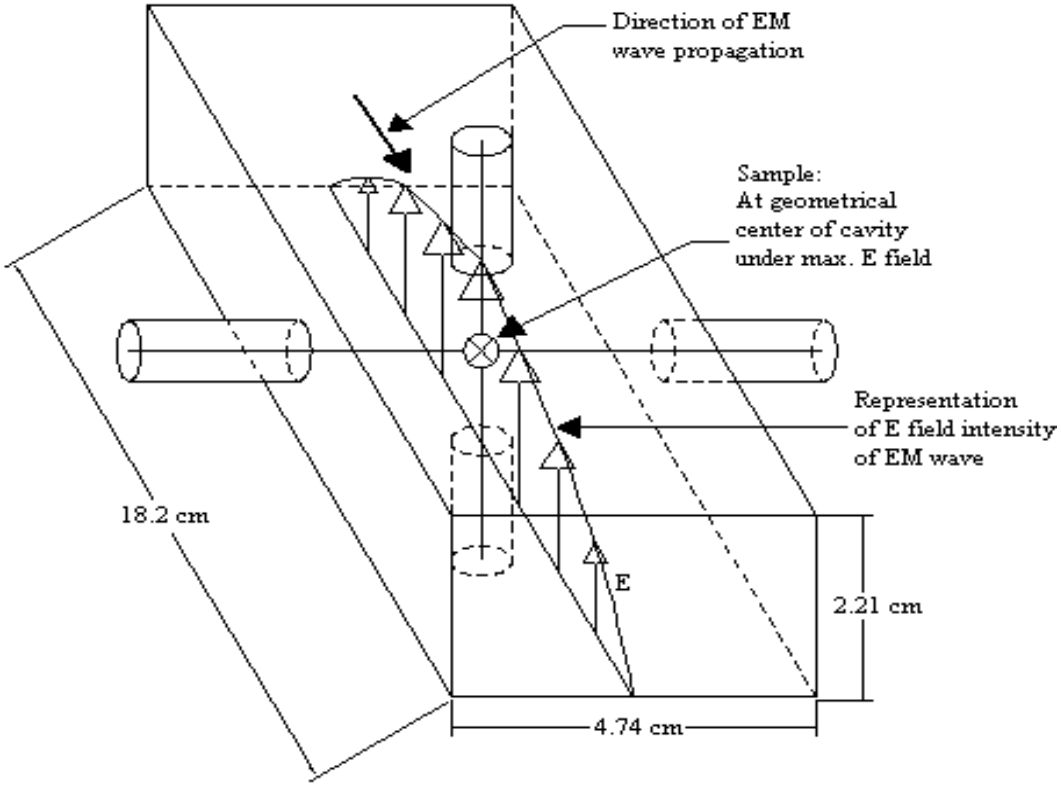

Figure 4: Representation of the waveguide and the electric field intensity of the electromagnetic wave in TE_{101} mode. The sample is inserted such that it is under the maximum intensity of the electric field. The tube containing the sample could be inserted either parallel to the width or parallel to the height.

Dielectric Measurements

The dielectric permittivity measurements of the samples are made using an HP 8753E network analyzer in the range of 3 GHz to 6 GHz. The samples are studied under zero electrical field bias and at room temperature and humidity. The waveguide is connected to the analyzer with standard probes. In addition, metal couplers with rectangular holes of dimensions 12.11 mm x 3.41 mm are inserted between the waveguide and probes to enhance the signal. The samples are placed at roughly the geometrical center of the waveguide and held in place in the quartz tube with small amounts of Styrofoam. The samples of different

composite ratios of $Ba_{0.5}Sr_{0.5}TiO_3$ to MgO (BST/MgO) are oriented in three main positions: perpendicular to the electric field, parallel to the electric field and parallel to the direction of the propagating electromagnetic wave, and parallel to the electric field but perpendicular to the electromagnetic wave. The SBN crystal sample is placed both perpendicular and parallel to the electric field and in each case, it is rotated to investigate any changes in the dielectric permittivity. All measurements are made at different resonant frequencies of the waveguide.

Theoretical Calculations

In a rectangular waveguide, the simplest and most commonly used setup to measure complex permittivity is TE_{10N} mode or transverse electric mode. In this setup, all electric fields are transverse to the direction of propagation and that no longitudinal electric field is present [5]. The first sub-number, 1, of the mode indicates that there is one electric half wave across the width of the waveguide and the second number, 0, says that there are no loops across the height of the guide. The N sub-number is the number of maximum electric field positions within the rectangular waveguide. Since these maximum electric fields are always spread out an equal distance from one another throughout the length of the waveguide, odd N numbers are usually chosen for measurement because the geometrical center of the guide will always be a position of maximum electric field.

The complex permittivity of materials is calculated by measuring the changes in resonant frequency (f_r) and quality factor (Q) of the cavity with and without the sample. The theoretical calculations for f_r and Q for a rectangular waveguide in TE_{10N} mode are [6], [7]:

$$f_r = \frac{c}{2}\left[\left(\frac{1}{a}\right)^2 + \left(\frac{N}{d}\right)^2\right]^{\frac{1}{2}} \tag{4}$$

$$Q = \frac{\pi\eta}{2R_s}\left[\frac{b\left(a^2+d^2\right)^{\frac{3}{2}}}{ad\left(a^2+d^2\right)+2b\left(a^3+d^3\right)}\right] \tag{5}$$

$$Q = \frac{\eta\pi bd^3}{2R_s\left(2N^2a^3b+2bd^3+N^2a^3d+ad^3\right)} \tag{6}$$

where a, b, and d are the dimensions of the waveguide (width, height, and length respectively), c is the speed of an electromagnetic wave in a vacuum, N is an integer referring to the mode number, η is the intrinsic impedance, and R_s is the surface resistance of the cavity. Equation 5 can be used for TE_{101} mode and equation 6 can be used for TE_{10N} modes.

$$\eta = \sqrt{\frac{\mu_o}{\varepsilon_o}} \approx 376\Omega \tag{7}$$

$$R_s = \left(\frac{\pi f_c \mu}{\sigma} \right)^{\frac{1}{2}} \tag{8}$$

where ε_o is permittivity of free space, μ_o is permeability of free space, f_c is the cutoff frequency of the waveguide, μ is magnetic permeability, and σ is the conductivity, both refer to the metal making up the waveguide.

$$f_c = \frac{1}{2\sqrt{\mu_o \varepsilon_o}} \sqrt{\left(\frac{m}{a}\right)^2 + \left(\frac{n}{b}\right)^2} \tag{9}$$

where m and n refer to the mode of the waveguide such that TE_{mnN}. The cutoff frequency for the mode is determined by the physical dimensions of the cavity. If the frequency is below the cutoff, the electromagnetic wave will be attenuated to an insignificant value in a relatively short distance. Otherwise, the electromagnetic energy can be transmitted through the waveguide.

The theoretical resonant frequency f_r is the frequency of the electromagnetic wave in the waveguide required to obtain a certain mode. The quality factor Q represents the sharpness of the resonant frequency and is inversely proportional to the surface resistance.

RESULTS/DISSCUSION

To calculate the dielectric permittivity and associated losses with a particular sample, certain reference measurements need to be taken in order to compare the resulting changes in the electromagnetic wave induced by the introduction of the sample. The reference state chosen for this experiment is with the rectangular waveguide unloaded (empty). Another possible reference state considered is with a small amount of Styrofoam (about 1 cm in length) placed in the center of the quartz tube and this combination inserted into the waveguide such that the Styrofoam is at roughly the center of the cavity. This reference may allow for greater accuracy when calculating the permittivity and losses of the sample; however the calculations would require the comparison of the volumes of the quartz, Styrofoam, and sample due to the fact that the volume of the sample is much smaller than the other two. It became apparent that simply using the reference as the empty cavity is more efficient. The dielectric permittivity and associated losses of quartz and Styrofoam are very small relative to the BST/MgO samples; their calculated permittivity and loss tangent are still within a very reasonable margin of error. Using this reference, f_f and Q of the empty cavity

need to be measured. Whereas f_r can be measured directly from the analyzer, Q is found as such:

$$Q = \frac{f_r}{\Delta f_{3dB}} \tag{10}$$

where Δf_{3dB} is the change in frequencies associated with a 3 dB drop from the peak resonant frequency. The measured values for f_r and Q of the odd numbered TE_{10N} modes in the 3 GHz to 6 GHz range are shown in Table I and Table II along with their respective theoretical counterparts.

Table I: Theoretical and measured resonant frequencies of unloaded waveguide

Mode	Theoretical Value (GHz)	Measured Value (GHz)
TE_{101}	3.26786	3.251656782
TE_{103}	4.01317	3.986737064
TE_{105}	5.19218	5.151949686

Table II: Theoretical and measured quality factor (dimensionless) of unloaded waveguide

Mode	Theoretical Value	Measured Value
TE_{101}	10292.8[#] 9327.88[##]	5529.51
TE_{103}	6990.33	4514.58
TE_{105}	4656.5	2680.12

It is clear that the measured values of f_r and Q are lower than their theoretical figure. As is the case in most theoretical calculations, many real-world losses are left out of the equations; such factors as losses of energy in the probes, metal couplers, and through the holes drilled for inserting the sample have dramatic effects on Q where as the integrity of the interior surface of the cavity can alter f_r. It is also seen that this particular waveguide, in the 3 GHz – 6 GHz range, only produces three different resonant frequencies in which the mode is odd (establishing a maximum electric field at the geometric center of the cavity).

With the reference values measured, each sample is placed in the quartz tube in one of the three desired positions and held in place with some Styrofoam. The three samples are all disk shaped and all have the same dimensions (radius – 2 mm, thickness - .75 mm). By inserting the tube into the waveguide such that

[#] Calculated using equation 5
[##] Calculated using equation 6

the sample is at the geometrical center of the cavity, small changes in the resonant frequency of the cavity and its quality factor are produced. Comparing these values with the previously measured reference values, the complex dielectric permittivity and loss tangent of each sample at that particular resonant frequency is calculated. The equations used to calculate the samples' permittivities are [8]:

$$\varepsilon' = \frac{V_c(f_c - f_s)}{2V_s f_s} + 1 \tag{11}$$

$$\varepsilon'' = \frac{V_c}{4V_s}\left(\frac{1}{Q_s} - \frac{1}{Q_c}\right) \tag{12}$$

where f_c and Q_c are the reference values, f_s and Q_s are the values with the sample inserted, V_c is the volume of the interior of the cavity, and V_s is the volume of the sample. The losses of each sample can then be calculated by using equation 3.

The following tables show the complex dielectric permittivity of each sample based on their positioning in the cavity:

Table III: Complex dielectric permittivity of samples – circular base parallel to electric field and parallel to direction of propagation

Mode	Resonant Frequency (GHz)	ε'	ε''
BST+MgO – 40:60			
TE_{101}	3.215516692	114.6788	.6764496
TE_{103}	3.947045249	102.7114	.6738963
TE_{105}	5.103513600	96.9932	.7071159
BST+MgO – 50:50			
TE_{101}	3.215380827	115.1109	.6830047
TE_{103}	3.946892293	103.1073	.6660858
TE_{105}	5.103323926	97.3727	.7101852
BST+MgO – 60:40			
TE_{101}	3.215000577	116.3207	.6818173
TE_{103}	3.946508644	104.1005	.6635684
TE_{105}	5.102783400	98.4543	.7351379

Table IV: Complex dielectric permittivity of samples – circular base parallel to electric field but perpendicular to direction of propagation

Mode	Resonant Frequency (GHz)	ε'	ε"
	BST+MgO – 40:60		
TE_{101}	3.215602730	114.4051	.6810072
TE_{103}	3.947122463	102.5116	.6727081
TE_{105}	5.103598126	96.8241	.7112347
	BST+MgO – 50:50		
TE_{101}	3.215481217	114.7916	.6729285
TE_{103}	3.947025431	102.7627	.6742897
TE_{105}	5.103443212	97.1341	.7232049
	BST+MgO – 60:40		
TE_{101}	3.215125655	115.9227	.6746770
TE_{103}	3.946633526	103.7772	.6602444
TE_{105}	5.102972212	98.0765	.7100668

Table IV: Complex dielectric permittivity of samples – circular base perpendicular to electric field

Mode	Resonant Frequency (GHz)	ε'	ε"
	BST+MgO – 40:60		
TE_{101}	3.217093666	109.6651	.6972845
TE_{103}	3.948692522	98.4496	.6921667
TE_{105}	5.105607768	92.8052	.7449793
	BST+MgO – 50:50		
TE_{101}	3.217075942	109.7214	.6967039
TE_{103}	3.948672620	98.5010	.6837230
TE_{105}	5.105595901	92.8290	.7333963
	BST+MgO – 60:40		
TE_{101}	3.216643666	110.1418	.7170810
TE_{103}	3.948540777	98.8420	.6891625
TE_{105}	5.105406301	93.2080	.7554840

Looking at this data, there are some very noticeable trends that begin to appear. Regardless of the sample or positioning, the ability of the sample to store electrical energy (ε') decreased as the frequency of the electromagnetic wave increases. At the same time, the dielectric losses (ε") increase because the

electrons have increasing probability of colliding with other electrons, generating heat, proportional to the increase in vibration frequency they are subject to. It is observed that the changes in dielectric permittivity between the same sample in the same mode positioned parallel to the electromagnetic field and also either parallel or perpendicular to the propagating wave are very negligible. However, when the sample is placed perpendicular to the electric field, a reasonable decrease in ε' and an increase in ε" occurs. This may be due to the fact that the electric field comes into contact with more of surface area and/or the thickness of the sample with respect to the electric field direction is much, much smaller. It may also be due to the intrinsic properties of the material or some extrinsic variable(s).

More important patterns, pertaining to this experiment, are those resulting from the comparison of the different ratios of composites. The first expected pattern is that as the ratio of BST to MgO increased, ε' increased since BST has a much higher dielectric constant. Examining the variation of ε" between the different composites, no perceivable relationship really stands out. A better evaluation of the losses of the different composites is done by comparing their loss tangent, shown in the following tables:

Table V: Loss tangent of samples – circular base parallel to electric field and parallel to direction of propagation

Mode	Composition - BST to MgO		
	40:60	50:50	60:40
TE_{101}	.0058986	.0059334	**.0058615**
TE_{103}	.0065611	.0064601	**.0063743**
TE_{105}	**.0072904**	.0072935	.0074668

*** Smallest values for each mode shown in bold**

Table VI: Loss tangent of samples – circular base parallel to electric field but perpendicular to direction of propagation

Mode	Composition - BST to MgO		
	40:60	50:50	60:40
TE_{101}	.0059526	.0058622	**.0058201**
TE_{103}	.0065623	.0065616	**.0063621**
TE_{105}	.0073456	.0074454	**.0072399**

*** Smallest values for each mode shown in bold**

It is seen that in all but one instance (Table V, TE_{105} mode), the loss tangent of BST+MgO with a ratio of 60:40 is the smallest for each particular mode. The errant case is most likely a result of an inaccurate measurement, assuming that the trend is correct. This is particularly interesting because BST has a larger loss tangent than MgO so it would seem that a composite with a

greater ratio of BST to MgO would have a larger loss tangent. However, this contradiction is most likely corrected by the fact that BST has a much, much greater dielectric constant than MgO, negating the relatively small differences in loss tangent.

A major shift in this pattern occurred when the samples are placed perpendicular to the electric field as shown in the following table:

Table VII: Loss tangent of samples – circular base perpendicular to electric field

Mode	Composition - BST to MgO		
	40:60	50:50	60:40
TE_{101}	.0063583	**.0063498**	.0065105
TE_{103}	.0070307	**.0069413**	.0069724
TE_{105}	.0080273	**.0079005**	.0081054

*** Smallest values for each mode shown in bold**

In this situation, the loss tangent of the composite with equal ratios of BST and MgO for each of the three modes is the smallest.

The next test involves the anisotropic SBN crystal. The cylindrically shaped crystal (radius - .5 mm, length – 2 cm) has a high dielectric constant perpendicular to the axis of the rod. It is held such that its length runs parallel to that of the quartz tube and is situated in the circular center of the tube with Styrofoam. The tube is then inserted in two different ways: with the length of the rod perpendicular to the electric field and, with it parallel to the electric field. In both cases, the length is perpendicular to the propagation direction of the electromagnetic wave. Also, in both setups, the sample is rotated inside the cavity to look for any possible changes in its dielectric constant induced by this alteration in its orientation to the electromagnetic wave. These measurements are compared with the reference measurements in order to calculate the dielectric permittivity and loss tangent shown in the following tables:

Table IIX: Permittivity and loss tangent of sample – oriented such that the length of rod is perpendicular to electric field

Mode	Resonant Frequency (GHz)	ε’	ε”	$\tan\delta$
TE_{101}	3.216454631	52.0264	.3431572	.0065958
TE_{103}	3.948080855	46.6983	.3288835	.0070427
TE_{105}	5.104889123	44.1595	.3317246	.0075120

Table IX: Permittivity and loss tangent of sample – oriented such that the length of rod is parallel to electric field

Mode	Resonant Frequency (GHz)	ε'	ε"	tan δ
TE_{101}	--	--	--	--
TE_{103}	3.834850937	180.7785	4.5046782	.0249182
TE_{105}	4.965858227	171.2246	7.1509610	.0417636

As was the case before, this sample continues to follow the predicted trend of decreasing ε' and increasing ε" and loss tangent as the frequency increases. However, there is now a significant change, as compared to the relatively same changes that occurred with the BST+MgO samples, in these values when the mode is held the same and only the orientation of the sample with respect to the electric field is changed. This clearly shows the anisotropic behavior of the sample. There is no noteworthy change in the dielectric permittivity of the SBN crystal caused by its rotation within the cavity; this means that there are only two major dielectric axes to this sample such that (refer to figure 2) $\varepsilon_A \neq \varepsilon_B = \varepsilon_C$. Also, in table IX, no values are able to be measured in TE_{101} mode because the large dielectric of the samples orientation causes the resonant frequency to drop below the cutoff frequency of the cavity.

CONCLUSION

By combining BST and MgO and their associated dielectric properties, a composite is created that is very useful for electrically tunable devices at microwave frequencies. The composite has a relatively good dielectric constant while also maintaining fairly reasonable losses, though far from ideal, non-tunable material. This experiment, in particular, shows that BST+MgO with a ratio of 60:40 provides the highest dielectric constant values while also managing the lowest lost tangent of the three proportions (except for the case with the circular base perpendicular to the electric field).

The anisotropic properties of SBN crystal could be measured by using the modified microwave cavity. The crystal has a very significant change in dielectric permittivity simply by changing its orientation to the electric field of the electromagnetic wave. However, no changes are noticed in its rotation inside of the cavity.

Further advancement of this experiment could involve extending the frequency range of which the samples are tested past 6 GHz. In addition, other different ratios of BST and MgO could be tested in the same manner to determine if there is in fact some peak ratio where the dielectric constant is maximized and the loss tangent is minimized. An extension of this experiment could also involve

applying varying electric fields to these composites in order in examine their tunable characteristics.

ACKNOWLEDGEMENT

I would first like to thank Dr. Amar Bhalla for his time and patients in explaining to me an area that I had almost no background in. His abundant amount of knowledge and expertise were indispensable in teaching me the theory behind the experiment as well as interpreting the data that I had recorded. Shashnk Agrawal was an invaluable asset in the lab. His experience and wholehearted helpfulness made this experiment possible. I would also like to thank Dr. Ruyan Guo, Dr. Kenneth Jenkins, and Mrs. Linda Becker for establishing such a wonderful REU program and allowing me the opportunity to take part in it.

This material is based upon work supported by the National Science Foundation under Grant No. EEC-0244030.

REFERENCES

[1] J.J. DeFrank, P.K. Bryan, C.W. Hicks, Jr., and D.H. Sliney, "Characteristics of Electromagnetic Radiation," "Chapter 15; Textbook of Military Medicine (Nonionizing radiation)", Department of Army – Office of the Surgeon General, United States

[2] "Dielectric Constant", "Handbook of Microwave Measurements – Volume II," pp. 495-548, 3rd Edition, Edited by M. Sucher and J. Fox, Polytechnic Press, Brooklyn, NY, 1963

[3] J.C. Anderson, K.D. Leaver, P. Leevers, and R.D. Rawlings, "Dielectric, piezoelectric, ferroelectric, and pyroelectric materials," pp. 574-598, "Materials Science for Engineers," 5th Edition, Nelson Thornes Ltd., United Kingdom, 2003

[4] S. Agrawal, "Modified cavity perturbation method to measure dielectric permittivity and losses in a ceramic sample," (unpublished results)

[5] "Microwave Waveguides and Coaxial Cables," "Electronic Warfare and Radar Systems Engineering Handbook", Naval Air Systems Command - Avionics Department, Washington D.C., April 1999

[6]. M.T. Lanagan, PhD. Thesis, Pennsylvania State University, 1987

[7]. J. Sheen, PhD. Thesis, Pennsylvania State University, 1993

[8] D. Dube, M. Lanagan, J. Kim, and S. Jang, "Dielectric measurements on substrate materials at microwave frequencies using a cavity perturbation technique," Journal of Applied Physics, 63 (7), 1988

DEMONSTRATION OF DISTRIBUTED SENSOR NETWORKS

Urenna Onyewuchi* and Sven G. Bilén[#]

Department of Electrical Engineering
The Pennsylvania State University, University Park PA 16802

*Undergraduate Student of:
Electrical Engineering Department
George Mason University
Fairfax, VA 22030

ABSTRACT

The purpose of this project is to determine the critical parameters and topologies needed to set up a distributed sensor network using the ZigBee data transmission standard. The major parameters being observed are the distance within which sensor nodes can transmit data, the rate of data transfer, and consumption of power by the entire network. Humidity and temperature sensors are being used as the source of real-time data for this analysis. Data transfer rates and distances are altered in ascending order, that is, from lowest to highest, until the range of the parameters is determined.

[#] Faculty Mentor

167

INTRODUCTION

Sensor networks can efficiently transfer information from one point to another as well as provide local data processing. Sensors measure signals, (e.g., forces, fields, etc.) from their surroundings and can determine an appropriate response, depending on their programmed tasks. Some of the applications of sensor networks are in environmental monitoring, motion monitoring, structural monitoring, etc. Sensor system hardware communicates and reads data, while the software is meant to provide a huge data processing capability collectively but not individually. This is the purpose of the sensor networks—to process data in the aggregate. Sensor network hardware consists of a microprocessor, data storage, sensors, analog-to-digital converters (ADCs), a data transceiver, controllers that tie the pieces together, and an energy source[1]. Sensor modules can be purchased with a majority of these components already integrated; however, sensors are generally purchased independently from the modules. Distributed sensor networks are more specific forms of wireless sensor networks.

Distributed Sensor Networks (DSNs) are ad-hoc mobile networks that include sensor nodes with limited computation and communication capabilities[2]. Sensor nodes communicate using one of a number of data transmission standards, which include ZigBee and Bluetooth. The data transmission standard selected for a project depends on its application. The ZigBee standard is preferred over Bluetooth for distributed sensor networks, because they transmit data in small packet sizes and allow for large networks, whereas Bluetooth transmits in large packet sizes but only allows for small networks. The Bluetooth standard is usually used in applications that deal with cable replacement, and over short distances to transmit both audio and data. It operates in the radio band around 2.4 GHz. ZigBee, on the other hand, is used for control and monitoring (an application for this project) and reaches a range of up to 30 meters[3].

Wireless networking faces a number of constraints when it comes to communication. Certain factors must be taken into consideration: how much storage is needed to pass data across the network, how much power is needed to keep all devices running and working effectively, does data need to be processed before it gets to the destination, how much processing capacity should be given to the computer, under what frequency or bandwidth should the data be transmitted, etc. Wireless companies produce devices that meet different frequency and processing requirements.

Challenges faced in networking include energy consumption and ability to work in harsh environmental conditions. Considering that some of these devices are used outdoors, they are built to withstand harsh environmental conditions; they are usually encased in weather-resistant coverings. More importantly, data processing and the inclusion of radios in most networking devices greatly affect the consumption of energy by the network. Most applications require devices that are able to last a long time. In order to increase the time that a network stays active, the radio (which consumes the most energy), is usually turned off when

not in use. This is another advantage that ZigBee has over Bluetooth for distributed sensor networks: its battery life is about 100–1000+ days, while Bluetooth lasts for a maximum of about 7 days. The drawback in using ZigBee is that its link rate is 20–250 kbps, compared to Bluetooth's 1-Mbps link rate. For this project and many other monitoring purposes, this low data rate is more than enough to meet the needs of the system. The advantages of ZigBee, including security, reliability, manageability and availability, far exceed its disadvantages.

The use of the ZigBee standard in distributed sensor networks reduces operational and support costs and capital investments and allows data to be shared in real-time while adjusting to changing conditions in the environment for the purpose of reducing major failures[3]. ZigBee devices are in compliance with the IEEE 802.15.4 standard: "The IEEE 802.15 Task Group 4 is chartered to investigate a low data rate solution with multi-month to multi-year battery life and very low complexity. It is intended to operate in an unlicensed, international frequency band." This shows that the low data link rate of ZigBee devices has been taken into deliberation and solutions provided to maximize their efficiency. The three network topologies for ZigBee networks are: star, mesh, and cluster tree, as shown in Figure 1. This project uses mesh (also called peer-to-peer) network topology, which is known for its high level of reliability and scalability by providing more than one path through the network[4]. Temperature-and-humidity sensors are used in this project to provide a source of real-time data in order to analyze the critical parameters (bandwidth range, distance range, power consumption) of distributed sensor networks using this standard.

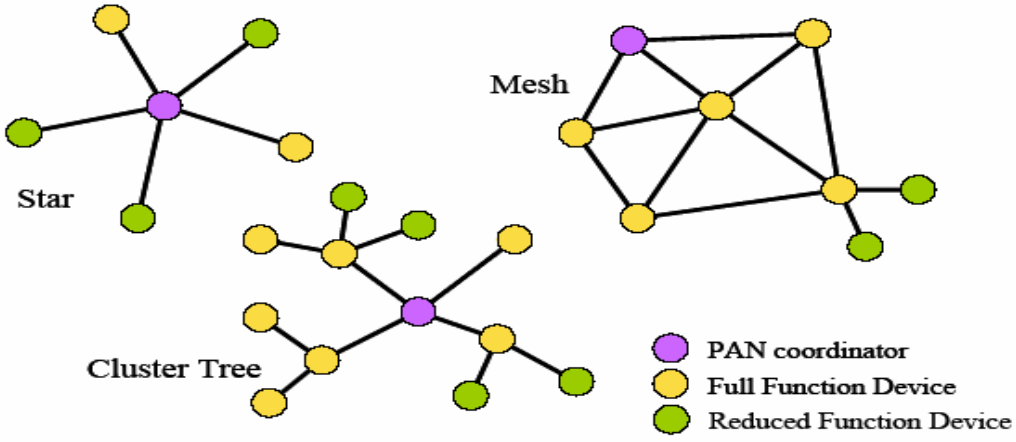

Figure 1: Network Topologies[4]

EXPERIMENTAL DESCRIPTION

Methodology

There are a number of companies that manufacture and distribute sensors and sensor modules, working in compliance with the ZigBee and IEEE 802.15.4 standards. The first step in carrying out this project was to perform a search to find these companies. A search for companies supplying ZigBee modules produced ten major companies; they are shown in Table I.

Table I: ZigBee Module Suppliers and Product Descriptions

Companies	Description
Helicomm	Helicomm's IPWiNS product portfolio provides a comprehensive platform for OEMs looking to integrate standards-based wireless networking for competitive advantage. *www.helicomm.com*
Millennial Net, Inc.	• Millennial Net is the leader in ultra-small, ultra-low power wireless computing devices in self-organizing networks for the consumer, industrial, medical and military markets. • Great company; too pricey *www.millennial.net*
Sensicast Systems, Inc.	Sensicast Systems, Inc. provides complete wireless sensor networks to a wide range of industries. *www.sensicast.com*
CrossBow Technology	Crossbow Technology is a leading supplier of sensor systems as well as the leading full solutions supplier in the wireless sensor networking arena and the only manufacturer of "smart dust" wireless sensors. *www.xbow.com*
AirBee	• Airbee is an innovator of intelligent software solutions for unwired voice, data and video networking. • Video or voice sensors are not needed for project *www.airbeewireless.com*
LS Research	With a core competency of wireless product development, L.S. Research offers a broad range of engineering services including RF design, antenna design, software design, PCB layout, prototyping, and product verification. *www.lsr.com*
Luxoft Labs	Luxoft Labs (IBS Group) enables complete M2M solutions by providing wireless ad-hoc mesh-networks software, hardware and integration services. *www.luxoftlabs.com*
Moteiv Corporation	Moteiv provides consulting services for wireless networking, specifically for embedded devices and sensor networks. *www.moteiv.com*

(Table 1 continues)

Table I: ZigBee Module Suppliers and Product Descriptions (cont.)

Daintree Networks	• Daintree Networks is a leading provider of analysis and test tools for wireless sensor and control networks. • Unable to contact the sales representatives. *www.daintree.net*
Innovative Wireless Communication	• IWT solves the toughest wireless design challenges and provides you with a competitive edge. • They do not produce a lot of ZigBee devices. *www.iwtwireless.com*

The next step taken in narrowing my options was to look through the application specifications provided by the companies. Some companies were eliminated because they produced already completed sensor networks; parts to make a network are needed. Using cost and lead-time as new constraints, my supervisor and I decided upon sensor modules from Moteiv Corporation, and purchased them.

Materials

The sensor board—called a "mote"—is shown in Figure 2 below. It consists of a USB microcontroller, a USB connector, USB transmit and receive LEDs, provisions for sensor connections, and CC2420 Radio. Other key features include:

- Integrated onboard antenna with 50m range indoors / 125m range outdoors
- Ultra-low current consumption with a nominal value of 21-23 mA for the radio transmitter and receiver respectively with the microcontroller unit on, and about 1200 μA in sleep mode.
- Powered by two AA batteries.

The physical dimensions of the mote are shown in Table II.

Table II: Physical Dimensions of Tmote Sky.

	MIN	NOM	MAX	UNIT
Width	1.24	1.26	1.29	in
Length	2.55	2.58	2.60	in
Height (without battery pack and SMA antenna)	0.24	0.26	0.27	in

Method

The equipment from Moteiv Corporation came with an installation CD and Quick Start Guide, which I read and used to install USB Serial Port Drivers

for the modules as well as *Cygwin*, a program used for programming applications into the modules. After installation, one of the modules was programmed.

The sensor modules are absolutely inactive before programming. The first step taken in programming the modules is locating and opening a *Cygwin* shell and changing the directory to */opt/tinyos-1.x/apps/*. A program that increments a counter, displaying it to the Tmote LEDs while sending a message of the count over radio, was then complied using the *make tmote* command. In order to figure out what module(s) is connected to the USB Port, the command *motelist* was entered. The *make tmote reinstall* command is meant to install the compiled program into the mote. However, it gave some error messages. The following command worked: */usr/local/mspgcc/bin/msp430-bsl --telosb -c 7 -r -e -I -p build/telosb/main.ihex.out*. Afterwards, another module was programmed in another directory.

The second module was connected to a USB port and the *make tmote* command used to compile the program again; this time, in the TOSBase directory. Then, the alternative command to the *make tmote reinstall* command was re-run to install the application into the second mote so that it received messages from the first mote. Opening the Java tool, Serial Forwarder, displayed the number of packets module 2 read from module 1. With this basic program tested on the motes, a nesC application is created to read temperature and humidity data, and relay it to the PC.

Figure 2: Top view of the Tmote sky module

RESULTS

With one of the sensor modules connected to a USB port right beside a base module (made by installing a TOSBase program into it), *Serial Forwarder* was run to test the activity occurring between the base module and the first module. *Serial Forwarder* is a Java tool that listens for TinyOS packets on a serial port and forwards them over a local TCP network socket[5]. The "Packets Read" section of the *Serial Forwarder* screen revealed that the counter on the base module was increasing. In other words, the first module was indeed communicating with the base module.

Based on the program installed in the mote, its count increased almost every second. As the distance between the first module and the base module increased, the rate at which they communicated decreased. This could be seen by how slowly the numbers on the Serial Forwarder screen went up. At a distance of about (350 ± 7) feet outdoors, equivalent to (106.68 ± 2.13) meters, the base module maintained a green light rather than blinking as it was doing initially. In other words, the modules stopped communicating with each other. Note that this was a direct line-of-sight distance.

When the same separation experiment was tried indoors with several obstacles in the path between the first module and the base module, the communication stopped after a distance of about 77.5 feet or 23.6 meters was reached.

Note that this experiment was run with the `CntToLedsAndRfm` program installed into the first module. This program increases a counter, displaying it to the Tmote LED's while sending a message of the count over the radio. The increment is made in binary, while the message as read by the *Serial Forwarder* screen is in decimal.

Power is largely conserved in this research due to the fact that when the modules are connected to the PC through USB ports, battery usage is unnecessary. However, when unplugged to test multi-hop networking, batteries need to be connected; throughout the experiment, I used the same batteries. Power consumption has been proven not to be a problem for ZigBee data transmission.

An *Oscilloscope* directory is available for displaying temperature reading, with a Sensirion temperature sensor soldered to the Tmote Sky sensor module board. The Sensirion SHT11 sensors are relative humidity and temperature sensors, fully calibrated with digital output. They have excellent long-term stability, ultra low power consumption, and are surface mountable. Their sensor performance specifications are as follows:

Temperature range: -40 to 123.8°C
Humidity range: 0 to 100 %RH

The *Oscilloscope* directory is accessed through *cd /opt/tinyos-1.x/ apps/Oscilloscope/*. Listening to the Java tool, through Serial Forwarder and the Listen Java tool, the following result was obtained:

TOS_Msg length is invalid: header_length=5, real_length=36 ... modifying msg to fit
Received message: 1A 00 00 00 00 00 7E 00 0A 7D 01 00 60 31 01 00 FF 0A 00 0B EC 0A 06 0B ED 0A 07 0B EF 0A FF 0A 07 0B F7 0A 1A 00 00 00 00

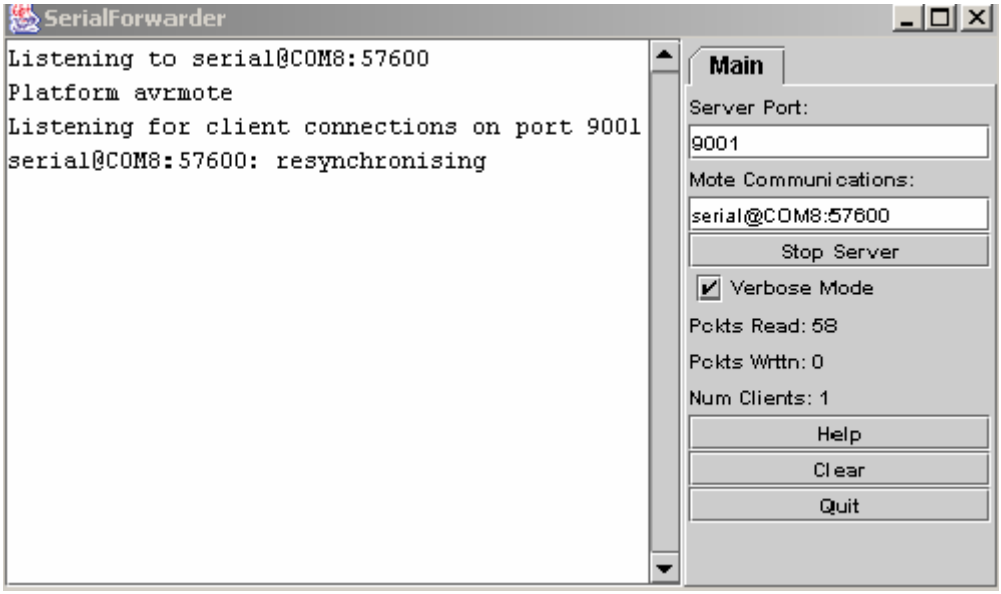

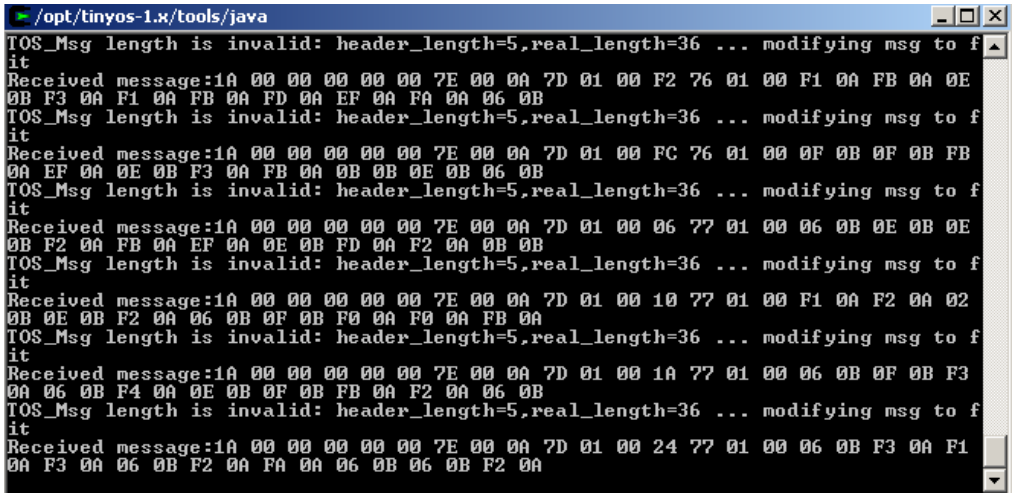

DISCUSSION

Based on the fact that Zigbee products are expected to be used indoors, past research shows that they reach a range of up to 30 meters. Therefore, its range of 23.6 meters indoors is expected; the outdoor range was shockingly high, in comparison with the indoor range. However, it does make sense since there were relatively no obstacles between the transmitter and the receiver while doing the readings outdoors.

Diffraction is a phenomenon that occurs when there are obstructions between a signal transmitter and a receiver. It allows for signals to reach their destination behind obstructions, and is explained by Huygen's principle, which states that all points on a wavefront can be considered as point sources for the production of secondary wavelets and that these wavelets combine to produce a new wavefront in the direction of propagation[6]. Received signal strength reduces

as well as the distance of propagation. This explains why the range indoors is less than that outdoors.

More research is needed to measure the bandwidth of signal transmission of the motes. We also intend to test the use of motes manufactured by other companies in the network of Moteiv sensors. Compatibility with other motes will greatly improve the usability and applicability of the sensors.

In addition, a *nesC* application to perform multihop routing should be created for temperature and humidity readings. There is a *surge* application in the *apps/surge* directory that reads light sensor data and hops these data from a source mote over several others to get to a destination mote, programmed as node 0 during installation of the *surge* program into the mote. Multihop routing for temperature readings could be done by reading through and understanding the *Surge* program and connecting the interfaces on the modules, *MultiHopEngineM* and *MultiHopLEDSM* appropriately. In other words, a C programmer is probably needed for this operation.

CONCLUSION

The ZigBee standard is a very good data transmission standard to send low data-rate packets in a network, within a distance of up to 30 meters. It is efficient in sending sensor readings, including light and temperature readings. Most operations can be carried out by re-programming, modeling, and/or using already written programs available on the Cygwin program files.

Based on my research as well as previous research, ZigBee applications include environmental monitoring, and control applications in industrial settings, among other similar applications.

ACKNOWLEDGEMENT

I want to thank my faculty mentor, Professor Bilén for constantly encouraging me and guiding me through the research at times when things got confusing. I also thank the EEREU program ((NSF Grant EEC 0244030) for partial support during the research; last but not least, the SROP program for supporting me financially and otherwise this summer. I could not have finished this research without encouragement from my family and boyfriend.

REFERENCES

[1] Culler, D., Estrin, D., Srivastava, M. "Overview of Sensor Networks." *IEEE Computer Society*. August 2004. June 14, 2005. <http://www.computer.org/computer/homepage/0804/GEI/>.

[2] L. Eschenauer, and V.D. Gligor, "A Key-Management Scheme for Distributed Sensor Networks." University of Maryland. May 2004. <http://www.cs.umbc.edu/courses/graduate/CMSC691A/Spring04/papers/eschenauer02keymanagement.pdf>

[3] M. Blazer, "Industrial-strength security for ZigBee: The case for public-key cryptography." *Embedded Computing Design*. May 2005, pp. 35

[4] W. Craig, "ZigBee: 'Wireless Control that Simply Works.'" ZMD America, Inc. <http://www.zigbee.org/imwp/idms/popups/pop_download.asp?contentID=5438>

[5] Moteiv TmoteSky Low Power Wireless Sensor Module Quick Start Guide, Page 10 of 18

[6] D. Button. "Effect of Obstructions on RF Signal Propagation," Don Button, Manager, EMS Wireless <http://www.emswireless.com/english/Tech_Articles/tech_art03.asp>.

INVESTIGATION OF FREQUENCY DEPENDENCE OF ELECTROOPTIC COEFFICIENTS IN EO CRYSTALS

Jonathan Taylor* and Ruyan Guo[#]
Department of Electrical Engineering and Materials Research Institute
The Pennsylvania State University, University Park, PA 16802

*Undergraduate student of
Department of Engineering
Cedarville University
Cedarville, OH 45314

ABSTRACT

The electrooptic (EO) effect (at λ= 633nm) in ferroelectric single crystals was investigated as a function of small signal modulation frequencies. An exploration of techniques was carried out, using the Senarmont compensation method and an examination of optically-coupled microwave cavity method to determine frequency dependence of the electrooptic coefficient of anisotropic electrooptic single crystals subjected to low and high frequency electric fields. The crystals investigated were Strontium Barium Niobate (SBN) and Lithium Niobate ($LiNbO_3$). Piezoelectric resonance measurements were also conducted to examine piezooptic coupling for the influence of piezoelectric lattice vibrations on the electro-optic behavior. Electrooptic coefficient in the crystals was found to have strong frequency dependence in frequencies below 100 kHz apparently due to space charge effects. Anomalous electrooptic properties near piezoelectric resonance frequencies are found that may be attributed to a synchronization of the piezoelectric resonance and dipolar/lattice vibrations.

INTRODUCTION

With optics becoming increasingly important in communications, effective ways of modulating laser pulses over wide frequency range becomes necessary for optimal efficiency and security. One way of doing this is using a ferroelectric single crystal fiber to modulate a laser beam by utilizing the electrooptic effect of the crystal using an electric field. The induced optic index of refraction, for linear approximation, is proportional to the amplitude of modulating electric field, and thus pulse width modulation becomes very easy using just the crystal with applied electric field. However, little research has been done into the frequency dependence of the electrooptic coefficient.

Frequency dependence of electro-optic coefficients on modulating field is

[#] Faculty Mentor

one aspect scarcely reported in literature; however is of significant importance for using the crystals as electro-optic modulators in optical engineering at different frequencies. Common assumptions are that EO coefficients are frequency independent based on the frequency independency of electronic polarizability of the material. Yet the EO coefficient measured by conventional technique contains without exception both primary and secondary effects arising from electronic and ionic polarizations which contain dispersive components (such as reorientation and electromechanical coupling of ions).

The Senarmont compensator method is the classic means of obtaining low frequency measurements for the electrooptic coefficient, and will be used in this experiment. A method recently developed to research high frequency dependence is using a microwave bender with a cavity, which holds the crystal fiber. The bender couples the microwave field and the laser light through the crystal. Huang [1,2] experimented to develop this method by measuring the full width half maximum (FWHM) of a laser pulse coupled through an SBN crystal in the microwave field, and then using that to calculate electrooptic coefficient r_{33}. Another method was devised and will be compared with Huang's method to see whether greater accuracy and precision can be achieved. This method calculate the electric field induced changes in index of refraction (Δn) from which r_{33} can be readily obtained.

This paper reports the electro-optic property of SBN and $LiNbO_3$ crystals as function of electric field frequencies (at low frequency and at near resonant frequencies) studied via dynamic EO modulating method and compared to a microwave waveguide method.

EXPERIMENTAL DESCRIPTION

The Senarmont compensator method uses a simple setup involving two polarizers, a quarter-wave plate, photodetector, pulse generator, and lock-in amplifier. A sinusoidal electric field is applied across the thickness of the crystal sample. The two polarizers are put on separate sides of the crystal and rotated to be 90° from each other. The polarizer behind the crystal is called the analyzer, and in front of it is a quarter-wave plate which has been rotated so it is 45° from the angle which allows the minimum light to reach the photodetector when no modulating field is applied. The photodetector is output to an SR844 lock-in amplifier, which is phase-locked to the modulating electric field, and thus cancels out most of the noise to allow for high precision measurement. The frequency range measurable using Senarmont method is theoretically <250 MHz, limited by the lock-in amp.

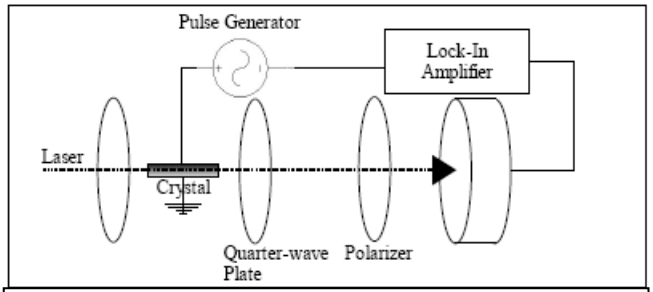

Figure 1: Senarmont Compensator Method

For the high frequency measurements, the microwave waveguide will be used to measure the electrooptic coefficient of SBN and LiNbO when they are subjected to a standing wave 10 GHz electric field. Two different methods of measurement were also studied. Both will use a microwave bender to hold the sample, coupling the light and microwave. The laser used was set to a very short pulse (<200 ns) in order to give greater precision in the measurements. The microwave generator was set to its maximum power of 20 dBm, and a network analyzer allowed precise measurement of the field at the location of the crystal.

The first method follows that used in reference [1]. The second method, shown in Figure 2, will use a light splitter to split the laser beam into two separate beams before entering the cavity, and two photodetectors will be used to measure the time difference between the pulses.

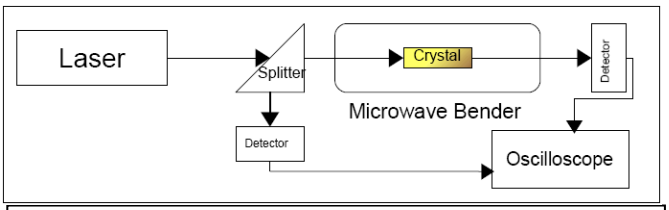

Figure 2: High Frequency Method

The SBN sample under test was cut from a single crystal fiber, grown from a ceramic feed rod using the laser heated pedestal growth technique [3,4]. The polar c-axis of the crystal sample was determined by back reflection X-ray Laue method. After careful orientation, the surfaces were polished to optical finish using 1/4 μm diamond paste. The samples were then Au-sputtered with parallel electrodes and poled to achieve single domain states and to minimize the scattering of light.

The $LiNbO_3$ crystal sample was cut from a Czochralski grown crystal, with periodic poled domains. In the experiment, both samples were measured with electric field parallel to their polar axes, and with incident light propagating perpendicular to it. In such a configuration, the effective EO coefficient is measured.

Before measuring the electro-optic coefficient near a resonant frequency, a materials impedance analyzer (HP model 4291) was used to determine the resonant frequency range according to the impedance spectrum.

Measurement Theory

In the Senarmont compensation method, when an electric field is applied to the crystal, it changes the index of refraction of the crystal through electrooptic effect, known as Pockels effect.

$$\Delta n \simeq -\frac{1}{2} n_0^3 r_c E \qquad (1)$$

Where Δn is induced index change, n_0 is the index of refraction under zero field, r_c is effective electrooptic coefficient ($r_c = r_{33} - \frac{n_o^3}{n_e^3} r_{13}$), and E is modulating field. This causes retardation (Γ) of the light, which can be recorded according to the equation

$$\frac{I_{out}}{I_{in}} = \sin^2 \frac{\Gamma}{2} \tag{2}$$

$\Gamma = \pi V_{appl}/V_\pi$, where V_{appl} is the electric field applied to the crystal and V_π is the voltage at which Γ is equal to π. Substituting this into equation (2) for Γ, and using trigonometric identities, the formula becomes

$$\frac{I_{out}}{I_{in}} \approx \frac{1}{2}(1 + \pi \frac{V_{appl}}{V_\pi}) \tag{3}$$

Thus, I_{out}/I_{in} is proportional to $\pi V_{appl}/V_\pi$, but only when the retardation is close to π/4, or when I_{out} is approximately its maximum value. When this is the case

$$V_\pi = -\frac{\lambda d}{n_e^3 r_c L} \tag{4}$$

$$r_c = -\frac{4\lambda}{\pi n_e^3}(\frac{d}{L})(\frac{V_{out}}{V_{p-p} V_{appl}}) \tag{5}$$

Where V_{out} is the voltage measured by the lock-in. All of the values in equation (5) are constants except for r_c, V_{out}, and V_{appl}. Because this study is mostly interested in the trend of the data rather than the actual value of r_c, equation (5) can be simplified to

$$r_c \propto -(\frac{V_{out}}{V_{appl}}) \tag{6}$$

By tracking the trend of V_{out}/V_{appl} over a frequency range, it is straight forward to track the frequency dependence of r_c.

Measuring the electrooptic coefficient at high frequencies is much different than that of low frequencies, because the electric field is not uniform in the crystal. The wavelength of a low frequency field is large enough that the field

can be treated as uniform throughout the crystal; however the wavelength of a 10 GHz field is only ~3 cm. Since it is spatial dependent, special care must be taken to include the position of the crystal relative to the microwave field strength.

In the first high frequency method, the FWHM of the pulse is used to calculate r_{33} from equations in reference [1,2]. Because the electric field is sinusoidal,

$$\Delta f = f \cdot n_e^2 r_{33} \frac{E_0}{\varepsilon_r} \cos\left(\frac{kL}{2} + kx_0\right) \sin\left(\frac{kL}{2}\right) \tag{7}$$

When $L=\lambda_m/2$ and $x_0=\lambda_m/4$, then the equation is reduced to

$$\Delta f = f \cdot n_e^2 r_{33} \frac{E_0}{\varepsilon_r} \tag{8}$$

Where Δf is change in FWHM, n_e is index of refraction without electric field, E_0 is maximum field strength, ε_r is relative permittivity of the crystal, and f is the frequency of the FWHM.

In the second method, the laser is split into two beams before entering the cavity. One beam bypasses the cavity and is measured by a photodetector. This beam will be used as a reference beam. The other beam enters the cavity and passes through a crystal before being measured by the other photodetector. The beam traveling through the crystal will have a time delay which changes as the microwave field is applied. The time delay peak to peak of the pulses can be used to calculate n by first finding the time delay between the two pulses without the crystal (Δt_r). Then the crystal will be inserted and with the electric field the time delay between the reference pulse and the second pulse will again be measured (Δt_s). From the difference between Δt_r and Δt_s, the change in the speed of light caused by the crystal can be calculated from

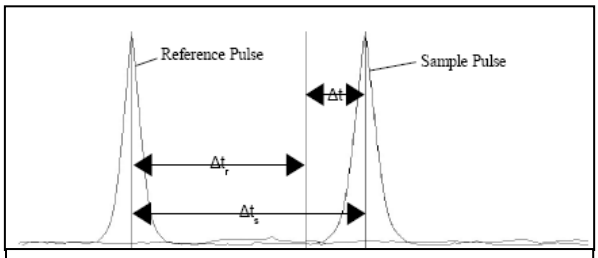

Figure 3: Time between pulses

$$v = \frac{dx}{dt} = \frac{L}{\Delta t_s - \Delta t_r} \tag{9}$$

$$n = \frac{c}{v} = c\frac{\Delta t_s - \Delta t_r}{L} \tag{10}$$

RESULTS

The Senarmont method was carried out multiple times for both crystals at frequencies between 2 Hz – 1.5 MHz. The data collected at frequencies well

below piezoelectric resonance frequencies are summarized in Figure 4 and 5, Figure 4 being the data of the SBN crystal and figure 5 is the data of the $LiNbO_3$.

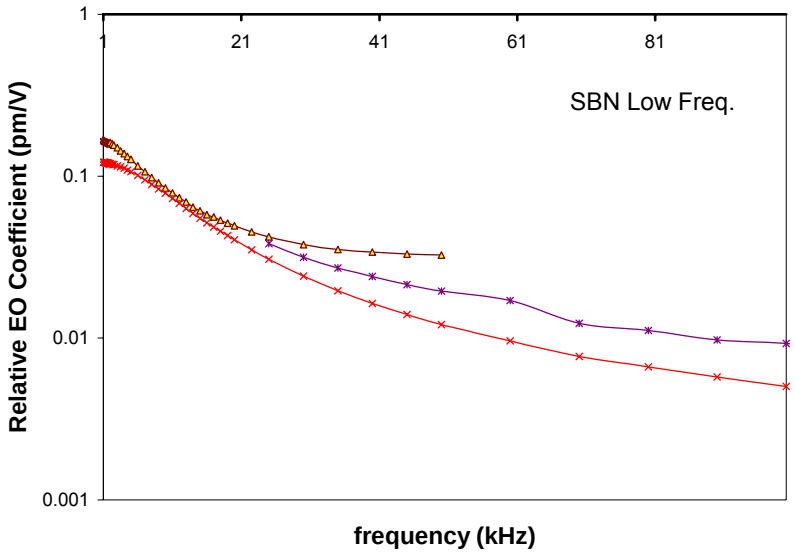

Figure 4. Relative EO coefficient of SBN crystal decreases as function of modulating frequency (below 100 kHz), plotted in half log scale.

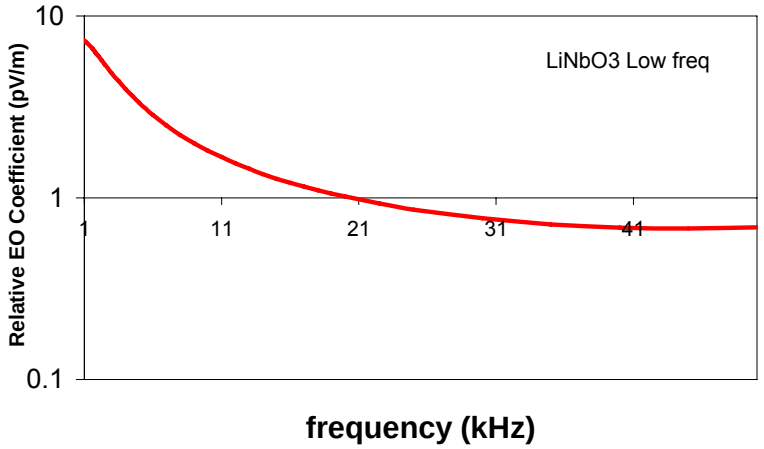

Figure 5. Relative EO coefficient of $LiNbO_3$ crystal decreases as function of modulating frequency (below 50 kHz), plotted in half log scale.

The resonant frequencies of SBN crystal were determined by material impedance analyzer. Near the resonant frequency the dielectric permittivity will change dramatically. It is found that piezoelectric transverse length resonant mode exists around 310 kHz. Similar measurement was conducted near the fundamental resonant frequency of the SBN crystal fiber.

The V_{out}/V_{appl} frequency dependence was then compared with the measured resonance of each crystal in the relevant frequency range, as shown in

Figure 6 and Figure 7, where D is dielectric loss factor that is proportional to the rate of change of dielectric constant of the crystal resonator.

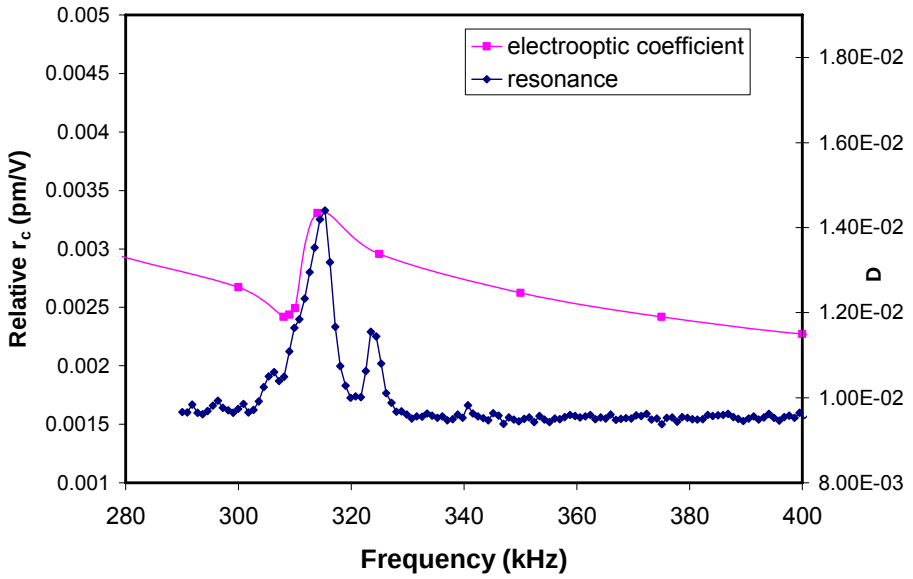

Figure 6: SBN electrooptic effect showing strong frequency dependence near piezoelectric resonance, signified by the peak in D.

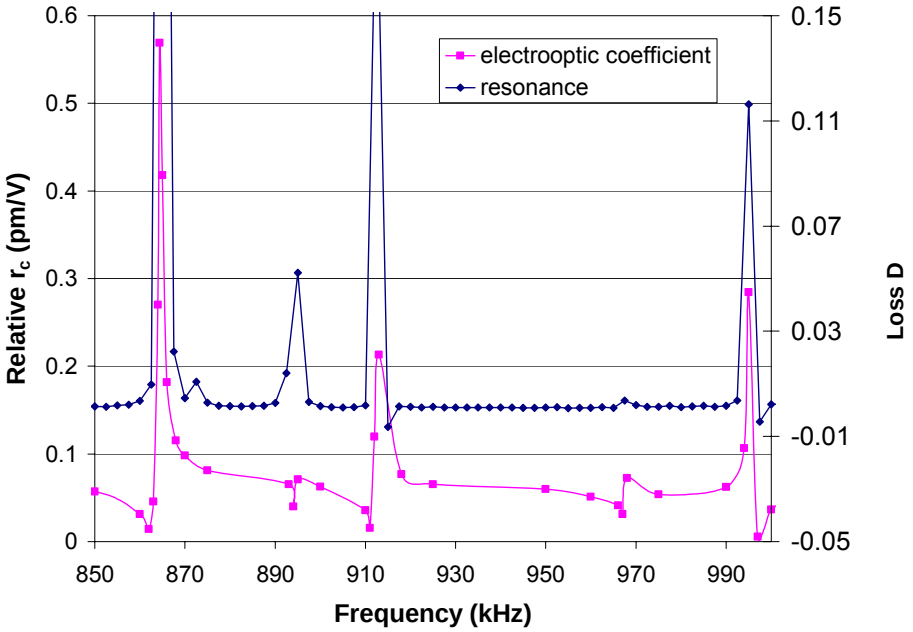

Figure 7: $LiNbO_3$ electrooptic effect showing strong frequency dependence near piezoelectric resonance, signified by the peak in D.

Measurement over a broad range of frequency for the $LiNbO_3$ confirms that the electrooptic effect indeed scales with the dielectric constant, as shown in Fig. 8.

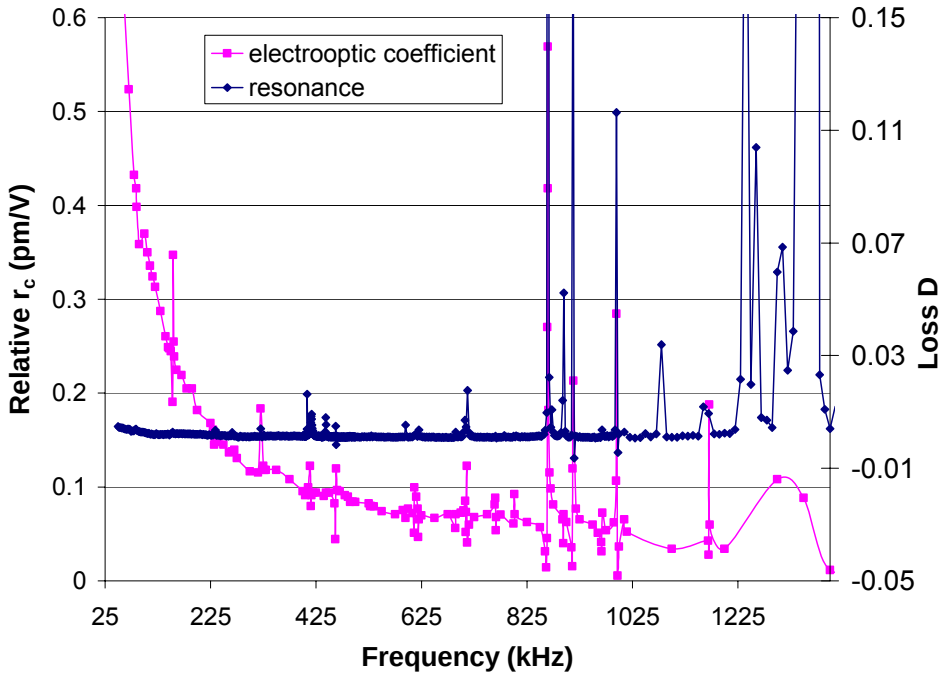

Figure 8: Correspondence of effective EO coefficient with the piezoelectric resonance in $LiNbO_3$ crystal.

No direct measurement at microwave frequency was conducted, due to lack of proper instruments to control the pulse width of the laser.

DISCUSSION

The frequency dependence of effective EO coefficient may be explained by the different contribution mechanism from the primary and secondary effect, which can be expressed as:

$$r_{ijk}^{X} = r_{ijk}^{x} + \pi_{ijlm} d_{lmk} \qquad (11)$$

where r_{ijk}^{X} is effective electro-optic coefficient at low frequency with constant stress, r_{ijk}^{x} is effective electro-optic coefficient at high frequency with constant strain, π_{ijlm} is elasto-optic coefficient and d_{lmk} denotes piezoelectric coefficient. Although it is not possible to separate the contribution of elastooptic and piezoelectric effect explicitly due to the lack of independent elastooptic coefficient measurement, the results obtained confirm that the effective

electrooptic coefficient at constant strain (free boundary condition) will scale with the dielectric constant that varies with frequency, especially near the crystal's electromechanical resonance. Near piezoelectric resonance, crystal lattice experiences standing wave vibration at resonant frequency $f_r = \frac{v}{2d} = \frac{1}{2d}\sqrt{\frac{1}{\rho s_{kl}^D}}$, where v is the phase velocity of the acoustic wave, ρ the density of the vibrator, s_{kl}^D the compliance coefficient at constant dielectric displacement, and d is the length in the vibration direction. Each elemental unit cell can be regarded as containing a dipole. When wavelength of lattice vibration is in harmony with piezoelectric resonance frequencies, it is found that EO coefficient is greatly amplified.

At low frequency ionic displacement and the crystal is free to respond to the applied electric field. In this situation values of effective EO coefficient contains both the primary and the secondary terms. A negative frequency dependence of effective EO coefficient is thus expected as the dielectric permittivity and that of the ionic polarization, decreases with increasing frequency. However near resonant frequency, the secondary effects scales with resonant behavior of the dielectric constant thus the EO coefficient experiences anomalous values as function of frequency.

Frequency dependence of the EO crystals' electrooptic coefficient has been reported very recently [5] in the literature to our knowledge. The mechanisms of the large frequency dependence of EO coefficient may be attributed to several possible processes, all of which involves time dependent charge distributions that cause dynamic changes of effective index of refraction, which effectively aggregate the apparent high EO coefficient measured. When the modulating electric field is in the low frequency range, space charges (due to oxygen vacancies or imperfections in the crystal) may contribute significantly to the EO dependence, through a reverse process of photorefraction (charge transported and trapped under incident light become mobile and begin to drift under driving electric field, destabilizing the photorefractive local field). Space charge effect is a slow process of typically millisecond time scale and is unable to stabilize at high frequencies. Another process covering wider frequency ranges is the dipole (such as $[Nb^{5+}\text{-}O^{2-}]$) reorientation in response to the modulating electric field. The reorientation can be considered a relaxation process with dispersion time constant of the form:

$$\tau = \frac{\pi}{\omega_0} e^{\frac{\mathbb{V}_0}{k_0 T}} \tag{12}$$

where $\mathbb{V}_0$ is energy barrier between two equivalent orientation states, ω_0 is the vibration frequency of the dipole, T is temperature, and k_0 is the Boltzmann constant. The energy barrier is decreased to $\mathbb{V}_0 - q\vec{E}\cdot\vec{r}$ in r-direction, where E is the modulating electric field.

CONCLUSION

Using the Senarmont compensator technique, the effective electrooptic coefficient of SBN and $LiNbO_3$ single crystals were measured to explore its frequency dependence. At low frequency (1 kHZ) the EO r_C coefficient decreases with increasing frequency, in a near exponential form. The relative dielectric constant of SBN single crystal fiber goes through extremes near its piezoelectric resonances and anti-resonances. It is shown that the value varies with the frequency and scales as the trend of dielectric constant near the resonant frequency. It is suggested that frequency dependence of electrooptic coefficient should be taking into consideration for the design of EO modulator, for optimizing working conditions and for possible selective amplification of electrooptic couplings.

ACKNOWLEDGEMENTS

This material is based upon work supported by the National Science Foundation under grant No. EEC-0244030. Thanks are given to the National Science Foundation and Penn State University for providing the opportunity for me to accomplish this research. I would also like to acknowledge and thank Hongbo Liu, who provided much of the experimental expertise.

REFERENCES

1 C. Huang, A.S. Bhalla, and R. Guo, *Measurement of Microwave Electro-Optic Coefficient in SrBaNbO Crystal Fiber* Appl. Phys. Lett. 86, 211907 (2005)

2 C. Huang, A.S. Bhalla, and R. Guo, *Real-Time Observation of Pulse Reshaping Using SrBaNbO Single Crystal Fiber In A Microwave Cavity* Appl. Phys. Lett. 86, 131106 (2005)

3 R. Guo, J. F. Wang, J. M. Povoa, and A. S. Bhalla, "Electrooptic Properties and their Temperature Dependence in Single Crystals of Lead Barium Niobate and Strontium Barium Niobate," *Materials Lett.,* **42,** 130-135 (2000).

4 Yamamoto, J. K. (1990). *Ph.D Thesis. University Park, Penn-State University*

5 Johnson, S., K. Reichard, Ruyan Guo, Developments in Dielectric materials & Electronic Devices, Ceramic Transactions, 277-287 Am. Ceram. Soc. Westville, OH (2004)

LABVIEW BASED FREQUENCY COUNTER AND VOLTMETER FOR A CONTINUOUS-WAVE QUADRUPOLE RESONANCE SPECTROMETER

Stephen A. Hall*, Michael A. Pusateri[+], and Jeffrey L. Schiano[#]

Department of Electrical Engineering
The Pennsylvania State University
University Park, PA 16802

*Undergraduate Student of
Department of Electrical Engineering
The Pennsylvania State University
University Park, PA 16802

ABSTRACT

We desire to implement a low cost continuous-wave (CW) quadrupole resonance (QR) spectrometer that is suitable for both research and undergraduate laboratory exercises. An existing CW spectrometer utilizes an external frequency counter and digital multimeter that are controlled using LabVIEW. The goal of this project is to replace these expensive instruments using the counters and analog inputs available on an inexpensive data acquisition board that is already a part of the CW spectrometer system. The key challenge is to measure frequency with a precision of 2 parts per million. In order to obtain this precision, it is necessary to replace the internal clock signal of the data acquisition board with that generated by a temperature stabilized oscillator. We present experimental results showing the frequency counter implemented with the data acquisition board and external reference clock provide the desired precision. Using the frequency counter and voltmeter implemented with the data acquisition board, we show the quadrupole resonance spectra obtained for the compound hexamethylenetetramine.

[+] Graduate Mentor
[#] Faculty Mentor

 187

INTRODUCTION

Quadrupole Resonance

Quadrupole resonance (QR) systems detect and discriminate specific nitrogen compounds using a search coil similar to those found in metal detectors. QR is an emerging technology for noninvasive, short-range detection of concealed explosives [1]. A primary advantage of QR is its ability to detect signals from the explosive components, such as RDX and TNT, within an explosive device. Unlike other technologies, QR detection systems can discriminate among different types of explosives and distinguish them from benign nitrogen compounds.

There are two methods for detecting quadrupole signals. In the first method, known as pulsed spectroscopy, the search coil broadcasts short duration radio frequency (RF) pulses and, if a target compound is present, receives a RF signal from nitrogen atoms during the interval between the applied pulses. In the second method, known as continuous-wave spectroscopy, the search coil produces a RF magnetic field whose frequency is swept across the range where the QR signal is expected. If the target compound is present, the nitrogen nuclei absorb energy and reduce the amplitude of the applied field. The first method is analogous to finding the impulse response of a system, whereas the second method is analogous to finding the frequency response of the same system. In fact, the Fourier transform of the signal obtained from pulse spectroscopy is identical to the absorption spectra obtained from the CW spectrometer.

In comparison to pulsed spectroscopy, CW spectroscopy offers two important advantages. In pulsed spectroscopy it is necessary to produce RF magnetic fields whose amplitude is on the order of 5 Gauss within the search volume. In comparison, CW spectrometers require significantly smaller RF fields, on the order of 0.05 Gauss. A smaller RF field is desirable both because it is less expensive to generate and its effect on electronic and biological systems can be neglected. Second, certain explosives such as pentaerythritol tetranitrate (PETN) are difficult to detect using pulsed spectroscopy because of unfavorable relaxation times. In contrast, the sensitivity of a CW detection system is not adversely affected by these unfavorable relaxation times.

Objectives

A previously implemented CW QR spectrometer[2,3] operates in conjunction with a Princeton Applied Research Model 124A lock-in amplifier, a Measurement Computing PCI-DAS6036 data acquisition board, a Hewlett Packard E3615A DC power supply, a Hewlett Packard 34401A digital multimeter, a Hewlett Packard 53131A universal counter, a GPIB interface board, and a personal computer. A LabVIEW program controls the operation of the CW spectrometer. The overall objective of this project is to replace the universal counter, the multimeter, and the GPIB interface board connecting these devices to the personal computer, by using the counters and analog-to-digital converter available on the data acquisition board.

The first objective is to eliminate the HP 53131A universal counter by replicating its function using an 8254 counter/timer integrated circuit (IC) present on the data acquisition board. The counter must be capable of resolving a 20 Hz difference between two frequencies at 5 MHz, or equivalently, a 4 part per million (ppm) precision.

The second objective is to eliminate the HP 34401A multimeter by replicating its function using a 16-bit analog-to-digital (A/D) converter on the data acquisition board. The multimeter monitors the output of the lock-in amplifier, whose output ranges from -10 Volts to + 10 Volts. The 0.3 mV resolution of the A/D converter exceeds the 10 mV resolution required for operation of the CW spectrometer.

EXPERIMENTAL DESCRIPTION

Design

Figure 1 shows the block diagram of the frequency counter formed from the 8254 counter/timer IC on the DAS6036 data acquisition board. The 8254 counter/timer IC contains three identical counters, two of which are accessible on the data acquisition board. Counter 1 counts the number of cycles, N, present in the input signal during a measurement window, T_s, determined by Counter 2. The observed frequency, f_o, is calculated as $f_o = N/T_s$.

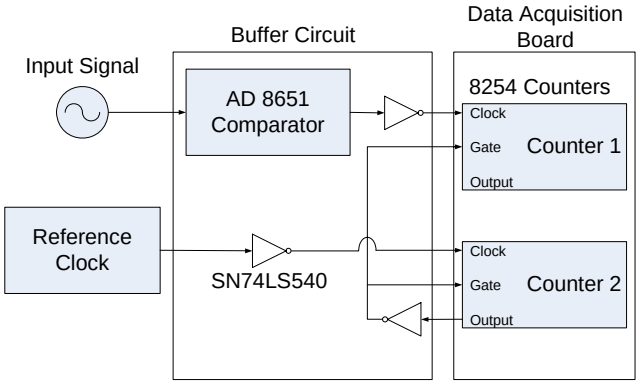

Figure 1: Block diagram of the frequency counter implemented with the data acquisition board.

As the input signals to both counters must be TTL-level compatible, an Analog Devices AD 8651 comparator converts the sinusoidal output signal from the CW spectrometer into a TTL-level signal. In order for Counter 2 to gate Counter 1, it is necessary to invert the logic level at the output of Counter 2, using a SN74LS540 IC. The output of Counter 2 also gates Counter 2 so that it stops counting at the end of the measurement window. LabVIEW loads, reads, and clears both counters.

As the frequency resolution is the reciprocal of the measurement window T_s, it is desirable to make T_s as large as possible. The value of T_s is the period that Counter 2 requires to count down from an initial count N_2 to 0. As the maximum value of N_2 is 65,535, and using a 10 MHz reference clock, we chose N_2 = 50,000, so that Counter 2 produces a measurement window of duration T_s = 5 ms. During the measurement window, Counter 1 records the number of rising edges of the input signal. For a single measurement window, the frequency resolution of $1/T_s$ = 200 Hz is inadequate. To improve the frequency resolution, we use N_m measurement windows to increase the effective measurement window to $N_m * T_s$. The observed frequency is $f_o = \langle N \rangle / T_s$, where $\langle N \rangle$ is the average count recorded by Counter 1 across the N_m measurement windows.

In part, the precision of the measurement $f_o = \langle N \rangle / T_s$ is determined by the stability of the 10 MHz reference clock. For this reason, in addition to using the 10 MHz clock on the data acquisition, we also performed measurements using an external oven controlled crystal oscillator (OCXO) mounted in a separate shielded enclosure. The stability of the OCXO is approximately three orders of magnitude higher than that of the onboard 10 MHz oscillator.

In comparison to the frequency counter, implementation of the voltmeter is trivial. The output voltage of the lock-in amplifier is connected to an A/D input channel on the data acquisition board. The input range of the 16-bit A/D converter is ±10V, and so the resolution of a voltage measurement is $20V / 2^{16} = 0.3$ mV. This resolution far exceeds the requirements for the CW spectrometer. To maximize the signal-to-noise ratio of a voltage measurement, we average 200 voltage measurements over a time window significantly less than the time constant of the lock-in amplifier.

Evaluation

A series of four experiments verify and assess the operation of the frequency counter and voltmeter. The first experiment measures the stability of the available 10 MHz reference clocks. In this experiment, a stable 10 MHz ± 1 mHz oscillator provides the reference clock to the system in Figure 1. The input signal is chosen as either the onboard 10 MHz clock or the external OCXO. We measure the frequency of each input using N_m =200, and repeat this measurement 1000 times. To assess the stability of the onboard and OCXO 10 MHz sources, we plot the frequency variation from the mean value across the 1000 experiments. The source that yields the smallest variation is chosen as the reference clock for the remaining experiments.

The second experiment aims to determine the smallest value of N_m that yields a standard deviation in frequency measurement that matches the desired measurement resolution of 20 Hz. This experiment uses the reference clock identified in experiment one, while the input signal, whose frequency is to be measured, is obtained form the stable 10 MHz ± 1 mHz oscillator. We report the frequency deviation from the mean, as well as the standard deviation of $\langle N \rangle / T_s$, as function of N_m.

The third experiment verifies the correct operation of the A/D based voltmeter. A regulated DC power supply set to 3 V is connected to the A/D input. As discussed earlier, an average of 200 A/D conversions form a single measurement of the input voltage. We obtain 1000 such measurements, and show the voltage deviation from the mean, as well as the standard deviation for the single measurements.

The fourth experiment is to verify the operation of the CW spectrometer by acquiring the spectra of hexamethylenetetramine (HMT), a commonly used chemical and a well-documented standard in QR spectroscopy [2]. HMT has a QR transition at 3.312 MHz at 17 ºC with a temperature dependence of -500Hz per +1ºC. For this reason, we searched for the room temperature transition frequency of HMT over the range of 3.304 to 3.310 MHz.

RESULTS

Figure 2 shows the results of the first experiment. The variation from the mean frequency is shown across a series of 1000 measurements, each obtained with $N_m = 200$. Comparing the results obtained using the internal 10 MHz clock (upper plot) to the external OCXO 10 MHz clock (lower) plot reveals that the variation in the frequency of the OCXO is three orders of magnitude smaller. Furthermore, while the mean value of the OCXO frequency is constant, that of the internal clock drifts. For these reasons, the OCXO is chosen as the reference oscillator for the frequency measurement system.

Figure 3 shows the effect of the number of measurements N_m on the accuracy (top) and precision (bottom) of measuring a 10 MHz ± 1 mHz source using the OCXO as the reference oscillator. A measurement window of $T_s = 5$ ms is used for each of the N_m measurement windows. The number of N_m measurement windows is varied from 1 to 1000. The upper plot shows the deviation of measured frequency from the true value of 10 MHz. For values of N_m measurement windows greater than 200, the accuracy of the measurement is within the desired 20 Hz resolution. The lower plot shows the standard deviation of $<N>/T_s$, as function of N_m, and therefore represents the precision of the measurement. Again, we observe that for values of N_m measurement windows greater than 200, the precision is adequate for the spectrometer. While values of N_m greater than 200 would improve both accuracy and precision of frequency measurements, we chose $N_m = 200$ to minimize measurement time.

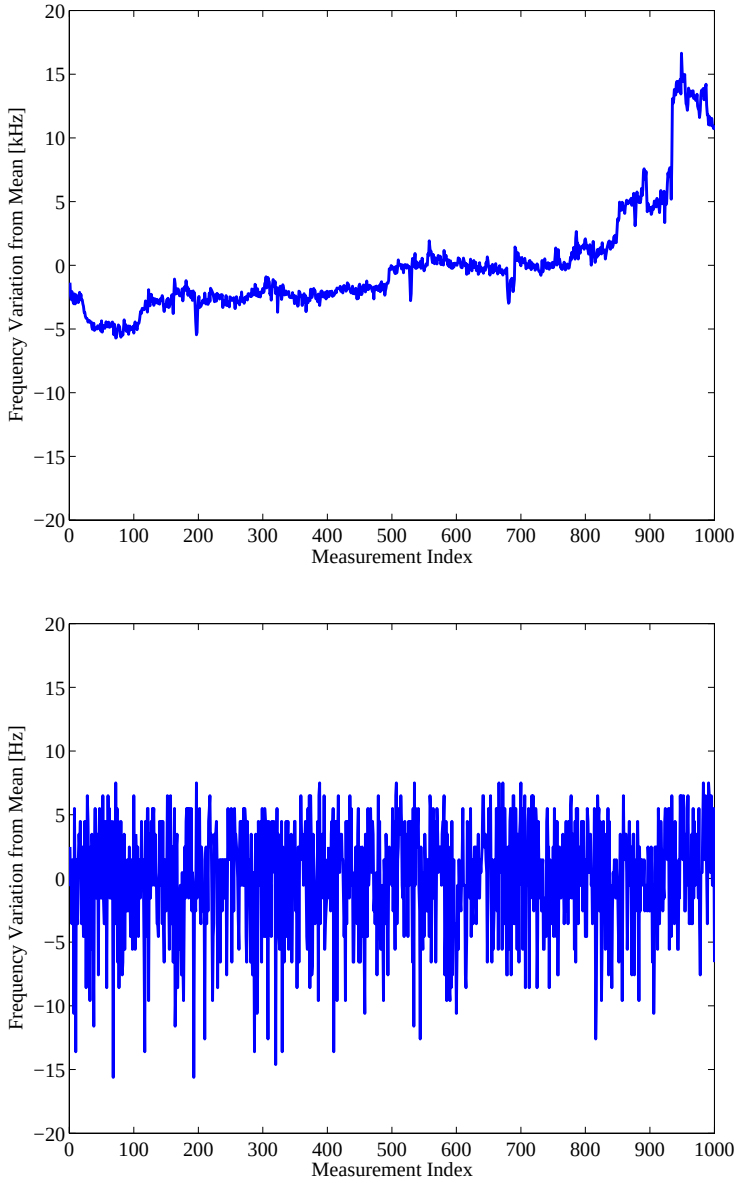

Figure 2: A comparison of the stability of the internal (top) and external OCXO (bottom) 10 MHz reference clocks.

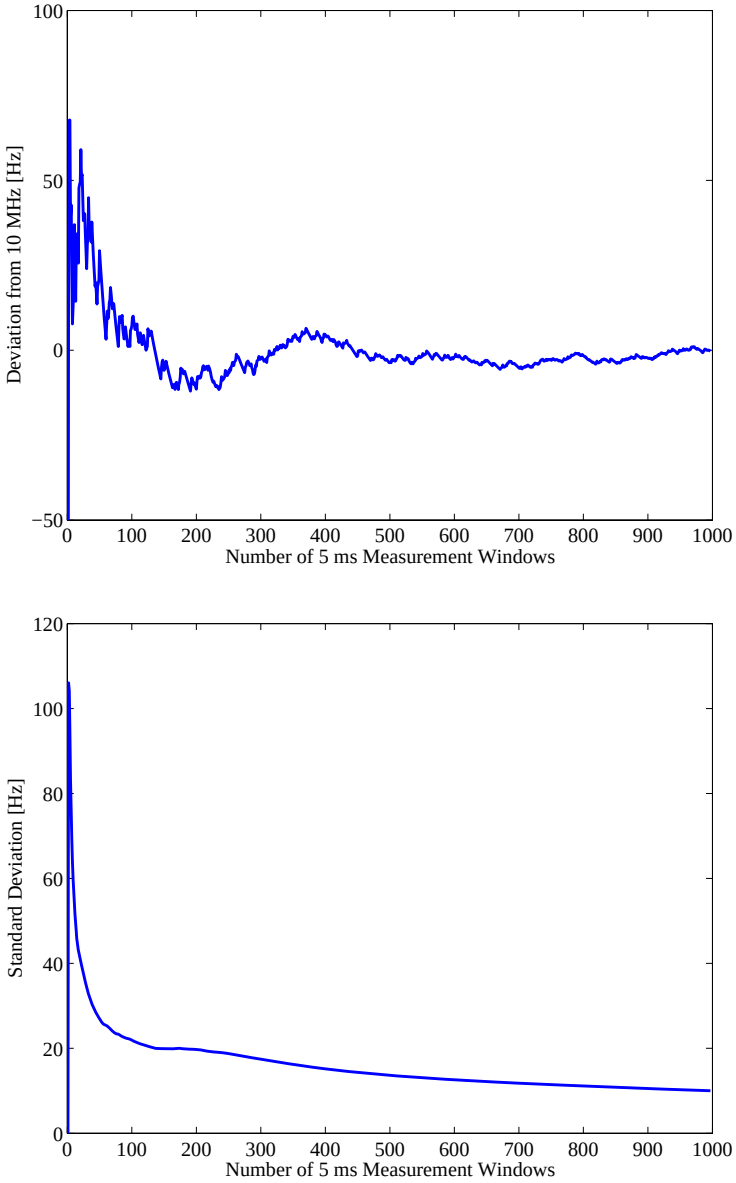

Figure 3: The effect of the number of measurements N_m on the accuracy (top) and precision (bottom) of measuring a 10 MHz ± 1 mHz source using the OCXO as the reference oscillator.

Figure 4 shows the results of the third experiment designed to assess the accuracy and precision of the A/D channel that measures the output voltage of the lock-in amplifier. A series of 1000 measurements were acquired, with each measurement representing the average of 200 A/D acquisitions. The upper plot shows the variation of the mean for each measurement from the applied voltage of 3 V and represents the accuracy of the voltage measurements, while the lower plot shows the standard deviation of each measurement and represents the precision of

the voltage measurements. Both the accuracy and precision of the voltage measurements exceed the requirements of the CW spectrometer.

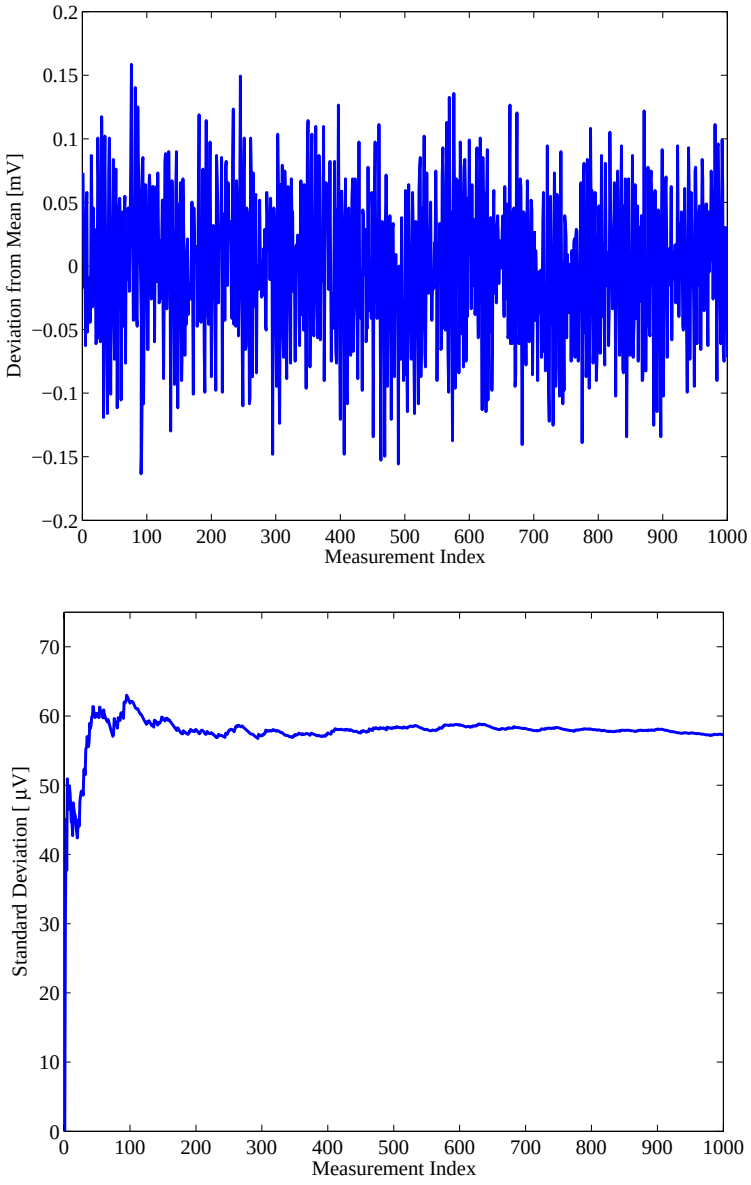

Figure 4: Measurement of the accuracy (top) and precision (bottom) of the A/D channel that measures the output voltage of the lock-in amplifier.

The final experiment is to acquire the QR spectra of HMT using the CW spectrometer with the frequency counter and voltmeter implemented using the data acquisition board. Figure 5 (top left) shows the personal computer, the CW spectrometer mounted on top of the cylindrical cryostat containing the sample,

and the lock-in amplifier. The small shielded box in front of the lock-in amplifier contains the OCXO. Figure 5 (top right) is a close-up view of the buffer circuit in Figure 1, mounted on a breakout panel for the data acquisition board. Figure 5 (bottom) shows the LabVIEW user interface for the spectrometer. The top plot within the interface display shows the successful acquisition of the HMT spectra.

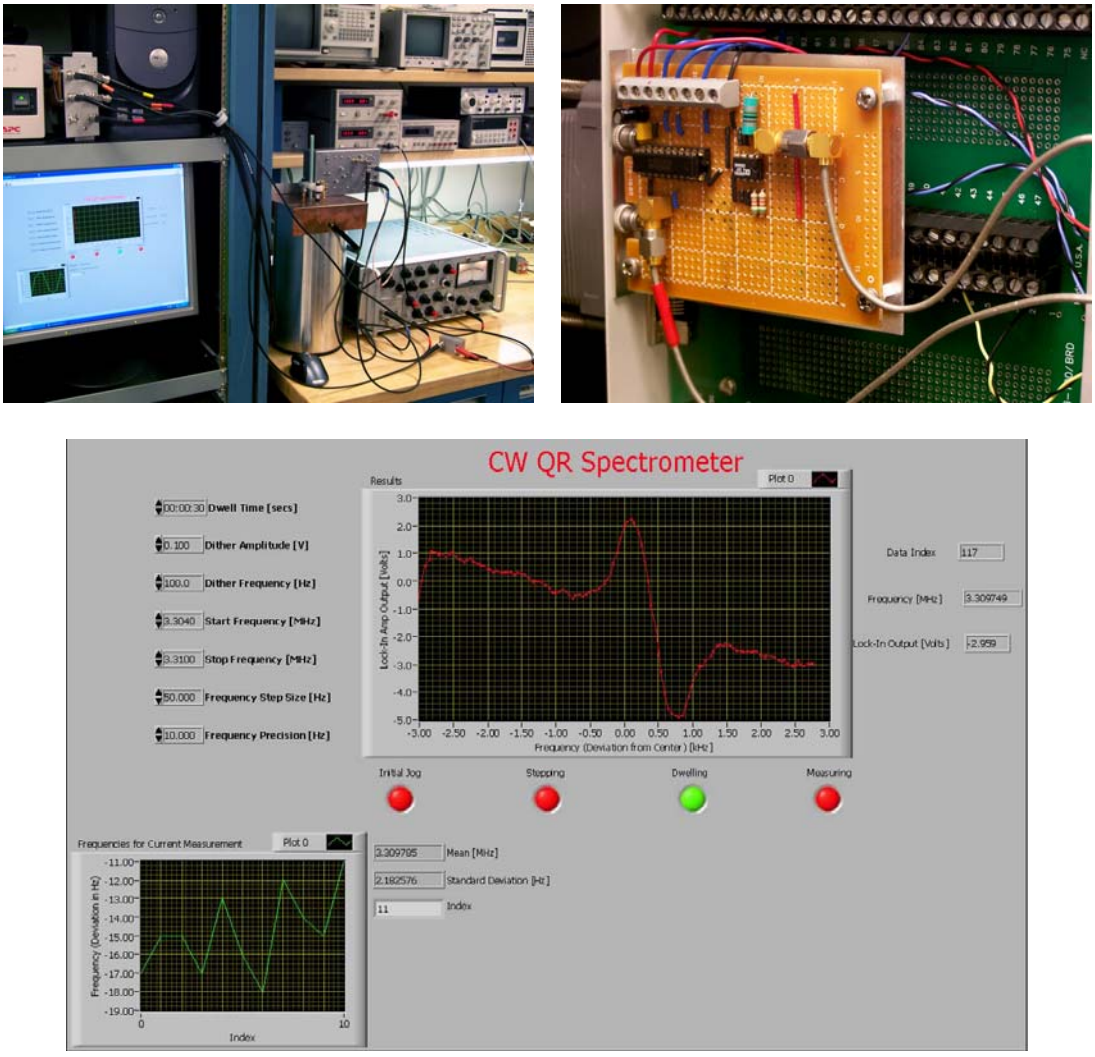

Figure 5: Photograph of the CW QR spectrometer (top left), the buffer circuit mounted within the data acquisition breakout panel, and the LabVIEW interface that shows the spectra of HMT obtained using the frequency counter and voltmeter implemented using the data acquisition board.

CONCLUSION

The final experiment conclusively demonstrates that the LabVIEW implementation of the DVM and frequency counter is suitable for acquiring QR spectra. Although the accuracy and precision of the frequency counter and voltmeter implemented with the data acquisition board are not as good as that of the Hewlett Packard instruments, they are sufficient for obtaining QR spectra. Replacing these instruments, and the GPIB board required to interface them, reduces the overall cost of the CW spectrometer by approximately $3,500.

ACKNOWLEDGEMENTS

I would like to thank Dr. Jeff Schiano, Mike Pusateri, Dan Swain, and Tony Skraba for their long hours of assistance with this project and for introducing me to QR spectroscopy. I would also like to thank Dr. Ruyan Guo, Dr. Ken Jenkins, Linda Becker, Amanda Skrabut, and Andrew Fontanella for administering the REU program at Penn State and providing myself and others the opportunity this summer to pursue production research as an undergraduate student. Finally, I would like to thank the National Science Foundation and the Pennsylvania State University at University Park for providing the funding and facilities that made this research possible.

This material is based upon work supported by the National Science Foundation under Grant No. EEC-0244030.

REFERENCES

[1] A. N. Garroway, M. L. Buess, J. B. Miller, B. H. Suits, A. D. Hibbs, G. A. Barrall, R. Matthews, and L. J. Burnett, "Remote Sensing by Nuclear Quadrupole Resonance," *IEEE Transactions on Geoscience and Remote Sensing,* **39** (6) 1108-1118 (2001).

[2] J. Lee, S. H. Choh, "Robinson-type Nuclear Quadrupole Resonance Spectrometer Adapted to Field-Effect Transistors", *Review of Scientific Instruments*, **53** (2) 232-235 (1982).

[3] C. L. Hilferty, *Design and Analysis of a Continuous-Wave Quadrupole Resonance Spectrometer*, Thesis, Pennsylvania State University, 2003.